Fast and ultrafast electron microscopies for skyrmions and plasmonics

Thèse N° 9663

Présentée le 5 juillet 2019

à la Faculté des sciences de base
Laboratoire pour la microscopie et la diffusion d'électrons
Programme doctoral en physique

pour l'obtention du grade de Docteur ès Sciences

par

Gabriele BERRUTO

Acceptée sur proposition du jury

Prof. H. M. Rønnow, président du jury
Prof. F. Carbone, directeur de thèse
Dr M. Kociak, rapporteur
Dr R. Krahne, rapporteur
Prof. D. Grundler, rapporteur

2019

ÉCOLE POLYTECHNIQUE
FÉDÉRALE DE LAUSANNE

Il sentiero girava tra gli scogli, sopra la riva. L'acqua non si vedeva: solo un clavier di barbagli sui frangenti lontani. A bei momenti si sentiva sciabordare.
–È bello sentire il mare che lavora.
–Si sente dal tuo paese?
–Si vede, ma distante, fra le rupi.

Francesco Biamonti, ref. [1].

Acknowledgements

First, I would like to express my gratitude to Fabrizio Carbone for having allowed me to carry out my doctoral studies under his supervision in the LUMES group. I deeply appreciated the research freedom and trust (while assuring guidance and support) my colleagues and I were accorded with throughout the years I spent here. I would also like to thank Henrik Rønnow, Mathieu Kociak, Roman Krahne, and Dirk Grundler for having kindly accepted to be part of the doctoral commission.

Little of what I wrote in this thesis would have been possible without the collaboration with my colleagues Ivan Madan and Giovanni Vanacore. I'm mostly indebted to you two for all the interesting work done together, for your patience, our never-ending conversations that greatly taught me, the irreverent coffee breaks, the scientific commitment, and all the time spent with buoyancy in the lab. In essence, for our friendship.

A warm thank you to the many other people I had the privilege to work with. In particular to Yoshie Murooka and Tom Lummen for the early works on Lorentz microscopy and plasmon imaging, respectively: you considerably helped me at the beginning of the Ph.D. To Asuka Nakamura for the work on transition metal dichalcogenides and your being an exquisite lab mate. To Simone Borroni and Edoardo Baldini for the project on broadband transient reflectivity on Cu_2OSeO_3, to Enrico Pomarico for the work with the OPA, and to Francesco Pennacchio for the ultrafast electron crystallography on Fe_3O_4, besides for happily sharing the same office for 3 years. Furthermore, I'm grateful to Luca Piazza, whose work allowed me to inherit such an interesting setup, and Thomas LaGrange for the wise expertise, support, and enthusiasm with electron microscopy. I should acknowledge all the LUMES and LSU colleagues, past and present, of the unforgettable moments we shared in the last years, and of the nice environment you created to work in. While sure to write down an inexcusably partial list, I cannot avoid mentioning Dominik, Raji, Andreas, Leonor, Giulia, Le, Paolo, Vittorio, André, Francesco B., Tania, Benjamin, Gloria, Luca L., Oliviero, Thomas R., Lijie, Malte, and Fabio... and many others!

In EPFL and Switzerland I benefited from the presence of a passionate group of skyrmion aficionados, mostly within the Nanoskyrmionics initiative. Among them, I'm grateful to Thomas Schönenberger for the collaboration, and more in general to all the LMGN and LQM members. I am indebted to Susmita Saha and Laura Heydermann from ETHZ&PSI for the stimulation discussions, encouragement, and patience about the Néel skyrmion project. The collaboration with Raymond Lamb and Damien McGrouther from Glasgow Un. has been crucial for sample preparations and for the work on pulsed domain wall motion in Py nanowires.

The projects related to electron-light and electron-plasmon interaction would not be as they are without the terrific work of Javier García de Abajo from ICFO. I enormously appreciated his availability at discussions and the skill to transform fuzzy impressions into neat ideas. I wish to also thank Kangpeng Wang and Ido Kaminer from Technion for the enthusiasm and flourish of innovative ideas they brought to our lab.
In the last 4 years I measured a decently large amount of samples, coming from several collaborations prof. Carbone created. In addition to the collaborations with Glasgow Un. and ETHZ-PSI, I have to mention Yoshihiko Togawa from Osaka Prefecture Un. (FeGe), Kostya Novoselov and his co-workers from Manchester Un. (few-layer graphene and $MoTe_2$), Andrea Ferrari from Cambridge Un. (graphene), Yoshinori Tokura from RIKEN (CoZnMn), Andrea Toma from IIT (plasmonic structures), Arnaud Magrez from EPFL (Cu_2OSeO_3), Kyoko Ishizaka from RIKEN ($MoTe_2$ and MoS_2), Regina Ciancio from CNR-INFM (MgB_2), Xuewen Fu and Yimei Zhu from Brookhaven Nat. Lab. (VO_2 and Py nano-geometries), and Luis Liz-Marzán from San Sebastián (AgAu nanowires). Albeit only a small selection of those samples is cited again in the thesis, I want to express my gratitude to all the collaborators who provided them. The FIB work has been done by Raymond Lamb, Yoshie Murooka, Ivan Madan, and Thomas Schönenberger.
The material in this thesis is structured around few articles I co-authored, which are the result of a collaborative effort. While it is impossible to credit all the intellectual contributions, I still try to make few of them explicit. In particular, the FDTD and electron-beam calculations in Chap. 4 come from Paolo Biagioni (PoliMi) and Vincenzo Grillo (CNR), respectively. The density matrix calculations in Sec. 3.2.4 and the Fourier-analysis in Sec. 4.3.2 were performed by Enrico Pomarico, while the data analysis in Sec. 3.1.3 has to be credited to Tom Lummen. The 2T model simulations in Sec. 5.3 were carried out by Ivan Madan, and the PINEM simulations in Chap. 2, Chap. 3, and Chap. 4 by Javier García de Abajo and Giovanni Vanacore.
The LN_2 holder we used has been borrowed from CIME, for which I thank Marco Cantoni and all the CIME staff. The direct electron camera was on loan from Quantum Detectors while for TEM maintenance I received invaluable technical assistance from Jeol (France) in the person of Lionel Cachoulet. Practical work in the lab was facilitated by the staff of the mechanical and electronic chemical workshops.
In the meantime, I carried out my teaching assistant duties with Marina Pivetta, to which I am very grateful for having been such a good model for me concerning education.

I'm finally obliged to Fabrizio, Francesco, Ivan, Gianmaria, Dirk Grundler, Riccardo Ravasio, and Mario Geiger for having given their feedbacks on longer or shorter parts of the dissertation manuscript. Ça va sans dire, every mistake, typo and omission is solely my fault.
To conclude, I would like to thank all my Lausanne friends from THEOS, LMSC, PCSL, LMGN, LSU, LUMES, FIMAP, SUNMIL, FSB Running Team [...], Gianluca, Riccardo, and my family, who were all very supportive outside the lab.

Lausanne, 11 June 2019 Ghil Berruto

Abstract

In recent years, topology gained a central role in physics. We learnt that energetics could be often explained better by classes of objects defined by having *qualitative* differences. In today's jargon, we say they are *topologically distinct*. The process of creation and annihilation of physical objects with topological charge has peculiar aspects, because it cannot proceed by continuous deformations. The consequent protection of these physical states against internal and external perturbations can therefore be striking.
In condensed matter, topologically-protected states are found in electronic systems in solids, spin textures, and particle or quasiparticle wave functions. Because of their general reluctance to change topological state, methods to manipulate their topological charge should be thoroughly designed.

In this dissertation, I illustrate dynamical manipulation of a topological charge in two distinct –yet connected– research areas: nanoscopic spin textures and free electrons. In both cases, the manipulation is performed via the interaction of ultrashort light packets with the system under investigation.
In the first, topologically nontrivial spin vortices, called skyrmions, are injected and controlled by the laser pulses. In FeGe, Bloch-type skyrmions are investigated via static, in-situ, and time-resolved Lorentz electron microscopy. Spin supercooling has been found responsible for the creation and stabilization of skyrmions in large regions of the phase diagram, controlling the amount of topological charge in the material. The cooling rate ensuing from the excitation of the material with strong laser pulses can reach tremendous values. This work enabled an estimate of the speed limit for laser-induced writing and erasing of such skyrmionic states.

In the second case, circularly-polarized light is used to convert an electron plane wave into an electron vortex with nonzero topological charge. A chiral plasmon photoinduced at the edges of a nanohole in a metal transfers the vortex phase structure to the electron beam via stimulated plasmon absorption and emission.
In a wider picture, the precise tailoring of the free electron wave function can be obtained by electron-photon inelastic scattering in proximity of a physical object, as extensively discussed in this thesis. The new awareness of our tools to control matter waves led to the implementation of an innovative type of time-domain holography, which can be used to image nanoscopic, propagating electromagnetic fields.

Besides the single results exemplified in the different chapters, such as the topological-charge manipulation studies, this thesis contributes to the refinement of time-resolved microscopy with ultrafast electrons for the investigation of magnetic, electronic, and structural degrees of freedom. Ideas for further original experiments that could push the discussed physics to new boundaries are debated throughout the chapters.

Keywords: Ultrafast transmission electron microscopy, In-situ microscopy, Lorentz microscopy, Pump-probe, Photon-induced near-field electron microscopy, Vortex beams, Surface-plasmon polaritons, Skyrmions, Bloch, Néel.

Résumé

La topologie joue un rôle de plus en plus remarquable dans la physique moderne. En effet, les propriétés spectroscopiques sont souvent bien expliquées par des classes d'objets avec des caractéristiques *qualitativement* différentes, qu'on peut associer à des genres topologiques. Le processus de création et annihilation d'une charge topologique ne peut pas survenir à travers des déformations continues du système. La protection topologique rend ces systèmes extrêmement robustes contre les perturbations internes et externes.
Dans la physique de la matière condensée, des états topologiquement protégés sont présents pour des systèmes électroniques des cristaux, pour des textures de spin, et pour des fonctions d'onde de particule et quasi-particule. Vu la réticence de ces systèmes à changer leur état topologique, les procédures pour manipuler la charge topologique doivent être conçues minutieusement.

Dans cette thèse de doctorat, je vais montrer la manipulation dynamique d'une charge topologique dans deux domaines de recherche distincts : des quasi-particules magnétiques confinées dans des espaces nanométriques, et des électrons libres. Dans les deux cas, la manipulation est possible grâce à une lumière à forte pulsation qui interagit avec le système physique.
Dans le premier cas, des vortex chiraux de spin, appelés skyrmions, sont injectés et contrôlés par les pulsations lumineuses. Les skyrmions dans une lamelle de fer-germanium sont analysés dans l'espace réel avec la microscopie de Lorentz. La surfusion des spins a été trouvé responsable de créer et rendre stables les skyrmions ; Donc le laser peut être utilisé pour contrôler la quantité de charge topologique dans le système. Au moyen d'une technique pionnière, la microscopie Lorentz ultrarapide, on a pu estimer la limite de vitesse pour écrire et effacer les skyrmions dans notre système physique.

Dans le deuxième cas, un faisceau de lumière polarisée circulairement est employé pour convertir une onde plane électronique en un vortex avec une charge topologique non nulle. Un plasmon chiral est photo-créé aux bords d'un trou nanométrique dans un métal. Le plasmon stimule l'émission et absorption des photons par les électrons quasi-relativistes, et ainsi les électrons prennent la structure de phase chirale du champ voisin.
Dans une perspective plus ample, il est possible de contrôler avec précision chirurgicale les fonctions d'onde des électron libres, grâce à la diffusion inélastique des électron qui interagissent avec des photons à proximité d'un objet physique. La connaissance et compréhension de ces mécanismes nous a fait développer une technique holographique dans le domaine du

temps, qui permets de prendre des images des champs électromagnétiques se propageant dans des nanostructures.

A part les résultats présentés le long de ces chapitres, cette thèse contribue au perfectionnement de la microscopie électronique ultrarapide pour l'étude des degrés de liberté électroniques, magnétiques, et structuraux. Des idées originales et innovantes pour des expériences futures sont aussi discutées.

Keywords : Microscopie électronique ultrarapide, microscopie in situ, microscopie de Lorentz, Études de pompe-sonde, Microscopie électronique du champ voisin photo-créé , Faisceaux à vortex, Polariton-plasmon de surface, Skyrmions, Bloch, Néel.

Sinossi

La topologia ha assunto in tempi recenti un ruolo sempre più centrale in fisica. In effetti le dinamiche spettroscopiche di molti sistemi possono essere spiegate da classi di oggetti con caratteristiche *qualitativamente* differenti, descrivibili da un genere topologico. Il processo di creazione e annichilazione di cariche topologiche ha la proprietà di non poter avvenire attraverso deformazioni continue del sistema. La protezione topologica può rendere questi oggetti straordinariamente robusti rispetto a perturbazioni interne ed esterne.
In fisica della materia condensata, stati topologicamente protetti sono presenti in sistemi elettronici di cristalli, in trame di spin, e in funzioni d'onda di particella e quasiparticella. Dato che questi sistemi sono intrinsecamente restìi a cambiare il loro stato topologico, i metodi per manipolare la carica topologica devono essere pianificati minuziosamente.

In questa dissertazione sono presentati risultati sperimentali di manipolazione dinamica della carica topologica in due dominî di ricerca distinti: quasiparticelle magnetiche confinate in spazî nanometrici e onde di elettroni liberi. In entrambi i casi, impulsi di luce ultracorti sono utilizzati per cambiare gli stati del sistema, dando loro le proprietà topologiche volute.
Nel primo sistema, vortici chirali di spin, detti skyrmioni, sono iniettati in una lamella metallica da impulsi laser. Le proprietà magnetiche della lamella metallica (di ferro-germanio) sono studiate nello spazio reale, grazie alla microscopia elettronica di Lorentz. Si è così indentificato un meccanismo di sopraffusione come responsabile della stabilizzazione degli skyrmioni in ampie regioni del diagramma di fase (scrittura ed eliminazione); in questo modo, l'eccitazione laser permette di controllare il numero di cariche topologiche nel sistema. Grazie a studî pioneristici di microscopia Lorentz risolta in tempo, si è inoltre identificato un limite alla velocità di scrittura ed eliminazione di stati skyrmionici con il nostro meccanismo di scrittura.

Nel secondo caso, si mostra come usare impulsi di luce polarizzata circolarmente per trasformare un'onda piana elettronica in un vortice elettronico con carica topologica. Il meccanismo di creazione del vortice avviene grazie ad un plasmone chirale eccitato in un piccolo foro metallico. Il campo del plasmone stimola gli elettroni quasi-relativistici ad assorbire ed emettere fotoni, in questo modo mutuando la struttura di fase del campo plasmonico, e quindi assumendo la topologia di fascio a vortice.
In una prospettiva più ampia, si riporta come un controllo preciso e adattabile delle funzione d'onda di elettroni liberi può essere realizzato attraverso un processo di diffusione inelastica tra fotoni ed elettroni in prossimità di un oggetto fisico. La conoscenza di come controlla-

re queste interazioni elettrone-fotone ha permesso di sviluppare un metodo olografico nel dominio dei tempi per creare immagini di campi elettromagnetici propaganti in materiali nanostrutturati.

Oltre ai singoli risultati presentati nei vari capitoli, questa tesi contribuisce alla rifinitura della microscopia elettronica ultraveloce per lo studio di gradi di libertà magnetici, elettronici e strutturali. Questo permette di presentare la discussione di alcune idee innovative per esperimenti futuri.

Parole chiave: Microscopia elettronica ultraveloce, Microscopia in situ, Microscopia di Lorentz, Esperimenti di eccitazione-verifica, Microscopia elettronica di campo vicino fotostimolato, Vortici elettronici, Plasmoni-polaritoni di superficie, Skyrmioni, Bloch, Néel.

Contents

Introduction

Preamble

The curiosity of humans intent on observing natural phenomena is innately linked to two main interconnected questions: how are objects located in space? How do they evolve in time? More properly, we ask ourselves which are the changes in object location. The concept of time is introduced as the dimension in which the position change of a moving object takes place. Humans predominantly perceive movements through sight. Visible light contains the majority of the information we use to comprehend the surrounding world. Still, human sight can directly probe space only with micrometer precision, and time with ~hundred milliseconds. Despite this biological limitation, we innately perceive that objects can be smaller, their motion faster.

Throughout history, humankind developed ingenious techniques to investigate nature, and generously speculated on what is small and what is fast. However, only with the advent of the optical microscope first, and photography later, a constant progress in probing small *or* fast scales could have started off. Since then, technological development allowed to observe matter at increasingly small spatial lengths.
Due to the diffraction limit, visible light cannot resolve objects better than few tens of micrometer. Starting from the last century, higher-frequency electromagnetic radiation, massive particles, confined light, and scanning tips have then been employed to investigate matter down to the atomic scale, and sometimes below. But what about its evolution in time? To track the motion of what is small, we need to be fast, because a small object will cover its characteristic length in a very short time.

Incidentally, the access to short (ns), and then ultrashort (ps, fs, as) light pulses has been made possible by advancements in laser physics. Such pulses are currently employed to probe the atomic and electron dynamics at the ultrafast time scale. When the events are evolving on such scale, it becomes practically impossible to follow their dynamics in real time, just with a fast detector. A shift in paradigm has to be adopted, in which the time scale of the physical phenomenon does not coincide anymore with the laboratory time. This new paradigm is embraced by the *pump-probe* approach, Fig. 1a.

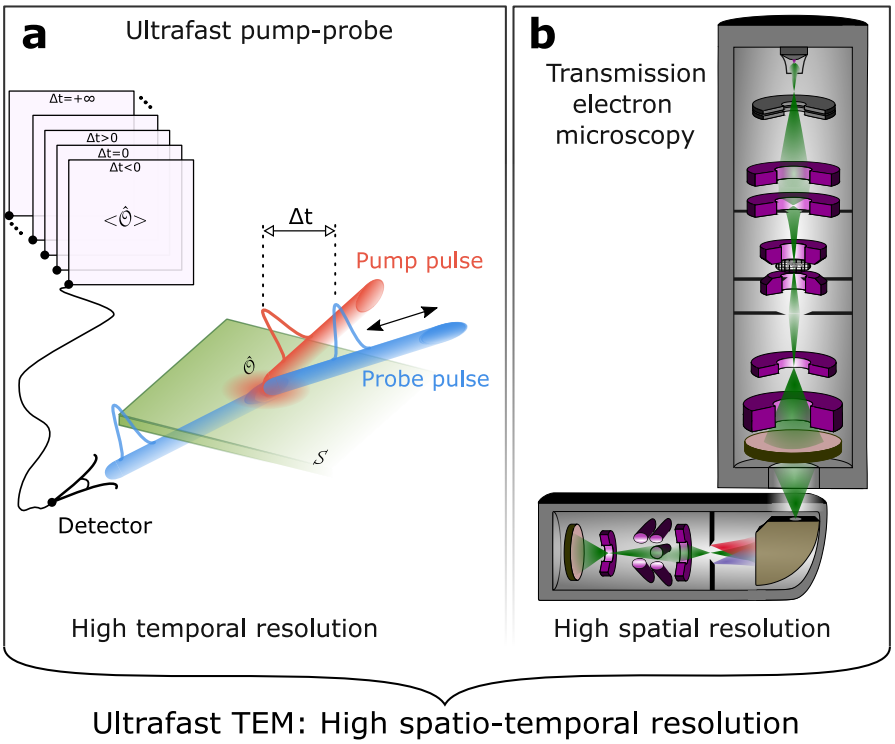

Figure 1 – **a**, Conceptual schema of pump-probe measurements. **b**, Graphical representation of a transmission electron microscope (TEM). For details see Chap. 1. The combination of **a** and **b** leads to simultaneous high spatial and temporal resolution.

In pump-probe experiments, the physical system S under study is excited by a short pulse (the pump), which initiates the dynamics. A second pulse (the probe) ideally serves as a nonperturbing tracker of the system evolution. The changes induced by the pump to a set of observables $\hat{O}$ are hence monitored by the probe pulse, and recorded by a detector. By varying the pump-probe delay time Δt from negative values up to $\Delta t \to +\infty$, the evolution dynamics of $\hat{O}$ can be reconstructed from its origin till the relaxation to the final configuration. The probe after the interaction with S is typically measured either in transmission (as shown in Fig. 1a), reflection, or emission –if the detected quantity is generated by the interaction of the probe with the system. Pump and probe pulses can be formed by photons, free electrons, ions, electric currents, or any other impulsive stimulus. The measurement of $\langle \hat{O} \rangle$ can consist of a spectrum, a diffraction pattern, an image, and so on.
Two considerations should be made. First, since the experiment has to be repeated many times (say, millions, or billions), only those processes that are fully repeatable can be studied. The final configuration must coincide with the original one, at least for the set of observables that are monitored. Second, this technique inherently studies out-of-equilibrium phenomena, the pump pulse having driven the physical configuration away from its equilibrium state.

Optical pulses as short as 90 fs have been reported in 1981 [2], as an advancement on the passive mode-locking of dye laser technique [3]. A large technological breakthrough happened in 1991, when self-mode-locking in Ti:sapphire lasers was achieved [4, 5]. The combination of that technology with chirped-pulse amplification [6] resulted in the development of table-top high-power fs lasers, which allowed for the full emergence of a new field: ultrafast science [7].

Researchers realized that these techniques allowed not only to investigate the fast evolution of physical or chemical systems, but also to access to the fascinating realm of out-of-equilibrium science. In a nonequilibrium state, the many degrees of freedom of a system can often be disentangled along the time coordinate. For instance, fermionic (electrons) and bosonic (phonons, magnons, excitons...) nonthermal populations in solids have different evolution in time; the coupling between these degrees of freedom can be studied as a function of the temporal coordinate, instead than in their complex static energy landscape. This aspect can be particularly important in strongly correlated systems [8]. Also, coherent bosonic modes can be excited impulsively or displacively [9, 10], and the energetics of those modes retrieved by Fourier analysis, exploiting the most basic relation between energy and time. Moreover, ultrashort pulsed excitations can be used to drive a system into new phases or states that are not accessible via adiabatic transformations. Or access to known phases via new nonequilibrium paths. Such photoinduced states can be transient or permanent. Striking examples of the former case are the insulator-metal transition in metal oxides, such as VO_2 [11–14], or the transient enhancement of superconductivity [15, 16]. The latter case can be showcased by the metamorphosis of TaS_2 into a hidden state [17].

Most efforts in ultrafast science have been devoted in the spectroscopic domain [18], with a variety of techniques employing photon frequencies ranging from the THz [19] to the hard X-rays [20], passing through the infrared, visible, UV, and soft X-ray regimes. Special attention has been devoted to $h\nu \approx 1.55$ eV, the fundamental frequency of Ti:sapphire lasers. Matter has been studied in solid, liquid, gas, and plasma phases. The focus of each technique can be diversified. For instance, transient reflectivity, absorption, and angle-resolved photoemission spectroscopy (ARPES) focus more on the electronic degrees of freedom, X-ray or electron diffraction on the structural component, and magneto-optical Kerr effect (MOKE) or X-ray magnetic circular dichroism (XMCD) [21] to the magnetic variables.
However, all these techniques can have superb time, energy, or momentum resolution, but very poor spatial resolution. The resolution in space is typically achieved by tightly focusing the probe to the sample, and eventually scanning its position, as in scanning transmission X-ray microscopy (STXM) [22]. The focusing performance for visible light is inherently limited by diffraction, while for X-rays it is currently limited by the optics.
On the other side, many techniques guarantee extremely high spatial resolution. Is it possible to combine high spatial and temporal resolution in the same instrument simultaneously? Ideally, we would aim at investigating matter down to the atomic scale, while preserving a high temporal resolution. Moreover, is it possible for such instrument to have high energy and

momentum resolution as well?

Here we can introduce the hero of this little scientific saga: *ultrafast transmission electron microscopy*, UEM in short, see Fig. 1.
We now ought to prevent a naïve reader that inadvertently opened this dissertation from thinking that we do possess to date an instrument with 1 Å and 1 fs simultaneous resolution. That said, in recent years ultrafast electron microscopy developed impressively along many directions. It qualified as a formidable ultrafast spectro-microscopy tool, with simultaneous sub-ps, nm, and sub-eV resolution.

Before ending this introductory section, I compel to attempt answering the common physicist's question: "why real space?"
Indeed, everybody sees why microscopy is vital for material science, biology, and engineering. However, one may argue that physics is intimately governed by energetics, and the relevant quantities in condensed matter are elegantly defined in reciprocal space. Not in real space. So?
Real space is also the reign of complex (and therefore intriguing) physics, where edges, defects, interfaces, and morphological landscapes strongly influence and even dominate the observable phenomena. There, the beautiful physics of infinite systems is bent down by confinement and imperfections. And how this happens, how light couples with real clusters of atoms, irregular particles and nanostructures, has to be treated (also) from a real space perspective.
Moreover, as we will see in the dissertation, the ultrafast microscope turned out to be a good apparatus for the investigation of the high-energy electron beam itself. With reference to Fig. 1a, we can choose $\hat{O}$ to be an observable *of* the probe. The pump is used to modify the probe, and the system S (if present) serves just to create the conditions for pump and probe to interact. This little shift in perspective guided us into a new class of experiments on the physics of the electron wave functions.

Scope of the thesis

With this thesis I would like to give few modest contributions to the advancement of time-resolved electron microscopies in the fast (10^{-9} s) and ultrafast (10^{-15} s) time scales. These contributions can be roughly catalogued in two distinct areas of interest. The first studies and exploits the inelastic interaction between high-energy electrons and electromagnetic fields. This inelastic interaction is possible each time that the light has enough momentum components outside the $k = \omega/c$ line to allow for energy-momentum conservation in the scattering event (e.g. in presence of localized fields, but not exclusively).
I aim at presenting a broad-enough picture of how these interactions take place, and how we can profit from them to image electromagnetic fields at the nanoscale, extending -if I am allowed to say- the domain of photon-induced near-field electron microscopy (PINEM).

The second area of interest concerns compact magnetic swirling textures, called skyrmions. The formation of these exotic twisted spin patterns is investigated by time-resolved Lorentz electron microscopy, with short light pulses used to trigger and control their dynamics. I hope to convey the idea that it is possible to use light pulses to modify their states, with tailored moves in the complex magnetic energy landscape.

Outline

In Chap. 1, the experimental techniques are introduced. First, I present the static and ultrafast electron microscopy state of the art, followed by a description of the setup I worked on, with a particular focus on the novelties recently implemented. These novelties include a nanosecond stroboscopic setup, and the characterization of a direct electron camera.
In Chap. 2, photon-induced near-field electron microscopy is outlined in its theoretical and experimental aspects. The electron-photon inelastic scattering from a semi-infinite light field is presented in the second part of the chapter, and its experimental characterization discussed thoroughly.
Chap. 3 is dedicated to imaging propagating surface-plasmon polaritons at the nanoscale. Two sets of experiments are examined, reflecting the advancement in the ability to visualize electromagnetic fields in transmission electron microscopy. In the first, the envelope of an ultrafast plasmonic wave packet is seen as it propagates out of a nanocavity array; in the second, the precise wavefronts of the plasmonic wave are imaged, and both wave carrier and envelope are tracked during the dynamics. This improved skill is the result of having developed a time-domain holographic approach, presented partly in Chap. 2 and more in details in Chap. 3.
The main topic of Chap. 4 is shaping the wave structure of free electrons. The first realization of an ultrafast electron vortex beam is presented. In the last part of the chapter, few considerations on imaging photo-excited near fields with ultrafast electrons are added, and a case of mapping a low-energy collective mode by tunable photon energy excitation is shown.
Finally, in Chap. 5, static and time-resolved Lorentz microscopy are introduced as methods to image magnetic field configurations in thin specimens and observe their light-induced changes. After a brief overview of skyrmionics, the laser-induced creation of skyrmions in a FeGe lamella is reported, and the speed limit of this kind of creation-annihilation process extracted.

1 Time-resolved electron microscopies

This chapter is organized as follows. In Sec. 1.1 and Sec. 1.2 I introduce static and time-resolved electron microscopies, while Sec. 1.3 focuses on our fs-ultrafast electron microscopy (UEM) setup at the Laboratory for Ultrafast Microscopy and Electron Scattering (LUMES), École Polythechnique Fédérale de Lausanne (EPFL). The development of a stroboscopic ns-TEM is the topic of Sec. 1.4. Finally, in Sec. 1.5 new opportunities recently made possible by fast detectors are discussed.

1.1 Electron microscopy

1.1.1 History

Transmission electron microscopy (TEM) [23] was developed in its early days by Knoll and Ruska in Berlin [24]. While optimizing magnetic electron lenses for cathode-ray oscilloscopes, they realized it was possible to form magnified images using electrons [25]. They immediately envisaged that electron images could overcome Abbe's resolution limit for visible-light microscopes [26, 27],

$$d = \frac{\lambda}{2n\sin\theta} \tag{1.1}$$

with λ wavelength, n refractive index, 2θ convergence angle, despite apparently ignoring the matter-wave relation introduced by de Broglie few years earlier [28]. "*Knoll and I hoped for extremely low dimensions for the electrons. As engineers we did not yet know about [...] de Broglie.*" Ruska confessed in his Nobel lecture [25].
Eq. 1.1 bounds the resolution of standard visible-light microscopes to 200 nm, or worse. A technique that could allow to break that limit would at that time have been disruptive. And indeed it was. Nowadays, many superresolution optical microscopies have been developed [29, 30], exploiting for example fluorescence [31] or near fields [32]. These optical microscopies can be superb in imaging particular systems, as molecular complexes, but lack of general applicability, and for example are unsuitable to resolve the atomic structure of solid state

matter.
Electron microscopes served therefore both as very practical tools to image matter at higher magnifications, and secondarily as a beautiful proof of concept for the fundamentally quantum mechanical de Broglie's matter-wave hypothesis [28]:

$$\lambda = \frac{h}{p} = \frac{h}{\gamma m_0 \beta c} = \frac{hc}{\beta m_0 c^2}\sqrt{1-\beta^2}. \tag{1.2}$$

Here h is the Planck constant, c the speed of light in vacuum, p the linear momentum, m_0 the rest mass, $\beta = v/c$ the particle speed in units of c, and $\gamma = 1/\sqrt{1-\beta^2}$ the relativistic Lorentz factor. Electrons accelerated as low as 10 kV have an associated wavelength as small as 12 pm, more than 4 orders of magnitude lower than the visible-light resolution limit, and much smaller than the diameter of an atom.
Once considered Einstein's relation for the energy $E^2 = p^2c^2 + m_0^2c^4$, the de Broglie wavelength (Eq. 1.2) of an electron accelerated by an electric potential V can be calculated as

$$\lambda = \frac{hc}{\sqrt{q_e V (q_e V + 2m_0 c^2)}}, \tag{1.3}$$

where $-q_e = -|q_e|$ is the charge of the electron.
For $V = 200$ kV, a common value for commercial instruments, included the TEM used in this dissertation, we get $\beta = 0.695c$, $\gamma = 1.39$, and $\lambda = 2.5$ pm. Such value of λ is so low that in practice the resolving power of electron microscopes is not limited by the diffraction limit, but by the aberrations of the electron optics [23]. Spherical and chromatic aberrations are the most deleterious. Once they are sufficiently corrected, the resolution can become better than 50 pm [33]. Similarly, improvements in monochromator and spectrometer design made the energy resolution better than 5 meV [34].

1.1.2 Technique

Today, we assist to a great variety of electron microscopes and related techniques. Standard microscopes can perform in the same instrument imaging, spectroscopy, and diffraction, utilizing the elastic, inelastic, coherent, and incoherent information carried by the electrons, as well as secondary signals produced by the electrons in the specimen, like secondary electrons [35], visible light [36] and X-rays [23, 35]. I will use the following pages to introduce the technical aspects of TEM that are required for the correct discussion of the thesis.
A sketch of the most important parts of a TEM is shown in Fig. 1.1. Although this scheme is modeled according to our system, a JEOL JEM-2100, with Gatan imaging filter (GIF) spectrometer [37], the described components are very general to most TEMs.

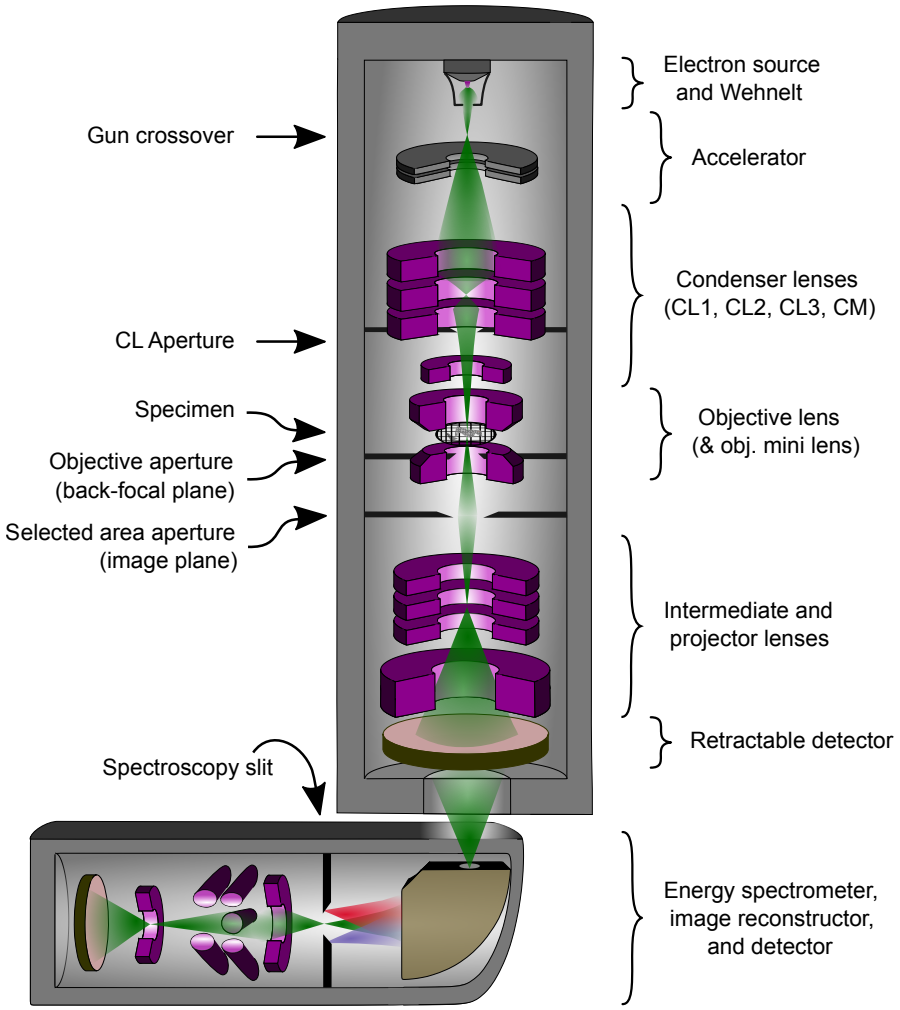

Figure 1.1 – Schema of a TEM. Beam deflectors, stigmators, and few other electron optics components are not drawn. The electron beam trajectory (in green) is just conceptually sketched, and its divergence angles are exaggerated for illustration purposes.

Electron gun

The electron gun consists of the electron source and the acceleration stage. The cathode is the source of the electrons, and several concentric anodes complete the acceleration stage. The high voltage to apply between anodes and cathode is built in a separate high-tension tank, and its stability is crucial for the TEM operation. High vacuum is required in the gun region, to avoid electrical arcing between parts at different tension. When a beam crossover is present in the accelerationstage, the crossover point can be considered as the virtual point source of the TEM optics.

Generally, an electron can be ejected out of a solid if it can overcome an energy barrier equal to the work function Φ of the solid. Φ varies among different materials, and for a given material

depends on the crystallographic phase, as well as on the presence of surface contaminants. Metals represent the natural choice of materials to be used as electron emitters, because they do not accumulate charge. Semiconductors can be used as sources of spin-polarized (photo)electrons [38], which in strained GaAs-GaAsP superlattices can reach up to 92% polarization [39].
Three are the distinguishable physical mechanisms employed to generate electron beams: thermal excitation of the electron bath, tunneling, and photon absorption. Combinations of the three are also common.

In **thermionic emission** the temperature of the quasi-free electrons inside the solid is increased to a nonzero value T. As schematized in Fig. 1.2a, the electrons occupy energy states according to the Fermi-Dirac distribution $f_{\mathrm{FD}}(E) = [\exp\big((E-\mu)/k_B T\big)+1]^{-1}$, where μ is the chemical potential, and k_B the Boltzmann constant. Statistically, some of the electrons have energy higher than Φ, and are freed from the potential of the solid. Richardson's law describes the free-electron current density, given T, Φ, and a material-dependent constant A:

$$j = AT^2 e^{-\frac{\Phi}{k_B T}}\,. \tag{1.4}$$

Only materials with either very high melting point, as tungsten (W), or particularly low Φ, as lanthanum hexaboride (LaB_6), are employable as thermionic sources. Apart from W and LaB_6, refractory metals as tantalum (Ta) and molybdenum (Mo) might also be employed.
Thermionic guns are usually equipped with a Wehnelt, a tunable electrostatic lens ($< 1-2$ kV) serving at forming the gun crossover. When no or little voltage bias is applied to the Wehnelt, the crossover is not tight, the current is maximized, and the electron distribution pattern has typically a ring structure, with some electrons in the center of the ring. As the bias is increased, the crossover gets tighter, the current is reduced, and the ring shrinks. At the *saturation* bias, the ring has fully merged with the central spot; this situation corresponds the standard working condition for thermionic sources.
As electrons are emitted from the source, they are coherent if they originate from the same point. Thus, the central spot in case of very low bias has a better transverse coherence than the beam at saturation. In fact, for LaB_6 sources, the electrons from the ring are emitted from the shanks of the LaB_6 cone, and once merged into a unique spot, contribute to lower the beam coherence, in exchange of an increase in counts.
The energy spread of the electrons, the zero-loss peak (ZLP), is on the order of 1 eV or higher. Only if the filament is kept at very low current the ZLP can be < 1 eV, at the expense of brightness.
Brightness is defined as current density j_e per unit solid angle Ω at a beam waist [23],

$$\beta = \frac{j_e}{\Omega} = \frac{i_e}{\pi r_0^2 \pi \alpha_0^2}\,, \tag{1.5}$$

with i_e electric current, r_0 beam waist radius, and α_0 divergence semi-angle. β has therefore

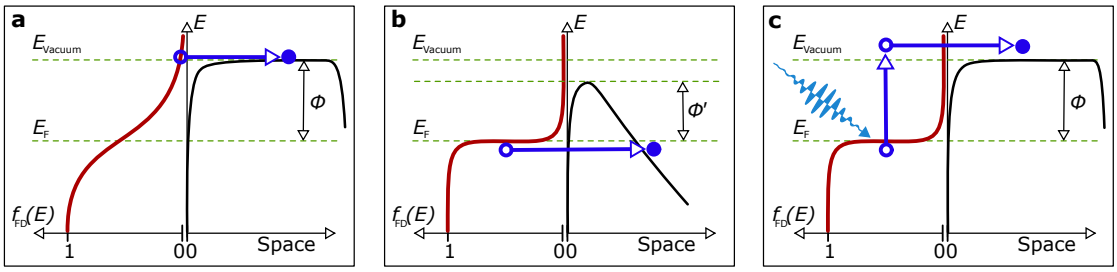

Figure 1.2 – Conceptual diagram for three types of electron ejection mechanisms from a solid. **a**: Thermionic emission; **b**: Field emission; **c**: Photoemission.

units of $[\mathrm{A}\cdot\mathrm{m}^{-2}\cdot\mathrm{sr}^{-1}]$, and it is a conserved quantity in absence of aberrations.

Differently from thermal sources, in **field-emission** guns a high electric field is used to lower the energy barrier set by the work function [40], as depicted in Fig. 1.2b. Extremely sharp needles, tips and even nanowires are used as sources, because of the electric field enhancement when the curvature radius of a metallic object goes to zero. In this way, the probability for an electron to tunnel out of the material can become very high. Since the electrons remain cold, these sources have a much higher monochromaticity with respect to thermionic sources, and outdo the latter also in the brightness. Due to the lack of heating that favors desorption, field-emission gun (FEG) sources require ultra-high vacuum (UHV) conditions in the gun area.
Schottky emitters differentiate from (cold) FEGs because they are resistively heated to a warm temperature, and the ejection process can be described as field-assisted thermal emission. Schottky FEGs have a ZLP of ~ 0.7 eV, and cold FEG down to ~ 0.3 eV [41]. I will not enter in further details about field emission, because their use in my work has been only marginal. Nonetheless, it is worth remarking that for most continuous wave (CW) and several pulsed applications they constitute the most advanced class of electron sources to date.

The **photoemission** is a photon in-electron out process, as schematized in Fig. 1.2c. Single-photon photoemission is possible (at $T = 0$ K) only if $h\nu > \Phi$, where $h\nu$ is the photon energy [42, 43]. When this happens, the electron current scales linearly with the light intensity. The ZLP in photoemission mode can be as small as 0.24 eV in semiconductor cathodes [38], and reach several hundreds eV in presence of colossal Boersch effect [44]. In light of the importance for my work, I will discuss photoemission further in 1.3, and 1.4.

Condenser system

This TEM section serves to set the illumination conditions of the microscope. The two common modes of operation are parallel and focused beam. Scanning transmission electron microscopy (STEM) works in focused mode, and its spatial resolution is directly related to the

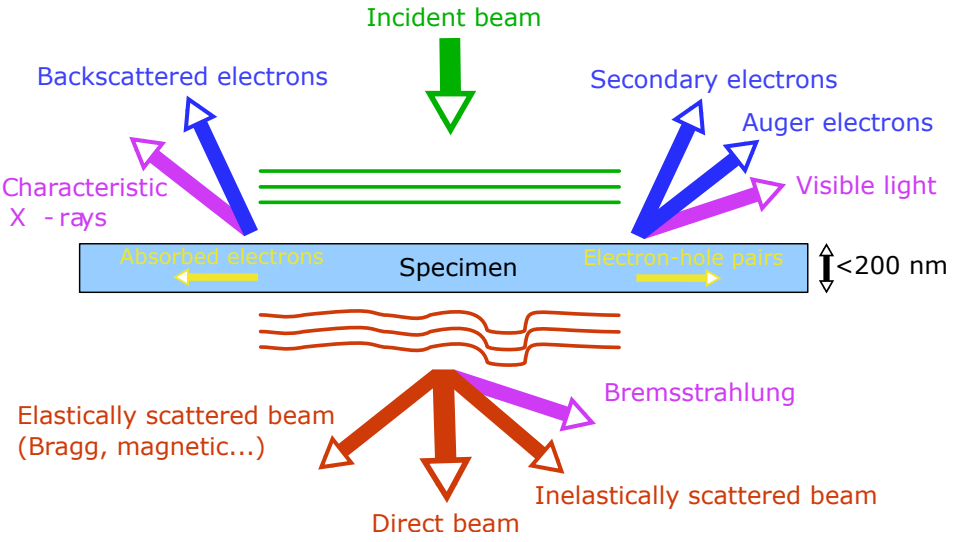

Figure 1.3 – Interactions of the high-energy electrons (green arrow and wave) with the TEM specimen. In magenta the photon signals; in red and blue the electron signals in transmission (forward scattering) and reflection (backward scattering), respectively. The incident free-electron plane wave (green lines representing constant phase surfaces) can acquire a position-dependent phase factor (red lines).

ability to finely focus the beam to a narrow spot. In-focus imaging can be performed in both modes, although with some differences. Diffraction is more commonly performed in parallel mode (selected-area electron diffraction (SAED)), but it can as well be carried out in focused mode (convergent-beam electron diffraction (CBED)).
The illumination system (including the upper objective lens) is also responsible to set the transverse (spatial) beam coherence. A small spotsize (high spot number, in electron microscopists' jargon), a small convergence semi-angle α, a high excitation of the last condenser lens or the use of a small condensed lens aperture (CLA) all contribute to a higher degree of transverse coherence. Being brightness a conserved quantity, higher transverse coherence corresponds to a lower current density at the specimen. Therefore, the optimal trade-off between current density and coherence has to be found for any given experiment. This is even more important in time-resolved measurements, where the average beam current is particularly low, and no luxury to waste electrons is permitted (see Sec. 1.2).

Specimen

A TEM specimen should be thin enough to allow for a significant portion of the incoming electrons to be transmitted through. This usually constraints the material to be at maximum $\sim 100-200$ nm, although there is no definite threshold, and the limit depends on electron energy, atomic number of the atoms constituting the specimen, and type of measurement. In practice, the specimen has often to be only few tens of nm thick, to avoid multiple scattering

processes in the material that make the extraction of useful information difficult. Fig. 1.3 shows the typical signals generated by the interaction of a high-energy electron beam with a thin solid-state target. The backward-scattered signals are used mostly in analytical electron microscopy (AEM). For example in energy-dispersive X-ray spectroscopy (EDX), or in cathodoluminescence (CL). The signals in transmission are the most relevant in our work, and –except bremsstrahlung, which is not used– both elastic and inelastic signals are considered.
Elastic signals include the direct, unscattered beam, the Bragg-scattered beams, and those acquiring geometric phases [45] by the interaction with electromagnetic potentials, as described by the Aharonov-Bohm effect [46, 47]. The electrons deflected by the magnetic Lorentz force are also elastic, and acquire a geometric phase by interacting with the vector potential around the specimen. The phases picked up by the electrons at the specimen cause a transverse phase modulation of the electron wave function, which we will treat again in Chap. 4 and Chap. 5.
The inelastically-scattered beam is the result of the energy lost by the electrons in the specimen, corresponding to atomic line or quasiparticle absorption. To the first group belong for example the K, M, and L atomic edges, while to the second the plasmon peaks and other low-energy excitations, like phonons. Contrary to elastically-scattered electrons, inelastic electrons are considered to constitute an incoherent ensemble. We will see in Chap. 2 that when the inelastic scattering is controlled by a coherent external field, mutual coherence can be imprinted also between these beams.

Objective lens and projection system

The objective lens is the strongest TEM lens, and serves to set the image magnification. Its magnetic field can be as strong as ~ 2 T, and fills the space around the specimen. Objective mini lenses, or ad hoc Lorentz lenses, can be employed at low and intermediate magnifications, if the specimen has to be kept at zero or low magnetic field. Just after the objective lens there is the back-focal plane, Fourier-conjugate of the image plane. There, a diffraction pattern (DP) is formed, and the objective aperture is used to select the spots to form the image. In bright field (BF) only the direct beam is selected, in dark field (DF) one of the Bragg-diffracted spots, and in Foucault imaging a Lorentz-reflected beam. By selecting different beams, we can decide the diffraction contrast in the image. The intermediate and projection lenses transfer the image or diffraction plane down to the column, and magnify it onto the detector.

Spectrometer

There are in-column and post-column electron spectrometers, with the second representing the most advanced type. In Fig. 1.1 an example of GIF, a post-column spectrometer, is sketched. It allows to perform electron energy loss spectroscopy (EELS) and energy-filtered transmission electron microscopy (EFTEM). The electrons are first dispersed in energy by a magnetic prism. After the prism, a mechanical slit is used to select an energy range, if needed.

A series of quadrupoles, sextupoles and octupoles reconstruct the image, correcting for the aberrations, usually up to the third order. Either the spectrum or the energy-filtered image or DP are then projected onto the detector.
Spectra are one-dimensional (1D) objects, while detectors are two-dimensional (2D) objects; when a spectrum is acquired only one dimension of the detector is used for spectroscopy purposes. The second dimension can still be used in certain circumstances to have real-space or reciprocal-space information of the specimen [48–51] with an approach that I will refer to as spatially resolved electron energy loss spectroscopy (SREELS) or momentum resolved electron energy loss spectroscopy (MREELS) mapping,[1] as we will see in Sec. 2.2 and following chapters..

Detectors

Each of the signals listed in Fig. 1.3 has its own dedicated detector. Non-pixelated semiconductor, scintillator-photomultiplier, charge-coupled device (CCD), and active-pixel sensor are the most used electron detectors. Old instruments still uses an electron-fluorescent viewing screen (usually ZnS), and photographic emulsions (polycrystalline silver halide). For transmitted electrons, CCDs are perhaps the most common. Although improperly, sometimes we refer to the full scintillator-fiber optics-CCD assembly as "CCD detector". The scintillator, for example Ce-doped yittrium aluminum garnet, $Y_3Al_5O_{12}$ (YAG), is a fluorescence substance which generates visible-light photons when it absorbs electrons. The light emitted by the scintillator is coupled into an array of optical fibers, which transfer it to the proper CCD. In the CCD, the charge generated by the light is stored in micro-sized potential wells. Each potential well is isolated from its neighbors, and constitutes a pixel. The reading is performed by shifting the registers and reading the accumulated charge line by line.
Recently, direct-electron detectors based on complementary metal-oxide semiconductor (CMOS) technology have been optimized for TEM use. With respect to CCDs, they provide unique advantages on camera noise, detector efficiency, and readout speed, as we will extensively see in Sec. 1.5.

[1] In the literature, it has been also known as electron energy loss profiling (ELSP), hybrid mapping, or energy-space mapping. SREELS is however the most used name.

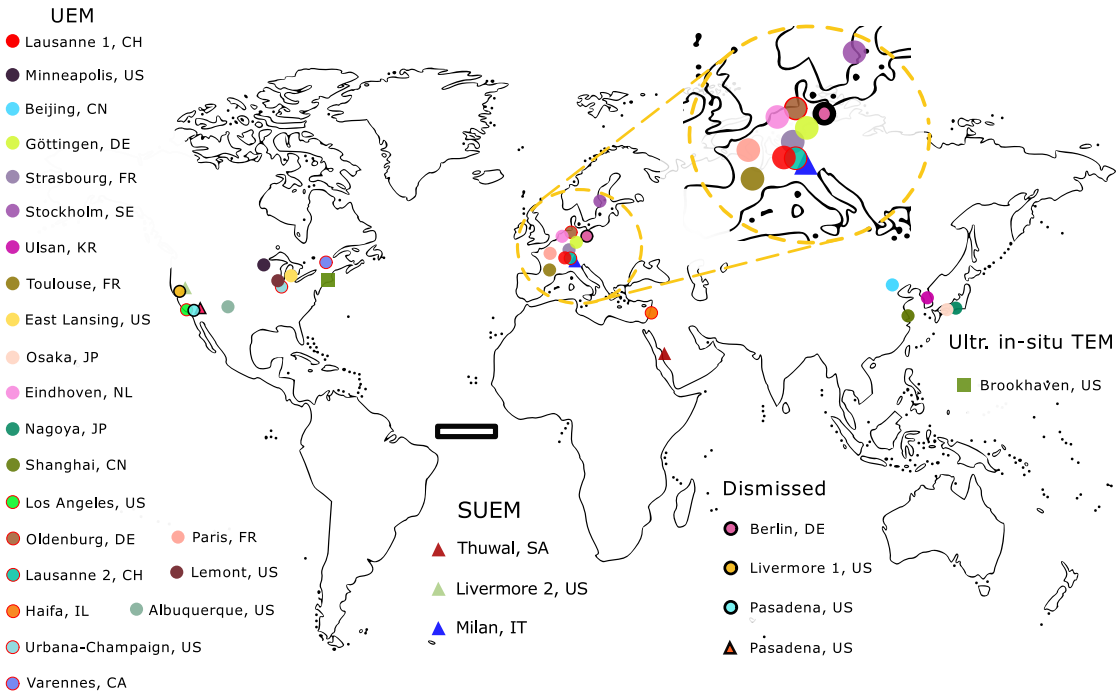

Figure 1.4 – UEM setups around the world, as at January 2019, to the best of my knowledge. No distinction between single-shot and stroboscopic systems is done here, but diffractometers without real-space imaging are not considered. Scale bar 2500 km on the equatorial line. See text for references.

1.2 Ultrafast electron microscopy

Fig. 1.4 gives us a taste of the growth of the high-energy ultrafast electron microscopy community. In the map, cities hosting a UEM system are marked with full circles. Red-bordered circles (at the bottom of the list) are -to the best of my knowledge- systems either already well operational or currently under construction or optimization, but which did not make publicly available any *experimental* report, yet. Scanning ultrafast electron microscope (SUEM) are shown with triangles, while TEMs with ultrafast excitation but without ultrafast probe are listed with squares. Important dismissed laboratories are marked by symbols with thick black contours, but first-generation stroboscopic scanning electron microscopy (SEM)s as [52] are not included. References, roughly in chronological order: Berlin [53], Livermore 1 (Lawrence Livermore National Laboratories) [54], Pasadena (UEM) [55], Pasadena (SUEM) [56], Lausanne 1 (LUMES) [57], Minneapolis [58], Beijing [59], Göttingen [60], Thuwal [61], Los Angeles [62], Strasbourg [63], Livermore 2 (Sandia National Laboratories) [64], Stockholm [65], Ulsan [66], Osaka [67], East Lansing [68], Eindhoven, Nagoya, and Shanghai (without proof of ultrafast pump excitation, yet - [69], [70], and [71], respectively), Toulouse [72], Milano [73], Brookhaven [74], Paris [75] (nanosecond chopping), and Haifa [76].

These systems have disparate characteristics, as well as technical and scientific challenges

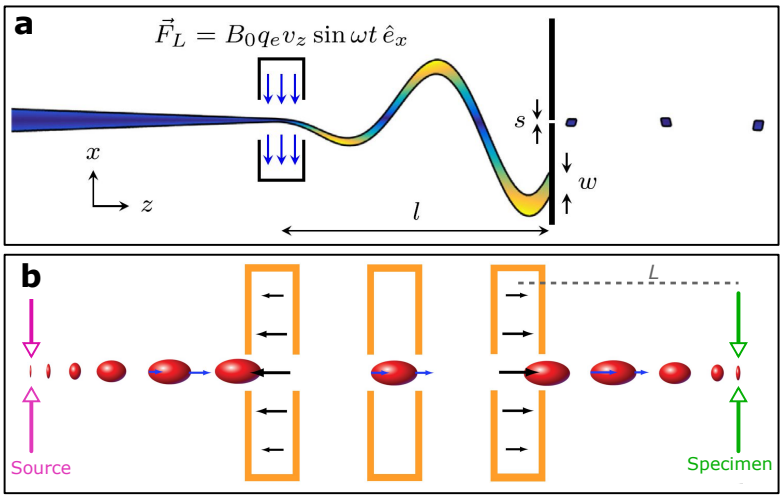

Figure 1.5 – **a**: Concept of electron chopping by a transverse radio frequency (RF) cavity and a pinhole. The electron beam is focused in the center of the cavity. The repetition rate is 6 GHz, Image from [69]. **b**: Electron bunching by a longitudinal RF cavity. The RF field acts to invert the longitudinal momentum-space distribution (chirp) acquired by the propagating electron pulse, such that the electron pulse is compressed at the specimen, after a certain drift distance L. The force of the RF field is shown in black arrows, the longitudinal momenta in blue arrows, for 3 different phases of the same RF cycle. Partially adapted from [77].

and targets. While fully reviewing the status of ultrafast electron microscopy goes beyond the scope of this introductory chapter, I will here first summarize the main traits of this technique and then present few selected examples of past and recent research from the field.
High temporal resolution in high-energy electron-based techniques can be achieved with the following approaches:

- Employing fast detectors for camera-rate acquisition;
- Chopping a continuous electron beam;
- Bunching a continuous or long-pulsed electron beam;
- Using short laser pulses to photoemit short electron pulses.

The first method is discussed in Sec. 1.5, and provides poor time resolution, 100s µs at best. The other three can reach similar temporal resolution, hundreds of fs, although they significantly differ in many other aspects, notably the number of electrons per pulse.

1.2.1 Chopping and bunching

Chopping methods have the merit to maintain grosso modo the electron properties of static TEMs, since the gun does not need to be modified [78]. At the same time, they present a natural

compromise between average pulsed brightness and time resolution. Regarding the current, 300 fs-long slices of a reasonably high-quality ~ 2 nA continuous beam contain an average of $0.3 \cdot 10^{-3}$ electrons per pulse. Accordingly, only very high repetition rates ($\gg$ 10 MHz) are used,[2] determining a limit in the out-of-equilibrium phenomena that can be studied –the system being required to relax back to equilibrium over a short time.
The chopping can rely on a photoconductive switch acting as ultrafast beam blanker [79, 80], or on a transverse RF cavity [81] sweeping the beam across a small aperture [69]. The latter method, developed by O. J. Luiten and co-workers, is schematically depicted in Fig. 1.5a.[3]
A larger aperture combined with other transverse cavities has been proposed [82] as a way to increase the electrons in the pulse, at the expense of temporal resolution but preserving the beam properties.
A simpler but similar concept, with electrostatic deflectors combined with an aperture, had been introduced in the '60s and '70s to chop the continuous beam in SEM [52, 83], with combined μm-ps spatio-temporal resolution [84]. Earlier approaches to chop the beam included also applying short pulsed voltage to the Wehnelt set at extinction [85].
Nanosecond electrostatic deflectors can also be installed in the post-specimen section of the microscope, to create pulses or streak the beam [86]. They can be placed as well just before the detector, as done in [75]. Interestingly, if a train of few pulses is present, a pair of deflectors can steer each pulse to a different portion of the camera [87]. Each section can be considered as a frame of a ns-resolved movie, useful for the investigation of irreversible phenomena [88].
The ultimate way to chop the beam without affecting the instrument is to perform short gated acquisitions of the continuous beam. We discuss this non-invasive approach in Sec. 1.5.

The third method exploits longitudinal RF cavities. These cavities are extremely common in accelerator physics [89] and have been largely employed in ultrafast electron diffraction (UED) beamlines [90–92], see Fig. 1.5b. Ellipsoidal electron-beam distributions are simply created by the longitudinal expansion of an initially short and dense electron beam [93].[4] Since their phase space is conserved, the RF cavity can temporally focus the pulses on the specimen plane, reaching values as short as 16 fs with relativistic photoguns [95].
Integrating longitudinal RF guns in TEMs or other microscopy-oriented beamlines can lead to instruments with superior performances for ps single shot imaging [62, 67, 68, 71].

1.2.2 Photo-emitting

Femtosecond electron pulses most commonly generated by fs photon pulses. If the number of electrons per pulse is kept small enough to avoid pernicious space-charge effects, the electron

[2] Otherwise, the average electron current would be so low to prevent any reasonable standard TEM application.
[3] The repetition rate of such system is 6 GHz, determined by the 3 GHz RF field [69]. By combining multiple RF cavity at different frequencies, and eventually electrostatic detectors, one may reduce the repetition rate –at the expense of counts.
[4] Created usually by photoemission [94], see Sec. 1.2.2.

pulse remains short. We refer to this particular condition as *single electron* regime, because typically less than 1 electron per pulse is coupled on average down the TEM column. Pulses with significant more electrons will be not only longer, but also distorted by the Coulomb repulsion inside the pulse. In absence of longitudinal RF cavities, the best way to have electron bunches with a number of electrons significantly higher than 1 is to employ longer pulses for photoemission. This strategy has been pursued to achieve single-shot imaging, with best combined spatio-temporal resolution being 100 nm and 4 ps, recently achieved by C. Lu and co-workers in their 3 MeV microscopy beamline in Shanghai [71].

An effective ps single-shot imaging is believed to be possible only with relativistic beams, where space-charge effects are smaller [62, 71, 96]. Single-shot imaging with ns pulses is instead possible at sub-relativistic accelerations. The best spatio-temporal resolution, 9 nm and 15 ns, has been reported by T. LaGrange and co-workers in Livermore [97], and it is about a factor 30 less than for relativistic electrons [71].
Single-shot experiments are useful to study transient irreversible processes in many diverse research fields, like solid state physics, material science, and metallurgy. For example, crystallization processes can be accurately followed, either in diffraction [54, 98, 99], or bright-field imaging [88], where the nucleation and growth of the new phase has been recorded with high accuracy. Martensitic crystal-phase transformations [97,100], and chemical reactions [101,102] have been studied as well. The investigation of other chemical transformation as oxidation and reduction can benefit also from single-shot EELS experiments [103]. Interestingly, a laser-induced heat pulse can cause selective material melting inside a nanotube. The material flow in the nanotube is then imaged, giving interesting insights in the domain of nanofluidics [104].

1.2.3 Old and new experiments: an expanding horizon

The most common measurements in UEM are performed with sub-relativistic (typically $100 < E(\text{keV}) < 300$) sub-ps or ps-long pulses in single- or few-electrons per pulse mode. They address fully repeatable transformations.
The power of this technique can be exemplified for example by the ability to resolve the lattice strain dynamics. The resonant excitation of cantilever modes by high repetition rate laser pulses can give selective cantilever vibrations in the MHz frequency range [107]. This produces effects similar to those of nano-drumming [108], that can be characterized in amplitude and phase.
At much higher frequencies, acoustic phonons can be visualized by bright- or dark-field imaging, observing the change in diffraction contrast. By ultrafast monitoring the wavefronts of these sound waves in microscopic lamellae, the role of defects in the emergence, propagation, dispersion, and decay of the acoustic phonons have been highlighted. This is the example shown by D. Flannigan and co-workers in ref. [105], see Fig. 1.6a-b.
In Fig. 1.6a a WSe_2 lamella is imaged in brigh field before the laser excitation. After the laser

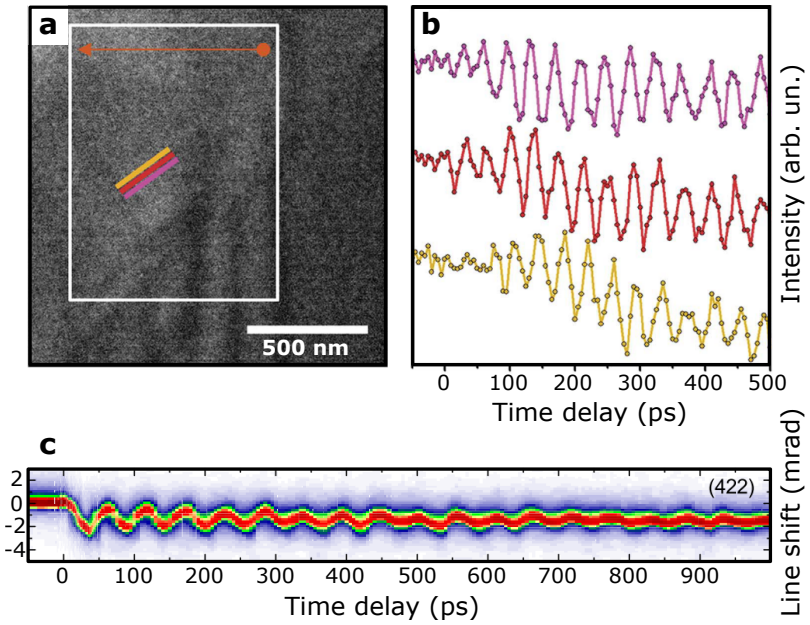

Figure 1.6 – Examples of acoustic waves visualized by UEM. **a**: Bright-field micrograph of the WSe_2 lamella. **b**: Contrast modulation in the three lines in (a) with corresponding color. Images adapted from ref. [105]. **c**: Kikuchi line shift in a graphite membrane, away from the membrane edges. Image adapted from ref. [106].

pulse, a local periodic modulation of the contrast is visible. In Fig. 1.6b the contrast intensity is plotted as a function of the time delay for three adjacent colored line in panel a, drawn parallel to the phonon wavefronts. Interestingly, in a similarly-shaped Ge lamella the emergence of the acoustic phonons can be delayed up to ~ 100 ps after the photoexcitation, and propagate at initial hypersonic phase velocities [109].

In reciprocal space, the ultrafast evolution of lattice strain is commonly imaged in UED [91], or ultrafast X-ray diffraction (XRD) [110]. The probe of local strain is instead better studied in microscopes, via SAED [111, 112], CBED [113], or –for thick specimens– Kikuchi diffraction [114–116].
In Fig. 1.6c an example of Kikuchi line oscillation is shown, from A. Feist et al., ref. [106]. The electron beam is there focused to a diameter of 28 nm, on the surface of a 120 nm-thick graphite flake, excited by an infrared fs laser. A representative Kikuchi diffraction line position is plotted as a function of time, featuring dumped oscillations, due to the deformation associated to an acoustic breathing mode of the membrane.[5] The dynamics depends on the position in the membrane, and differs significantly when in proximity of the edges (here not shown) [106].

[5]The temporal trace of Fig. 1.6c is relative to a position in the membrane away from the physical edges.

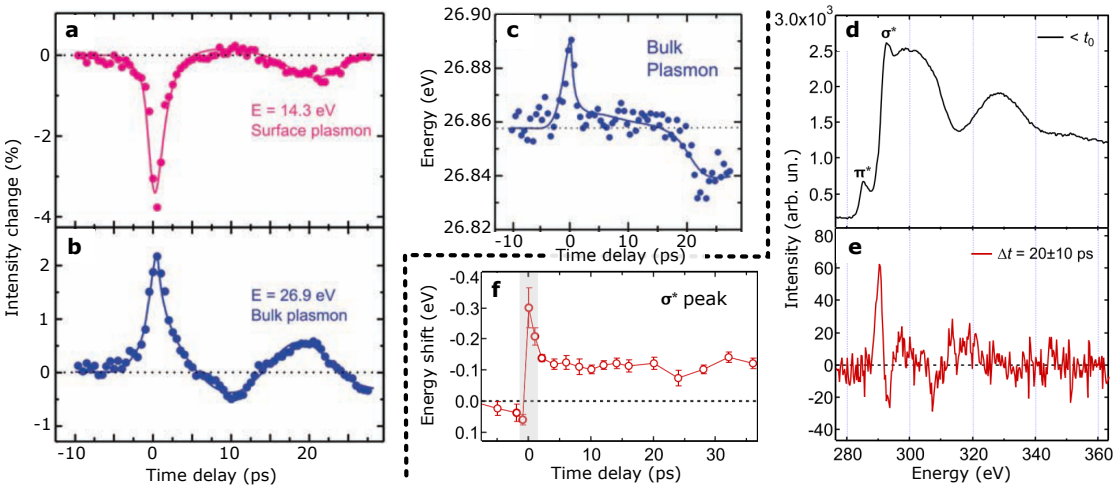

Figure 1.7 – Examples of low- and high-loss fs-EELS in graphite. **a**,**b**: Surface (a) and bulk plasmon (b) intensity change, which have opposite sign. **c**: Transient blue shift of the bulk plasmon peak. (a-c) adapted from ref. [117]. **d**,**e**: Static and differential transient C K-edge spectra. **f**: The $\sigma^\star$ band red shifts of ~ 120 meV. The points around t_0 should not be considered, because of spurious PINEM effects. (d-f) adapted from ref. [118].

The dynamics of chemical bonds can be analyzed more properly in spectroscopy. For this reason, ultrafast EELS has been developed, both for low-loss excitations [111, 117], and core-loss levels [111, 118]. In graphite, it is possible to directly correlate the shift in energy of plasmon peaks to a modulation in the stacking distance along the c axis. From ref. [117], Fig. 1.7a-b show the photoinduced change in intensity of the surface and bulk plasmon peaks, respectively. In Fig. 1.7c, the tiny energy shift of the bulk plasmon is plotted. From that, one could see that in the initial part of the dynamics graphite contracts along the c axis, moving towards a diamond-like structure, while at later times it expands, becoming more similar to a stack of graphene-like layers.
From ref. [118], instead, we can appreciate the dynamics seen by a core-loss perspective: in Fig. 1.7d the static spectrum around the carbon K edge is presented. A red shift of the $\sigma^\star$ band can be seen in the differential spectrum of Fig. 1.7e, acquired after photoexcitation. The red shift is confirmed by Fig. 1.7f, and is has been attributed to an photoinduced bandgap renormalization.

A particular sub-field of ultrafast electron microscopy sprang recently from the discovery of photon-induced near-field electron microscopy (PINEM) [119]. It involves EELS and either real-space imaging or diffraction. In view of the importance in this dissertation, I will introduce it in details at the beginning of the next chapter, Chap. 2.

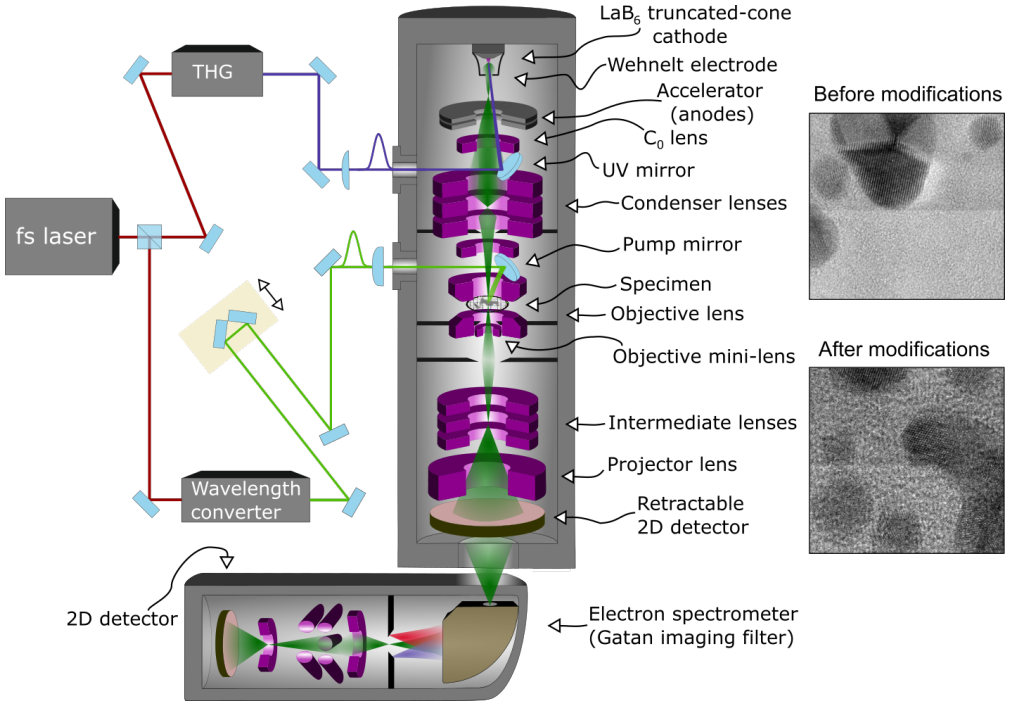

Figure 1.8 – Scheme of the fs-UEM at LUMES. On the left, two high-resolution micrographs of Au nanoparticle (NP)s acquired with the continuous beam, before and after the instrument modifications. Micrographs ref. [57].

1.3 fs-UEM at LUMES

The design and implementation of the fs-UEM at LUMES, Lausanne, is described by L. Piazza and co-workers in ref. [57]. Its modeling is inspired by the development of instruments of the same family, such as 'UEM-1' [120] and 'UEM-2' [121], at Caltech. Among the differences, the addition of an extra condenser lens, C_0, between the anode and the first condenser lens, allows to collect more electrons, and gives one more handle to select the beam properties [122]. Since ref. [57] the system system underwent few updates. I describe below today's status of the instrument, schematized in Fig. 1.8. A fs-laser system serves to generate the ultrafast laser pulses for pump and photoemission.

1.3.1 Description

Laser system

The system is composed by a 80 MHz Ti:sapphire oscillator (Griffin, KMLabs), and a Ti:sapphire regenerative amplifier with tunable repetition rate from 10 Hz to 1 MHz (Wyvern X, KMLabs). The crystal of the oscillator is pumped by 8 W from a CW laser (Verdi-8, Coherent). 20 fs-long pulses are generated thanks to Kerr-lens modelocking. The associated bandwidth is around

100 meV full width at half maximum (FWHM). The central wavelength of the pulses can be tuned approximately from 765 nm to 820 nm. We typically work at 790 nm to better match the gain bandwidth of the amplifier. The average power at the output of the oscillator is ~ 1.1 W, corresponding to 13.8 nJ per pulse.
The crystal of the amplifier is kept cooled at 80 K by a closed-cycle He cryostat. It is pumped by three CW lasers (Finesse, Laser Quantum), for a total power of ~ 35 W. A long BBO[6] Pockels cell, synchronized with the oscillator, governs the timing in the amplifier cavity. The amplifier can work in CW mode, generating up to ~ 6 W, in Q-switched mode, or in seeded mode. In seeded mode, the pulses from the oscillator are negatively chirped in a pair of grisms, combinations of gratings and prisms. After the amplification in the cavity, the pulses are temporally compressed by passing multiple times in a 30 cm-long slab of glass, which positively compensates the dispersion.
The average power in seeded mode is ~ 3.6 W for repetition rates higher than ~ 180 kHz. For lower repetition rates, the energy per pulse remains roughly constant, 20 μJ. The majority of our experiments are performed with 300 kHz, which means 12 μJ per pulse available. The laser spectrum at the output of the amplifier is 36 meV FWHM, peaked around 1.57 eV (= 790 nm), and the pulse duration 55 fs FWHM. Pulse duration and bandwidth are measured independently, by a spectrometer and an optical autocorrelator, respectively. They are Fourier-limited, $\Delta E \cdot \Delta t = \hbar/2$. Δt = 55 fs is extracted from the autocorrelation measurement assuming a Gaussian temporal profile.
The photon energy of the amplifier is not easily tunable outside the photon bandwidth. Nevertheless, it is possible to have pulses with narrower bandwidths, down to ~ 2 meV by simply selecting a correspondingly small bandwith from the seed pulses. This can be done in the grism-based stretching stage before the amplification, by inserting a narrow slit where the beam is dispersed in energy. The pulses with narrower bandwidth will be naturally longer, up to ~ 1.0 ps. If the amplifier is run in absence of seed, and the number of roundtrips in the cavity is made high enough, the laser works in Q-switched mode. The pulses generated in this way have a duration of ~ 100-200 ns, but we did not use them in experiments, because we have a dedicated ns Q-switched laser system, see Sec. 1.4.

Right after the amplifier the beam is split in two. One of the two portions is frequency upconverted to generate ultraviolet (UV) pulses at 4.71 eV, the third harmonic of the 1.57 eV fundamental. The third harmonic generation (THG) is performed in two steps. The fundamental is first frequency doubled in a BBO; once adjusted the polarizations and accumulated time delay, the fundamental and its second harmonic are frequency summed in a second BBO, generating the third harmonic. The beam is then energy filtered and recollimated. UV pulses can have in principle a duration as short as 32 fs. The propagation through dispersive material, accentuated for short wavelengths, makes them easily longer. We calculated the pulses to be ~ 90 fs-long at the cathode, if they are compressed in the THG stage.
The shortest infrared pulse duration at the specimen is obtained by pre-chirping the pulses

[6] β-barium borate, β-BaB_2O_4 (BBO).

in the amplifier, so that they arrive compressed in the microscope. The same optimization procedure is not crucial for the UV, since the temporal limitation is given by the photoemitted electron bunch length, anyway 250 fs or longer.
The UV pulses are finally focused on the cathode surface. We use a lens with +1000 mm focal length, placed just outside the TEM column. An Al mirror inside the column is added above the condenser system, in a new custom-designed column section, developed by IDES Inc. [123]. The mirror has a hole in the middle, to let the electrons pass through, and can be moved in the three axis by a manipulator placed outside the column. With this geometry, the illumination of the cathode is in normal geometry, and the spot size roughly 100 μm FWHM.

The second portion of the beam is what is employed as pump in the TEM. Most of the physical systems behave very differently when excited with different photon energies. For example the absorption of semiconductors and insulators can change dramatically if excited above or below the optical gap. The ability to widely tune the pump photon energy in a pump-probe setup is therefore highly beneficial.
In our system, the photon wavelength can be tuned in a wide –although not continuous– range, from 266 nm (4.71 eV) to 10 μm (125 meV). With the exception of the second and third harmonics of the fundamental, the other wavelengths are obtained by frequency down-conversion methods [124]. A high-repetition rate optical parametric amplification (OPA) setup (TOPAS-HR, Light Conversion) [125] is used for this purpose. This OPA has a double-pass noncollinear first amplification stage, and a single-pass second stage with collinear geometry, and the white light is generated in a sapphire crystal. Being based on BBOs, it has an infrared absorption cutoff at ~ 3.5 μm for the idler, corresponding to 1040 nm for the signal. Either the signal, the idler, or both beams can be selected. The second harmonics of those beams can also be obtained, by a broadband frequency-doubling stage (Lyra, Light Conversion), which covers most of the visible region.
To reach longer wavelengths, deeper in the mid-infrared (MIR), a difference frequency generation (DFG) has been built, which takes as input the signal and idler beams from the OPA. The frequency down-conversion is made there in a ZnSe crystal, and the DFG radiation is characterized by Fourier-transform infrared spectroscopy (FTIR).
The nonlinear frequency down-conversions have an intrinsic poor efficiency [124]. In our case, since the initial energy per pulse is only ~ 10 μJ, and the focusing inside the microscope is limited by geometrical constraints, the effective energy density of the MIR on the specimen plane is very low. In order to achieve higher fluences, a laser with higher energy per pulse and lower repetition rate should be used. The lower repetition rate, however, would make imaging more challenging, since the average electron current would diminish proportionally.
A computer-controlled mechanical delay stage is used to change the pump-probe delay time. For some experiments, two pump pulses are focused on the specimen, and a second computer-controlled delay stage is employed to change the relative time between the two pumps. The pump polarization is also controlled by a fully-motorized half- or quarter-wave plate. The beam is focused by a +250 mm-focal length lens, placed outside the column. A small Al mirror

inserted in the upper pole piece of the objective lens reflects the beam to the specimen plane. This mirror, fixed in its position by a thread, has a hole for the electrons to pass through. The angle between the laser pump and electron probe is $\sim 4.5°$, as explained in Sec. 2.2.

For diagnostics, we placed a beam picker just after the last focusing element before the specimen. The reflected beam is imaged by a CCD whose distance from the beam picker equals the distance from the beam picker to the specimen. In this way, the exact shape of the focused beam as used in the experiments can be recorded, which is usually roughly circular, with $\sim 30-40$ μm FWHM at 790 nm.
Furthermore, a second pellicle beam splitter can be inserted in the beam path. This pellicle takes part of the light reflected or diffused by the TEM grid, which is imaged by a second camera. A real-time view of the position of the focused laser spot on the specimen in therefore achieved, although with only limited lateral resolution.
The precise alignment of the beam is done by burning in-situ a test material. A sacrificial membrane with low damage threshold is imaged by the electron beam at the same conditions of the experiment. We usually employ holey carbon, thin polymer films, or ultrathin carbon. For a laser fluence above the specimen-dependent threshold, the laser pulses cause a localized damage. The damage is in these cases related to the local temperature of the specimen, which closely remaps the spatial profile of the focused spot on the membrane. Once individuated the position of the laser, it can be adjusted and optimized to coincide with the center of the area imaged by the electrons in the detector.
Another strategy we adopted to precisely optimize the pump overlap for electron diffraction experiments is to locally observe in reciprocal space the thermally-induced phase transition in a β-$MoTe_2$ flake.

TEM modifications

The microscope is a 200 keV Jeol JEM-2100 TEM equipped with a retractable Gatan UltraScan US-1000 detector, and a Gatan Quantum GIF. The main hardware modifications consisted in the addition of the C_0 magnetic lens, and the new mechanical parts for the pump and probe internal mirrors. Two optical ports have been opened for the laser access. The vacuum system has been adapted to accommodate the new section of the column. The gun was not modified. The shortest electron pulses are produced when the minimum bias voltage is applied to the Wehnelt electrode. In those conditions, the electrons coupled to the column are a small fraction of the total emitted. C_0 helps to increase the collection angle of the electrons exiting the acceleration stage and efficiently entering in the condenser system [122]. The focusing done by C_0 is performed on the fully accelerated beam. Therefore, this lens does not spread the beam in time, because the pulses are formed only by few electrons, and Boersch effects are reduced due to the high electron velocity.
One could as well increase the collection angle of the electrons by tuning the Wehnelt bias,

which decelerates and reaccelerates the pulses when they still have little energy, < 1 keV. In that way, the energy dispersion of the electron pulses is increased, and the bunches experience significant lengthening. Since brightness is a conserved quantity, a higher excitation of C_0 brings in general a higher number of counts and a lower transverse coherence. The optimal trade-off between the two can depend on the experiment.
In the insets of Fig. 1.8, high-resolution transmission electron microscopy (HRTEM) images of Au NPs dispersed on amorphous C film are reproduced. Both images are acquired with the continuous thermionic beam. In the top micrograph, the NPs are imaged before the TEM modifications, and lattice fringes are clearly resolved. The distance between crystal planes in Au is 0.288 nm [126] or smaller, depending on the crystallographic orientation. In the bottom image, similar NPs are imaged after the modifications. The lattice fringes are still visible, though not as neatly as before. The modifications introduce therefore only a minor loss in spatial resolution to the instrument.

1.3.2 Characterization

Photoemission

Single-photon photoemission is possible when $h\nu > \Phi$. For weak optical fields, the energy E of the electron ejected from the material and the electron current i are

$$0 \lesssim E \lesssim h\nu - \Phi \qquad\qquad i(I) \propto I, \quad \text{if } h\nu > \Phi, \tag{1.6}$$

where I is the light intensity. The probability for the photoelectrons to have an energy in the range indicated by Eq. 1.6 is weighted by the density of states (DOS) and matrix elements. Fig. 1.2c schematizes this process. For strong optical fields, deviations are observed from this linear regime. Multiphoton photoemission is possible whenever the material absorbs N photons simultaneously, and $Nh\nu > \Phi$. In that case, $i(I) \propto I^N$. We will however deal here only with single-photon photoemission.
In the emission of an electron out of a metallic surface, the momentum parallel to the surface, $\mathbf{p}_\parallel$, is conserved. This is not the case for the longitudinal component $p_\perp$, the electron being slowed down by the potential difference between the vacuum state and its initial state. The kinetic energies of the electrons will be distributed between 0 and the maximum excess energy $h\nu - \Phi$. The energy spread of the distribution is then further increased by the finite bandwidth of the light, and by the finite width of the Fermi-Dirac distribution at temperature $T \neq 0$.
A truncated-cone LaB_6 single crystal is used as photocathode. The diameter of the truncated section can vary between 15 and 50 μm, but usually we worked with 15 μm. The single-crystallinity of the cathode makes Φ more homogeneous across the surface. Surface roughness and the presence of adsorbates can however change Φ significantly. A lowering of Φ reduces the photoemission quantum efficiency. The distribution of Φ across the photocathode introduces a further broadening to the initial electron momentum $p_\perp$.
LaB_6 has a work function Φ_{LaB_6} = 2.66 eV for the (100) surface [127], and melting temper-

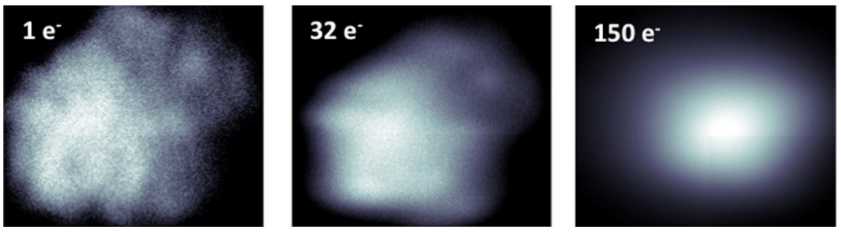

Figure 1.9 – Spatial blurring due to the intrapulse electron-electron scattering. From left to right, the beam possesses an increasing number of electrons; the beam structure results consequentially blurred. Image adapted from ref. [57].

ature 2988 K. We observe that the quantum efficiency does not vary significantly with the temperature from room temperature (RT) up to the threshold of thermal emission. In order to keep the cathode as clean as possible from adsorbates, we warm it to a temperature just below the onset of thermionic emission. At a temperature of ~ 1800 K, the energy spread contribution is $\sim 2k_{\mathrm{B}}T = 300$ meV. The UV pulses –instead– have a ~ 60meV bandwidth, hence not contributing significantly to the energy linewidth.
Other cathodes than LaB_6 have been tested. Tantalum disks are used in nanosecond mode, see Sec. 1.4. In fs mode, they show a narrower ZLP than LaB_6, but we observed a slightly longer response in time, consistent with other reports [63]. Guard-ring cathodes –designed to suppress the shank emission– have been characterized as well. They are constituted by a LaB_6 microrod embedded in graphite, whose role is to prevent photoemission, thanks to its high work function. Despite existing positive reports on guard rings [65] we did not find any practical advantage over the more standard truncated-cone geometry.

To conclude the paragraph, I should mention that photoemission in FEG instruments is also possible [60, 72, 128]. The sharpness of the source guarantees a higher brightness also for ultrafast operations. A quite intensive research on tip-based sources of ultrafast pulses is present nowadays [129–133]. The recent advancements led not only to the development of field-emission based UEM and SUEM [128], but also of ultrafast low-energy electron diffraction (ULEED) [134, 135].

Optimization in the parameter space

Many are the relevant beam quantities that could be optimized, such as counts, energy spread, pulse duration, transverse and longitudinal coherence, and chirp. They are all interconnected. The Wehnelt electrode is the most important element to change the electron pulse characteristics. At nearly-zero Wehnelt bias the beam has a ring shape with a central spot in the middle (same shape as in Fig. 4.12). The ring possesses a 4-fold symmetry, inherited from the geometry of the shanks of the LaB_6 cathode. The central spot is the beam used for imaging. The ring electrons have a different arrival time, pulse duration, and chirp [63].
For nearly-zero bias, the pulse duration can be as short as 250 fs. The ZLP is narrow (~ 1 eV)

only when space-charge effects are negligible. This happens for low UV pulse energies, when only few electrons are photoemitted per pulse. When a larger number of electrons is present in the same pulse, the primary effect is a dramatic broadening of the energy distribution (called Boersch effect). In those conditions, the ZLP can become larger than 100 eV. To a larger ZLP corresponds a longer pulse duration, that in first approximation can be ascribed to linear chirping of the pulse. We note that the energy distribution has a nearly-Gaussian shape when ZLP= 1 eV, while for larger ZLP it is more structured, with two little 'horns' at the distribution extrema. This spectral shape is well reproduced by particle-tracing numerical simulations that include Coulomb electron-electron interaction [65]. The distribution in time of those electrons has a main linear positive chirp, with the tails of the initial speed distribution having negative chirp. Such tails give rise to the 'horns' in the energy distribution.
The temporal broadening is quite moderate for low bias, the pulse duration being ~ 500 fs for ~ 8 eV ZLP. Being the chirp fairly linear [65], a ~ 100 eV-broad beam would have a duration of ~ 6 ps. A systematic study can be found in [63], [65]. However, such beams have poor spatial resolution, compromised by the chromatic aberrations, and even before by transverse coherence deterioration due to space-charge intrapulse interactions. This effect is exemplified in Fig. 1.9, where the image of the cathode (in absence of specimen) is shown for different numbers of electrons per pulse. Those numbers refer roughly to the number of electrons counted on the detector; the number of photoemitted electrons can be generally 1-2 orders of magnitude higher.
At higher bias, the ZLP becomes narrower, because the Wehnelt acts as a sort of energy filter, but the pulses become irremediably longer, up to 10 ps, and possibly longer [63]. Time-zero also shifts, because it takes more time for the electron to reach the specimen. At saturation, the beam spot has the shape of one round disk. At extinction, both the shift of time-zero and the duration of the pulses diverge.
Another important parameter to choose is the Wehnelt gap [136], namely the distance between the cathode and the Wehnelt electrode. The behavior of the electron pulse characteristics as a function of the Wehnelt bias is quantitatively different for different Wehnelt gaps. Smaller gaps give in general a higher current (but less transverse coherence), and have their saturation peak at higher Wehnelt biases. Since the Wehnelt gap cannot be changed as smoothly and easily as the bias, we worked usually at a fixed Wehnelt gap, 625 μm.
The temporal characterization of the electron pulses is carried out by means of PINEM, see Chap. 2 for details. In the weak-field approximation, the PINEM signal is a cross-correlation between electron pulse, excitation pulse, and lifetime of the induced plasmonic field [137]:

$$(\Delta t)_{\mathrm{PINEM}} = \sqrt{(\Delta t)_{\mathrm{e}}^2 + (\Delta t)_{\mathrm{ph}}^2 + \tau_{\text{near field}}^2}\,. \tag{1.7}$$

The intrinsic near-field lifetime can be often neglected. In the strong regime, or when strong- and weak- fields are probed together, the analysis of the high-order inelastic peaks allows to extract the same information [138], because the highest excited sidebands can be considered to be in a low-excitation regime, with pulse duration $(\Delta t)_{\mathrm{ph}}/\sqrt{\ell}$. Here ℓ is the PINEM sideband

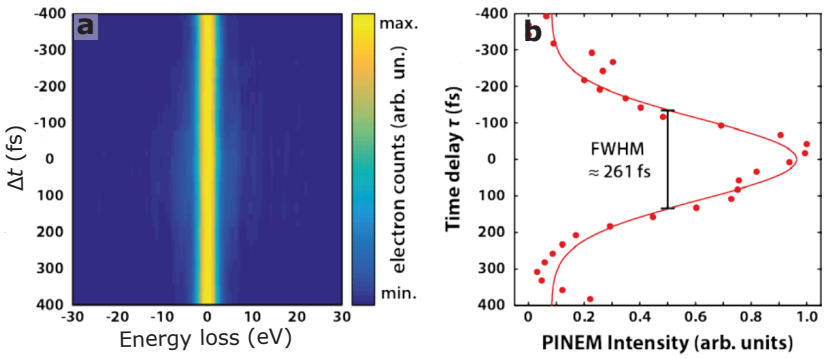

Figure 1.10 – With the PINEM technique we follow the evolution of the inelastically scattered electrons around a single, isolated silver nanowire excited at 1.57 eV by 55 fs-long pulses. **a**: Energy-time map. **b**: Temporal cross-correlation profile obtained by summing the inelastically-scattered electrons after ZLP subtraction.

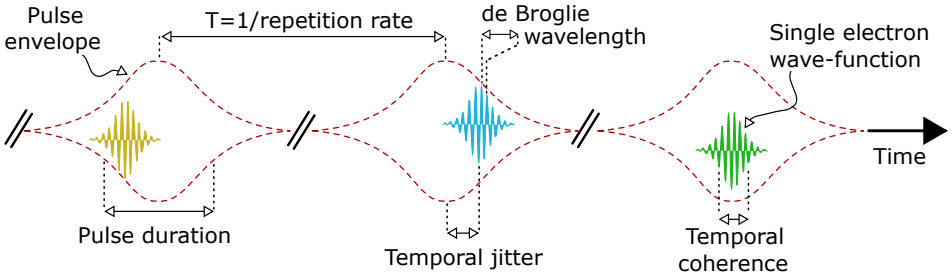

Figure 1.11 – Temporal coherence and pulse duration for single-electron pulses. Three electron pulses are conceptually skeched. Their color represent their mean velocity. Yellow slower, green intermediate speed, blue faster.

order, see Chap. 2.1. In this general case, we have

$$(\Delta t)_{\mathrm{PINEM};\ell} \simeq \sqrt{(\Delta t)_{\mathrm{e}}^2 + (\Delta t)_{\mathrm{ph}}^2/\ell}\,, \tag{1.8}$$

which reduces to $(\Delta t)_{\mathrm{e}}$ for the highest ℓ, in case of short pump pulse.
As shown in Fig. 1.10, ≈ 260 fs-long PINEM signal is typically achieved. Considered a 55 fs-long pump pulse and a sub-100 fs lifetime of the near field around the nanowire (NW)s, we can conclude that the pulse is ≈ 230 fs long. If we make the laser pulses longer (both the IR pump and UV), $(\Delta t)_{\mathrm{PINEM}}$ have the same duration of the IR-UV optical cross-correlation.

Temporal coherence

So far we have introduced the pulse duration $\Delta t_e = (\Delta t)_{\mathrm{electrons}}$ and the energy spread ΔE_e. Those quantities are proper to the statistical ensemble of the electron pulses collected on the detector, and they do not minimize Heisenberg uncertainty principle. In Fig. 1.11 three single-electron pulses are drawn. Each individual electron wave-function has its own central

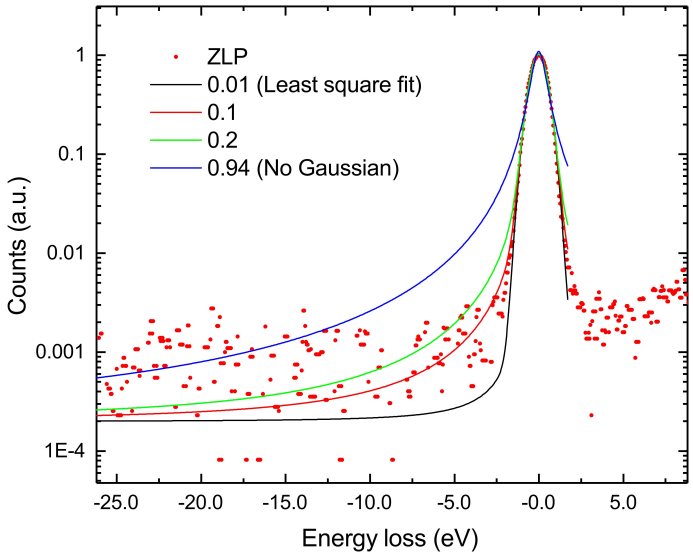

Figure 1.12 – Determination of the Lorentzian and Gaussian broadening of the ZLP. Fits are Voigt functions. The number in the legend indicates the value of Lorentzian broadening, in meV. The spectrum has been acquired with the beam passing through a (thin) material; hence the gain-loss asymmetricity.

de Broglie wavelength and associated bandwidth δE_e. The duration of the single-electron wave-function, ξ_t^2, is the temporal (aka longitudinal) coherence of the wave-function. For consistence with the literature [139], we call $\xi_t^e = 2\sigma_t^e$. We thus have $\xi_t^e = \delta t^e / \sqrt{2\ln 2}$, with δt_e FWHM.

The initial velocity of an electron just after photoemission scatters from pulse to pulse; the final velocities and arrival times will be therefore distributed according to a certain curves. Those curves determines ΔE_e and Δt_e, and as we will see they have nearly-Gaussian shapes. In particular, Δt_e is the cross-correlation between the temporal coherence and the statistical distribution of the temporal jitters. Analogously, ΔE_e can be calculated as the cross-correlation between the intrinsic single-electron linewidth δE_e and the statistical distribution of single-electron energies.

However, δE_e and ξ_t^e are not easily-measurable quantities [139, 140], and no experimental account on their values is available for UEM and UED, to the best of my knowledge. In Fig. 1.12 we show how to roughly estimate δE_e, and hence ξ_t^e, via the Heisenberg's formula

$$\delta E_e \xi_t^e \geq \hbar\sqrt{\ln 2/2}. \tag{1.9}$$

Single-electrons with different velocities (different colors in Fig. 1.11) are photoemitted from different initial states in the cathode, and they have therefore a Gaussian (inhomogeneous) distribution in the ZLP. A Lorentzian (homogeneous) contribution to the ZLP will be given by the coherent part, δE_e. We can extract δE_e by fitting the photoelecton spectrum in single-electron regime with a Voigt function, i.e. a convolution of a Gaussian and a Lorentzian. Fig. 1.12 shows

the results. The best fit is shown in black, and gives a Lorentzian broadening δE_e = 10 meV FWHM, and a Gaussian broadening of 1.16 eV. If we constraint δE_e to be larger, for example 100 meV, a poorer fitting is clearly observable.
Consistently with what measured, pulses with final kinetic energy 200000 ± 0.58 eV energy will distribute their arrival times over ~ 250 fs. We have a first estimate of δE_e being at most in the range of tens of meV. The corresponding ξ_t^e would be in the orders of several tens of fs. For eq. (1.9) to be valid, we assume no decoherence of the electron wave-function during the propagation. This assumption is good as long as electrons are emitted in single-electron wave-packets, and in absence of external scattering fields.
A second way to tentatively extract δE_e is by considering the photoemission process. Our ultrafast UV pulses have a bandwidth of ~ 60 meV FWHM. In the case of one electron emitted per UV pulse, the bandwidth of its wave-function is determined by the UV bandwidth. More correctly, it is safe considering the UV bandwith as the upper possible value for δE_e.
In this conservative scenario, choosing δE_e = 60 meV, the temporal coherence would be $\xi_t^e \geq 26$ fs. Such a large value for ξ_t^e could be surprising. As we will see in Sec. 2.2, it is compatible with other observations, and essential to explain novel electron-mediated quantum-interference effects between optical fields placed at different positions along the time coordinate of the electrons [141]. In that section, we will also introduce a further indirect method to estimate ξ_t^e, which gives a value between 52 and 78 fs.

Conclusions

Overall, the duration and energy spread of the pulses can be tuned via the Wehnelt excitation. Adding the C_0 lens allows to minimize the loss of electrons after the anode, without introducing extra space-charge effects. These characteristics, together with the wide choice of excitation wavelengths, make LUMES fs-UEM a highly versatile tool for ultrafast microscopy, spectroscopy, and diffraction [57, 111, 141–144].

1.4 Nanosecond stroboscopic microscopy

As seen in the previous sections, the key feature of a given time-resolved TEM setup is the balance between time resolution, electron counts, and spatial coherence of the electron beam. It is understood that the three parameters are heavily linked, and originate from a unique quantity, brightness. For a given brightness, the higher the counts in the image, the lower their coherence, and vice versa. The degree of transverse coherence needed to properly form an image depends on the details of the specimen and the imaging technique. While a minimum degree of coherence is required in all conditions,[7] some techniques solely rely on coherent contrast. Among them, Lorentz microscopy, and —at an even higher degree— electron holography.

Our attention to high-coherence imaging comes in large part from the interest in skyrmions, magnetic quasiparticles with typical radii of few tens nm (see Chap. 5). So far, such magnetic states have been imaged by Lorentz microscopy, in Fresnel (coherent) mode [145], but limited to static [146–148] or camera-rate [149–151] observations. The extension of Lorentz microscopy to the ultrafast time scale has been realized first by the group of A. H. Zewail [152], imaging the dynamics of large domain walls in strongly magnetized specimens, and optimized further for similar systems [153]. Imaging tiny, weakly magnetized structures such as skyrmions requires however a higher number of counts per degree of coherence.

For this reason, we implemented a ns-stroboscopic setup, which maximizes the number of counts, sacrificing time resolution. If a fs UV beam is used to photoemit many electrons ($\gg 10^3$ per pulse), the resulting electron bunches will suffer severe space charge effects [154], and they will lengthen in time and spread in energy. Which of the two effects dominates is dependent on the specific electron gun settings, as we saw in Sec. 1.3.2. It derives that, besides the pulses being possibly very long (potentially, $\gtrsim 100$ ps [63, 155]), the beam properties are also affected, in terms of coherence, chromatic aberrations, et cetera (see for example Fig. 1.9). For these reasons, a long-pulsed electron beam photoemitted by a short-pulsed laser beam is undesirable.

A ns electron beam photoemitted by a ns laser beam can contain up to $\sim 10^7$ electrons without their Coulomb interaction affecting considerably the spatio-temporal properties of the beam [54, 156], and up to $> 10^8$ with a careful design [97]. In this way, space-charge effects become negligible, favoring a higher electron beam quality and losing only in time resolution.

Our ns TEM setup adapts the fs UEM of LUMES, Sec. 1.3, with high-power ns lasers. The design makes the system easily switchable between fs and ns photoelectron mode. A simplified scheme of the setup is presented in Fig. 1.13.

[7] Bright field imaging –for example– can be referred as semi-coherent imaging, because its contrast originates both from coherent (Bragg) and incoherent (Rutherford) scattering.

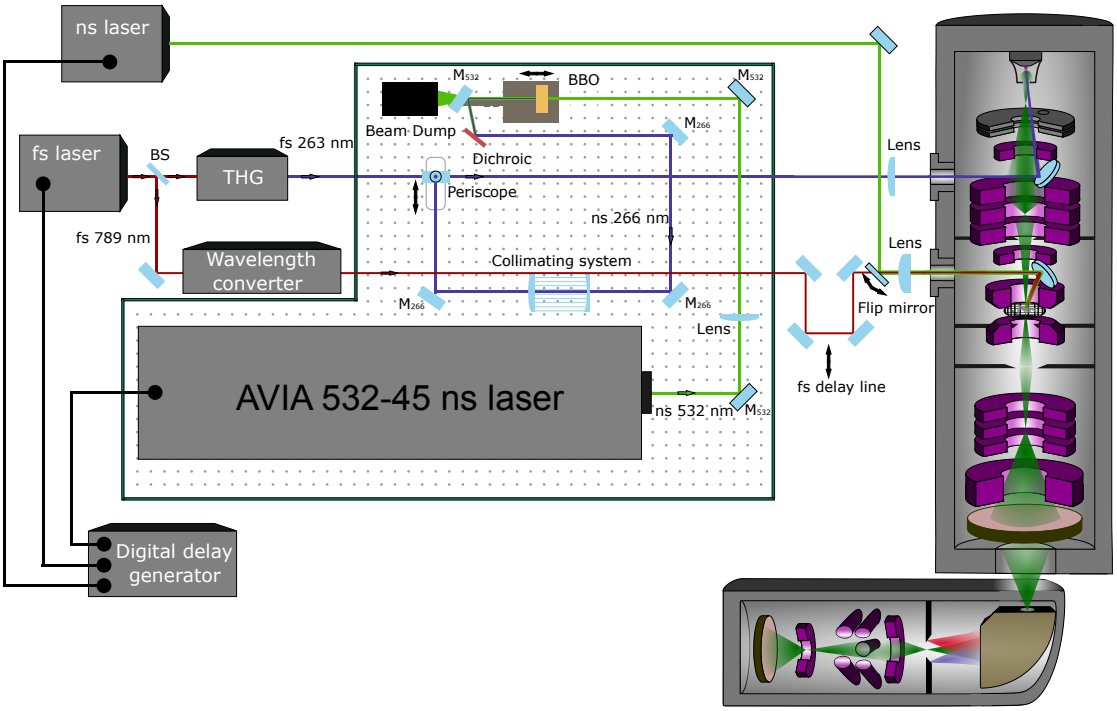

Figure 1.13 – Sketch of the ns stroboscopic TEM setup and its combination with the fs UEM. The optical scheme for the ns UV pulses generation is drawn in scale on the L-shaped board.

A Coherent Avia-45 Nd:YAG Q-switched laser is in-box frequency doubled to 532 nm (2.33 eV). This output is again frequency doubled to deliver UV light at 266 nm (4.6 eV). The laser has a tunable repetition rate from single shot to 300 kHz, with average green (532 nm) power up to 50 W, and pulse duration ranging from 10 ns for single shot to 75 ns at 300 kHz. The second harmonic generation of the 532 nm light (i.e the fourth harmonic generation of the fundamental frequency) was designed to work with two different nonlinear crystals: one (thin) assuring a high-quality spatial profile, with intermediate UV power, and the other (thick) maximizing the UV power, at the expense of the transverse mode quality. The crystal that guarantees a better spatial mode, also provides the best long-term stability, important because of the typical long overall duration of the experiments. This crystal is a 1.2 mm-thick BBO. Its efficiency as a function of the green pulse energy is shown with black circles in Fig. 1.14a, while panels b and c contain the UV energy per pulse and average power reached in the optical setup, respectively.

The efficiency scales linearly with the energy per pulse, as expected for low intensities, since η, the efficiency of the process, is $\eta = E_{SHG}/E_0 \propto |\mathscr{E}_{SHG}|^2/|\mathscr{E}_0|^2 \propto |\mathscr{E}_0|^2 \propto E_0$. Here, E is used to indicate the pulse energy, and $\mathscr{E}$ the amplitude of the electric field. The average power can be as high as 2 W.
If the second crystal, a 6 mm-thick BBO, is used, the conversion efficiency can exceed 20% at low repetition rate, and the average power surpass 4 W. In this case, the efficiency does not scale linearly with the input pulse energy. It does however vary significantly with the repetition

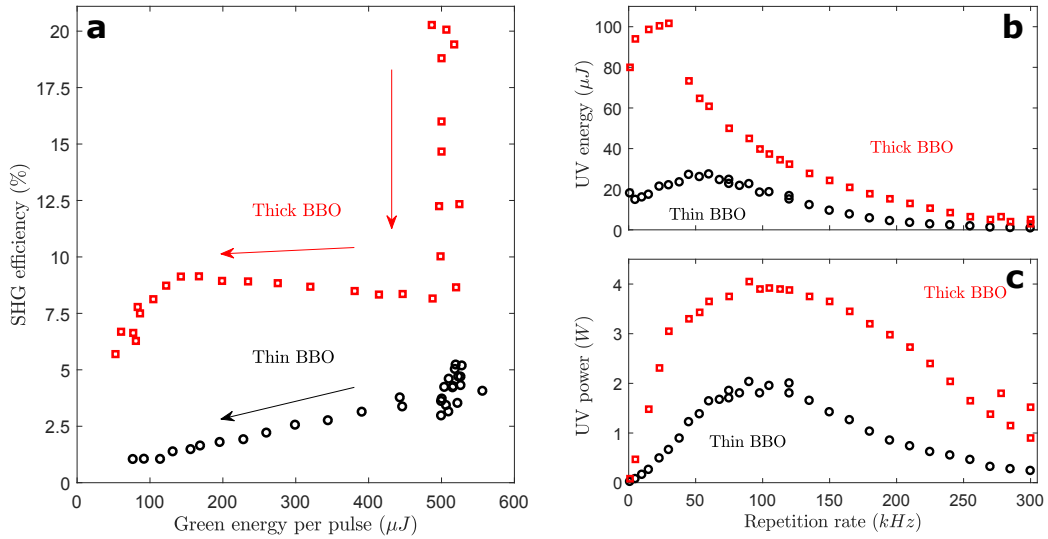

Figure 1.14 – **a**: Ns second harmonic generation (SHG) efficiency for the thin (black circles) and thick (red squares) frequency-conversion crystals. The arrows indicate the increasing repetition rate, from 1 to 300 kHz. **b**, **c**: Ns UV energy per pulse and average power, respectively, plotted as a function of the laser repetition rate. The green energy per pulse (not shown) is nearly constant for < 100 kHz-repetition rate, and decreases as $1/f$ for f > 100 kHz.

rate, highlighting the role of the interpulse cooling of the crystal (arrows in Fig. 1.14a). Unfortunately, the thick-crystal configuration manifests problems in assuring long-term stability, and therefore the thin-crystal configuration has been mainly employed in our experiments. It is also true that if we want to work away from the space-charge regime, the peak optical power of the UV pulses should be < kW, according to our estimates with the fs beam with LaB_6 cathodes [57]. Therefore, 20 µJ-pulses with 20 ns duration are already at that limit, and more energy might result in a worsening of the photoelectron beam quality.

After filtering out the visible light, the ns UV beam (266 nm) is collimated in a telescope employing a combination of spherical and cylindrical lenses to adjust the divergence and correct the beam ellipticity and astigmatism, which are significant when a thick BBO is used as SHG medium. The beam is then recombined into the same path of the fs UV beam (263 nm) via a mobile periscope, and is finally focused on the photocathode. There is no need to readjust the beam alignment after the periscope.
As shown in Fig. 1.13, both the fs beam (with its tunable photon energy) and a second ad hoc ns laser can be used to optically pump the specimen. The ns laser is again a frequency-doubled Q-switched Nd:YAG (Sol SW-532, Bright Solutions). The pump-probe synchronization and delaying is adjusted electronically by a digital delay generator (DDG) (DG645, Stanford Research Systems), which takes as input the signal from the Q-switch for the probe, and uses it to clock

either the Pockels cells in the fs amplifier, or the acousto-optical modulator in the second Q-switched laser. The repetition rate of the fs system covers all the possible repetition rates of the ns UV pulses, while the ns pump beam works efficiently from single shot up to 120 kHz. The Ti:sapphire fs amplifier can be used in Q-switched mode as well, delivering ~ 15 μJ at 789 nm. It may hence be employed as ns pump beam, although with lower time resolution, since the pulses are longer than ~ 100 ns.

Two types of photocathodes have been tested with the ns beam: polycrystalline Ta disk [157] and crystalline LaB_6 truncated cone [158]. Although having a longer experience with LaB_6 cathodes, used always in fs mode, we started the ns experiments with Ta disks. The reason is twofold. On one side, tantalum has a high melting point (3290 K [159]), and is expected to support high laser intensities with little or no degradation [103]. On the other, polycrystalline tantalum work function is $\Phi = 4.25$ eV [159], which well matches our photon energy $h\nu = 4.66$ eV. In fact, an optimal work function should be few fractions of eV below the photon energy. If the two quantities are too close, quantum efficiency is typically reduced, scaling roughly quadratically in $(h\nu - \Phi)$ [160, 161]. Oxidation, roughness, and other surface contamination might increase Φ a little further, making quantum efficiency drop even more with time. If the two quantities are too separated, the energy spread of the photoemitted electrons would possibly increase, which is undesirable for many applications, and especially in EELS.

Given a photoemission quantum efficiency $\eta_{266} = 10^{-5}$ [162], which already includes a nonzero reflectivity $R_{266} = 0.4$ [163], we can roughly estimate the number of photoemitted electrons. To consider that, we can assume the throughput of the UV pulses from their generation to the photocathode being ~ 0.2, and therefore using pulses with 4 μJ energy. This means a total number $5 \cdot 10^7$ of photoemitted electrons per pulse, generated from a UV-focused area of about $5 \cdot 10^{-5}$ cm^{-2}. For such long pulses, the electron pulse duration is solely determined by the UV pulse duration [63], and hence the peak current density at the photocathode should be ~ 10 A/cm^2. Considering that the effective area from which the photoelectrons are collected is ~ 0.1 of the total focus area, and that the electron coupling to the column is 0.2, our in-column pulses are expected to contain $5 \cdot 10^4$ electrons. This would give an average current of 750 pA at 150 kHz repetition rate, which is a high value for pulsed sources.[8]

We systematically measured the photoelectron current on the detector as a function of input UV energy and repetition rate. We note full linearity in the measured range (Fig. 1.15c). This observation is consistent with previous characterizations in similar conditions [164], once the different laser pulse duration and quantum efficiencies [165] are taken into account. There, E_{UV} is the estimated effective pulse energy delivered at the photocathode, which takes into account a measured throughput of ~ 0.5 through the UEM. The counts are measured here

[8] Femtosecond pulses at 1 MHz with 1 electron per pulse in the column generate a current 4 orders of magnitude lower.

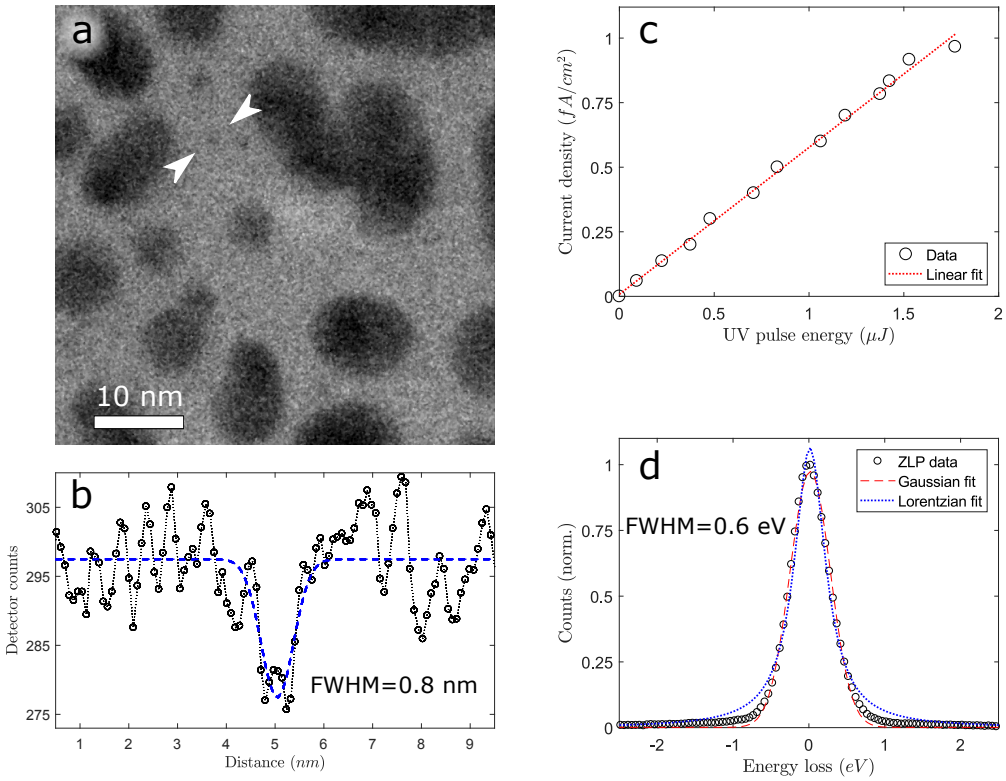

Figure 1.15 – **a**: Photoelectrons image of Au NP. Magnification 250000×, integration time 20 s. **b**: Line profile of panel a along the direction set by the pair of white arrows. Black circles are raw data, the dashed blue line a Gaussian fit with offset. **c**: Photoemission current density vs UV pulse energy shows linearity in the range considered. The ordinate axis is here the current density per pulse measured on the phosphorescent screen. **d**: Photoelectron energy spectrum, and its Lorentzian and Gaussian fits, whose FWHMs are 0.51 and 0.63 eV, respectively. Acquisition time 3 s. For all panels we utilized the Ta disk photocathode, saturation bias, 120 kHz repetition rate, and pulse duration ~ 20 ns.

via the current density generated in the phosphorescent screen, at 120 kHz repetition rate. Average powers as high as 500 mW have been shone on the cathode surface, and we noticed no dependence of the quantum efficiency on the repetition rate, up to 300 kHz, highlighting a good interpulse heat dissipation in the cathode assembly.
In Fig. 1.15d a typical electron energy profile of the ns pulses is shown to be 0.6 eV FWHM. This value is better than what can be achieved with thermionic LaB_6 cathodes. The energy spread mostly comes from the surplus energy of the photoemitted electrons before acceleration, $h\nu - W = 0.41$ eV. Noteworthy, a component of the measured energy spread may come from electric and mechanical noises in the TEM and spectrometer. Indeed, for thermionic emission we systematically measure narrower energy profiles for shorter acquisition times. For example, a spectrum which is 0.5 eV wide for an exposure of 1 μs becomes 0.6 eV when acquired for 10 s.

Fig. 1.15a shows the gold NPs dispersed on amorphous carbon film imaged by the ns electron

pulses. We can estimate the spatial resolution by selecting the tiny particle comprised between the white arrows. In case we assume conservatively that the particle has a lateral size smaller than our resolution, its profile would be given by the spatial resolution. By a Gaussian fit, we get the FWHM to be 0.8 ± 0.25 nm, whose uncertainty comprises both the statistical fit error and the systematic scale bar calibration uncertainty. While observing that we can reach sub-nm resolution, we do not observe interference fringes of atomic origin. Since the nearest-neighbor distance in gold is 0.288 nm [126], we can conclude that our spatial resolution d_0 is approximately $0.3 < d_0[\text{nm}] < 0.8$.
What prevents us attaining atomic resolution with photoelectrons is probably the mechanical stability. The system was not designed to make use advanced antivibration systems coupling the optical tables and the TEM, because the sub-nm scale is not our target for pump-probe experiments, and mechanical vibrations are not the limiting noise factor for pump-probe on larger objects. The challenges of atomic pump-probe would go anyway beyond mechanical noise reduction, since they would have to deal also with the response and stability of the sample to the excitation pulse. For these reasons, an atomically-resolved image can be acquired in thermionic mode, as in Fig. 1.8, but not in photoelectron mode, where the acquisition time has to be much longer.

To conclude this characterization section, we can say that the ns stroboscopic setup successfully combines some of the advantages of ns single-shot, as the higher pulsed current with reduced space charge and Boersch effects, with a stroboscopic approach. The combination of the two returns an apparatus useful to investigate reversible phenomena requiring high current or high spatial coherence, such as Lorentz microscopy.

1.5 Fast and direct detectors

Advancements in detector technology recently allowed efficient direct particle or photon detection in pixelated cameras [166]. In the near future they may replace CCDs in a significant portion of electron microscopy laboratories [167–169]. Three are the main aspects time-resolved experiments could benefit from:

- Virtually zero-noise camera, with high detection efficiency, which is important for all the low-dose microscopies, as UEM;
- Higher frame rate acquisition, for sub-ms camera-rate experiments;
- Short gated acquisition, for stroboscopic ns experiments with a continuous electron beam.

I will briefly introduce the detection principles, and then discuss the three key aspects just listed, which vary from detector to detector. I will discuss more in details the Quantum Detector MerlinEM detector [170], and show its preliminary characterization for time-resolved

applications.

Direct detection

In traditional detectors for electron microscopy [171], the primary electrons are converted to photons before being optically transduced to the detector, usually a CCD, see Sec. 1.1.2. This indirect detection suffers from some limitations. The spread of the photon signal due to scattering in the scintillator and at the interfaces leads to a worsening in the resolution [172]. A large point-spread function then implies a low modulation transfer function.
The paradigm of direct detection relies in a direct coupling of the primary electrons to the detector. Due to their radiation softness, standard CCDs are not suitable to be used as direct detectors [173]. Photographic films can be considered a sui generis type of direct detector, not relying on any intermediate process. They outperform CCDs at high magnification [174]. However, with their long and tedious processing time they are not suitable for modern microscopes. Rapid recording and large volumes of data have to be handled, processed, and stored for many applications, for example tomography of biological structures.
CMOS-based detectors offers the possibility to overcome the limits of indirect detection, without suffering relevantly from radiation damage [175]. Two types are commercially available, monolithic and pixelated [176]. In a monolithic active pixel sensor (MAPS) the semiconductor sensor and the readout electronics are in one single plane. A hybrid pixel detector (HPD) has instead a pixelated readout chip connected by bump bonds to the semiconductor sensor, in a pixel-by-pixel fashion. As shown in Fig. 1.16, the high-energy electron (or X-ray) generates electron-hole pairs in the silicon chip of the hybrid pixel detector (HPD). The charge (here made of holes) drifts to the bottom electrode, and, passing across the solder bump, is transferred to the integrated readout electronics.
Medipix detectors [177, 178] successfully implemented the hybrid-pixel concept. Conceived originally for particle physics applications [179, 180], they found applications also in electron microscopy [181] and biomedical imaging [182]. The MerlinEM [183] detector integrates the Medipix3RX chip with the Merlin readout system, in turn based on National Instruments' technology. It consists of a 256×256 pixel detector with a 300 μm-thick sensor, and each pixel is 55×55 μm^2.
It is robust and stable, and does not need any active cooling, working slightly above room temperature, nor pneumatic system. Among the generic limitations of MerlinEM, a narrow field of view, large pixel size, and the presence of dead pixels due to fabrication imperfections. The 55 μm pixel pitch of the detector is much larger than the typical pitch in CCDs. For example, the Gatan UltraScan-1000 camera, installed in our laboratory, has a 14 μm pitch, $\sim 4\times$ smaller than MerlinEM's. Higher magnifications are therefore needed with MerlinEM to attain the same resolving power.

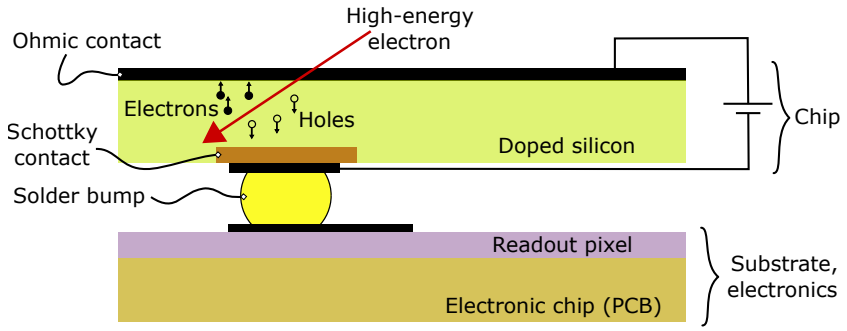

Figure 1.16 – Single pixel simplified diagram in a HPD, inspired by drawings in literature, e.g. [176]. Ohmic contacts are in aluminum.

Noise

Low-dose microscopy covers a broad area of biological imaging, as electron cryomicroscopy (cryoEM) [184, 185], and embraces also fs stroboscopic imaging. In biological application the dose is limited by the elevated radiation softness of the specimens, while in fs imaging it is set a priori by the source characteristics.
The development of direct detectors has been prompted in large part by cryoEM, and in cryoEM direct detectors saw their first applications [186–188]. The scarcity of electrons makes each count more precious, and an efficient detection essential. In short, a high detector quantum efficiency (DQE) is required.

For UEM, it is somehow less vital to detect all the electrons, provided that the sum of camera and external noises is low enough to allow long or repeated exposures.
In CCDs, the camera noise has contributions from the dark current and the electronic readout. Readout noise is a purely electronic noise, and is independent on the exposure time. It is added by the detector in the signal transfer and conversion process, for example in the digital-to-analog conversion of the voltage into discrete counts. In general its level varies from pixel to pixel, but for CCDs there is also a second component, associated with the line-by-line reading mode, in which the charge is sequentially transferred to the neighboring potential well.
Thermal noise is the statistical noise of the dark current, created by the thermally excited electron-hole pairs in the semiconductor, and follows the Poisson distribution, as shot noise does. It depends on some material and geometrical parameters, such as bandgap and pixel size, and notably on the operation temperature of the device. That is why CCDs are kept cooled by Peltier cells, usually around -20 °C. Yet, they have a considerable amount of thermal noise, deleterious for long acquisitions. For the Gatan UltraScan-1000, the thermal noise equals the readout noise for an acquisition time $t \approx 1$ s, and dominates for longer exposures.
We can perhaps better catch what said so far writing down explicitly the signal-to-noise ratio (SNR) contributions. If A is the electron current on the detector, Q the detection efficiency, t the acquisition time, B the dark current per unit of time, $C(r)$ the readout noise contribution[9]

[9]The variable r here indicates that the amplitude of C varies in space, i.e. it is pixel dependent.

then

$$\mathrm{SNR}_1 \sim \frac{AQt}{\sqrt{AQt + Bt + C(r)}} \tag{1.10}$$

is the SNR for one frame. If N frames are averaged, in principle we might expect SNR_N to simply be $\sqrt{N} \cdot \mathrm{SNR}_1$. As we observe with our UltraScan-1000 CCD, deviations from this ideal scenario, the readout $C(r)$ is higher or lower in different pixels, and does not average out for multiple acquisitions. This is reflected in the empirical fact that it is preferable to work with long exposures rather than averaging several shorter frames.
For large enough t, Eq. 1.10 scales with $\sqrt{t}$, as expected for the sum of Poissonian events. If furthermore $AQ < B$, which is a typical scenario in fs experiments, the signal has to fight mostly with the thermal noise, and very large acquisition times are needed to overcome the noise. However, t cannot be extremely large. Camera electronics do not allow to acquire for longer than typically ~ 6 minutes, and the signatures of cosmic rays start to cluster. At the same time, the mechanical stability of the sample (and in more rare cases of the electron beam) also does not allow to integrate for a time longer than several minutes, even in low magnification and at room temperature.

In MerlinEM, the integrated pixelated electronics enable the high speed of the readout system, and a key point is its ability of single electron counting. Two independent thresholds suppress the camera noise. An event is registered only if it produces a current ranged between the two thresholds. With this dual energy discrimination, thermal and readout noise can be fully disregarded in the event counting. In Eq. 1.10 terms, it means $B = 0$ and $C = 0$. The measurements become hence virtually noise-free, i.e. virtually limited by shot noise only:

$$\mathrm{SNR}_N = \sqrt{N} \cdot \mathrm{SNR}_1 \sim \sqrt{AQNt}. \tag{1.11}$$

When working at very low average electron dose and with very long exposures, internal and external sources of radiation can contribute significantly to the noise level, and in some case overshadow the signal. These sources include [171]

- low-energy photons, notably reflections of the laser pump pulses, or of the photoemitting laser as well –when operating with flat cathodes–,
- high-energy cosmic rays,
- X-rays generated in the microscope, bremsstrahlung radiation mostly,
- radioactive decay of material inside the detector.

In CCDs, X-rays are substantially attenuated. Cosmic rays have a very high energy, and in CCDs generate many counts per event, up to thousands, often distributed throughout several

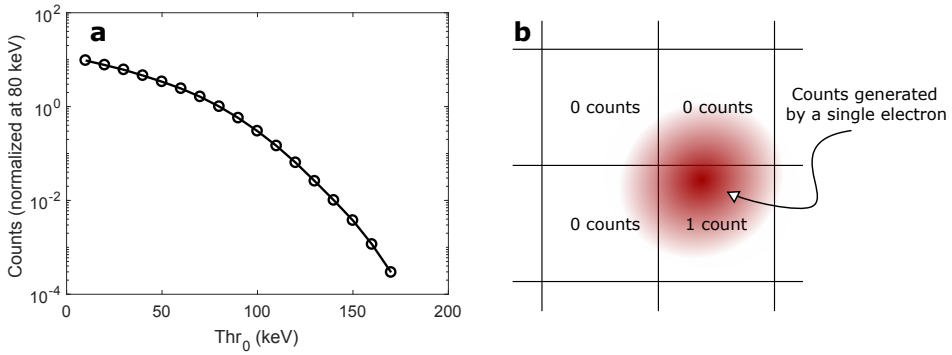

Figure 1.17 – **a**: Collected electron counts as a function of Thr_0. Thr_1 is 500 keV. The counts have been normalized ar 1 for $\mathrm{Thr}_0 = 80$ keV. **b**: Concept of 'charge summing mode'.

pixels. The MerlinEM detector is invisible to all the radiation at energy lower than its first threshold, as visible light and part of the X-rays. The counting system is made such that, within the overall $\sim 100-200$ ns of detection time, at most one count per pixel can be registered. Cosmic rays of intermediate energy are detected, but generate only 1 count, regardless of their energy, and give therefore a negligible contribution.
More in general, if 2 or more electrons hit a pixel within the minimum detection time mentioned above, only 1 event is registered. Also, it makes direct counting cameras unsuitable for any single-shot application.

Thresholds and efficiency

By changing the two independent energy thresholds, different counts are registered. One threshold (Thr_1) should be always higher than the electron energy, in our case 200 keV. We typically kept it fixed at 500 keV. An incident high-energy electron ceases its energy to several adjacent pixels. When the other threshold (Thr_0) is very low, the energy in many pixels is higher than the set threshold, and all of them register a click. With reference to Fig. 1.17a, this is the case of $\mathrm{Thr}_0 \lesssim 80$ keV. In these conditions, also the spatial resolution is worsened. When Thr_0 is higher, some events are instead lost, because they do not deposit enough energy to overcome the set threshold in any individual pixel. An optimum can be found experimentally, with the caveat that if few-pixel resolution is not required, a lower Thr_0 may bring count benefits. An analysis that considers the number of total counts versus the numbers of electron clusters in the image suggests that the optimal condition (number of counts $\simeq$ number of incident electrons) is set for $\mathrm{Th}_0 \approx (0.45 \pm 0.05) E_0$ [189], which for $E_0 = 200$ keV electrons corresponds to 90 ± 5 keV.[10]

[10] The value $\mathrm{Th}_0 \approx 0.45$ is found for $E_0 = 60$ keV. Electrons at 200 keV have a higher spread function, and therefore the optimal Th_0 may be lower.

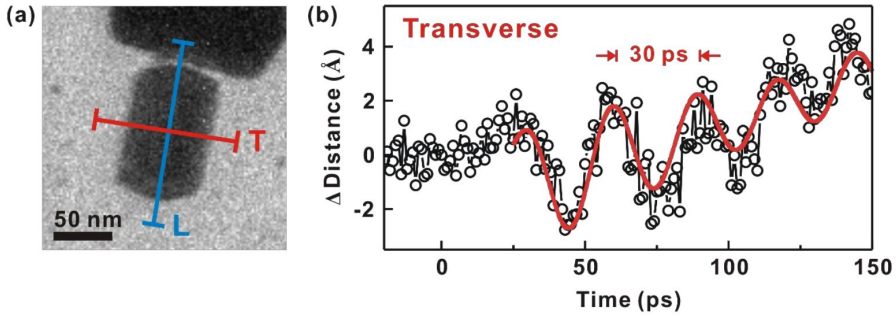

Figure 1.18 – **(a)**: Bright-field image of a gold nanorod. Ultrafast laser pulses excite longitudinal (L) and transverse (T) acoustic modes in the nanorod. **(b)**: The acoustic contraction and expansion of the nanorod is monitored by accurately fitting the nanorod edges. Here variations on the transverse direction are shown. Image reproduced from ref. [190].

1.5.1 Direct detectors in time-resolved microscopies

Direct electron cameras have been introduced in ultrafast microscopy laboratories only recently [66]. Kwon and co-workers reported the coherent ps-resolved acoustic expansion and compression of a gold nanorod with unprecedented spatial accuracy, ~ 1 Å, as shown in Fig. 1.18 [190]. A Gatan K2 Summit camera is used in that work, placed before the electron spectrometer.

In MerlinED, and similarly in Gatan K2 and K3 cameras [191], each electron can be assigned to a single pixel, despite it deposits above-threshold energy in more than one pixel. The software evaluates the center of mass of the deposited energy, and assign the count only to that pixel. This is the 'single counting' or 'charge summing' mode, Fig. 1.17b. It works only if the electrons in each frame are very sparse. Otherwise, the coincidence losses become important.
K2 and K3 cameras can have an effective sub-pixel resolution by what is called super-resolution mode. It is based on the same principle of the single counting mode, with the idea that the center of mass can be calculated with sub-pixel accuracy. The principle is already present in some optical super-resolution microscopies [192]. Effectively, it was reported to increase the number of 'pixels' by a factor 4 [188]. It can be especially useful to avoid aliasing when imaging objects whose magnified image is slightly smaller than the pixel size [193].

Camera rate

In MerlinED, due to the parallelized digital readout, large dynamic range acquisition options are available. They have a natural tradeoff with the readout speed. Maximum readout rates are 14.4 kHz at 1 bit, 2.4 kHz at 6, 1.2 kHz at 12, and 600 Hz at 24 bits. No dead time between frame acquisitions can be reached exploiting two readout counters, rows and columns. Bursts of faster acquisitions are also possible, for a limited time, until the data flow experiences a bottleneck at the exit of the buffer.

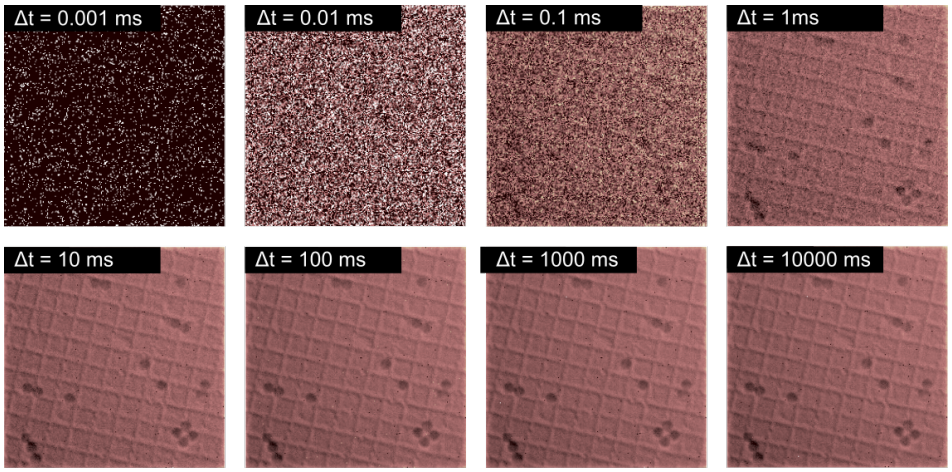

Figure 1.19 – Low magnification images of an alignment specimen (optical replica), with countinuous thermionic beam. The spatial pitch of the squared grid is 463 nm, and the color scale is adapted in each micrograph to go from black (0 counts) to white (maximum), with terracotta shades in between. The beam is not focused, therefore another order of magnitude in intensity can be achieved.

The direct detection, the fast reading, and the possibility to acquire continuously with the dual channel are ideal features for fast camera-rate experiments. Typical acquisition rates in CCD-equipped TEMs are ~ 25 Hz or slower, limited by their electronics. For imaging applications, sub-ms acquisitions would be also very hard to be carried out with CCDs because of the readout noise.
With direct detection cameras, instead, the camera noise in negligible, and the SNR is limited exclusively by shot noise. μs-resolved real-space videos can be shot in high-brightness TEM. However, being our TEM based on thermionic emission, it has a lower brightness with respect to FEGs. It is not obvious to record good images in the sub-ms range, excluding special cases with high contrast and low magnification. This is confirmed by Fig. 1.19, where the exposure of the camera is varied from 1 μs to 10 s: a well recognizable image is obtained at 1 ms exposure, or longer. At the highest beam current possible, brightness can be increased by at least ~ 1 order of magnitude, so 2.4 kHz videos could be acquired, even though for contrasts not requiring high electron coherence. Due to the small dynamic range at 2.4 kHz (6 bits), the observable contrast variation should be quite large.
Diffraction patterns on the other side can easily have a good SNR, since counts are limited to regions of few pixels. Actually in diffraction the problem is the dynamic range, which should not saturate. As a proof of principle, we studied a structural deformation of a β-$MoTe_2$ flake, induced by the heat produced by a continuous train of ns UV laser pulses (20 kHz, 25 ns, 266 nm, ~ 1 kW/cm average power). The time resolution is 410 μs, and we employ the dual-counter reading mode to have no dead time between consecutive frames.
In Fig. 1.20a a diffraction pattern is shown before the transition occurs. It is acquired in selected-area diffraction mode. In Fig. 1.20b the difference between after and before is represented, while in Fig. 1.20c we plotted a parameter linked to the amplitudes of some Bragg

reflections which vary of ~ 80% across the transition. The time coordinate is calculated from the opening of a mechanical shutter, which let the laser pulses heat the specimen. The shutter has an opening time of ~ 50 ms. The position and FWHM of the peaks show instead only small modifications, < 2%. Here we have a laser repetition rate higher than the probe sampling. If we would do vice versa, one could perhaps resolve the temperature buildup. We notice that the transition happens abruptly, within our resolution. We can therefore safely say that the heat-induced transition occurs on less than 410 µs, and that no modifications are visible before. In reality, since we are acquiring without dead times, and the transition is sharp between two consecutive frames, one could argue that the transition has had to occur in a much shorter time than the frame time, towards the end of one frame or the beginning of the following.

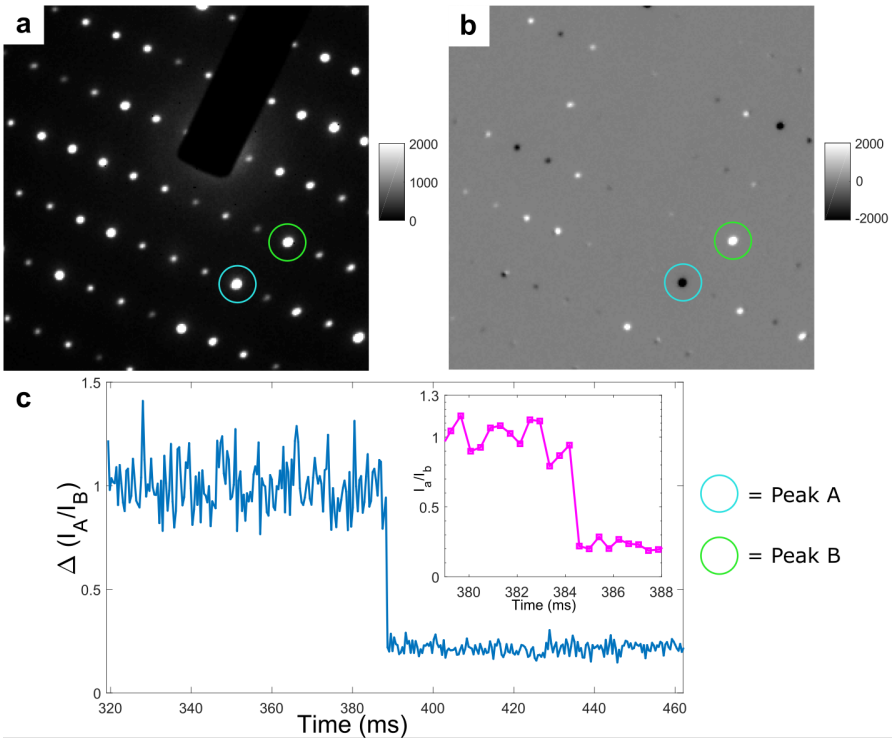

Figure 1.20 – Thermally-induced transition in a β-$MoTe_2$ flake, seen by in-situ sub-ms camera-rate electron diffraction. **a**: Diffraction pattern (DP) before the transition. **b**: Difference between the DP before and after the transition ("After−before"). In both (a) and (b) the patterns considered are averages between 400 frames, and the color scales are saturated at high counts, to make more DP features visible. We label with A and B the two Bragg reflections undergoing the biggest changes. **c**: The variation of the ratio of the peak amplitudes I_A / I_B is plotted as a function of time. The inset is an enlarged view of the points across the transition.

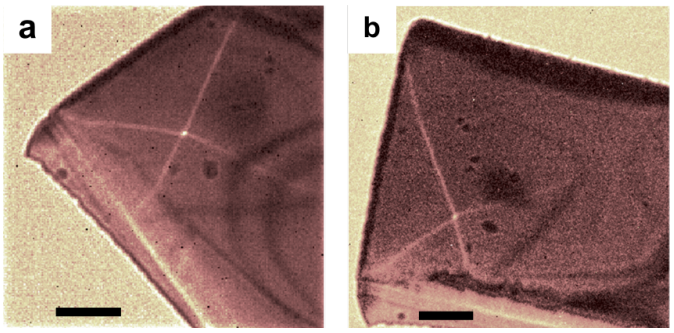

Figure 1.21 – Lorentz transmission electron microscopy (LTEM) micrographs of a Fe_3O_4 lamella, showing a vortex state. **a**: Acquired with MerlinED. **b**: Acquired with Gatan UltraScan-1000. Image (a) and (b) are both acquired with ns-photoelectrons, for 10 s at 20 kHz and 360 s at 90 kHz, respectively. Scale bars approximately 600 nm.

Pump-probe

The immediate advantage of these cameras for stroboscopic pump-probe studies is in the suppression of the camera noise. A comparison between Gatan UltraScan-1000 CCD and MerlinED is presented in Fig. 1.21. A Lorentz micrograph of a vortex state in a thin ferrimagnetic lamella is shown, for a similar value of magnification and defocus. The alignment of the microscope is not exactly the same for the two images, and it would be improper to extract a quantitative comparison. It gives however the hint of how better the MerlinED camera could be.
A significant advantage of the fast acquisition may be in performing lock-in measurements. They would greatly improve the sensitivity of the instrument. One could set the frequency of the chopper to ≤ 7.2 kHz, and ideally set the camera acquisition and laser repetition rate to ≤ 14.4 kHz. Otherwise, one could work at N times that repetition rates, chopping every N pulses. The introduction of lock-in measurements would be particularly interesting for diffraction experiments, where the instability of the electron beam intensity is the main factor limiting the resolution. This could allow to see variations in the diffraction spot intensity orders of magnitude lower than actual ones. Extra care should instead be paid for peak position and FWHM of the spots.
Notably, the success in implementing a lock-in approach is linked to the camera noise suppression. Without it, lock-in measurements would be hardly beneficial.

Detector gating - chopping the dynamics

As seen in Sec. 1.2, one of the schemes adopted to achieve high temporal resolution consists in chopping a continuous wave beam. Chopping methods aim at minimizing the TEM modifications, so preserving of the high beam quality typical of continuous beams. The ultimate level of this approach consists in chopping the response from the detector, rather than the

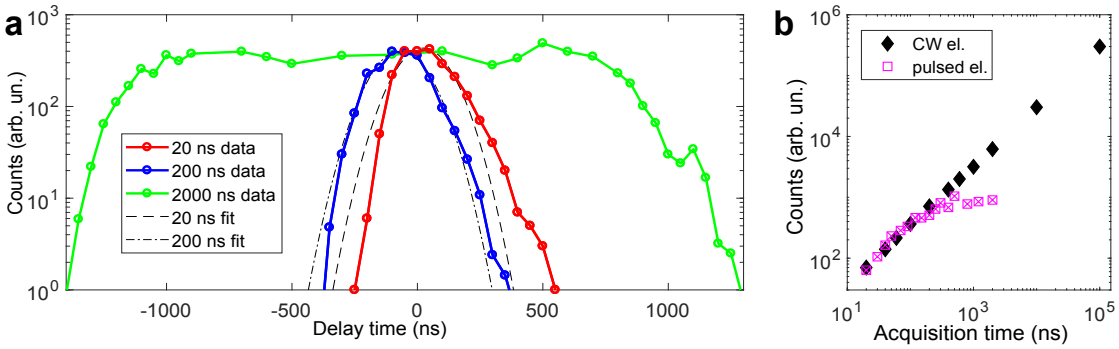

Figure 1.22 – **a**: Cross-correlation signal between 30 ns electron pulses and the gated camera acquisition, for different acquisition times, as indicated in the legend. The counts for 200 and 2000 ns acquisitions are rescaled to the same height of the 20 ns curve. Gaussian fits are shown as dashed and point-dashed lines, for 20 ns and 200 ns, respectively. They fail in fitting the tails of the distributions. **b**: Counts for CW and pulsed electrons, for decreasing acquisition times.

beam itself. In this way, every microscope could be turned into a time-resolved microscope just by choosing the right detector and a suitable synchronized excitation. The application of impulsive excitations can also be non invasive for the TEM; for example transmitted through the sample holder. Electric and magnetic pulses can be applied locally, and laser pulses as well –with properly designed optical fibers.
The acquisition with the MerlinED detector can be gated by a clock with ~ 8 ns accuracy (electronic jitter). The minimum acquisition time of the detector is 20 ns, but the overall temporal resolution is inherently related to the physics of the semiconductor device, and in our experiments currently limited to ~ 200 ns with $Th_0 = 30$ keV. In fact, the hole diffusion and drift time to the collecting electrode is ~ 100 – 120 ns. It means the counts are redistributed over such temporal window, and if one integrates all the counts, it is impossible to extract any faster information.[11]

The temporal resolution in Fig. 1.22a is measured as the cross-correlation between the gated camera acquisition and a synchronized ns-pulsed electron source.
For the synchronization, we utilized as trigger start the external raising edge coming from the ns laser, while the trigger end is internal. The delay is changed electronically in the DDG. The sum of all the external electronic jitters is ~ 10 ns, and the 600 Hz repetition rate UV pulses are ~ 20 ns FWHM-long. The electron pulses inherit the same duration [88]. An experimental upper boundary to the electron pulse duration is independently set to ~ 100 ns by the absence of double counts per pixel when a single pulse is focused on the camera. Pulses longer than ~ 100 ns would temporally leak out of the window that limits a single count per pixel, and

[11] One may expect however an improved time resolution for high values of Th_0, at the expense of the sensor efficiency. For instance, it has been proven [151] that for $Th_0 = 51$ keV and $E_0 = 60$ keV, a resolution as low as 70 ns is obtained, compared with 140 ns with $Th_0 = 28$ keV. This strategy may lead our 200 keV instruments to sub-100 ns resolution in gating mode.

double counts would be observed.
In Fig. 1.22a, for 20, 200, and 2000 ns-long acquisitions, the electron-camera cross correlation has ~ 220, ~ 260, and ~ 2000 ns FWHM duration, respectively. Time-zero also shifts of ~ −100 ns between the 20, and 200 ns-long acquisitions. Note the logarithmic scale on the ordinate, and the asymmetry of the tails, more striking if compared to the Gaussian fits. In Fig. 1.22b, continuous wave and pulsed electron counts are plotted for short acquisition times. For exposures shorter than ~ 200 ns, both are linear, while for longer acquisitions the photoelectrons reach the saturation. This is a second, independent proof of a ~ 200 ns camera resolution. The noise on the photoelectron counts is due to intensity fluctuations, which are not averaged out because only a single pulse per point was measured.

A simple way to improve the temporal resolution is to fabricate a thinner Si chip, sacrificing some signal. Semiconductors with a higher atomic number, such as CdTe or CdZnTe, could guarantee maximum efficiency for a thinner chips, for a possibly higher temporal and spatial resolution, especially for high electron energies (200 – 300 keV) [176]. CdTe pixelated detectors are however reported to suffer of some unwanted fluorescence, which broadens the point-spread function (PSF) [194, 195].

The maximum repetition rate for slicing is 14.4 kHz. With reference to Fig. 1.19, we need as little as 1 ms of continuous wave acquisition to form a low magnification structural image. It means 5000 200 ns-long acquisitions, which at 14.4 kHz can be acquired in ~ 350 ms. In Fig. 1.19 the electron current was in standard condition, but if needed, it can be increased of at least a factor 10. However, for imaging requiring higher transverse coherence, as magnetic imaging, an extra factor of ~ 100 in electron counts may be lost. Assembling all together, the acquisition of a well-resolved image could be carried out in several seconds, a very reasonable time.

2 PINEM and inverse transition radiation

In the first part of this chapter I will introduce photon-induced near-field electron microscopy (PINEM) concepts and methodologies. The second part is about stimulated transition and inverse transition radiation, a phenomenon very similar to PINEM, but which does not rely on near fields. An extended characterization and discussion of the effect is presented. This second part is largely based on ref. [141]: "*Attosecond coherent control of free-electron wave functions using semi-infinite light fields*", Nat. Commun. **9**, 2694 (2018).

2.1 PINEM

When a swift electron passes through matter, or in its proximity, it generates a broadband excitation of the sample, and it can therefore spontaneously transfer energy to the sample, as for example in Fig. 2.1a. The energy lost by the electron is absorbed by the internal degrees of freedom that have been excited. They can be photons [196, 197], plasmons [198, 199], or other low-energy bosonic modes. In electron energy loss spectroscopy (EELS), the energy lost by the electrons is measured [41]. Complementarily, the excitation in the specimen can be radiated, and measured in the far field by cathodoluminescence (CL), as in Fig. 2.1b.
The inverse process, where swift electrons gain energy after interacting with the specimen, is also possible, although requires the interaction with highly populated excited states in the material. This process is termed electron energy gain spectroscopy (EEGS) [200].
Avant-guarde electron energy gain (EEG) have been observed in LiF films at RT but not at low temperature, suggesting the role of the excited-state density [201]. Indeed, the gain and loss scattering cross section are proportional to the occupation probability of the initial state: for EELS the ground state, $\propto (n+1)$, for EEGS the excited state, $\propto (n)$ [200]. n is here the Bose-Einstein statistical occupation number $n = 1/(\exp(E/k_{\mathrm{B}}T) - 1)$, which is a function of the temperature T. This simple argument explains the scarcity of EEGS events, and their localization near the ZLP, with a gain of $\sim k_{\mathrm{B}}T$, which is well in the sub-100 meV range, at RT. For this reason, an exceptional spectroscopic resolving power is required [34]. Intriguingly, by measuring the gain/loss ratios, the precise temperature of the specimen can be retrieved, with sub-nm spatial resolution [202, 203].

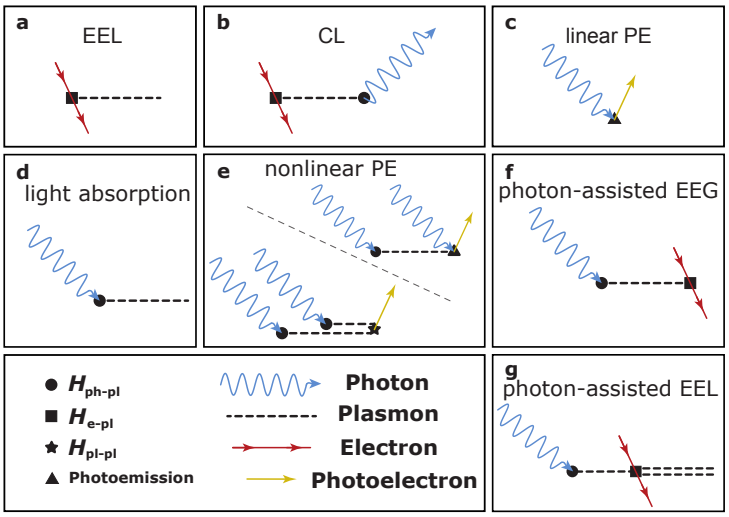

Figure 2.1 – Diagrammatic view of some of the photon-plasmon-electron absorption and emission processes, partially adapted from [204]. In each panel, time flows from left to right.

A good strategy to overcome the limitations in EEG consists in optically pumping the sample at a frequency ω [205, 206]. A mode in the material at the excitation frequency ω can be densely populated, reaching highly nonthermal states. In these conditions, the swift electron can have a high probability to absorb the excitation at energy $\hbar\omega$. And, for high occupancies, a symmetrically high probability to cede an excitation quantum. Examples of the two stimulated processes are depicted in Fig. 2.1f and g, respectively. They are referred to as *photon-assisted* or *stimulated* electron energy gain and loss processes.
Crucially, the net absorption or emission of photons cannot take place if the (nearly-relativistic) electron and light plane waves are in unbounded vacuum (Lawson–Woodward theorem) [207, 208]. The photon momentum $\left|\boldsymbol{p}_{\mathrm{ph}}\right| = \hbar\omega/c$ cannot match the longitudinal component of the electron momentum variation upon photon absorption or emission, $\left|\Delta\boldsymbol{p}_{\mathrm{e}}\right| = \hbar\omega/v_{\mathrm{e}}$. When light has instead a certain degree of localization, as in near fields, the photon momentum distribution become broader, $\Delta x\Delta p \gtrsim \hbar/2$, and the four-momentum conservation can be fulfilled. For these processes to happen, the presence of a third body is therefore necessary. We usually identify this third body with the specimen of the experiment.
Secondarily, for the nonthermal population to be high, a very intense optical illumination is required. Hence the need of ultrafast light pulses, which can provide a very strong transient electric field (i.e. extremely high photon densities) without thermally damaging the specimen. At the same time, ultrafast pulse excitation makes this phenomenon difficult to study by CW electrons, because of the tiny duty cycle of the process compared to the total acquisition time. This is the simple historic reason why only with the development of UEM the process has been observed [119]. In UEM, the duration of the probe electrons can match the duration of the photon pulse. Thus, the stimulated photon absorption and emission can be observed easily, even if it has a high probability only during the few 100s fs excitation.

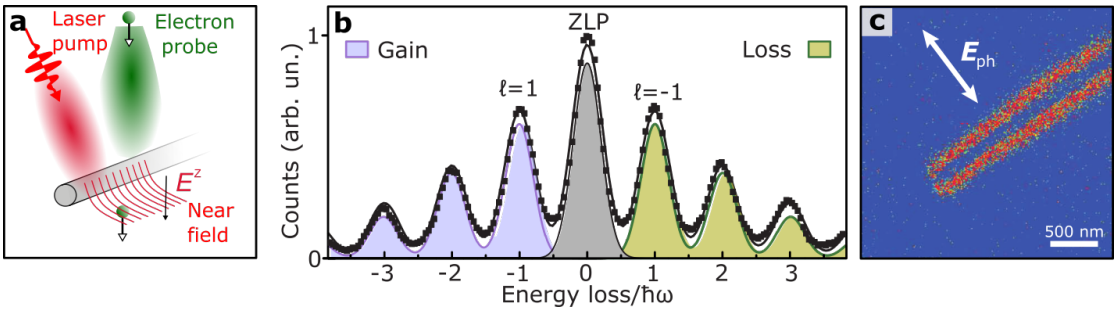

Figure 2.2 – **a**: Scheme of the experiment. **b**: PINEM spectrum, acquired at temporal overlap between pump and probe ($\Delta t = 0$). The abscissa is the energy loss, in units of $\hbar\omega = 2.4$ eV. Because of the EELS convention, gain and loss peaks have negative and positive abscissas, respectively. **c**: Image of the near field around the nanotube, acquired with the EEG electrons only (lavender-colored area). The polarization of the light is indicated by the double white arrow. Panels b and c adapted from [119].

Using a UEM [121], B. Barwick *et al.* [119], observed a giant, multiple exchange of energy quanta with gain-loss symmetry, as shown in Fig. 2.2b. Multiwalled carbon nanotubes were irradiated with femtosecond visible light at frequency ω, Fig. 2.2a. The photon-induced near field created at the edges of the nanotube oscillates at the same frequency ω, and is strongly confined. The sidebands are peaked at energies $E_\ell = \ell\hbar\omega$, with $\ell = 0, \pm1, \pm2\ldots$. Since the population of the mode is very high, $n \gg 1$, then $n+1 \approx n$, so that absorption and emission have the same probability [209].

If only the gain part of the spectrum is selected in energy-filtered transmission electron microscopy (EFTEM), a real-space image of the near-field distribution is obtained, as in Fig. 2.2c. Hence explained the acronym PINEM. Although the acronym refers explicitly to microscopy, we use it as well when dealing with the spatially-integrated spectral analysis. Imaging with the gain is generally preferable than with the loss side, because it is background-free. If the whole spectrum is used to construct the image, it will generate instead just the structural contrast, since spectrally integrated quantities are insensitive to small variations in beam energy distribution.[1]

After the first work on nanotubes, PINEM succeeded in imaging near fields surrounding metallic nanoparticles [210], steps in graphite [211], and even biological samples [212].

Time-resolved PINEM experiments are doable in principle by varying the delay between a short excitation and the electrons. However, photoexcited near fields and plasmons have typically a shorter lifetime (10 – 100 fs) than the electron pulses (> 250 fs, and often longer). As

[1] Rigorously, the spread in energy of the beam couples to nonidealities of the electron optics (chromatic aberrations), and the resulting image can be affected, even though it is a second-order problem, relevant typically only for high magnifications. Conversely, in the reciprocal space often there is no need to perform energy-filtered measurements to extract PINEM information, although EFTEM may be beneficial. This happens because a transverse momentum exchange is often associated with the energy transfer. We made use of this effect for the first time in ref. [141], and we will see it recurrently throughout the thesis.

a result, time-resolved PINEM traces are usually temporal cross-correlation measurements, as seen in Sec. 1.3.2. By imaging propagating SPPs, we recently succeeded in resolving their temporal evolution [143, 213], as we will see in Chap. 3.
Closely-related physics can result also from the scattering of electrons at lower energies (e.g. 1 keV) with a strong laser beam, in presence of a third body, for example an atom [214]. Based on that, spectrally-resolved gas-phase diffraction from molecules has been reported [215, 216]. The real-space imaging capability is however a prerogative of PINEM, which has been performed also in scanning diffraction [217, 218] and SREELS [142] modes. Recently, we showed it in momentum space as well, i.e. in MREELS [141].

2.1.1 Elements of PINEM theory

A theoretical description of PINEM can be found in [137] and [219]. Here I will give the elements needed for the following discussions [141].
A generic electron wave packet can be expressed as a sum of plane waves with momentum $\hbar\boldsymbol{k}$. Let $\hbar\boldsymbol{k}_0$ be the central momentum, whose norm is $\hbar k_0 = \sqrt{2m_\mathrm{e}E_0(1+E_0/2m_\mathrm{e}c^2)}$. E_0 is the central electron kinetic energy ($E - m_\mathrm{e}c^2$), and m_e the electron rest mass. If the momenta are narrowly peaked around $\hbar\boldsymbol{k}_0$, namely $|\boldsymbol{k}-\boldsymbol{k}_0| \ll k_0$, the electron wave packet can be described as

$$\psi(\boldsymbol{r},t) = e^{i(\boldsymbol{k}_0\cdot\boldsymbol{r}-E_0 t/\hbar)}\phi(\boldsymbol{r},t)\,, \tag{2.1}$$

with $\boldsymbol{r}$ and t spatial and time coordinate, respectively, and $\phi(\boldsymbol{r},t)$ a slower envelope function, which accounts for the different momenta $\hbar\boldsymbol{k}$ centered around $\hbar\boldsymbol{k}_0$. The electron velocity $\boldsymbol{v}_0$ is linked to $\boldsymbol{k}_0$ by the relation $\boldsymbol{v}_0 = (\hbar\boldsymbol{k}_0/m_\mathrm{e})(1+E_0/m_\mathrm{e}c^2)$. For 200 keV electrons, $k_0 = 2.5$ pm^{-1}, and $v_0 = 0.695c$, as calculated in Sec. 1.1.1. We aim at describing the interaction of the electron wave packet with an optical field, solving the time-dependent Schrödinger equation

$$(H_0 + H_1)\psi(\boldsymbol{r},t) = i\hbar\partial_t\psi(\boldsymbol{r},t)\,. \tag{2.2}$$

Here, H_0 is the kinetic term (free-space Hamiltonian), H_1 the interaction term with the optical field, which can be written as $H_1 = (-iq_\mathrm{e}\hbar/m_\mathrm{e}c)\boldsymbol{A}(\boldsymbol{r},t)\cdot\nabla$. The last expression is correct in a Coulomb gauge ($\nabla\cdot\boldsymbol{A}=0$) with a vanishing scalar potential ($\varphi = 0$). The unperturbed energy term can be expanded to first order, i.e. $H_0 \approx E_0 + (\partial_k \boldsymbol{E})_{\boldsymbol{k}_0}\cdot(\boldsymbol{k}-\boldsymbol{k}_0) \approx E_0 - \hbar\boldsymbol{v}_0\cdot(i\nabla+\boldsymbol{k}_0)$. The light interaction term can instead be approximated by considering $\nabla \approx i\boldsymbol{k}_0$, resulting in $H_1 \approx (q_\mathrm{e}\hbar/m_\mathrm{e})\boldsymbol{A}(\boldsymbol{r},t)\cdot\boldsymbol{k}_0$. It follows that Eq. 2.2 can be rewritten as

$$(\boldsymbol{v}_0\cdot\nabla+\partial_t)\phi(\boldsymbol{r},t) = \frac{-iq_\mathrm{e}}{\hbar c}\boldsymbol{v}_0\cdot\boldsymbol{A}(\boldsymbol{r},t)\phi(\boldsymbol{r},t)\,. \tag{2.3}$$

The solution of the Schrödinger equation in this form is

$$\phi(\boldsymbol{r},t)=\phi_0(\boldsymbol{r}-\boldsymbol{v}_0 t)\exp\left\{\frac{-iq_e}{\hbar c}\boldsymbol{v}_0\cdot\int_{-\infty}^{t}\boldsymbol{A}(\boldsymbol{r}+\boldsymbol{v}_0 t'-\boldsymbol{v}_0 t,t')\mathrm{d}t'\right\}. \tag{2.4}$$

We indicated as $\phi_0(\boldsymbol{r},t)$ the wave packet before the interaction with the optical field, which for our experiments can be described by a Gaussian function with 250 fs FWHM, or longer. The optical excitation, represented in Eq. 2.4 by the vector potential $\boldsymbol{A}(\boldsymbol{r},t)$, is a pulse whose envelope is much longer than an optical period. Therefore, we can write $\boldsymbol{A}(\boldsymbol{r},t)\approx(-ic/\omega)\boldsymbol{\mathcal{E}}_0(\boldsymbol{r},t)e^{-i\omega t}+$ c.c., where $\boldsymbol{\mathcal{E}}_0(\boldsymbol{r},t)$ is the envelope function of the electric field amplitude. In our experiments, this envelope has a duration of 55 fs FWHM, or longer, while the optical period is 2.63 fs for excitation at $\hbar\omega=1.57$ eV.
Once we substitute the expression of the vector potential in Eq. 2.4, we get

$$\phi(\boldsymbol{r},t)=\phi_0(\boldsymbol{r}-\boldsymbol{v}_0 t)e^{-\mathscr{B}+\mathscr{B}^\star},\ \text{where}\ \mathscr{B}(\boldsymbol{r},t)=\frac{q_e}{\hbar\omega}\boldsymbol{v}_0\cdot\int_{-\infty}^{t}\boldsymbol{\mathcal{E}}_0(\boldsymbol{r}+\boldsymbol{v}_0 t'-\boldsymbol{v}_0 t,t')e^{-i\omega t'}\mathrm{d}t'. \tag{2.5}$$

Finally, we use the identity $e^{iu\sin\varphi}=\sum_{\ell=-\infty}^{+\infty}\mathrm{J}_\ell(u)e^{i\ell\varphi}$, where $\mathrm{J}_\ell(u)$ are Bessel functions of the first kind, $|u|=2|\mathscr{B}|$, and $\varphi=\arg\mathscr{B}$. We end up with the following expression:

$$\phi(\boldsymbol{r},t)=\phi_0(\boldsymbol{r}-\boldsymbol{v}_0 t)\sum_{\ell=-\infty}^{+\infty}\mathrm{J}_\ell\left(2|\mathscr{B}|\right)e^{i\ell\arg\mathscr{B}}. \tag{2.6}$$

From the definition of $\mathscr{B}$ in Eq. 2.5, we can see that only the projection of the electric field along the electron trajectory is relevant for the interaction. Net electron acceleration and deceleration are in effect possible only when subjected to an electric field in the electron propagation direction. Without loss of generality, we can now consider the electron beam propagating along the direction $\hat{\boldsymbol{z}}$, the optical axis of the microscope. We also describe the optical excitation as a Gaussian pulse $\boldsymbol{\mathcal{E}}_0(\boldsymbol{r},t)=\boldsymbol{\mathcal{E}}_0(\boldsymbol{r})e^{-t^2/4\sigma_{\mathrm{ph}}^2}$, with $\Delta_{\mathrm{ph}}=2\sqrt{2\ln 2}\sigma_{\mathrm{ph}}\approx 2.355\sigma_{\mathrm{ph}}$ the FWHM of the pulse intensity. The pulse duration Δ_{ph} is taken to be much longer than the optical period and the interaction time with the electron around the specimen[2]. For simplicity, we also considered the optical pulse to be Fourier transformed, i.e. in absence of chirp.
Under these assumptions, $\mathscr{B}=\beta(\boldsymbol{r})e^{-(z/v_0-t)^2/4\sigma_{\mathrm{ph}}^2}e^{-i\omega(z/v_0-t)}$, with

$$\beta(\boldsymbol{r})=\frac{q_e}{\hbar\omega}\int_{-\infty}^{z}\mathscr{E}_0^z(x,y,z')e^{-i\omega z'/v_0}\mathrm{d}z'. \tag{2.7}$$

β is perhaps the most recurrent physical quantity in this thesis, because it sets the strength and phase of the interaction.[3] Since we measure the electron states at the detector, far away from the interaction region, we usually deal with $\beta=\beta(x,y)=\beta(x,y,z=+\infty)$, which –apart from a multiplicative factor– is the spatial Fourier transform of $\mathscr{E}_0^z$ along z, calculated at the spatial frequency ω/v_0. This spatial frequency is actually the angular wavenumber of the light field that allows for momentum conservation in the interaction: $|\Delta k_e|=\omega/v_0$. In other terms,

[2] Usually hundreds as, but at most few fs, for a visible or near-infrared field extending over $\sim\lambda_{\mathrm{ph}}$ in the $\hat{z}$ direction.

[3] β is sometimes termed 'PINEM field' [137].

the momentum (in units of $\hbar$) for which the phase velocity of the light field is derived from the exchanged momentum for an emission or absorption process, that is: $v_{\mathrm{ph}}^{\mathrm{phase}} = \omega/\Delta k_{\mathrm{e}} = v_0$. The expression of β correctly implies that if the Fourier component of the z component of the optical field configuration at the momentum-matching value is vanishing, no electron-photon interaction is possible, since the wave packet ϕ, Eq. 2.5 or Eq. 2.6, would be equal to the incident, unperturbed electron wave. Once considered the expression for β and the finite photon pulse width, the final expression of the electron wave packet at a generic position and time $(\boldsymbol{r}, t)$ becomes

$$\phi(\boldsymbol{r},t) = \phi_0(\boldsymbol{r}-\boldsymbol{v}_0 t) \sum_{\ell=-\infty}^{+\infty} \mathrm{J}_\ell\left(2\left|\beta(\boldsymbol{r})\right| e^{-(z/v_0-t)^2/4\sigma_{\mathrm{ph}}^2}\right) e^{i\ell \arg\{-\beta(\boldsymbol{r})\}+i\ell\omega(z/v_0-t)}. \tag{2.8}$$

The Bessel functions have a dumped oscillatory behavior, for high-enough β. The last part of the exponential corresponds to an energy $\ell\hbar\omega$ and a linear momentum component $\ell\hbar\omega/v_0$ gained or lost by the electron in the interaction. The higher the value of $\mathrm{J}_\ell(2\left|\beta\right|)$ for a given ℓ, the more populated the ℓth sideband in the energy spectrum.

In case of monochromatic light, as the light coming from a CW laser source, the expression of $\mathscr{B}$ gets simplified by the Gaussian prefactor accounting for the pulse, and it does not depend on the temporal variable t. Similarily, in Eq. 2.8 the argument of the ℓ^{th}-order Bessel functions would be just $2\left|\beta\right|$, without the Gaussian term. Indeed, apart the Gaussian prefactors, the theory works for a continuous, monochromatic optical field.

The electron pulse envelope can be assumed to be $\phi_0(\boldsymbol{r}-\boldsymbol{v}_0 t) \propto e^{-(t-z/v_0-\Delta t)^2/4\sigma_{\mathrm{e}}^2}$. Again, the pulse duration is $\Delta_{\mathrm{e}} = 2\sqrt{2\ln 2}\sigma_{\mathrm{e}} \approx 2.355\sigma_{\mathrm{e}}$. The electron is here modeled to have perfect longitudinal coherence over its wave packet extension, and that no statistical incoherence is considered. This hypothesis is not strictly correct, see Sec. 1.3.2, but we will show that it is not restrictive in our description of PINEM.

We wrote explicitly only the dependence of ϕ_0 on the longitudinal coordinate z. On the transverse coordinates x and y the pulse profile can be assumed Gaussian as well, or even top-hat, in certain experimental conditions. In both cases, it is valid the normalization $\int \left|\phi_0(\boldsymbol{r},t)\right|^2 \mathrm{d}^3\boldsymbol{r} = N_{\mathrm{e}}$, where N_{e} is the number of electrons per pulse. In most of the measurements, we can use $N_{\mathrm{e}} = 1$, as seen in Sec. 1.3.2.

In general, the excitation field is inhomogeneous in the plane of the specimen. The probability for an electron measured on the detector having absorbed or emitted ℓ photons would depend therefore on the transverse position (x, y). Indeed, we have $\mathscr{P}(x,y) = \int \left|\phi(\boldsymbol{r},t)\right|^2 \mathrm{d}z$, evaluated for large values of t. The integral extrema are here $\pm\infty$, having placed the electron source at $z = -\infty$, and the detector at $z = +\infty$. We can separate the variables in the function ϕ, and write it as $\phi(\boldsymbol{r},t) = \phi_\perp(x,y)\phi_\parallel(z,t)$. For a Gaussian beam in the transverse direction, we get $\phi_\perp(x,y) = \phi_{0\perp}(x,y) = \mathscr{C}(x,y) = 1/(2\pi\sigma_{\mathrm{x}}\sigma_{\mathrm{y}}) e^{-x^2/2\sigma_{\mathrm{x}}^2 - y^2/2\sigma_{\mathrm{y}}^2}$. We called this factor $\mathscr{C}(x,y)$ to stress that is just a normalization function.

We have therefore (for $N_{\mathrm{e}} = 1$):

$$\mathscr{P}(x,y) = \sum_{\ell=-\infty}^{+\infty} \mathscr{P}_\ell(x,y), \tag{2.9}$$

with

$$\mathscr{P}_\ell(x,y;\Delta t) = \mathscr{C}(x,y)\frac{v_0}{\sqrt{2\pi}\sigma_\mathrm{e}}\int_{-\infty}^{+\infty} e^{-(t-z/v_0-\Delta t)/2\sigma_\mathrm{e}^2} J_\ell^2\left(2\left|\beta(x,y)\right|e^{-(z/v_0-t)^2/4\sigma_\mathrm{ph}^2}\right)\mathrm{d}z \quad (2.10)$$

the probability to have exchanged a net number ℓ of photons. Here we used the orthonormality property of the Bessel functions $J_\ell(u)$. By changing integration variable, we can rewrite Eq. 2.10 as

$$\mathscr{P}_\ell(x,y;\Delta t) = \mathscr{C}(x,y)\frac{1}{\sqrt{2\pi}\sigma_\mathrm{e}}\int_{-\infty}^{+\infty} e^{-t^2/2\sigma_\mathrm{e}^2} J_\ell^2\left(2\left|\beta(x,y)\right|e^{-(t+\Delta t)^2/4\sigma_\mathrm{ph}^2}\right)\mathrm{d}t\,. \quad (2.11)$$

In the last two equations the interaction strength parameter $\beta(x,y)$ defined by Eq. 2.7 has to be calculated for $z\to+\infty$.
From Eq. 2.9, Eq. 2.11, the definition of $\mathscr{C}(x,y)$, and once recalled the identity $\sum_{\ell=-\infty}^{+\infty} J_\ell^2(u)=1$, we confirm the correct probability normalization

$$\sum_{\ell=-\infty}^{+\infty}\int_{-\infty}^{+\infty}\int_{-\infty}^{+\infty}\mathscr{P}_\ell(x,y;\Delta t)\mathrm{d}x\mathrm{d}y = 1\,. \quad (2.12)$$

The time integral in Eq. 2.11 can be evaluated term by term by developing the Bessel functions in their Taylor expansions, $J_\ell(u)=\sum_{j=0}^{\infty}(-1)^j(u/2)^{\ell+2j}/(\ell+j)!\,j!$, finally yielding

$$\mathscr{P}_\ell(x,y;\Delta t) = \mathscr{C}(x,y)\sum_{j=0}^{\infty}\sum_{j'=0}^{\infty} C_{\ell j}(x,y)C_{\ell j'}(x,y)\frac{1}{\sqrt{\lambda}}e^{-n_0/\lambda[(\Delta t)^2/2\sigma_\mathrm{ph}^2]}\,. \quad (2.13)$$

Here we have introduced the quantities $n_0=\ell+j+j'$, $\lambda=1+n_0(\sigma_\mathrm{e}/\sigma_\mathrm{ph})^2$, and $C_{\ell j}(x,y)=(-1)^j\left|\beta(x,y)\right|^{\ell+2j}(\ell+j)!/j!$.

All the derivation above assumed implicitely that each sideband ℓ is a well-separated energy channel. We already assumed before Eq. 2.7 that for the light pulse it should hold $\sigma_\mathrm{ph}\omega\gg1$, and analogously for the electron pulse $E_0\sigma_\mathrm{e}\gg\hbar$. When the (inhomogeneous) statistical distribution of the electron velocities leads to ZLP FWHM$\sim\hbar\omega/2$, the sidebands in the PINEM spectrum may merge into each other. This fact would partially hinder the PINEM data analysis, but the physics of the interaction would not need another description, because $\Delta E_0\neq\hbar/2\sigma_\mathrm{e}$. Moreover, if in the analysis we consider separately the coherent and incoherent temporal broadenings, σ_e and $\sigma_\mathrm{e,inc}$, respectively, the result is unchanged, once considered the total broadening $\sigma_\mathrm{e}^\mathrm{tot}=\sqrt{\sigma_\mathrm{e}^2+\sigma_\mathrm{e,inc}^2}$ instead of the sole coherent part σ_e [141]. In other words, in all the equations in the current section the temporal broadening σ_e can be thought without loss of generality as the total duration of the electron wave packets as measured in the experiments, which include both coherent and incoherent contributions.

So far, all the measurable quantities (the probabilities $\mathscr{P}_\ell$) have been expressed as a function of the transverse coordinates (x,y). If we think about a simple experiment in which the near field

of a single NWis measured [137, 219], as in Fig. 2.2a, we readily see that the electric field $\mathscr{E}_0^z$ is maximum at the edge of the NW, and it fades away with a certain decay constant $\lesssim \lambda_{\mathrm{ph}}$. We call *impact parameter* b the distance from the near field source. In a typical experiment [119, 142], data are collected on the detector from a large field of view, resulting in an average over many impact parameters. Or in other words, over many β. The measured spectrum would be formed by sidebands whose amplitudes are set by the probabilities

$$\mathscr{P}_\ell(\Delta t) = \iint_{\mathrm{Area}} \mathscr{P}_\ell(x, y; \Delta t)\mathrm{d}x\mathrm{d}y\,, \tag{2.14}$$

where the integration is performed over the specimen area probed by the electrons. When integrated over all the impact parameters b, the PINEM sidebands have a monotonically decreasing intensity with $|\ell|$ [137].

The particular case in which a single impact parameter b probed is significant, see also Sec. 2.1.2. It is the case for which Eq. 2.7 contains a constant excitation field, that is $\mathscr{E}_0^z(x, y, z') = \mathscr{E}_0^z(z')\,\forall(x, y)$ probed by the electrons. This condition can be realized in two ways. With a parallel electron beam, when the system probed is perfectly homogeneous: for example a laser beam reflecting on a plane mirror, with a laser spotsize much larger than the electron beam transverse dimensions [141, 220, 221]. Otherwise, the same condition can be reached by tightly focusing the electron beam on the specimen plane [217, 222]. For visible wavelengths, generally the strength of a near field varies across tens of nm. If the electron beam is focused on a diameter of 10 nm or less, the field amplitude $\mathscr{E}_0^z$ can be typically considered homogeneous. Apart from one of these two conditions being fullfilled, it is necessary also $\sigma_{\mathrm{ph}} \gg \sigma_{\mathrm{e}}$ for the single-electron pulses to undergo the same interaction at each pulse. In fact, even at $\Delta t = 0$, if $\sigma_{\mathrm{ph}} < \sigma_{\mathrm{e}}$ the electrons would statistically sample both peak and tails of the optical pulse, with a consequent averaging over many interaction strenghts, as can be seen from the argument of the Bessel functions J_ℓ in Eq. 2.11. Ideally, a long top-hat temporal profile would be optimal to guarantee a constant argument of J_ℓ at all probed times; in practice a long Gaussian beam is already very good [141, 222]. This last condition in the formalism described above corresponds to the monochromaticity limit of the optical excitation.

Under the conditions of monochromaticity, constant b, and time overlap ($\Delta t = 0$)[4], Eq. 2.11 is simplified into

$$\mathscr{P}_\ell = \frac{1}{\sqrt{2\pi}\sigma_{\mathrm{e}}} \int_{-\infty}^{+\infty} e^{-t^2/2\sigma_{\mathrm{e}}^2} J_\ell^2\left(2|\beta|\right)\mathrm{d}t = J_\ell^2\left(2|\beta|\right). \tag{2.15}$$

If we lift the strict condition of monochromaticity, but keep the other two, Eq. 2.11 would instead read

$$\mathscr{P}_\ell = \frac{1}{\sqrt{2\pi}\sigma_{\mathrm{e}}} \int_{-\infty}^{+\infty} e^{-t^2/2\sigma_{\mathrm{e}}^2} J_\ell^2\left(2|\beta| e^{-(t+\Delta t)^2/4\sigma_{\mathrm{ph}}^2}\right)\mathrm{d}t\,. \tag{2.16}$$

[4] Although time-zero is not defined for monochromatic light, here we have always in mind the $\sigma_{\mathrm{ph}} \gg \sigma_{\mathrm{e}}$ case.

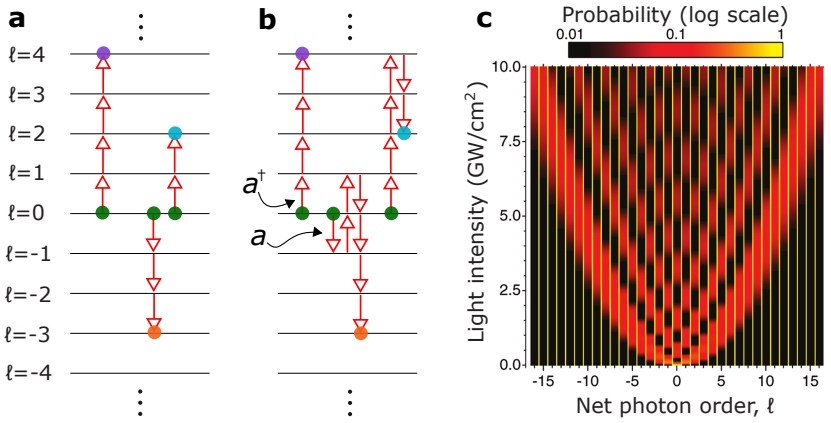

Figure 2.3 – **a**,**b**: Multilevel system for the electron in presence of the driving field. In (a), examples of either (multi)photon absorptions or (multi)photon emission processes are represented. In (b), examples of complex pathways in the multilevel system resulting in the same net exchanged photons as in (a) are depicted. $a^\dagger$ and a are raising and lowering operators, respectively. **c**: Population probability for the net ℓs as a function of the driving optical intensity, corresponding to the general (b) case. Panel (c) adapted from [219].

Similarily, Eq. 2.13 becomes

$$\mathscr{P}_\ell = \sum_{j=0}^{\infty}\sum_{j'=0}^{\infty} C_{\ell j} C_{\ell j'} \frac{1}{\sqrt{\lambda}} e^{-n/\lambda[(\Delta t)^2/2\sigma_{\rm ph}^2]}. \tag{2.17}$$

The analytical theory presented in this section well describes the PINEM interaction and its effects [141, 152, 219, 223]. The non-relativistic description is fully correct as long as one considers the relativistically corrected electron velocity [224], as we did at the beginning. In the following section we focus on some captivating consequences in a more quantum-mechanical perspective.

2.1.2 Quantum coherences and Rabi oscillations

We now focus on the simple case of Eq. 2.15, in which the probability to populate the $\ell^{\rm th}$ sideband is given by the square of the $\ell^{\rm th}$ Bessel function of the first kind, with argument $2|\beta|$.

Gain and loss energy photon orders can be represented as energy states in a multilevel, evenly-spaced quantum ladder Hamiltonian, of the type shown in Fig. 2.3a,b[5]. We label the states by their photon order ℓ. The spacing between the levels is $\hbar\omega$, and in absence of interaction ($\beta = 0$) the probability to have an electron in the state $\ell = 0$ is unitary. When the excitation field is turned on, nonzero-order states start getting populated, with probabilities $\mathscr{P}_\ell$ as in

[5] In analogy with diffraction jargon, the configurations in panel a and b are sometimes referred as 'kinematical', and 'dynamical', respectively [217]

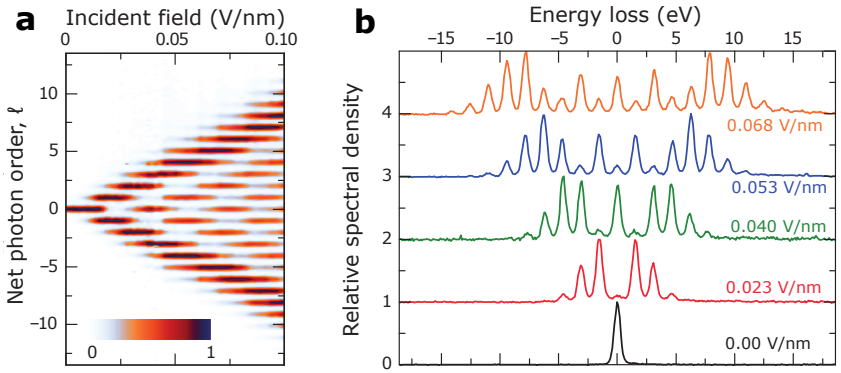

Figure 2.4 – **a**: Experimental measurement of the multilevel Rabi oscillations: energy-field map. **b**: Some representative spectra from panel (a); offset for clarity. Both panels adapted from [222].

Eq. 2.15. Being $J_\ell^2(2|\beta|)$ oscillatory as a function of $|\beta|$, the population of the ℓ^{th} photon order oscillates as a function of the field strength. A theoretical map of this oscillatory phenomenon is reported in Fig. 2.3c. We note for example that the 0^{th} order, i.e. the ZLP, gets depopulated till it is vanishing. At the first zero of the ZLP, the $\ell = \pm 1$ levels hold the majority of the spectral weigth. For higher field intensities the ZLP repopulates, and so on.
Experimental evidence of $\mathscr{P}_{\ell\neq 0} > \mathscr{P}_0$[6] has been reported and explained in ref. [137] and [217]. The oscillations are not observed to reach zero, because of the partial averaging in space (over different b) and time ($\sigma_{\text{ph}} \sim \sigma_{\text{e}}$). In ref. [222], high-quality experimental data are reported, together with a description based on coherent quantum superpositions generating Rabi-like oscillations in the multilevel system, which I will succinctly outline it in the following paragraph.

On the quantum ladder of Fig. 2.3b, a higher level can be described by an electron having absorbed a photon as the result of the action of a raising operator $a^\dagger$. Similarly, an electron energy loss (EEL) level is reached by a lowering operator a, with $[a, a^\dagger] = 0$. We have $a^\dagger|m\rangle = |m+1\rangle$, and $a|m\rangle = |m-1\rangle$, where $|m\rangle$ is the electron state in the m^{th} level of the ladder. We assist to a net exchange of ℓ photons by applying ℓ times $a^\dagger$, but also $\ell+1$ times $a^\dagger$ and once a, and any other combination of $\ell + N$ $a^\dagger$ and N a, $N = 0, 1, 2\ldots$. The strength of the interaction (β) sets the maximum number of scattering events, say n. The highest populated photon order is $|\ell| = n$. Therefore, the highest measured order is directly related to the maximum interaction strength, as visible in Fig. 2.3c.
For $|\ell| < n$, the occupation probability is set by the coherent sum of all the possible pathways in the ladder yielding ℓ net exchanged photons. Each pathway has its own associated phase, and their coherent superposition leads to constructive or destructive quantum interference. This argument gives the physical explanation to the oscillations in the occupation probability of the sidebands.

[6] Condition sometimes referred to as 'inverted population' [137].

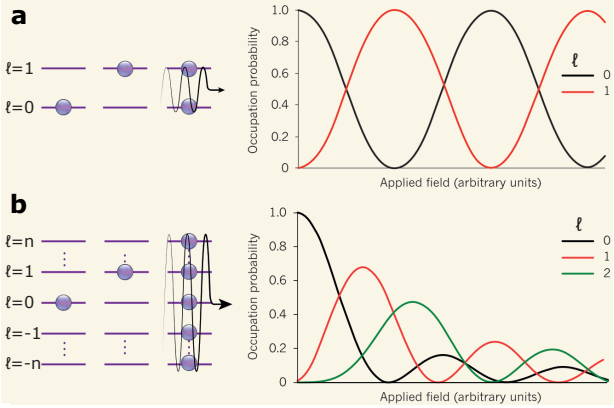

Figure 2.5 – **a**: Rabi oscillations in a two-level system. The electron is in a superposition state $A|1\rangle + B|0\rangle$, with $AA^\star$ and $BB^\star$ oscillating as square cosine and sine functions, respectively. **b**: Rabi-like oscillations in a multilevel system. The electron is in a superposition state of the $2n+1$ levels. The probability to occupy a state ℓ oscillates as the square of the Bessel function of order ℓ. Image adapted from [225].

Fig. 2.4a, from ref. [222], contains a map of experimental spectra as a function of the incident field amplitude, closely reproducing the probability distribution map calculated analytically (Fig. 2.3c). Note that the two maps are plotted against different quantities: light intensity for the theory, and field amplitude for the experiments. In Fig. 2.4b few representative spectra are plotted. In order to probe a constant $\mathscr{B}$ in the experiment, a narrow (~ 15 nm diameter) electron beam has been focused far away from the near field source, a metallic needle.
The oscillations in this multilevel system have close resemblance to the Rabi oscillations in an atomic two-level system. Fig. 2.5 [225] well highlights the similarity of the coherent superposition of states in two- and multi-level systems. In Fig. 2.5a, an electron is placed in a superposition of state $|0\rangle$ and $|1\rangle$ by a strong electromagnetic field. The occupation probability of the two states is cyclic as a function of the applied field [226, 227]. In panel b, the multilevel system is considered, with states $-N,\dots 0,\dots N$. The strong electromagnetic field drives the system in a superposition of the $2N+1$ states. Like in the two-level case, the occupation probabilities show an oscillatory behavior, albeit they are not cyclic, since the effective number of levels in the system is not fixed, but it increases as a function of the applied field strength. The curves in Fig. 2.5b represent the functions $J_\ell^2(2|\beta|)$, and describe the occupation probability for the 0^{th}, 1^{st}, and 2^{nd} photon orders.

Notably, ref. [222] offered a shift in narrative, based on imprinting the Rabi phase onto the free-electron wave function. Its fascinating quantum mechanical aspects can be exploited to obtain attosecond pulse trains by dispersive bunch reshaping [222, 228], free-electrons quantum optics experiments [228], and control over the electron wave function by spatially- [213, 229] or temporally- [141, 213]separated fields.

2.2 Far-field interactions

Controlling free-electron wave functions with light pulses has fundamental applications, from free electron laser (FEL)s [230], to PINEM and dielectric laser accelaration (DLA) [231–233]. We provide here a robust characterization of stimulated transition and inverse transition radiation, a process where photons are emitted (direct) and absorbed (inverse process) by an electron in the proximity of a surface.[7] The simultaneous observation of quantized longitudinal (energy) and transverse exchanged momentum components is for the first time reported for nearly-relativistic electron beams. By the interaction with two temporally-separated phase-locked fs light pulses, the interaction strength (hence Rabi phase) can be modulated by only varying the mutual phase between the two pulses. Significant changes in the electron wave function are determined by phase delays which are fractions of 2π; on the temporal coordinate, they corresponds to delays in the attosecond timescale. The electron-photon process is shown to be as or even more efficient than the interaction with near fields employed in PINEM studies. It is simple and general: the spatial homogeneity makes it ideal to observe Rabi oscillations with the electron beam in field-of-view mode. Furthermore, not relying on plasmonic excitation in materials, it can be easily scaled to higher photon energy, providing interesting scenarios for the manipulation of the electron wave function to the few-attosecond timescale, and possibly below.

2.2.1 Introduction

By making use of two temporally-separated laser pulses, a dynamical manipulation of the free electron wave function is demonstrated. The coupling between free-electrons and light is in general weak. The elastic scattering of free electrons by a photon in vacuum is rare; its scattering probability is quantified by the Thomson cross-section $(8\pi/3)(\alpha\hbar/m_e c)^2 \sim 10-100$ mb $= 10^{-28}-10^{-29}$ m^2, for $\hbar\omega \ll m_e c^2$ [209][8]. As we saw in Sec. 2.1, the inelastic scattering between a free photon and a free electron is forbidden. Electrons can however diffract in vacuum from an electromagnetic standing wave formed by two counter-propagating light beams (Kaptiza-Dirac effect [234–236]). Virtual absorption-emission processes allow there for an effective interaction while conserving the momentum in the scattering process ($+\boldsymbol{k}-\boldsymbol{k}=0$).
Electrons can spontaneously radiate light through different schemes [237], such as synchrotron emission, transition radiation [238], Smith-Purcell effect [239], Compton scattering [240], and Čerenkov radiation [241]. As a general rule, every spontaneous process can have its stimulated counterpart, as in inverse-FEL [242] and DLA (inverse Smith-Purcell effect [232, 243]). In PINEM, the electron is stimulated to absorb and emit photons by a localized near field, whose strong localization allows relaxing the strict photon-electron momentum conservation law in unbounded vacuum.

[7] We will refer to this process mostly as 'inverse transition radiation', giving for understood the gain-loss spectral symmetry, meaning that stimulated transition radiation is present as well.

[8] α is here the fine-structure constant.

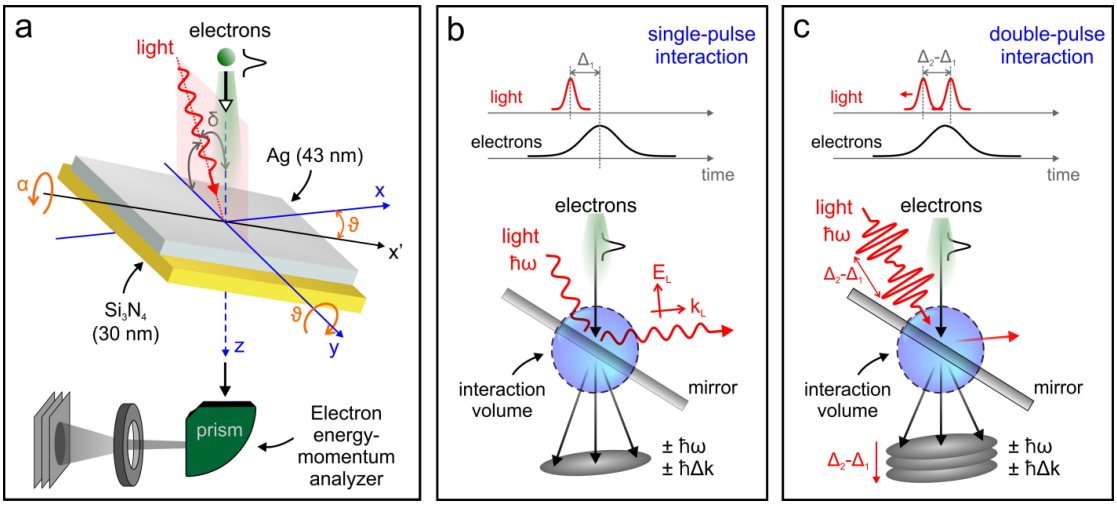

Figure 2.6 – Schematic of the experiments with semi-infinite light fields. **a**: Electrons (along $\hat{z}$) and light impinge the mirror at different angles, with the indicated geometry. The mirror can be tilted along $\hat{x}$ and $\hat{y}$. **b**: In the single-pulse interaction, electrons scatter from a single light pulse. Quantized energy and transverse momentum exchanges are measured on the transmitted electron beam. **c**: In the double-pulse interaction, the electrons scatter from a double-peaked field configuration. Quantized exchanges are measured as a function of the phase delay between the two peaks.

We use here an inverse transition radiation process [220, 221, 244–248], with the geometry of Fig. 2.6a. The light is confined in a semi-infinite field by the presence of a mirror, which acts as a symmetry-breaking element. The localization induced by this geometry is weaker than what provided by a near field. Nonetheless, it is enough to overcome the momentum mismatch, as visible from Fig. 2.7. In panels a and b we represent the instantaneous electric field of a monochromatic light beam with $\hbar\omega = 1.57$ eV along its propagation direction. The mirror abruptly interrupts the electric field, being the optical penetration depth in Ag (~ 11 nm) much smaller than the free-space wavelength. In other words, the translation invariance of the electric field is broken by the presence of the mirror. Instead of a fully reflective, a refractive or absorbing element could have been used as well, although with lower efficiency. In Fig. 2.7c and d the spatial Fourier transforms of the infinite and semi-infinite cases are shown. In the first case (panel c) the momentum is perfectly known, $k = \pm k_{\mathrm{ph}} = \pm\omega/c \simeq 8\ \mu\mathrm{m}^{-1}$, and it is represented by a Dirac δ-distribution (blue arrow). There is no overlap between the momentum distribution and the electron momentum exchange for the absorption or emission of a photon in vacuum, $\Delta k_{\mathrm{e}} \simeq \omega/v_0 \simeq 11.4\ \mu\mathrm{m}^{-1}$. When the mirror is present (panel d), the momentum distribution experiences a certain broadening around $\pm k_{\mathrm{ph}}$, with a $\sim 1/(k \pm k_{\mathrm{ph}})$ profile, enabling the light-electron inelastic coupling.

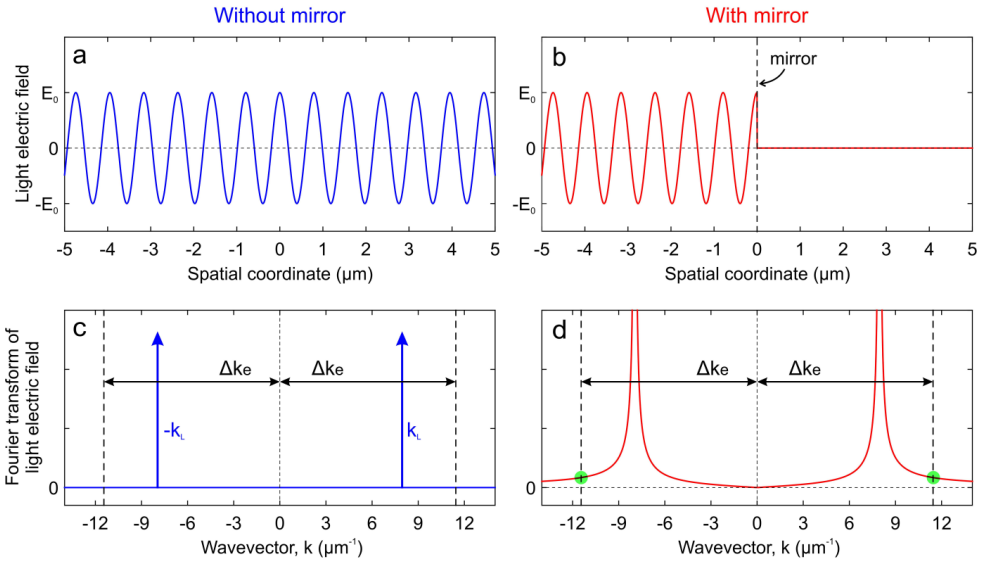

Figure 2.7 – Conservation of momentum for a semi-infinite field in vacuum. **a**-**b**: Snapshot of the incident light electric field for an infinite (a) and semi-infinite geometry. For the semi-infinite case, a reflected component will be also present (here not shown), and the total electric field will be null at the interface. **c**-**d**: Corresponding spatial Fourier transforms. k_{L} is the free-photon wavevector, Δk_{e} the momentum acquired by a free electron in a photon absorption process.

2.2.2 Methods

We designed the mirror to maximize light reflection, minimize spurious near fields, and at the same time guaranteeing a significant transmission of the incident 200 keV electrons through the structure. It is formed by a 43 ± 5 nm-thick Ag film sputtered on a squared 30 nm-thick Si_3N_4 membrane on a Si TEM grid. Given the large permittivity of Ag ($\epsilon_{\mathrm{Ag}} = -30.3 + 0.39i$ [249], while $\epsilon_{Si_3N_4} = 4.04$ [250]) at 1.57 eV, and the skin depth ($\sim$ 11 nm) much smaller than the Ag thickness, the mirror reflects > 98% of the incident light. The lateral dimensions of the Ag-Si_3N_4 bilayer membrane are 80×80 μm^2. As shown in Fig. 2.6a, the mirror is mounted on a double-tilt sample holder, which allows to rotate around the $\hat{x}$ axis (angle α), and $\hat{y}$ axis (tilting angle, ϑ), over a range of $\pm 35°$.

The 300 kHz laser excitation pulses have tunable pulse duration, polarization, and intensity. With reference to Fig. 2.6a, $\boldsymbol{k}_{\mathrm{ph}}$ lies on the $< yz >$ plane, forming an angle $\delta = 4.5°$ with the propagation direction of the electrons, $\hat{z}$[9]. The laser spotsize has $\sim$ 58 μm FWHM diameter, much larger than the field of view (< 10 μm), making the excitation spatially homogeneous. EELS data are acquired with a GIF Quantum. We always used 50 meV-per-channel energy dispersion, and a ZLP of $\sim$ 1.1eV in spectroscopy. Spectroscopy data are acquired with the

[9] The value of δ is found as the (α, ϑ) tilt for which the electromagnetic field doing inverse transition radiation is parallel to the specimen surface, as we will show in Sec. 3.2.3. Its value perfectly matches what retrieved from the experiment-theory comparison for the inverse transition radiation experiment, and it is compatible with an estimate based on geometrical constraints of the optical access in the TEM ($2° \lesssim |\delta| \lesssim 5°$).

microscope aligned in imaging mode, at a nominal magnification of ~ ×4000, although it does not influence the results, being our specimen, namely the mirror, invariant by translations in the $< \hat{x}\hat{y} >$ plane. Typical exposures times for spectra are ~ 30 – 60 s, spectra were realigned to their ZLP peak position in post-processing analysis, using a differential-based maximum intensity alignment algorithm. The transferred-momentum maps are the sum over many ~ 200 s micrographs for a total integration time ranging from several minutes to several hours. Patterns in momentum space were realigned with an algorithm based on cross-correlation maximization.

2.2.3 Single-pulse experiments

These experiments systematically study the inverse transition radiation effect for the configuration depicted in Fig. 2.6b, with a single excitation pulse.

Energy quantization

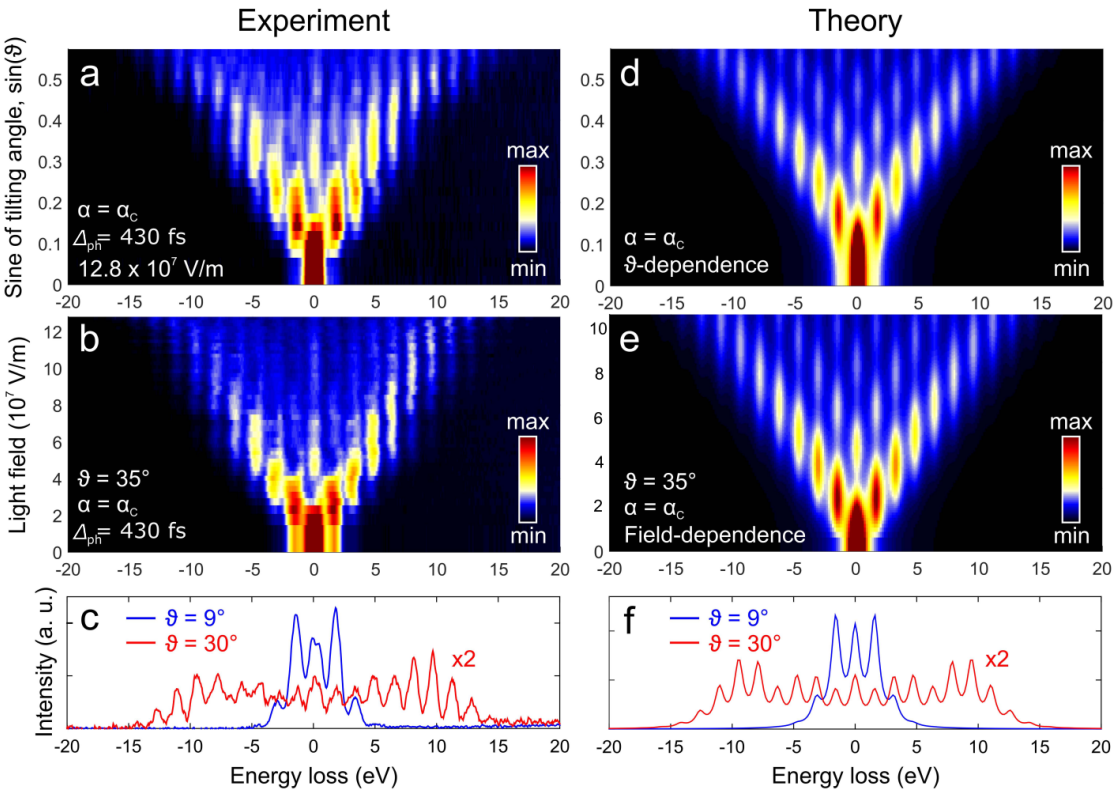

Figure 2.8 – Energy exchange for inverse transition radiation. **a**,**b**: EEL spectra as a function of increasing tilting angles, at a fixed field amplitude (a), and increasing field amplitudes, at a fixed tilting angle (b). **c** Two representative spectra taken from panel a. **d**-**f**: Simulated EEL spectra for the same experimental conditions of panels a-c.

To prove the strong electron-photon coupling by inverse-transverse radiation we systematically varied several parameters of the electromagnetic excitation, notably the angles of incidence on the mirror, the polarization, and the intensity. In Fig. 2.8a we show the EEL spectrum for increasing tilting angles $0° \leq \vartheta \leq 35°$. The light pulse is temporally stretched to become slightly longer than the electron pulse: 430 and 410 fs, respectively.[10] The electric field amplitude has been kept constant at $\mathscr{E}_0 = 12.8 \cdot 10^7$ V/m. Analogously, in Fig. 2.8b the EELS signal is recorded for increasing field amplitudes, at a fixed $\vartheta = 35°$. Fig. 2.8c shows two representative spectra at small and high tilting angle, highlighting the great difference in populating low- and high-photon orders.
In both cases, the spectral width is increasingly transferred towards higher photon orders. Rabi oscillations of the multilevel system are also observable, strikingly in the external parameter evolution of the ZLP population. In addition, the comparison of the fixed-field and fixed-angle cases tells us about their equivalence in the determination of the interaction parameter $|\beta|$.
As seen, the population of the ℓ^{th} sideband is given, in first approximation, by Eq. 2.15: $\mathscr{P}_\ell = J_\ell^2(2|\beta|)$. Neglecting the residual light penetrating in the mirror, we can describe the total electric field projected on the incident electron momentum direction as

$$\mathscr{E}(z) = \left(\mathscr{E}_0^{\mathrm{i},z} e^{ik_z^{\mathrm{i}} z} + \mathscr{E}_0^{\mathrm{r},z} e^{-ik_z^{\mathrm{r}} z}\right)\Theta(-z), \tag{2.18}$$

with superscripts i and r labeling incident and reflected field, respectively, and $\Theta(\cdot)$ representing the Heaviside function. The use of this field into Eq. 2.7 yields

$$\beta \approx \frac{i q_{\mathrm{e}}}{\hbar\omega}\left\{\frac{\mathscr{E}_z^{\mathrm{i}}}{\omega/v_0 - k_z^{\mathrm{i}}} + \frac{\mathscr{E}_z^{\mathrm{r}}}{\omega/v_0 + k_z^{\mathrm{r}}}\right\}. \tag{2.19}$$

This expression depends directly on the electric field amplitude and the tilting geometry, via the reflected wavevector projection k_z^{r}. For p-polarized light and $\vartheta = 0$, we have $\mathscr{E}_z^{\mathrm{i}} = \mathscr{E}_0 \sin\delta$, $\mathscr{E}_z^{\mathrm{r}} = \mathscr{E}_0 \sin(\delta - 2\alpha)$, $k_z^{\mathrm{i}} = (\omega/c)\cos\delta$, and $k_z^{\mathrm{r}} = (\omega/c)\cos(\delta - 2\alpha)$, with $\mathscr{E}_0$ the incidence amplitude. Inserting these expressions in Fig. 2.19 we get

$$\beta \approx \frac{i q_{\mathrm{e}} v_0 \mathscr{E}_0}{\hbar\omega^2}\left\{\frac{\sin\delta}{1 - (v_0/c)\cos\delta} + \frac{\sin(\delta - 2\alpha)}{1 + (v_0/c)\cos(\delta - 2\alpha)}\right\}. \tag{2.20}$$

This very simple theory assumes valid the hypothesis of Eq. 2.15, plus the mirror ideality, and still well reproduces qualitatively the inelastic scattering evolution of Fig. 2.8a-c. We reach a quantitative experiment-theory agreement once the finite pump pulse duration and the real mirror are considered, see Fig. 2.8d-f. The best agreement is obtained when the electric field value used in the theoretical calculations is 1.22 times smaller than what estimated in the experiments (see vertical scale in Fig. 2.8e). We attribute this small discrepancy to unaccounted intensity losses of the pump pulse inside the TEM, or from an underestimation of its spotsize.
If $\delta = 0°$, we see immediately from Eq. 2.20 that $\beta = 0$ for $\alpha = 0$, and $\beta = \beta_{\max} = i q_{\mathrm{e}} v_0 \mathscr{E}_0/(\hbar\omega^2)$

[10] The electron pulse duration is calculated with Eq. 1.8.

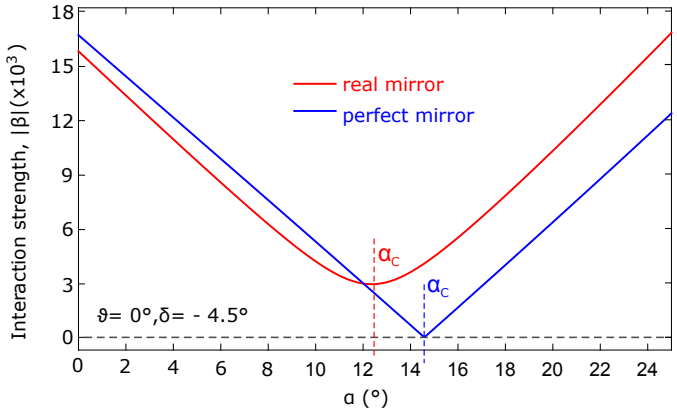

Figure 2.9 – Calculated interaction strenght $|\beta|$ for real and perfect mirrors, as a function of the angle α, for $\vartheta = 0°$, and $\delta = 4.5°$.

for $\alpha = 45°$. Since in our setup, Fig. 2.6a, light and electrons are not collinear, β vanishes only at a certain angle $\alpha \neq 0$ for p-polarized light. For an ideal mirror ($\epsilon \to -\infty \in \mathbb{R}$), $\beta = 0$ in Eq. 2.20 for

$$\alpha_C^{\text{ideal}} = \arctan\left(\frac{\sin\delta}{\cos\delta - v_0/c}\right). \tag{2.21}$$

For our real mirror, the calculated β is shown in Fig. 2.9, together with the ideal mirror curve. The minimum of $|\beta|$ is predicted to be at $\alpha = \alpha_C = 12.9°$, which is actually the experimental value for which the interaction is minimized. Fig. 2.8 and most of the other data in this section are acquired with $\alpha = \alpha_C$.
Incidentally, the ideal-real mirror comparison gives also a further proof that the electrons in our experiment are interacting with the far-field photons in proximity of the mirror, and not the near-field confined at the interface. This can be understood from the > 98% reflectivity of the mirror. The effect of the near field is so small to be experimentally hard to observe. It can be quantified by the $|\beta|$ value in the real-mirror curve in Fig. 2.9, at $\alpha = \alpha_C$, and it gives a negligible contribution for any tilt angle > 2° away from the interaction minimum.

The effect of the finite pump pulse duration on the EELS signal is shown in Fig. 2.10. For the real (panels a-c) and an ideal (panels d-f) mirror, the calculated spectra are plotted as a function of the tilting angle. The experimental conditions of Fig. 2.8a, $\Delta_{\text{ph}} \gtrsim \Delta_{\text{e}}$, correspond to those of Fig. 2.10a. We clearly see that its ideal mirror counterpart Fig. 2.10d differs almost imperceptibly. From a meticulous inspection of the calculated spectra we can appreciate slightly sharper features in the ideal mirror case; though, the differences are so tiny to be experimentally negligible. When the light pulse become much shorter than the electron, $\Delta_{\text{ph}} \ll \Delta_{\text{e}}$, as in Fig. 2.10b and e the Rabi oscillations are washed out by averaging in time over many $|\beta|$, see Sec. 2.1.1. Among the electrons that gained or lost energy, we notice a population highly peaked at low photon orders, in particular $\ell = \pm 1$. In fact, the mismatch between electron and light pulse duration makes the effective interaction time reduced, and

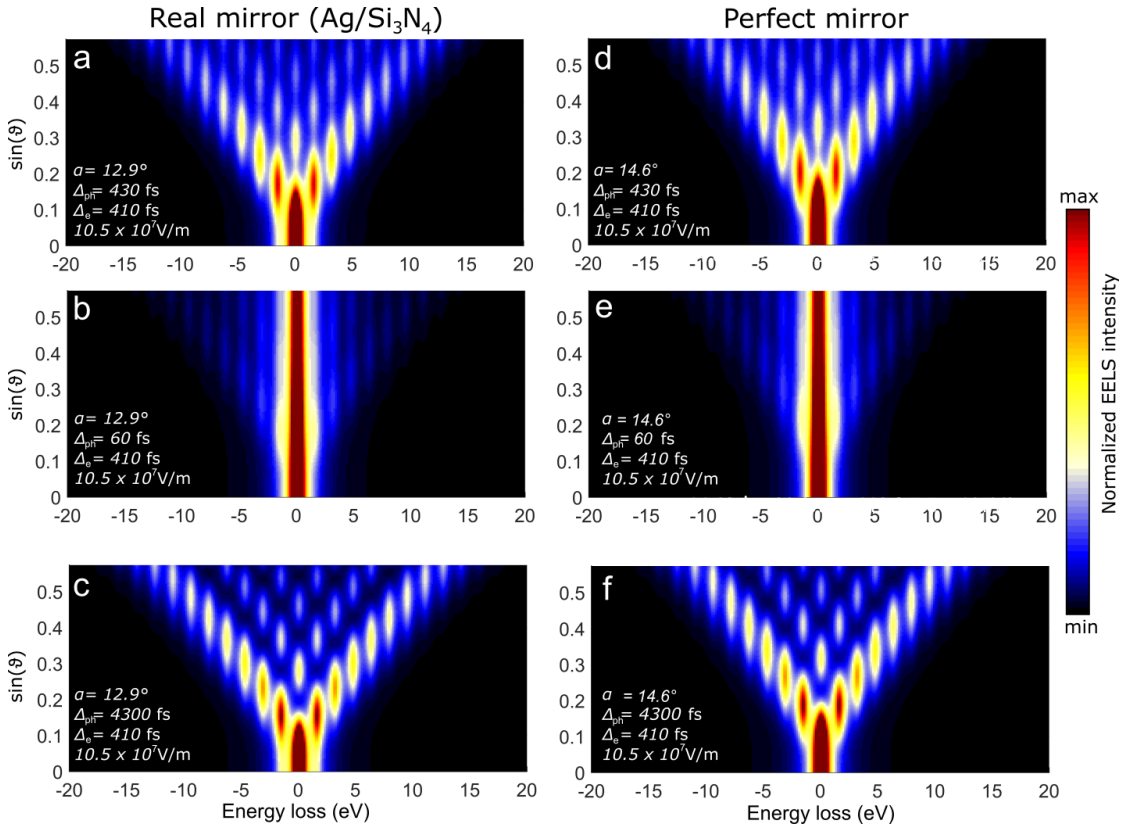

Figure 2.10 – Effects of the experimental nonidealities in theoretical description. **a**-**c**: Calculated spectra as a function of the tilting angle for the real mirror, for $\Delta_{\mathrm{ph}} = 430$, 60, and 4300 fs, respectively. **d**-**f**: Corresponding curves for an ideal mirror.

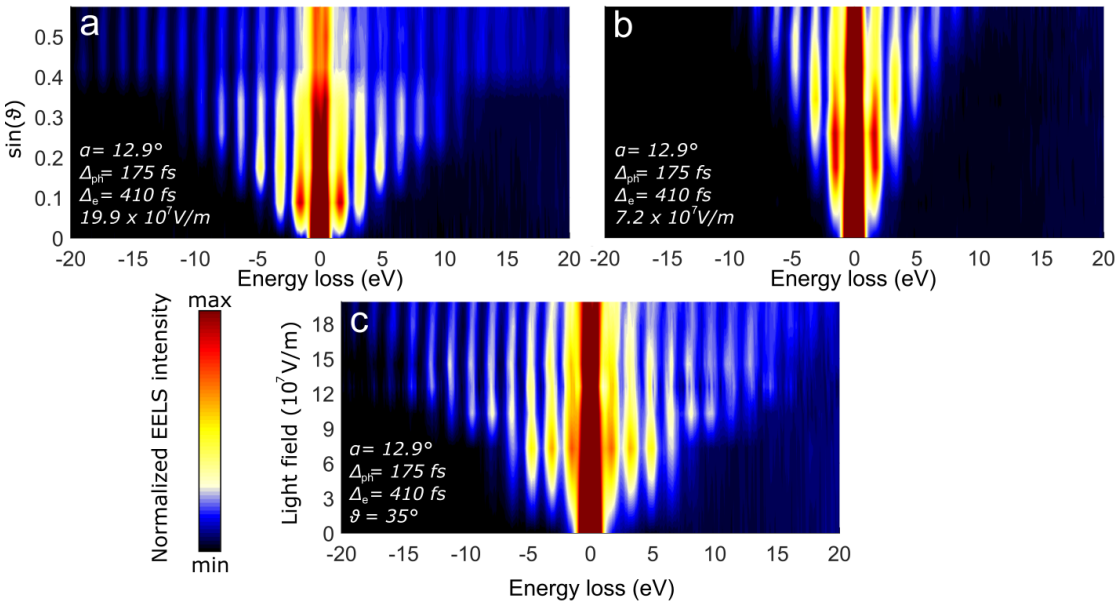

Figure 2.11 – Experimentally measured evolution of the EEL spectra for 175 fs = $\Delta_{ph} < \Delta_e \simeq$ 410 fs. **a**,**b**: Spectra for a field amplitude of $19.9 \cdot 10^7$ and $7.2 \cdot 10^7$ V/m, respectively, as a function of the tilting angle. **c**: EEL spectra as a function of the field amplitude, at fixed $\vartheta = 35°$.

multiphoton processes much less probable. Also, the portion of electrons that underwent a net energy gain or loss is severely reduced, since only a small fraction of the electron wavepacket is temporally overlapped with the light pulse, and the interaction becomes highly inefficient. Finally, in Fig. 2.10c and f the ideal $\Delta_{ph} \gg \Delta_e$ case is shown. With respect to Fig. 2.10a and d we can appreciate sharper Rabi oscillations, because of a more temporally homogeneous $\mathscr{B}$.

Experimental spectra for shorter pulses are presented in Fig. 2.11. The pulse duration has been chosen to be Δ_{ph} = 175 fs, 2.3 times shorter than the electrons. We hence confirm the considerations about the privilege of small $|\ell|$s over large $|\ell|$s, with the photon-order populations which monotonically decrease as a function of $|\ell|$ even at very high incident fields. At the same time, this condition does not allow to see Rabi oscillations. We nonetheless observe very clear quantized energy exchanges, and a high fraction of electrons interacting with the field. An intuitive measure of the electron-photon coupling is given by the fraction of electrons that have acquired or lost a net number of photons. This number, that we call 'coupling fraction', represents, in the weak-field limit, the number of electrons that have interacted with the field. At higher fields, Rabi oscillations complicate the picture, but it still remains a useful experimental parameter, especially in the cases in which the spectra are the result of important temporal or spatial averaging over different $|\beta|$s. In Fig. 2.12 we show the experimental and theoretical values of the coupling fraction as a function of the tilting angle (Fig. 2.12a and c), and field amplitude (Fig. 2.12b and d). The values are obtained by integrating the counts in the spectral regions away from the ZLP. The general behavior of the coupling fraction is to have a parabolic-like shape around 0, then a steep increase, followed by a second, slow increase,

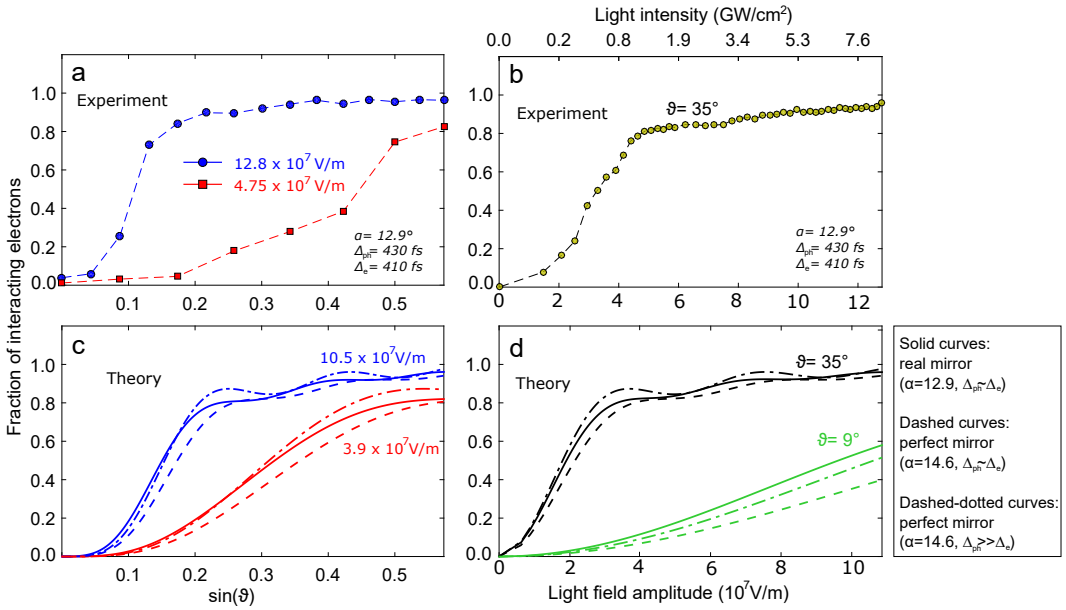

Figure 2.12 – Quantification of the net coupling fraction. **a**,**b**: Experimental fraction of electrons having exchanged a nonzero net photon number with the field, as a function of the tilting angle (a) and field amplitude (b). **c**,**d**: Same, for an ideal mirror.

which asymptotically reaches 1. The details of its evolution are controllable by the external parameters, and theory and experiments satisfactorily agree.

Further insights into the geometry of the interaction are given by a systematic study of the laser polarization effects. Until now we discussed only p-polarized light, which provides the largest interaction strength. By tuning the polarization, the strength parameter $|\beta|$ can be precisely controlled from ≈ 0 to maximum. This method has the advantage that does not require to move the specimen position. In Fig. 2.13 we report the experimentally-measured coupling fractions as a function of the polarization angle ϕ and tilting angle ϑ, for two different values of α. Since we are here in the $\Delta_{\mathrm{ph}} < \Delta_{\mathrm{e}}$ case, the coupling fraction remains far away from saturation (< 0.5 even for a field higher than in Fig. 2.12a), and represents a good parameter for evaluating the interaction strength. When $\alpha = \alpha_{\mathrm{C}}$, Fig. 2.13a, the map shows a nodal line for s-polarized light ($\phi = 0$, electric field along the $\hat{y}$ direction in Fig. 2.6), meaning that for s polarization the effects of the incident and reflected field efficiently cancel out. At $\vartheta = 0$ the interaction is minimized for all polarizations, while for $\vartheta \neq 0$ the coupling fraction is maximum for $\phi = 90°$, i.e. p-polarized light. A more complex behavior is present when $\alpha \neq \alpha_{\mathrm{C}}$. In Fig. 2.13b we plot the experimental data for $\alpha = 0°$. The nodal and maximum polarization lines here move linearly as a function of $\sin\vartheta$. All the effects described here are well reproduced in the theory by Eq. 2.19 and Eq. 2.20 (not shown here).

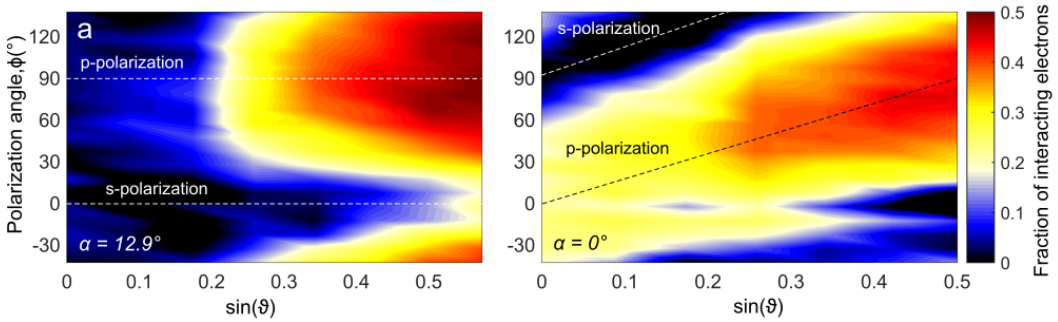

Figure 2.13 – Polarization dependence. **a**: Experimental coupling fraction as a function of the tilting angle ϑ (abscissa), and polarizationa angle φ (ordinate), for $\Delta_{\rm ph} = 175$ fs, $\mathscr{E}_0 = 19.9$ V/m, and $\alpha = \alpha_{\rm C}$. **b**: Same, for $\alpha = 0°$. Dashed lines are guides to the eye.

The requirements for the inverse transition radiation to take place are rather loose[11], only a partially reflecting or refracting surface being needed to break the translational invariance of the light field. In Fig. 2.14 we report the ϑ-dependence for a Si_3N_4 surface covered by monolayer graphene,[12] at fixed light intensity. As for the Ag mirror, we assist at the spectral redistribution towards higher photon orders for increasing ϑ. Despite in this experiment the incident light intensity $\mathscr{E}_0$ is comparable to what used with the Ag mirror, only low-order sidebands gets populated, corresponding to a low $|\beta|$ value. The reason is that the good infrared transmittivity of the graphene-Si_3N_4 system makes $\mathscr{E}^{\rm r}$ in Eq. 2.31 much smaller than for Ag ($\mathscr{E}^{\rm r} \approx \mathscr{E}_0$), with a consequent poorer coupling.

Transverse momentum quantization

In the electron-photon inelastic scattering the four-momentum has to be conserved. We discussed the quantized exchange of energy and the energy conservation, which is basically the longitudinal momentum conservation: $|\boldsymbol{p}| \simeq p_z$. Along the $\hat{x}$ and $\hat{y}$ directions, the momentum should be conserved as well. In particular, along the plane parallel to the mirror the translational invariance imposes a strict momentum conservation.
The measurement of such momentum components scattered at nonzero diffraction angle presents significant experimental challenges, due to the extremely small associated deflection angles: < 10 μrad. To give a comparison, the Bragg deflection angles are around 3 orders of magnitude higher. In order to make visible the tiny exchanged momenta, the direct beam should have a very narrow distribution in momentum space, meaning that the incident beam

[11] Actually, while ignoring the previous work on inverse transition radiation carried out by other groups, we first experimentally got aware of this effect by observing some spectral modulation in graphene specimens at $\alpha = \vartheta = 0°$. We first interpreted it as standard PINEM, but soon realized that the effect was present also in very homogeneous areas, where no near field coupling is expected. Imaging confirmed the complete homogeneity of the contrast on the film surface, hence 'uselessness' for direct imaging. Only after imaging some time after the unexpected snapshots of propagating plasmon waves we could not ignore further this effect, and we started to fervently discuss the origin of such baffling, omnipresent PINEM-like effect.

[12] The effect of the graphene is minimal: it just slightly changes the reflection, absorption, and transmission coefficients. Apart a small correction in the field intensity, the results would have been the same for bare Si_3N_4.

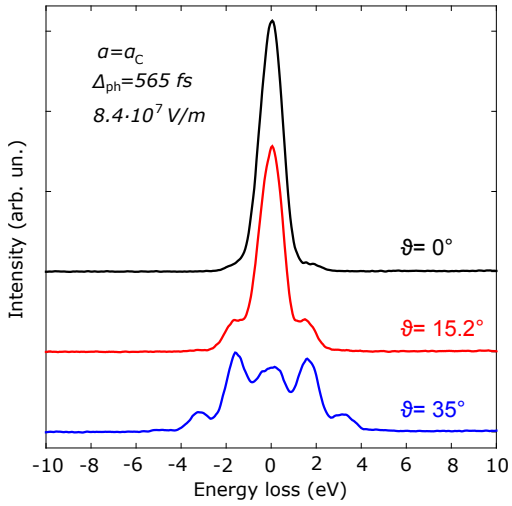

Figure 2.14 – Inverse transition radiation in a graphene-on-Si_3N_4 film. The three spectra (offset for clarity) are obtained at the three ϑ angles indicated, with a long, constant excitation pulse, at $\alpha = \alpha_C$.

should be highly parallel. In other words, the beam should possess a high transverse coherence ξ_e. In addition, the camera length, i.e. the effective distance between specimen and detector in diffraction mode, should be long enough to spatially separate the small-angle diffracted components. The transverse coherence of the electron wave packets can be increased at the expense of the number of counts per unit of time at the detector. Extremely high camera lengths are reachable is high dispersion diffraction (HDD) mode, also called 'small-angle electron diffraction'.
The cartoons in Fig. 2.15 represent conceptually the challenges of HDD with ultrafast electrons. In Fig. 2.15a an electron pulse with partial transverse coherence ξ_e interacts with the light in proximity of the mirror. In (standard) diffraction the momentum spread of the beam, Δk_e, is much larger than $q_{T,x}$, the transverse momentum exchanged in the scattering process. The pattern is composed by the direct spot (0,0) and the satellite spots at distance $\ell q_{T,x}$ from (0,0), whose centers are indicated by black dots. Since $q_{T,x}$ is very small at this camera length (~sub-pixel), and $\Delta k_e \gg q_{T,x}$, it is impossible to see any effect. In HDD the centers of the satellite peaks are well separated from the direct beam, but the large Δk_e still prevents to resolve them. In Fig. 2.15b, an electron pulse with high transverse coherence ξ_e is employed, in the same configurations of panel a. Its associated Δk_e is much smaller; yet, in diffraction the satellite peaks cannot be resolved, and only in HDD they are.

By carefully tuning the parameters just described, with camera length = 80 m, we measured the quantized momentum exchange. For a pump-probe delay time $\Delta_1 \ll 0$, i.e. in absence of any electron-light interaction, the direct beam in the $< k_x k_y >$ diffraction plane is shown in Fig. 2.16a, together with a line profile along k_x. In Fig. 2.16b the direct beam is shown at time-zero ($\Delta_1 = 0$) for $\alpha = \alpha_C$ and $\vartheta = 0°$; the momentum distribution is still the same,

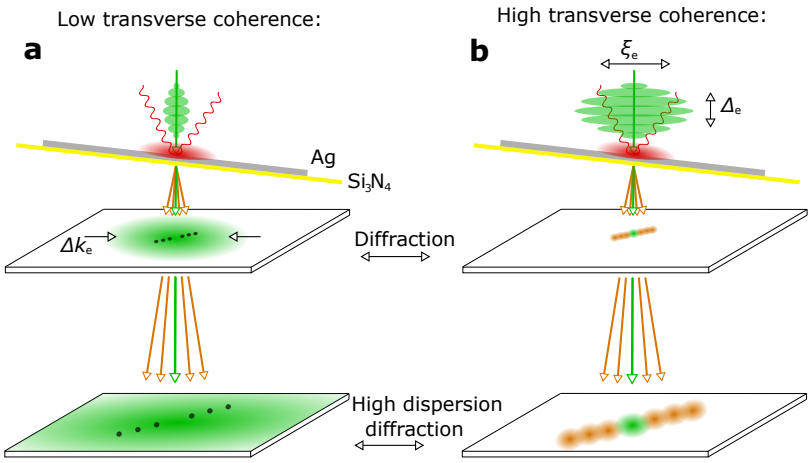

Figure 2.15 – Concept of HDD measurement for transverse momentum exchange in inverse transition radiation experiments. **a**: Sketch of diffraction and HDD for electron pulses with limited transverse coherence $\xi_e \ll 2\pi/q_{T,x}$, where $q_{T,x}$ is the exchanged transverse momentum. **b**: Same, for pulses with high transverse coherence, $\xi_e \approx 2\pi/q_{T,x}$. Drawings not in scale for clarity.

in agreement with the results of Sec. 2.2.3. Only when the mirror is tilted the interaction is efficient. When $\vartheta = 35°$, the direct beam streaks along the $\hat{k}_x$ direction (Fig. 2.16c). The amount of streaking can be controlled by rotating the laser polarization angle ϕ, as can be appreciated in Fig. 2.16d, where the streaking is minimum at $\phi = 0°$ (polarization s) and maximum at $\phi = \pm 90°$ (polarization p).

The exchanged transverse momentum peaks are not individually resolved, because the direct beam has still a larger momentum spread than $q_{T,x}$. Nonetheless, the streaking we observe has to be ascribed to the quantized momentum exchange, and not to a purely classical deflection due to the Lorentz force. The effect of the Lorentz force of the light is indeed negligible at optical frequencies [251–253].

We can prove it by visualizing simultaneously the energy and transverse momentum exchanges (Fig. 2.16e-g). The TEM and spectrometer were aligned to have the direction $\hat{k}_x$ along the vertical CCD axis, while the horizontal is the spectroscopic axis. Before time-zero, Fig. 2.8e, the electrons occupy a state with a narrow energy and k_e^x momentum distribution, centered around 200 keV and 0, respectively. At time-zero, in the same conditions of Fig. 2.8c, the MREELS map shows a streaking of the free electrons with a constant, nonzero energy-momentum dispersion. Indeed, electrons in the $\pm\ell^{\text{th}}$ photon order must have simultaneously gained or lost an energy $\ell\hbar\omega$ and a transverse momentum $\ell q_{T,x}$. The slope of the dispersion is therefore $q_{T,x}/\hbar\omega$. The derivation of $q_{T,x}$ is reported in the paragraph below. Its expression, for the geometry employed here, is $q_{T,x} \approx (k_{ph}/2)\sin 2\vartheta \cos^2\alpha_C = 3.55\ \mu\text{m}^{-1}$, where $k_{ph} = \omega/c$ is the light free-space (angular) wavenumber. The theoretical dispersion $q_{T,x}/\hbar\omega$ (dashed white line in Fig. 2.16f and g) well reproduces the experimental dispersion, confirming an excellent agreement between the developed analytical theory and the experiments.

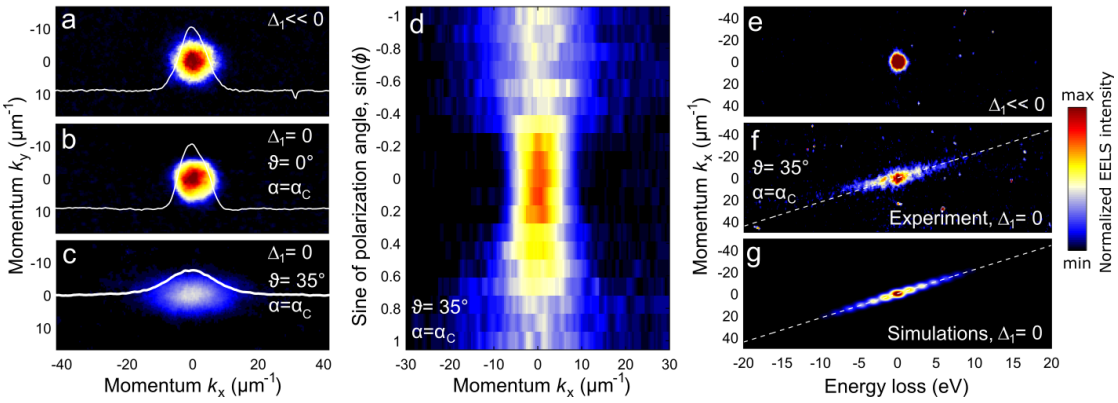

Figure 2.16 – Transverse momentum exchange. **a**: Direct beam in the HDD diffraction plane, before time-zero. **b**: Same, at time-zero, with $\vartheta = 0°$, $\alpha = \alpha_C$, $\Delta_{ph} = 560$ fs, $\mathscr{E}_0 = 11.1 \cdot 10^7$ V/m. **c**: Same as b, with $\vartheta = 35°$. **d**: Polarization dependence of the momentum component along $\hat{k}_x$. **e**: Direct beam in the energy-k_x plane, in the same conditions of c, but before time-zero. **f**: Same as e, at time-zero. **g**: Energy-momentum theoretical map relative to panel f.

The investigation of the electron-photon interaction in the transverse momentum space has been revealed technically challenging, but its successful implementation allows now to think about innovative experiments that could exploit this new method. Our exchanged transverse momentum was very small, making it difficult to single out the individual peaks. Higher exchanged momenta can be easily obtained for example at higher photon energies and at grazing incidence. In general, for larger exchanged momenta, it would be much easier to distinguish the single peaks, and one could disentangle the energy axis from the momentum axis. In that way, the energy resolution limitations in EELS could be bypassed: even a small spectroscopic feature that in conventional EELS would be hidden in the tails of the ZLP, it might be measurable with this method, as long as its associated momentum transfer is large enough.

Determination of the transferred transverse momentum

In diffraction mode, the detector measures the electron momentum components along $\hat{x}$ and $\hat{y}$. We hence aim at finding the expression for the transferred momentum as a function of the tilting geometry and light incidence angle. Let (x, y, z) be the spatial coordinates in the laboratory (unrotated) frame, see Fig. 2.6a, (x', y', z') the coordinates in the frame after having rotated by ϑ, and (x'', y'', z'') after a further rotation by α. ϑ rotates around $\hat{y}$, while α rotates around $\hat{x}'$. We have therefore:

$$\begin{bmatrix} x' \\ y' \\ z' \end{bmatrix} = \begin{bmatrix} \cos\vartheta & 0 & \sin\vartheta \\ 0 & 1 & 0 \\ -\sin\vartheta & 0 & \cos\vartheta \end{bmatrix} \begin{bmatrix} x \\ y \\ z \end{bmatrix}, \tag{2.22}$$

and

$$\begin{bmatrix} x'' \\ y'' \\ z'' \end{bmatrix} = \begin{bmatrix} 1 & 0 & 0 \\ 0 & \cos\alpha & -\sin\alpha \\ 0 & \sin\alpha & \cos\alpha \end{bmatrix} \begin{bmatrix} x' \\ y' \\ z' \end{bmatrix}. \tag{2.23}$$

By matrix multiplication of Eq. 2.22 and Eq. 2.23, we find

$$\begin{bmatrix} x'' \\ y'' \\ z'' \end{bmatrix} = \begin{bmatrix} \cos\vartheta & 0 & \sin\vartheta \\ \sin\alpha\sin\vartheta & \cos\alpha & -\sin\alpha\cos\vartheta \\ -\cos\alpha\sin\vartheta & \sin\alpha & \cos\alpha\cos\vartheta \end{bmatrix} \begin{bmatrix} x \\ y \\ z \end{bmatrix}. \tag{2.24}$$

We can invert the transformation matrix to find the laboratory frame coordinates (x, y, z) as a function of the rotated cordinates (x'', y'', z''). The inversion yields

$$\begin{bmatrix} x \\ y \\ z \end{bmatrix} = \begin{bmatrix} \cos\vartheta & \sin\alpha\sin\vartheta & -\cos\alpha\sin\vartheta \\ 0 & \cos\alpha & \sin\alpha \\ \sin\vartheta & -\sin\alpha\cos\vartheta & \cos\alpha\cos\vartheta \end{bmatrix} \begin{bmatrix} x'' \\ y'' \\ z'' \end{bmatrix}. \tag{2.25}$$

The incident light wavevector has laboratory-frame components $(x, y, z)^{\mathrm{i}}_{\mathrm{ph}}$, which in the rotated frame are (using Eq. 2.24)

$$(x'', y'', z'')^{\mathrm{i}}_{\mathrm{ph}} = (\cos\delta\sin\vartheta, \sin\delta\cos\alpha - \cos\delta\sin\alpha\cos\vartheta, \sin\delta\sin\alpha + \cos\delta\cos\alpha\cos\vartheta). \tag{2.26}$$

The momentum components parallel to the mirror need to be strictly conserved in the electron-photon interaction, and therefore they are transferred to the free electron. In the rotated-frame coordinates they are expressed by the vector

$$(x'', y'', z'')^{\parallel}_{\mathrm{ph}} = (\cos\delta\sin\vartheta, \sin\delta\cos\alpha - \cos\delta\cos\vartheta\sin\alpha, 0), \tag{2.27}$$

which in the laboratory frame can be expressed via Eq. 2.25, resulting in

$$\begin{bmatrix} x \\ y \\ z \end{bmatrix}^{\parallel}_{\mathrm{ph}} = \begin{bmatrix} \sin\vartheta\cos\alpha(\cos\delta\cos\alpha\cos\vartheta + \sin\delta\sin\alpha) \\ \sin\delta\cos^2\alpha - \cos\delta\sin\alpha\cos\alpha\cos\vartheta \\ \cos\delta(\sin^2\alpha\cos^2\vartheta + \sin^2\vartheta) - \sin\delta\sin\alpha\cos\alpha\cos\vartheta \end{bmatrix}. \tag{2.28}$$

The general form for the momentum transfer is therefore $\boldsymbol{q}_{\mathrm{T}} = k_{\mathrm{ph}}(x, y, z)^{\parallel}_{\mathrm{ph}}$, with $k_{\mathrm{ph}} = \omega/c$. The data reported in Fig. 2.16 are all relative to the condition $\delta = 4.5°$ and $\alpha = \alpha_{\mathrm{C}} = 12.9°$. For these conditions, some terms can be neglected, ending with

$$\boldsymbol{q}_{\mathrm{T}} \approx k_{\mathrm{ph}} \begin{bmatrix} \sin\vartheta\cos\vartheta\cos^2\alpha_{\mathrm{C}} \\ -\cos\vartheta\sin\alpha_{\mathrm{C}}\cos\alpha_{\mathrm{C}} \\ \sin^2\vartheta \end{bmatrix}. \tag{2.29}$$

The component along $\hat{y}$ is approximately 3 times smaller than the component along $\hat{x}$, for $\vartheta = 35°$, and can be neglected in first approximation. The contribution along $\hat{z}$ cannot be measured in our experiment, and it is anyhow smaller than the x component. Moreover, in Fig. 2.16f and g only the k_x component can be measured, therefore considering only $q_{\mathrm{T},x}$ is exact.

2.2.4 Double-pulse experiments

The results presented in Sec. 2.2.3 provide a full energy-momentum characterization of the inverse transition radiation. We saw how long and short pulses influence energy and momentum exchanges, i.e. the Rabi phase in the multilevel quantum ladder of Fig. 2.3b. We present here a method to coherently control such Rabi phase by the interaction with a properly synthesized field distribution formed by two same-color, mutually phase-locked light pulses, with relative delay $\Delta_2 - \Delta_1$, as shown in Fig. 2.6c. In practice this is a three-pulse experiment (electron probe +2 pump pulses) [254, 255], but it can be equivalently thought as a single-excitation experiment with a doubly-peaked excitation pulse.
A Michelson interferometer along the 1.57 eV-beam path creates two 55 fs FWHM-long pulses. Their mutual delay can be changed with a resolution of 330 as by a direct current (DC) motorized stage. This minimum delay step correspond to a phase of $\sim \pi/6$ for the 1.57 eV optical wave.

Attosecond coherent control of the free-electron wave function

The coherent control on the parameter $\mathscr{B}$ can be appreciated in Fig. 2.17. EEL spectra have been acquired as a function of $\Delta_2 - \Delta_1$ (Fig. 2.17a), and a spectral modulation is observed with period ≈ 2.63 fs, which corresponds to the optical cycle $2\pi/\omega$. In this experiment, the first of the two pulses has been kept synchronous with the 350 fs FWHM-long electron pulse. The second pulse has been initially moved to $\Delta_2^0 = 100 \pm 5$ fs, in order to make negligible the direct optical interference between the two pulses, while remaining roughly within the electron longitudinal coherence time. From that initial value, we delayed it further with 500 as steps, and recorded the spectral evolution as a function of $\Delta_{12} = \Delta_2 - \Delta_1 - \Delta_2^0$. Altough Δ_2^0 is not known with sub-cycle precision, leading to an absolute phase uncertainty, the delay Δ_{12} is known with as accuracy. We worked at $\alpha = \alpha_{\mathrm{C}}$, $\vartheta = 35°$, with an electric field amplitude $\mathscr{E}_0 = 21.4 \cdot 10^7$ V/m for each pulse.
Two representative spectra are reported in Fig. 2.17b for delays corresponding to the dashed white lines in Fig. 2.17a, which differs by a phase $\approx \pi$. A large variation in the sideband population is observed, especially at high photon order. In Fig. 2.17c we plot the intensity of the $\ell = +9$ and $\ell = +14$ sidebands as a function of Δ_{12}. They show sinusoidal oscillations, with a relative phase shift of $\approx \pi$.
It is important to stress that the coherent modulation of the population in the different photon orders is the result of directly modulating the Rabi phase in the multilevel system, which redis-

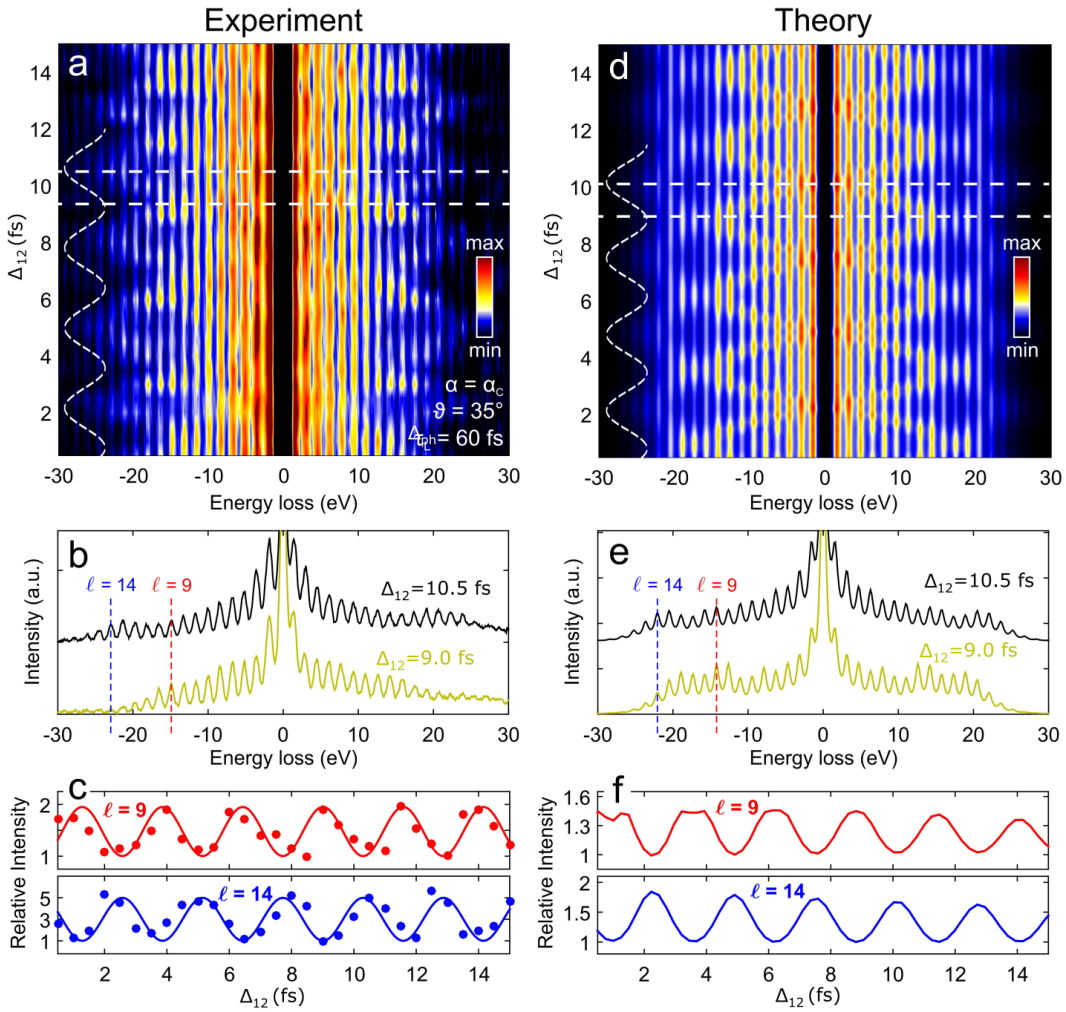

Figure 2.17 – **a**: Measured EELS as a function of $\Delta_{12} = \Delta_2 - \Delta_1 - \Delta_2^0$, with $\Delta_2^0 \approx 100$ fs. **b**: Two EEL spectra taken with the two pulses shifted by a phase $\approx \pi$, corresponding to the white lines in panel a. Offset for clarity. **c**: Temporal evolution of the 9^{th} and 14^{th} gain sideband intensity, with corresponding sinusoidal fits. **d**-**f**: Corresponding calculated spectra and spectral dependence.

tributes the spectral weight of each component. It is not a mere optical interference effect, but rather a quantum interference in the multilevel system, which coherently modulates the value of $\mathscr{B}$. We carried out several control experiments to evaluate other possible spurious effects, which we present after the following paragraph on the theoretical description of the two-pulse experiments. The theory quantitatively reproduces the experimental data.

The theoretical description presented in Sec. 2.1.1 accounted for a single Gaussian pulse, and was used for the calculations in Sec. 2.2.3. We can easily extend that formulation to account for the presence of any field configuration. In particular, for a configuration made of two same-color Gaussian pulses, Eq. 2.16 becomes

$$\mathscr{P}_\ell = \frac{1}{\sqrt{2\pi}\sigma_\mathrm{e}} \int_{-\infty}^{+\infty} e^{-t^2/2\sigma_\mathrm{e}^2} J_\ell^2 \left(2 \left| \beta \sum_{i=1}^{2} A_i e^{-i\omega\Delta_i} e^{-(t+\Delta_i)^2/4\sigma_\mathrm{ph}^2} \right| \right) \mathrm{d}t, \tag{2.30}$$

where A_i, $i = 1,2$, are the relative weights of the two amplitudes ($|A_1| + |A_2| = 1$, in our case $A_1 = A_2 = 0.5$). Eq. 2.30 gives an idea of the phenomenon: the spatial dependence of the two pulses, which is the same, enters only in β, via Eq. 2.7, while the temporal dependence enters in the coherent sum of the field amplitudes (sum over i). If $\Delta_2 - \Delta_1 \lesssim \Delta_\mathrm{ph} = 2.355\sigma_\mathrm{ph}$, and $\sigma_\mathrm{e} \gg \sigma_\mathrm{ph}$, the obvious constructive and destructive optical interference is obtained by the sum of the $\exp\{-i\omega\Delta_i\}$ terms: $\mathscr{B}$, the argument of the absolute value, is modulated by $\cos[\omega(\Delta_2 - \Delta_1) + \varphi]$, φ a phase. We confirmed that by experimental measurements (not reported here).

According to Eq. 2.30, when $\Delta_2 - \Delta_1$ is large enough for the optical interference to be negligible, the electron still interacts with both fields, and the value of $\mathscr{B}$ is modulated accordingly. In a way, we could say that an 'interference' between the two light pulses is mediated by the probing electron, which has memory of the Rabi phase acquired during the first interaction, and sums it to the phase of the second interaction. More properly, the probability amplitude for the electron to acquire a certain phase is obtained by the coherent sum over the whole field configuration.

To find the theoretical $\mathscr{P}_\ell$ values, for a theory-experiment comparison, it is useful to express Eq. 2.30 in a easily computable form, similarly to what done in Eq. 2.17 for a single pulse. Once we expand the Bessel function with Taylor, we use the Newton binomial expansion to explicit the sum over $i = 1,2$, and we calculate the integrals over time, we end up with

$$\begin{aligned} \mathscr{P}_\ell = \sum_{j=0}^{\infty} \sum_{j'=0}^{\infty} \sum_{s=0}^{n} \sum_{s'=0}^{n} C_{\ell j} C_{\ell j'} \binom{n}{s} \binom{n}{s'} A_1^{2n-s-s'} A_2^{s+s'} \cos[(s-s')\omega(\Delta_2 - \Delta_1)] \cdot \\ \cdot \frac{1}{\sqrt{\lambda}} e^{-n\{[(2n-s-s')\Delta_1 + (s+s')\Delta_2]/2n\}^2/2\lambda\sigma_\mathrm{ph}^2} e^{-[1-(s-s')/2n](s-s')\Delta_{21}^2/4\sigma_\mathrm{ph}^2}. \end{aligned} \tag{2.31}$$

In Fig. 2.17d-f we report the results of the analytical model, with the same parameters used in the experiments Fig. 2.17a-c. We note again a good agreement, both in the overall dynamics over time and in the individual spectra and photon order evolutions. Since we did not include

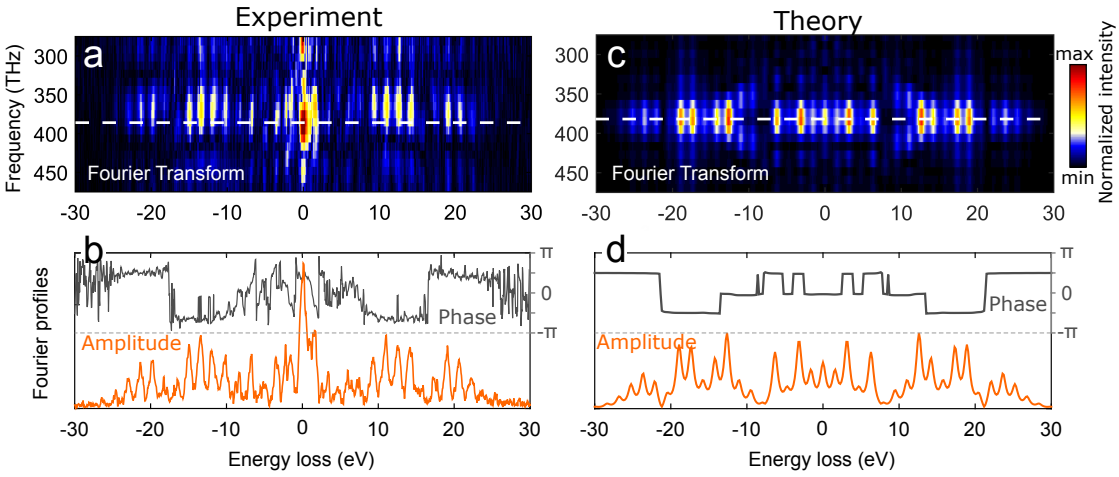

Figure 2.18 – **a**: Amplitude of the temporal Fourier transform of the experimental time-energy map. **b**: Selected phase and amplitude of the experimental Fourier transform at 380 THz. **c**,**d**: Theoretical calculations for same conditions as panels a,b.

in the model the EEL contribution from the material, the computed spectra (see Fig. 2.17e) do not show the broad valence plasmon peak of Ag and Si_3N_4 at $17-25$ eV. The calculations have been adjusted to match the temporal phase of the experiments, to account for the experimental uncertainty on the absolute value of Δ_2^0. In Fig. 2.17f we also see that the oscillations are softly dumped, reflecting the fact that Δ_2 is slowly drifting away from the center of the electron wave packet.

The temporal Fourier transforms of the experimental and theoretical maps in Fig. 2.17a and d are shown in Fig. 2.18a and c, respectively. We notice strong peaks at the optical frequency $1/(2.63\text{ fs}) = 380$ THz and a satisfactory agreement between theory and experiments. The details of the amplitude and phase of the Fourier transform are shown in Fig. 2.18b and d, extracted at the driving frequency 380 THz. Both experimental and theoretical phase plots have a sudden π jump around ∓ 20 eV, corresponding roughly to the $\ell = \pm 12$ orders. The oscillating $\ell = 9$ and $\ell = 14$ photon orders of Fig. 2.17c and f are here confirmed to be in antiphase, being one before an the other after the π phase jump.

The coherent modulation of the free-electron wave function by means of our double-pulse semi-infinite field configuration is schematically summarized by the cartoon of Fig. 2.19. It represents, for different $\Delta_2 - \Delta_1$ values, the probability density ρ of the electron to be in a state with energy-momentum (E, q_x). In the leftmost snapshot, the absence of interaction implies $\mathscr{B} = 0$, and the electron remains at $E = 0$, $q_x = 0$; in the three following snapshots, ρ is represented for the two light pulses delayed by half of the optical period (π phase). For each snapshot, the probability of the energy-momentum states are determined by the Rabi phase of the electron in the multilevel system, which emerges from the complex multi-photon ab-

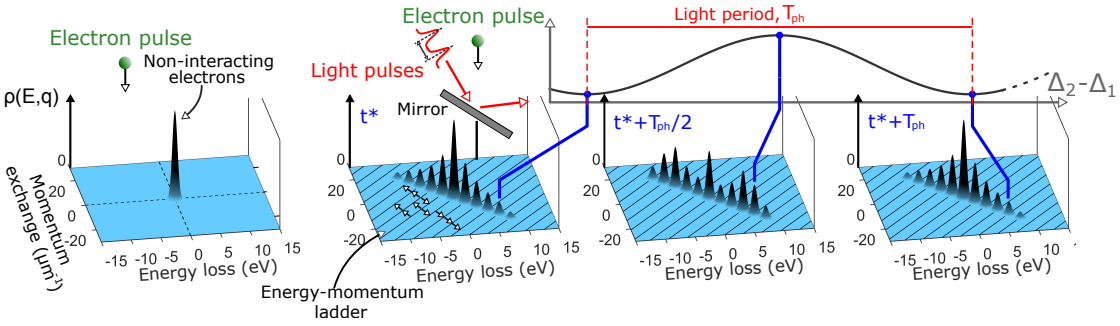

Figure 2.19 – Conceptual scheme of the coherent control on the free-electron wave function. $\rho(E,q)$ is the probability density. From left to right: zero-interaction ρ, and ρ after the interaction with the two-pulse configuration at delays $\Delta_{21}=0$, $\Delta_{21}=1.32$ fs, and $\Delta_{21}=2.63$ fs, corresponding to 0, π, and 2π phase, respectively.

sorption and emission in the quantum ladder. The change of temporal phase between the two pulses induces a strong reorganization of the population density in the energy-momentum states, modulated in time at the optical driving frequency.

Quantum or classical interference?

The experimental data and analytical model well describe the physical behavior of the system in our experiment, proving the role of the probability amplitudes' interference in the quantum ladder system even when the optical pulses do not interfere directly. Since it may appear at first sight a surprising result, we report in the following paragraphs further evidence to support the unimportance of the residual optical interference[13] and of the separate (incoherent) electron interaction with the two pulses. As a logical conclusion, these results suggest a long longitudinal coherence for the free-electron wave functions.

In the experiments, the two pulses have been separated by 100 fs and more, as measured by the intensity autocorrelator, with ±5 fs uncertainty. We also measured the amplitude autocorrelation with the Michelson interferometer, see Fig. 2.21d. In Fig. 2.20a-b we simulated the intensity of the incident field in our configuration. The two phase-locked pulses are described by Gaussians with 55 fs FWHM, and –as we see in Fig. 2.20b and c– the optical interference is appreciable only in the middle of the two pulses; the pulse energy (integrated intensity) varies within ±7% from phase to antiphase. With Fig. 2.21 we demonstrate that if we consider an incoherent interaction between the electron wave function and the two pulses, the modulation of the sidebands would be determined only by the ±7% optical interference, which would result in a tiny effect, compared to what we observe in Fig. 2.17.
The two intensity envelopes of the maximum constructive and destructive optical interfer-

[13] Here we refer to the local interference that modifies the electric field amplitude. We discuss explicitly the spectral interference in Sec. 4.2.3.

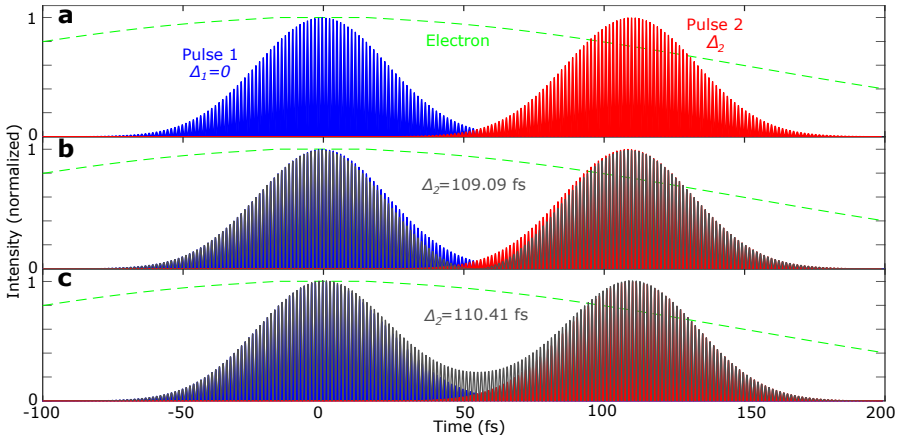

Figure 2.20 – Calculated laser intensity for the two light pulses (blue and red). **a**: Two pulses plotted, without summation. **b**: The two pulses are summed (dark grey profile), with delay 109.09 fs (pulses in antiphase). **c**: Same, with delay 110.41 fs (pulses in phase). The green dashed line is the electron pulse envelope. The parameters of the pulses are taken from the experiments.

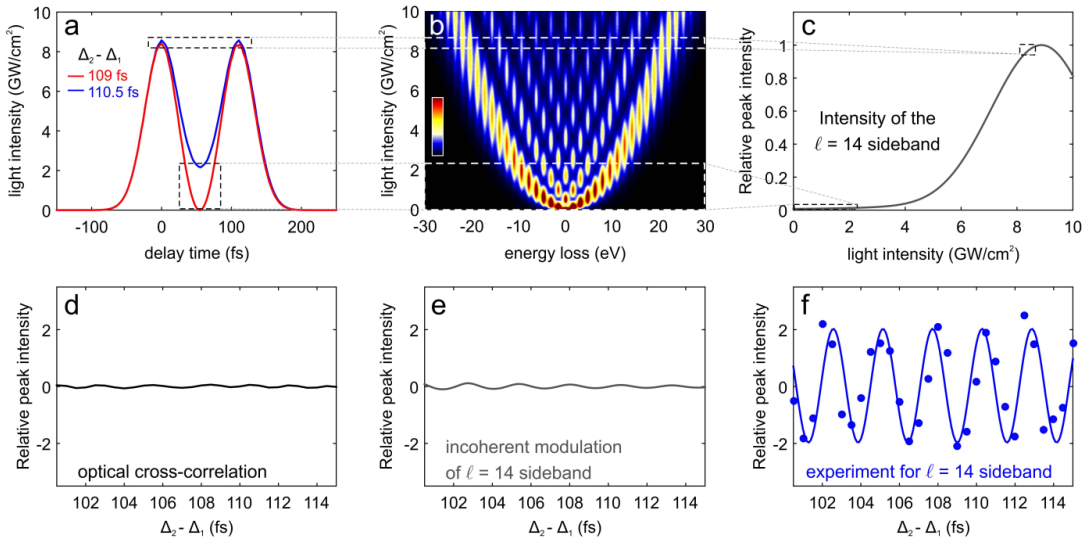

Figure 2.21 – Why the two-pulse coherent modulation is not an optical interference effect. **a**: Intensity profiles, from Fig. 2.20b and c. **b**: Spectral distributions for increasing light intensity. **c**: Normalized $\mathscr{P}_{\ell=14}$ as a function of the light intensity. **d**: Measured amplitude autocorrelation of the two optical pulses. **e**: Calculated modulation of the 14$^{\text{th}}$ sideband for incoherent light-electron interaction. **f**: Measured modulation of the 14$^{\text{th}}$ sideband, as in Fig. 2.17c.

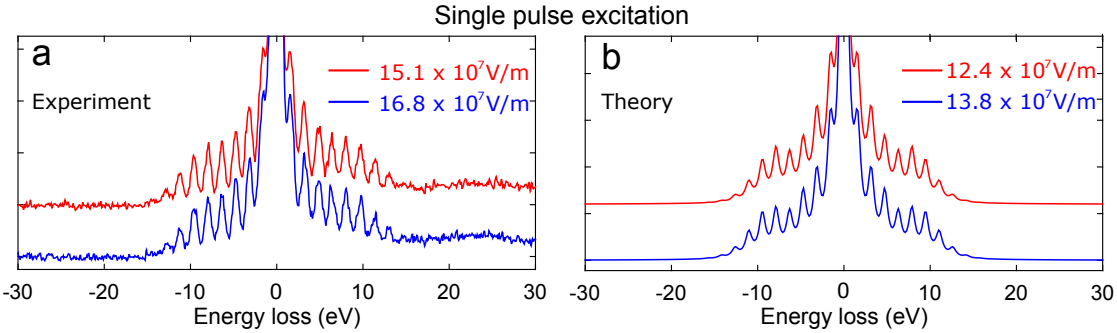

Figure 2.22 – EELS dependence on the intensity of the single-pulse short excitation. **a**: Measured EEL spectra at two field amplitudes with ≈ 11% difference (⇒ 23% intensity difference. **b**: Relative calculated spectra. $\alpha = \alpha_C$, $\vartheta = 35°$, $\Delta_{ph} = 60$ fs.

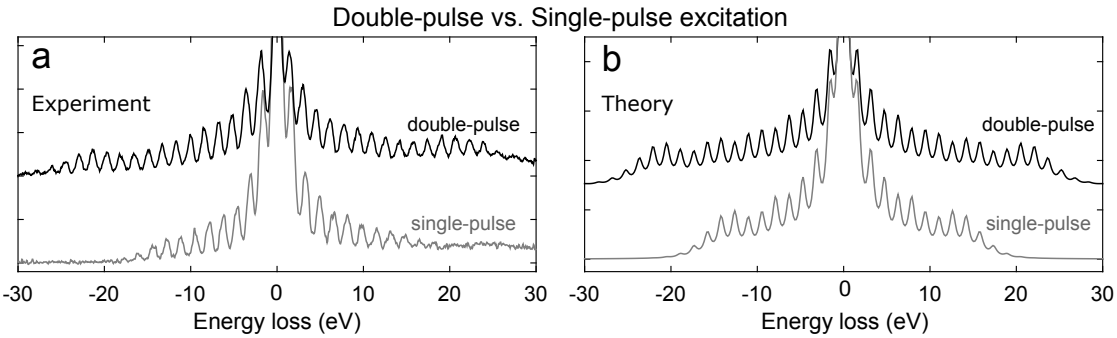

Figure 2.23 – Single- vs. double-pulse excitation. **a**: EEL measured spectra for single (light gray) and double (dark gray) excitations. **b**: Relative calculated spectra. $\alpha = \alpha_C$, $\vartheta = 35°$, $\Delta_{ph} = 60$ fs for both pulses.

ence configurations as plotted in Fig. 2.21a, roughly corresponding to the delays $\Delta_{12} = 109$ and 110.5 fs of Fig. 2.17b. The theoretical population of the sidebands as a function of the instantaneous light intensity is presented in Fig. 2.21b. The high photon orders are reachable only by the highest intensities, at the very top of the pulses, which are little modulated by the optical interference. The intensities that are significantly modulated by the optical interference are those below $|\ell| \simeq 8$. The population of the 14^{th} sideband (normalized to its maximum occupancy) is plotted in Fig. 2.21c, as a function of the light intensity. No appreciable change in the population of the $|\ell| = 14$ orders is therefore possible by changing the amount of light with intensity $\lesssim 2-3$ GW/cm^2. The small intensity difference at the peaks due to optical interference can instead give a contribution, which is however rather small. From Fig. 2.21a and Fig. 2.20 we get a modulation on the peak intensities of 1.6%, while the measured optical amplitude autocorrelation gives a value of ~ 5%, Fig. 2.21d. In panel e we quantify the modulation of the 14^{th} sideband given by optical interference contribution (incoherent modulation). It is about 7% at 109 – 110.5 fs. This value has to be compared with the ~ 250% modulation observed experimentally, Fig. 2.21f.

As a last control experiment, we performed a series of EELS measurements for a single light pulse as a function of its intensity (Fig. 2.22), in the same intensity range of the two-pulse

experiment. For a 11% variation in the field amplitude, we note a barely visible spectral change, as expected for short pulses, see Fig. 2.10b. For such short light pulses, a significant population of the high-order sidebands ($|\ell| \gtrsim 11-12$) is possible only at much higher fields. In Fig. 2.23 the EEL spectra for single-pulse and double-pulse are reported, showing the empty $|\ell| > 12$ photon orders for the single-pulse excitation, and populated orders up to $|\ell| = 18$ for the double-pulse optical configuration.
We can hence conclude that the observed modulations, Fig. 2.17, cannot be interpreted as a result of an intensity change of the semi-infinite electromagnetic field due to optical interference. They have to be associated to a coherent coupling of the electron wave function with the properly synthesized field distribution.

Since the two optical pulses are separated in time, and the free-electron interacts coherently with both, it follows that the electron wave functions extend in time over a long distance, with little decoherence. As a collateral result of our studies, we conclude that the temporal (i.e. longitudinal) coherence of the single-electron wave packet is long, at least several tens of femtoseconds.
We discussed in Sec. 1.3.2 the homogeneous and inhomogeneous contributions to the ZLP, and brought arguments supporting a coherence length ξ_t^e of several tens of fs. Those arguments assumed no significant decoherence of the free-electron wave function. Here we try to experimentally estimate the electron longitudinal coherence at the specimen plane, based on the interpretation of the temporal evolution of the spectra in Fig. 2.17. The high-energy sideband population oscillates as a function of Δ_{12}. The oscillations are dumped, and we describe the dumping by a Gaussian function centered at 0, the center of the electron pulse envelope and the first light pulse, and with standard deviation σ_t. The width of this Gaussian curve represents the homogeneous broadening in time of the free-electron wave function. A Gaussian having the same width of the pulse envelope would mean a fully-coherent electron pulse, which goes against the arguments of Sec. 1.3.2, while an extremely short value would prevent the observation of such large oscillations. By fitting the data for the $\ell = 13$, 14, and 15 sidebands, we find a longitudinal electron coherence $\xi_t^e = 2\sigma_t$ in the $50-80$ fs range, with ± 10 fs uncertainty. The experimentally estimated value agrees within a factor 2 with the tentative values discussed in Sec. 1.3.2.

2.2.5 Attosecond-nanometer control of plasmonic near fields

The understanding of the inverse transition radiation effect, and its detailed characterization in our apparatus enabled us to make some progresses in imaging and controlling ultrafast electromagnetic fields at the nanoscale. Here we first briefly anticipate an imaging scheme which exploits the inverse transition radiation, that will be extensively explained and used in the Chap. 3 and Chap. 4; then we present a method to modulate plasmonic fields with the two-pulse-control scheme, without semi-infinite field contributions.

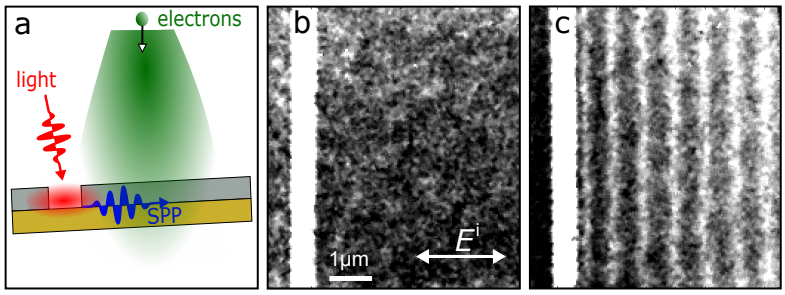

Figure 2.24 – Visualization of a propagating SPP. **a**: Sketch of the experiment. The light pulse illuminates the nanoslit and the surrounding film. **b**: PINEM micrograph for vanishing inverse transition radiation ($\alpha = \alpha_C$, $\vartheta = 0°$). **c**: PINEM micrograph for non-negligible inverse transition radiation. E^i represents the direction of the projection of the incident light electric field on the plane of the specimen.

The pure inverse transition radiation effect was obtained by having a homogeneous mirror as a specimen. In general, if any partially reflecting or refracting material is used, for example as substrate for nano-objects, the inverse transition radiation effect would coexist with the PINEM effect from the near field of the nano-object. While in some conditions the presence of the homogeneous field from inverse transition radiation may be unwanted and complicate the image interpretation, in other cases it can be exploited to visualize fields otherwise impossible to see. In this latter case, the semi-infinite (far) field acts as a spatially-homogeneous reference field, synchronously oscillating with the near field around the nano-object. They would therefore interfere, creating a stationary pattern whose spatial dependence is a function of the phase difference between the far and near field (say, 0). In Sec. 3.2 we will describe it in details. Here, I will show only an example.
Let's consider the geometry of Fig. 2.24a, with a nanoantenna (a slit) carved in the Ag of the mirror. The excitation light generates an SPP at the slit, which propagates at the Si_3N_4/Ag interface [143], at a speed of $0.3-0.6c$, hence covering approximately 30 μm in the electron pulse duration of ~ 300 fs. When the inverse transition radiation effect is negligible (see Fig. 2.24b), a PINEM experiment would only be sensitive to the slowly decaying SPP envelope that extends away from its source. If instead a non-negligible contribution from the semi-infinite field is present (Fig. 2.24c), an interference pattern is produced, corresponding to a snapshot of the SPP propagation away from the nanocavity.

The two-pulse experimental configuration has the advantage to control the (electron-mediated) interference by having temporally-separated pulses. An example is the coherent modulation of a plasmonic Fabry-Perot interference pattern. For that purpose, we created a structure as displayed in Fig. 2.25a. The two lines of couplers are designed to produce a directional SPP emission when excited by circularly-polarized light [256]. The directionality comes from constructive and destructive interference of the SPPs radiated by the individual nanoantennae that constitute the couplers (see Fig. 2.25b). These nanoantennae are oriented with their main axis forming a 45° angle with the principal axes of the couplers. The spacing in the other

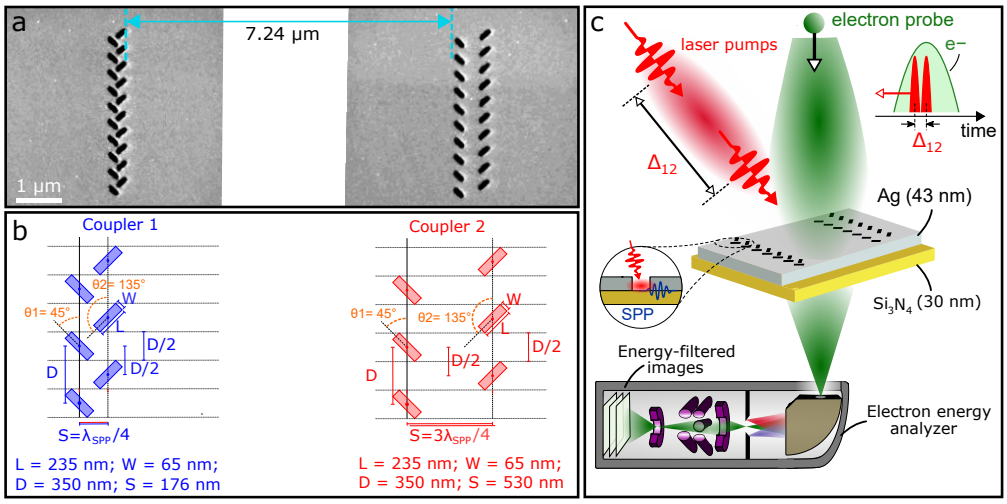

Figure 2.25 – **a**: SEM micrographs of the plasmonic sources and Fabry-Perot resonator. **b**: Design of the directional SPP sources, modeled on ref. [256]. **c**: Schematics of the experiment.

direction is $\lambda_{SPP}/4$ for the left coupler, and $3\lambda_{SPP}/4$ for the right coupler. In this way, for a fixed light handedness (spin-angular momentum), the two couplers mainly emit in opposite directions. We chose the handedness to have counterpropagating SPPs inside the Fabry-Perot cavity in between the two couplers. Away from the couplers' edges, the plasmonic field can be considered as a propagating plane wave (Huygens' principle), and if the cavity length allows for a Fabry-Perot resonance, a standing-wave pattern is stabilized inside the cavity, with period $\lambda_{SPP} \approx 350$ nm. The standing wave is properly imaged only when the semi-infinite field contribution is null, i.e. when $\alpha = \alpha_C$, $\vartheta = 0°$. Otherwise, the propagating SPP with period $\lambda_{SPP} \approx 700$ nm is imaged as well, as in Fig. 2.24c.

The scheme of the experiment is presented in Fig. 2.25c. The two optical pulses have been separated in time by more than $\Delta_2^0 = 100$ fs, to minimize direct optical interference, and the only standing wave (Fabry-Perot mode) has been imaged in a genuine PINEM measurement. In Fig. 2.26a we present such interference pattern, with the intensity spatial profile of the field in the inset. When we change the temporal delay Δ_{12}, the intensity of such pattern is coherently modulated, as shown in the space-time map in Fig. 2.26b and in the extracted intensity change plot, Fig. 2.26c. The temporal Fourier transform of the latter trace gives a peak centered at ≈ 380 THz, as expected.

This three-pulse experiment deals with SPP interference, which gives a stronger or weaker Fabry-Perot mode when it is constructive or destructive. At the same time, we also observed a modulation in the Fabry-Perot periodicity, with change of λ_{SPP} within the excitation bandwidth. Spectral interference may qualitatively explain this phenomenon: a modulation of the laser pulse spectrum is obtained when the two pulses are delayed in time, even when direct interference is negligible. For our experimental conditions, we calculated a spectral interference peak shift of ±1.6 THz between 109.09 and 110.41 fs delay, which is about 40% of the laser bandwidth. In Sec. 4.2.3 we will develop the argument further.

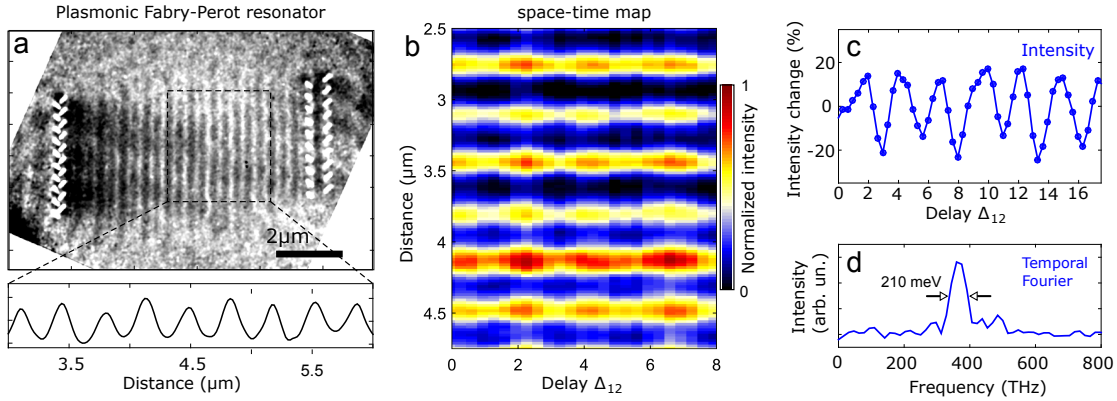

Figure 2.26 – Attosecond-nanometer modulation of a SPP field. **a**: PINEM micrograph of the SPP in the Fabry-Perot resonator. **b**: Spatiotemporal mapping of the Fabry-Perot field intensity, as a function of Δ_{12}. **c**: Temporal evolution of the Fabry-Perot intensity change. **d**: Fourier transform amplitude of the measured temporal trace. $\alpha = \alpha_C$, $\theta = 0°$, $\Delta_{ph} = 60$ fs, $\Delta_2^0 \approx 100$ fs.

2.2.6 Attoseconds and beyond

As seen, the two-pulse configuration enables to finely control the probability density of the photon orders in the free-electron multilevel-split wave function. For 1.57 eV photons, a noticeable change in phase between the two phase-locked pulses is mapped into a temporal delay down to the sub-fs timescale. Since the semi-infinite field method is very general, and –contrary to plasmonic excitations– does not rely on any specific property of the material but a nonzero reflectivity at the excitation wavelength, it can be extended easily to higher photon energies, although with decreasing efficiencies. In the X-rays, the modulation of the electron wave function would eventually be performed with optical delays in the sub-as timescale [257]. In ref. [141], we carried out simulations to calculate the sideband modulations in an ideal three-pulse experiment with two 100 fs-long, 777 eV X-FEL pulses, focused to 50 TW/cm^2 peak power each on a Co-Au multilayer surface, which reflects ~ 35% of the light at 45° incidence (see Fig. 2.27a). The Co-Au mirror [258] is kept thin enough (78 nm) to be transparent for the 200 keV electrons, and the X-ray parameters are similar to what is possible to achieve with current FELs [259]. The electron duration has been chosen to be always 300 fs. The $|\ell| = 1$ photon orders are visible in Fig. 2.27c, with $\sim 10^{-5}$ intensity relative to the ZLP. Assuming perfectly phase-locked pulse pairs, and $\Delta_2^0 = 150$ fs, the spectral modulation as a function of Δ_{12} is shown for $\ell = 1$ in Fig. 2.27b and d. The period is ≈ 5.3 as, and the intensity changes of up to ≈ 1% in a 511 zs interval.

These simulations with realistic parameters suggest that modulations with ~ 1 as are indeed possible with our method, although technically challenging, and with an associated small signal. A coherent modulation on such timescales may stimulate experimental ideas for extremely fast processes, such as intramolecular electronic motion [260], and nuclear processes [141, 261, 262].

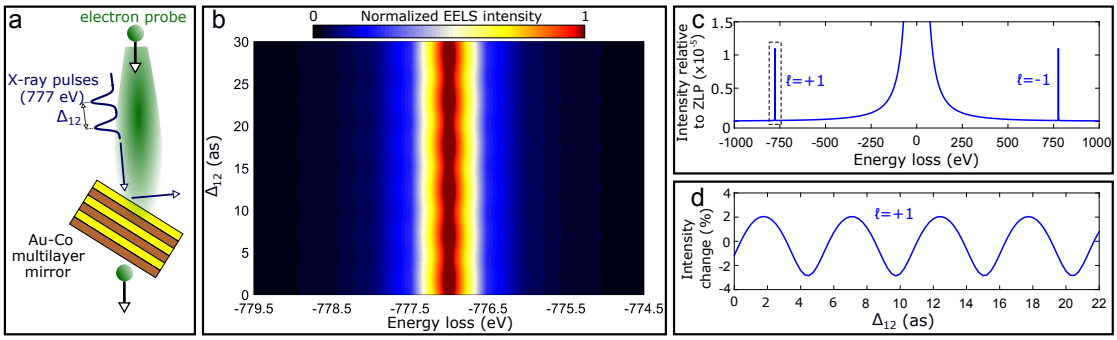

Figure 2.27 – Sub-as sideband modulation with X-ray light. **a**: Scheme of the thought experiment. **b**: Calculated EEL spectra as a function of Δ_{12}. **c**: Caluclated EELS, with ZLP and $\ell = \pm 1$ sidebands. **d**: Relative $\ell = 1$ intensity change as a function of Δ_{12}. $\Delta_2^0 = 150$ fs, $\delta = 0°$, $\alpha = 0°$, $\theta = 45°$, $\Delta_{\mathrm{ph}} = 100$ fs, $\Delta_{\mathrm{e}} = 300$ fs.

Conclusion and perspectives

Recently, significant innovative research has been carried out about extending high-energy electrons into the attosecond range [221, 222, 228, 231, 253, 263–267]. While attosecond science is a well-established field for photons [268], ultrafast electrons are a rather novel probe, and their potential has not yet been fully disclosed in the as range. In particular, attosecond electrons could combine the highest spatial and temporal resolution in the same probe.
If a fs-electron pulse acquires a large bandwidth, modulated by the external pump pulse, its dispersive reshaping creates points along the longitudinal direction where the phase-space distribution presents as-long electron-density spike trains. The as-spikes are separated in time by the period of the driving optical field. The coherent spectral modulation is therefore mapped into a longitudinal pulse bunching at specific distances from the interaction [228], just via ballistic propagation[14] of the free-electrons [265]. Despite not having isolated as-electron pulses, these as trains can already be used in pump-probe experiments [253, 269].

In this chapter I presented a complete characterization of a method to control the energy and momentum spectrum of the electrons via the inverse transition radiation effect, in a semi-infinite field geometry. The coherent modulation of the free-electron wave function, in the three-pulse experiments, adds a handle to the spectral control, in a particularly general and flexible configuration. Differently from schemes adopted by others [229, 251], in our experimental setting the two optical pulses are separated solely along the temporal coordinate, and not in space. The coherent spectral population we imprint into the free-electron wave function causes its longitudinal structuring in an attosecond pulse train, which may be employed for investigating or manipulating matter at that extremely rapid timescale, and eventually below.

[14] Namely, in absence of external forces.

3 Filming plasmonic propagation with a holographic principle

In Chap. 2 we stated the limit of PINEM to measure rapidly-varying fields and gave a partial preview of how to overcome this problem. In this chapter I will start discussing about SPPs, and describing an early method we developed to capture the propagation of plasmonic waves; later, I introduce the longitudinal-holography approach we recently developed. The latter method utilizes the electron-photon interaction described in Chap. 2, and enables filming the temporal evolution of nanoscale electromagnetic fields with extremely high accuracy. The research reported is mainly adopted from ref. [143] "*Imaging and controlling plasmonic interference fields at buried interfaces*", Nat. Commun. **9**, 13156 (2016), and ref. [213]: "*Holographic imaging of electromagnetic fields via electron-light quantum interference*", Sci. Adv. **5** (5), eaav8358 (2019). Some paragraphs are reported quasi-verbatim.

3.1 SPP at a buried interface

3.1.1 Surface-plasmon polariton

A surface-plasmon polariton (SPP) is a coupled optical and electronic excitation trapped and propagating at a metal-dielectric interface [270–272]. In the dielectric, the SPP mode, which is always transverse magnetic-polarized, is represented by an optical wave (polariton) peaked at the interface and rapidly decaying in the direction orthogonal to the interface; inside the metal, an electron density wave oscillates at the same frequency (surface plasmon). While in the perpendicular direction the plasmon-polariton shows subwavelength confinement[1] –giving a certain field enhancement, it can non-radiatively propagate within the boundary surface. An SPP is commonly distinguished from a localized surface plasmon excitation because the latter does not propagate, being typically confined around the edges of a nano-object with subwavelength dimensions.
As mentioned in Sec. 2.1 and sketched in Fig. 2.1, both swift electrons and light can excite plasmonic resonances and waves. In particular, far-field electromagnetic radiation (as our

[1] Its localization is exponential in both the dielectric and the metal, although with different decay lengths.

laser pulses) can be coupled into localized SPPs by nano-asperities on the metal-dielectric surface. Slits, holes, grooves, kinks and discontinuities can all radiate SPPs when illuminated by light with the proper wavelength and polarization. In the metallic nano-asperities the external light induces a dipolar excitation, which generates the SPP waves. Incidentally, the same asperities may scatter the SPP, acting as mirrors, beam-splitters, lenses (i.e. refracters), reproducing in a planar geometry many elements of 3D optics. They are extremely sensitive to changes in the local refractive index, which in turn is affected by many internal and external parameters, as the presence of adsorbates, external fields, temperature, et cetera [273]. Also, these plasmon waves can often travel undisturbed through curved and bent surfaces [274]. For all these reasons, they are considered interesting physical objects for optical circuitry miniaturization in a planar geometry.

In the most simple case, imagine an SPP propagating in one direction, $\hat{y}$, within the $< xy >$ plane defined by the metal-dielectric flat interface. Let $\hat{z}$ be the orthogonal direction, with the dielectric in the positive-z space. Since the mode is transverse magnetic, a nonzero electric field will be present both along $\hat{y}$ and $\hat{z}$, while the magnetic field will be along $\hat{x}$. The fields oscillates at a frequency ω, set by the external light excitation. We can write the electric fields as

$$\mathscr{E}_y^{\mathrm{SPP}}(\boldsymbol{r},t) = \mathscr{E}_0^{\mathrm{SPP}} e^{ik_{\mathrm{SPP}}y - i\omega t - \kappa(z)|z|} \tag{3.1}$$

$$\mathscr{E}_z^{\mathrm{SPP}}(\boldsymbol{r},t) = i\,\mathrm{sign}\{z\}\frac{k_{\mathrm{SPP}}}{\kappa(z)}\mathscr{E}_0^{\mathrm{SPP}} e^{ik_{\mathrm{SPP}}y - i\omega t - \kappa(z)|z|}. \tag{3.2}$$

Here we indicated $\kappa = \kappa(z)$ meaning that κ assumes different values in the metal ($\mathrm{sign}\{z\} < 0$) and dielectric ($\mathrm{sign}\{z\} > 0$). The SPP wavevector k_{SPP} is the same in the two materials, for continuity reasons, and is the quantity determining the plasmon wavelength. It can be expressed in terms of the permittivities in the simple form

$$k_{\mathrm{SPP}}(\omega) = \frac{\omega}{c}\sqrt{\frac{\epsilon_{\mathrm{M}}(\omega)\epsilon_{\mathrm{D}}}{\epsilon_{\mathrm{M}}(\omega)+\epsilon_{\mathrm{D}}}}, \tag{3.3}$$

where ϵ_{M} and ϵ_{D} are the permittivity constants in metal and dielectric, respectively.
A loss-free dispersion curve is shown in Fig. 3.1, together with the light line $\omega = ck$. There, the simplest model has been considered: a vacuum-metal interface with ϵ_{M} given by the free-electron model. For low photon energy, the SPP dispersion well overlaps the dispersion of light in free space. At higher energies $\epsilon_{\mathrm{M}} \to \epsilon_{\mathrm{D}}$, and we assist to a slow-down of the plasmon wave, which approaches asymptotically the surface plasmon frequency $\omega_{\mathrm{sp}} = \omega_{\mathrm{p}}/\sqrt{1+\epsilon_{\mathrm{D}}} = \omega_{\mathrm{p}}/\sqrt{2}$, with ω_{p} the (bulk) plasma frequency in the metal. For this reason, the SPP wavelength at frequency ω in the visible range can be much shorter than the corresponding free-space wavelength, allowing for very high sub-diffraction confinement. In 2D materials, as graphene, the confinement volume can be as small as $\sim 10^{-6}\times$ the diffraction limit volume [275], making it ideal for strong light-matter interaction [275–278]. In Fig. 3.1, k_{SPP} is real for $\omega < \omega_{\mathrm{SP}}$ and $\omega > \omega_{\mathrm{P}}$, and fully imaginary in between, where only bound states are allowed. We are interested

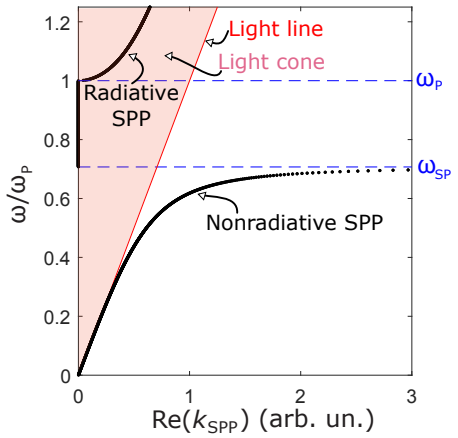

Figure 3.1 – Loss-free SPP dispersion at a metal-vacuum interface, according to Eq. 3.3, with ϵ_M represented by its free-electron model formula $\epsilon(\omega) = 1 - \omega_P^2/\omega^2$, and $\epsilon_D = 1$. ω_P and $\omega_{SP} = \omega_P/\sqrt{2}$ are the plasma and surface plasma frequencies, respectively.

in this chapter to the nonradiative plasmon, at $\omega < \omega_{SP}$.

3.1.2 About imaging SPPs

Since these waves propagate at a significant fraction of c and vary spatially in the optical subwavelength scale, their imaging requires simultaneous fs temporal and nm spatial resolution. Their direct real-space characterization presents a significant experimental challenge, especially in materials and devices involving buried interfaces and complex heterostructures. Several optics-based approaches have been developed to track surface-bound SPPs with appropriate resolution, notably dual-color coherent anti-Stokes Raman spectroscopy (CARS) [279] and scanning-tip-based techniques such as scanning near-field optical microscopy (SNOM) [280, 281]. In recent years, the spatial and temporal resolution limits of these optical techniques have been pushed to tens of nm and hundreds of fs [282, 283].
In an alternative approach, the use of electron photoemission for detection, as in time-resolved photoemission electron microscopy (tr-PEEM) [284–286], has allowed for comparable spatial resolution in imaging SPPs, with time resolution extending down to the few-fs single optical cycle regime. Recent advances in tr-PEEM methods have facilitated the successful spatiotemporal mapping of localized and propagating surface plasmons in a variety of systems [287–292]. However, as tr-PEEM relies on sample-emitted photoelectrons, and scanning-tip-based techniques require physical probe proximity to the evanescent field, both are inherently limited to the study of the exposed material surface, with damped sensitivity for fields beneath it. Although images of sub-surface SPPs are sometimes possible in SNOM [293] and especially tr-PEEM [294–296], the spatial resolution reaches at best ~ 40 nm [294]. Furthermore, the connection between the probed field and the local density of photonics states is not always direct [294, 297]. Due to these restrictions, these techniques have limitations for studies of advanced multilayer systems and heterostructured devices that rely on plasmonic waves

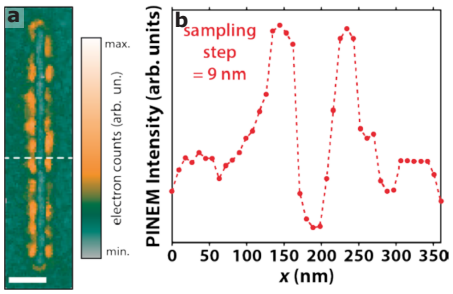

Figure 3.2 – PINEM spatial and temporal resolution. **a**: PINEM micrograph of the field around an Ag NW, from ref. [142], with the very same apparatus and parameters of the experiments I am describing. Scale bar 200 nm.

bound to buried interfaces.

Complementary, EELS, either in scanning (spectrum-imaging [298]) or parallel-beam EFTEM configuration, can image with great spatial and spectral resolution SPPs in thin films and nanostructures [198, 299, 300]. In these experiments, plasmonic guided modes are excited by the transient electric field generated by the swift electrons in proximity of the specimen [274, 301]. Being a transmission technique, it can be used also to probe plasmon waves in complex heterostructures, even with completely noninvasive schemes, in aloof geometry. However, as already discussed, the temporal resolution for this static TEM technique cannot exceed the ~ ms range.
In this scenario, PINEM guarantees high temporal and spatial resolution,[2] with the advantage –compared to CARS, SNOM, and tr-PEEM– to be able to probe even fields buried inside complex 3D structures, provided that they can be photoexcited [302]. PINEM and tr-PEEM give in a way complementary information: the former is sensitive only to the z component of the electric field, while the latter is sensitive to the in-plane components. Despite an SPP is poorly localized in the propagation plane, it is strongly localized in the orthogonal direction $\hat{z}$, the direction along which the momentum conservation law has to be fullfilled in the stimulated SPP absorption or emission process.
So far, PINEM has been used to image optical near fields at the edges of a variety of materials, nanostructures and biological specimens [119, 142, 222, 302], although these efforts did not track the dynamical behavior of the photoinduced plasmons or target the material properties of the specimens. So far, the use of PINEM to experimentally access SPP dynamics has remained an open challenge due to the typical SPP lifetime (on the order of 100 fs) being beyond instrumental temporal resolution, limited by the electron bunch duration.

In this work we employ localized, embedded SPP sources to launch SPPs in a 2D plasmonic waveguide, provided by a buried Ag-Si_3N_4 interface, allowing the photoinduced plasmons

[2] ~ 10 nm in our setup, and possibly beter, as can be seen from Fig. 3.2.

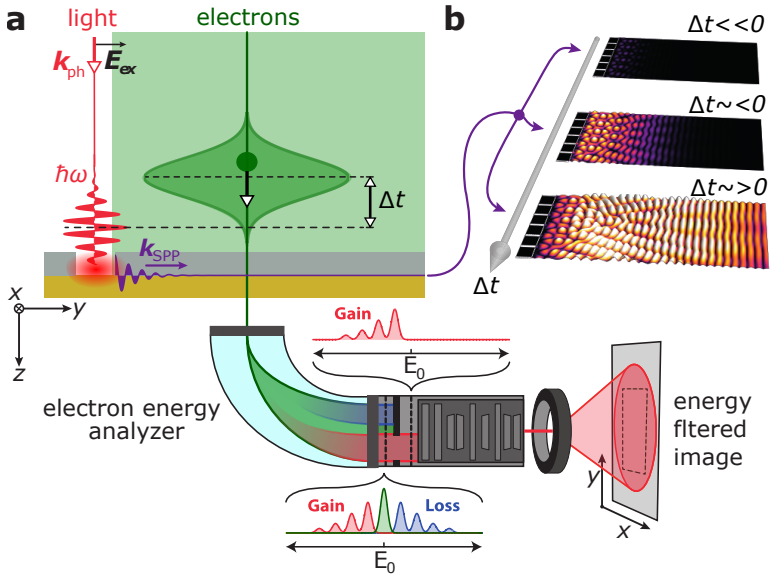

Figure 3.3 – First PINEM plasmon propagation experiment. **a**: Simplified scheme of the experimental apparatus measuring the PINEM from the photoexcited SPP. **b**: The variation of Δt in the vicinity of $\Delta t \approx 0$ generates a time-resolved movie of the buried plasmonic near field's ultrafast evolution.

to propagate and interfere over several μm. In this geometry, we partially circumvent the temporal-resolution limitations by observing the electron-plasmon scattering at different distances from the source. This interaction occurs at different times due to the finite time delay needed for the plasmonic wave to propagate. In this way, we could film the dynamical evolution of the collective plasmonic field propagating at the buried interface. Although still temporally within the long electron probe pulse, we managed to extract the propagation speed of the SPPs.

3.1.3 Ultrafast SPP propagation

A conceptual scheme of the experiment is sketched in Fig. 3.3a. A linearly-polarized optical pump pulse is incident on a nanocavity carved in the Si_3N_4-supported Ag thin film, launching an SPP of energy $E_{SPP} = \hbar\omega$, confined to the Ag-Si_3N_4 interface. At a variable time delay Δt, the propagating plasmonic wave is then probed by the parallel ultrafast electron pulse, which inelastically scatters from the optically excited SPP by PINEM interaction [137, 219, 223]. EFTEM micrographs utilizing only EEG counts give spatially-resolved snapshots of the $\mathscr{E}_z^{SPP}$ component of the buried plasmonic near field. Due to the large field-of-view of the electron beam employed here, snapshots recorded at different relative time delays Δt thus capture the spatiotemporal evolution of the photoinduced plasmonic wave, see Fig. 3.3b.

The sample studied consisted of a 30 nm Ag thin film deposited on a 50 nm Si_3N_4 membrane,

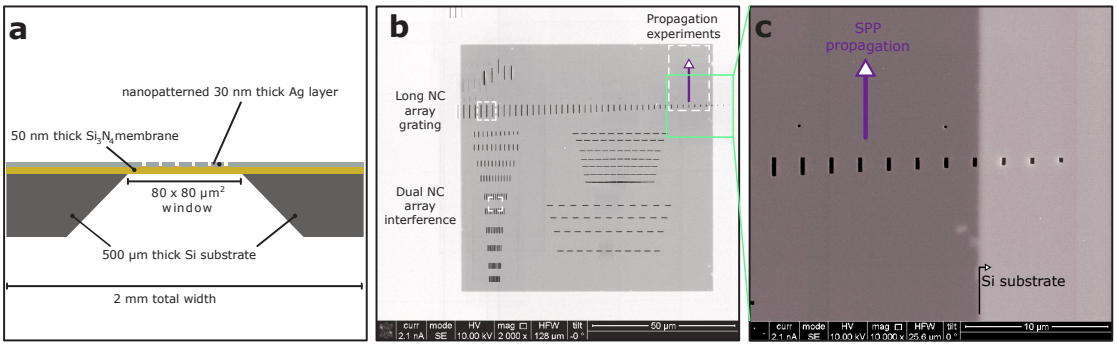

Figure 3.4 – **a**: Design of the specimen (cross-section view). **b**: SEM micrograph of the perforating nanocavities written in the Ag film. Areas from which experiments are reported are indicated by labeled dashed white rectangles. **c**: Zoom-in of the green-framed area with the nanocavity (NC) array imaged in the propagation experiment of Fig. 3.5 and Fig. 3.8.

Fig. 3.4a. The Ag film was sputtered onto a Si_3N_4-on-Si support membrane using an EMITECH K575x sputter coater equipped with an Ag target (100 mA, 60 s exposure, $3 \cdot 10^{-4}$ mbar base pressure). A variety of different rectangular NC arrays were patterned in the Ag layer using a raster-scanned focused-ion beam (FEI Nova Nanolab 200 focused ion beam (FIB)/SEM) with typical beam currents of 9 – 10 pA at a 30 kV voltage. Fig. 3.4b and c show an SEM characterization of the sample surface, which was kept in low oxygen conditions and measured within few days from the FIB patterning. For the first experiment on plasmon propagation, nominal NC widths were 250 nm, with nominal NC lengths incrementing from 700 to 1300 nm in 100 nm steps. The SEM-measured widths were ~ 274 nm, and the lengths 698, 809, 919, 982, 1113, 1175, and 1273 nm.
These studies made use of a fs-laser system slightly different than what described in Sec. 1.3 and utilized in the other experiments in this thesis.[3] We used as excitation a 300 kHz train of linearly-polarized pulses with ~ 100 fs FWHM duration, centered at ~ 786 nm. The laser was weakly focused on the specimen to a spotsize of ~ 60 μm FWHM diameter, such that the electric field of the pump beam was uniform across the field of view of the electron beam. Optical pump fluences employed were of the order of $1 - 4$ mJ$\cdot$cm^{-2}, corresponding to a peak excitation energy density of $\simeq 50$ GW$\cdot$cm^{-2}. The electron bunch duration is here about ~ 600 fs FWHM.

In order to experimentally measure the propagation speed of the SPPs at the buried interface, we monitor a large, nearly-featureless area adjacent to a linear array of NCs, as sketched in Fig. 3.5a and visible in Fig. 3.4c. The light polarization has been set parallel to the long axis of the NCs. In first approximation, each NC edge effectively acts as an antenna that launches plasmon waves radially outward in a point dipole-like pattern at the buried interface [303]. Consequently, according to the Huygens-Fresnel principle, the plasmonic wave propagating

[3] Same laser amplifier, but seeded by a 20 MHz Femtosource XL oscillator (FemtoLasers Produktions GmbH, now Spectra Physics), with narrower, multiple-peaked spectrum.

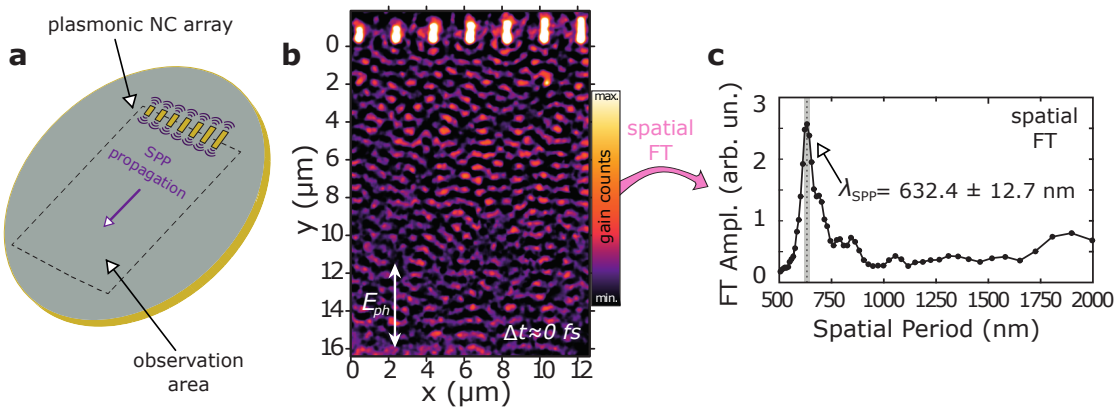

Figure 3.5 – **a**: Schematic of the specimen. **b**: Experimental PINEM micrograph of the photoinduced plasmonic wave propagating at the buried Ag/Si_3N_4 interface, at $\Delta t \approx 0$. As the electron and optical pulse durations satisfy $\Delta_e \gg \Delta_{ph}$, the plasmonic interference pattern is observed in the entire window at this delay. The linear false color scale corresponds to relative electron gain counts. **c**: Radially integrated Fourier transform (FT) amplitude of the spatial frequency components contained in the interference pattern of panel b as a function of the corresponding spatial period. The position of the singular peak corresponds to λ_{SPP}, and its uncertainty is indicated by the shaded gray line.

away from the NC array (along the y axis in Fig. 3.5b) corresponds to the coherent superposition of the SPPs launched from the different NCs.

Fig. 3.5b shows the experimental PINEM image of the resulting plasmonic interference pattern, recorded at $\Delta t \approx 0$. The spatial Fourier transform of the entire frame in Fig. 3.5b gives direct access to the spatial frequencies present in the interference pattern [281], and its radial integral is singularly peaked at the spatial period corresponding to the wavelength of the optically driven SPP wave, Fig. 3.5c. We can thus directly extract λ_{SPP} and $k_{SPP} = 2\pi/\lambda_{SPP}$ as 632 ± 13 nm and 9.94 ± 0.20 μm^{-1}, respectively, where the errors are dominated by the uncertainty in the calibration of the PINEM image.[4] Fig. 3.6 depicts the calculated EEL probability for the 200 keV electrons transmitted through a model of our bilayered sample, plotted as a function of energy loss and momentum transfer normal to the beam direction, i.e. in the interface plane. Given the known energy of the optically driven SPPs in the measurements ($E_{SPP} = E_{ph} = 1.58$ eV), we find that the SPP characteristics obtained experimentally well match the theoretical dispersion of the plasmonic mode propagating at the buried interface.

Fig. 3.6 strongly resembles Fig. 3.1, although in our case we see two dispersion branches. Indeed, in the thin bilayer, SPPs can propagate both at the exposed Ag-vacuum and buried Ag-Si_3N_4 interface. For a given excitation frequency, the plasmon-polariton at the exposed surface has always a longer wavelength than the plasmon wave at the buried interface. While the far-field electromagnetic wave can in principle couple to both modes simultaneously at 1.58 eV, theory suggests a much higher cross section for the buried wave. Experiments fully confirm it, as can be seen by the Fourier transform of the spatial interference pattern, Fig. 3.5c.

[4] Including the 'projection effect' uncertainty due to the specimen tilt, which is however small; indeed, we worked at nearly optical and electron normal incidence.

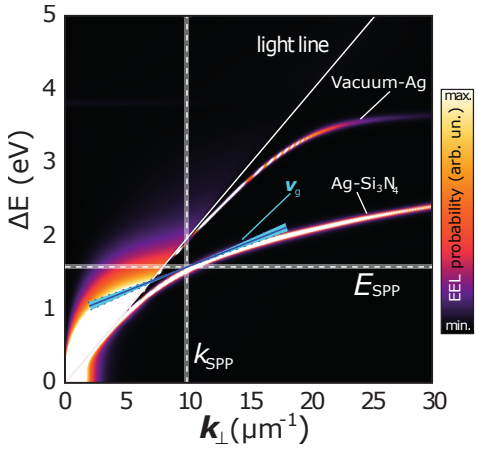

Figure 3.6 – Analytically calculated [301] EEL probability of 200 keV electrons traversing the specimen at normal incidence as a function of energy loss ΔE and transversal momentum transfer $k_\perp$. Experimental E_{SPP} and k_{SPP} values are indicated by dashed lines, with corresponding uncertainties represented by the shaded lines. The experimental values of v_g, retrieved from Fig. 3.8, is indicated by the straight line tangent to (k_{SPP}, E_{SPP}), the hourglass-shaped area representing its uncertainty. For methods, see refs. [143, 301].

At higher visible frequencies, the buried plasmon become lossier and more difficult to excite, but not the SPP at the vacuum interface. For this reason, light at 3.14 eV excites the latter mode. We confirmed it experimentally by exciting a long nanoslit in a similar Ag-Si_3N_4 bilayer (50 nm Si_3N_4, 90 nm Ag) by linearly-polarized light, and the SPP imaged by the holographic method (data not shown here, see Sec. 3.2 for the method).

Considering the 3D dataset of PINEM micrographs at different pump-probe delay times Δt, we can get some insight into the SPP build-up and evolution by performing a slice analysis of the images as a function of Δt. Some of those micrographs are reported in Fig. 3.7, while the complete video can be found in ref. [143]. As sketched in Fig. 3.8a, we divide up the image in a series of horizontal slices centered at different distances y from the NC array.

By taking the spatial Fourier transform of these slices for each delay, and integrating the Fourier features corresponding to the SPP peak, we can track the propagation of the plasmonic wavefront in time, as is sketched for a number of discrete slices in Fig. 3.8b. These temporal traces correspond to the sub-ps cross-correlation of the electron probe and the photoexcited SPP pulse in the different discrete y-ranges in the sample, offset by a temporal difference $\Delta^\star$ due to the SPP wave propagation. Combining the data of all slices yields a quantitative description of the dynamic behavior, which directly captures the SPP propagation. Fig. 3.8c depicts the temporal center of Gaussian fits to the cross-correlation time traces of different slicing schemes as a function of the distance y from the NC array. For a robust analysis, the positive y-range of the PINEM micrographs recorded at different Δt were divided up into a series of discrete horizontal slices, according to various slicing schemes. In particular

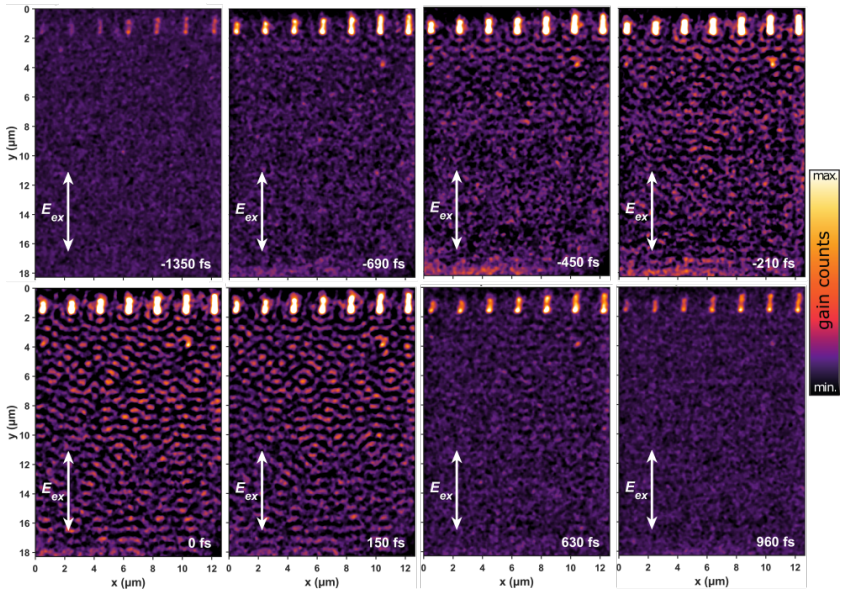

Figure 3.7 – Selected frames from the plasmon propagation movie. First row, from the left; $\Delta t = -1350$, -600, -450, and -210 fs. Second row, from the left: $\Delta t = 0$, $+150$, $+630$, and $+960$ fs. $\Delta t = 0$ is set as delay for which the light and electron pulse peaks coincide, and has an associated uncertainty of $\approx \pm 25$ fs.

with $\Delta y = 140$, 280, 420, 560 and 700 nm, in each case with a y-center offset equal to $0.5\Delta y$, i.e. with 50% slice overlap. The resulting data points for each of the slices in the different slicing schemes are combined and fitted with a single straight line, Fig. 3.8c. The slope of that line represents the group velocity of the composite plasmonic wave, and corresponds to approximately a third of the free-space speed of light, $v_g = (9.4 \pm 1.3) \cdot 10^7$ m$\cdot$s^{-1}. The refractive index for our SPP wave is therefore $n_{SPP} \approx 3$. This value is consistent with that expected from theory for the buried SPP mode, as indicated in Fig. 3.6. Although SPP group velocities at surfaces have been previously extracted from both time domain [294, 304] and frequency domain [305] experiments, this experiment demonstrates the direct measurement of the SPP propagation speed at a buried interface in a transmission geometry.

3.1.4 Controlling plasmon gratings

The ability of PINEM to directly access plasmonic interference patterns opens up a multitude of possibilities for creating arbitrarily shaped plasmonic transient gratings, as the obtained interferometric structures can be precisely tailored by combining appropriately arranged nanoscale features with suitable photoexcitation [256, 303]. Moreover, experiments can be supported by simulations applying Maxwell's equations to the nanopattern architectures, providing effective feedback and enabling the predictive design of transient plasmonic patterns. Fig. 3.9 illustrates this flexibility in designing transient plasmonic gratings. Panels a and b show the PINEM micrograph of consecutive parallel NCs under photoexcitation using different

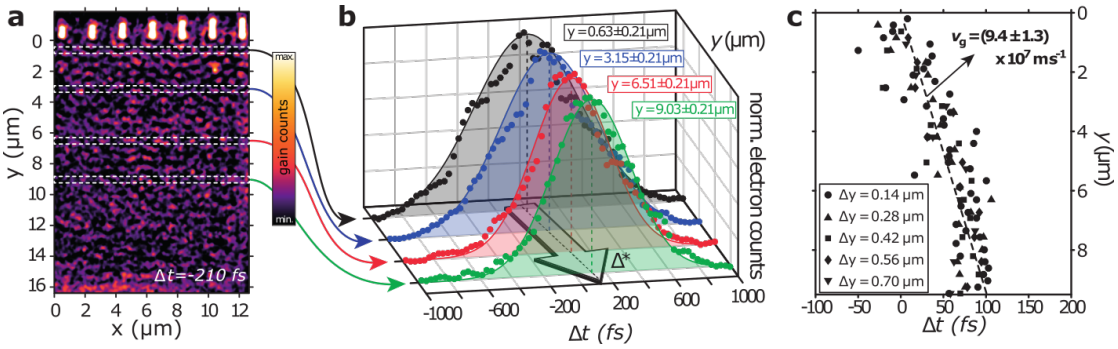

Figure 3.8 – **a**: PINEM micrograph at $\Delta t = -210$ fs. White dashed rectangles exemplify the discrete slicing of the image for spatial Fourier analysis.**b**: Temporal traces of the SPP wave intensity in the different discrete slices indicated in a. For each slice at each δt, the SPP wave intensity is calculated as the integrated intensity of the corresponding features in the spatial Fourier transform (FT). The y-range of each of the slices corresponds to $\Delta y = 0.42$ μm. **c**: Temporal center positions of Gaussian fits to the cross-correlation time traces versus distance traveled by the wave. Data points corresponding to different slicing schemes (Δy) are combined.

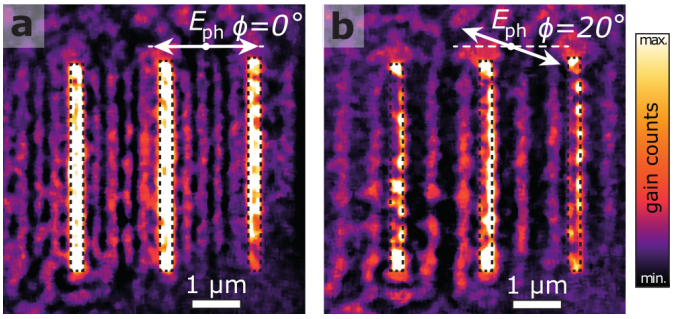

Figure 3.9 – Transient plasmonic patterns. **a**: PINEM micrograh for NCs irradiated by linearly-polarized light at $\phi = 0°$: a transient grating is formed. **b**: Same, at $\phi = 20°$.

linear polarization orientations, demonstrating that it is indeed possible to obtain transient plasmonic gratings using relatively simple nanostructures. The NCs in Fig. 3.9 are 4.3 μm long, and 260 nm wide. The space between two sources form a Fabry-Perot cavity, thus what we observe is a standing-wave pattern, Fig. 3.9a, with spacing $\lambda_{SPP}/2$. Curiously, in Fig. 3.9b the tilted polarization excites both the SPP perpendicular to and along the nanoslit. As a result, periodic intensity lobes are visible, especially in the rightmost cavity, with $p = 8$ nodes, due to the counterpropagating modes along the cavity (Fabry-Perot resonance of order 8) [306].
More complex patterns are visible with short NCs, where the emitted SPPs are circular waves more than planar waves. In Fig. 3.10 we report two examples. Interestingly, Fig. 3.10b shows two arrays of short NCs[5] facing each other at ~ 4.5 μm distance. The interference plasmonic pattern is a sequence of lines again spaced by $\lambda_{SPP}/2$, from which it is easy to extract the value $\lambda_{SPP} = 638 \pm 32$ nm.

[5] ≃ 2.1 μm long and ≃ 270 nm wide.

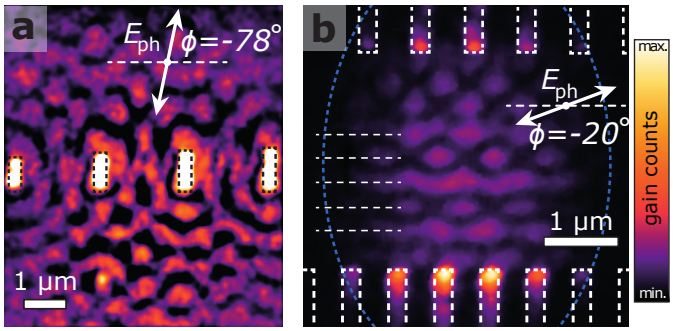

Figure 3.10 – Complex interference patterns for short NCs. **a**: PINEM micrograph of the SPP pattern from an array of short NCs (0.6, 0.7, 0.8, and 0.9 µm-long, and ≃ 275 nm wide), photoexcited by linearly-polarized light at $\phi = -78°$. **b**: PINEM micrograph of a plasmonic standing-wave pattern generated by two vertically-offset linear arrays of NCs photoexcited by linearly polarized light at $\phi = -20°$. The dashed elliptical shape depicts the approximate outline of the electron beam footprint.

Summarizing, in this section we demonstrated the visualization of photoinduced plasmonic interference patterns confined to otherwise inaccessible buried interfaces, enabling a critical tool for the investigation and development of complex plasmonic heterostructures and advanced multilayer devices. Our experiments introduce the feasibility of ultrafast imaging of plasmon dynamics using PINEM, allowing us to experimentally measure the carrier wavelength and propagation speed of SPPs traveling at buried interfaces directly in the time domain. Furthermore, we show that transient plasmonic interference patterns can be shaped via both the polarization of the excitation light and the nanopatterning architecture, thus facilitating a widely tunable range of nanoscale near-field structures. Finally, the standing-wave plasmon grating presented here represents a good plasmonic configuration for the electrons to diffract from. As shown theoretically [307], the elastic (Kapitza-Dirac) and inelastic electron scattering from a plasmonic standing wave can result in nontrivial patterns in the energy-transverse momentum plane. In turns, such patterns can give important insights into the Rabi oscillations within the standing-wave pattern.

3.2 Time-domain holographic imaging

Where do the PINEM contrast in Sec. 3.1.3 and Sec. 3.1.4 come from? Some contrast, like Fig. 3.9a and Fig. 3.10b, have a clear standing wave origin, as a result of counter-propagating plasmon-polaritons. However, the contrast in Fig. 3.7 cannot be explained by counter-propagating polaritonic waves. At the same time, since we are probing waves whose crests and troughs travel a distance $\lambda_{SPP}/2$ in ~ 1 fs, it is not possible to image the spatial pitch of the SPPs without an interference measurement with another phase-locked oscillating signal. A priori, this reference signal may have different nature: another propagating SPP at the same interface, an SPP at another interface, close enough for the evanescent fields in the $\hat{z}$ direction

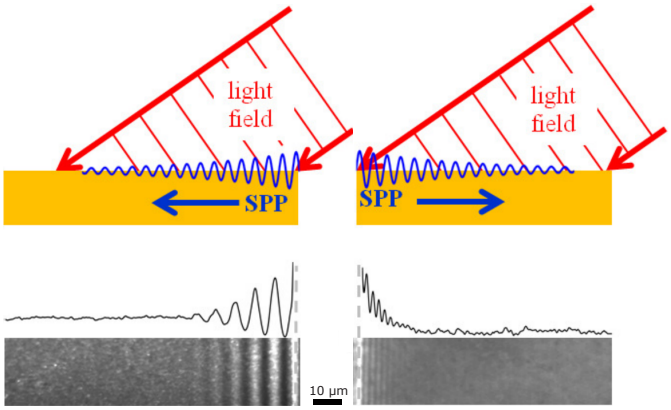

Figure 3.11 – Schematics and experiments of the tr-PEEM interferometric method to measure propagating SPPs. **a**: Co-propagating case. **b**: Counter-propagating case. The SPP propagates at a Au-vacuum interface, and the images were taken at $\Delta t = 0$. Adapted from Lemke *et al.*, ref. [294].

to interfere, the sum of photo- or plasmon-excited localized fields around crystal grains in the film, et cetera. As a speculation, if the last of the few options mentioned were true, the observed plasmonic pattern would be actually the localized plasmon field that brights up when the SPP passes by.[6]

A detailed understanding of the interference contrast origin is necessary to correctly interpret the data, and extract information on the material and electromagnetic fields. Furthermore, a substantial difference has to be made between standing-wave patterns, and holographic patterns. In the formers, an observed high contrast in a given position of the specimen corresponds to a high density of electromagnetic states in that position during the electron probe time Δ_e.[7] For the latters, this fact is no longer valid, because the exact contrast would depend on the phase and geometry between the two interfering fields. For example, we might ask ourselves whether the bright fringes in Fig. 3.9b comprised between the nanoslits truly posses a higher $\left|\mathscr{E}_z^{\mathrm{SPP}}\right|$ compared to the dark fringes.

In most of the tr-PEEM experiments we cited in Sec. 3.1.2 (and shown in Fig. 3.11) the spatial contrast of propagating SPPs originates from the interference of the excited SPP with the excitation light. Could an analogous scheme be adopted in PINEM? As I briefly showed in Sec. 2.2.5, the inverse-transition radiation effect has to be accounted for in these type of experiments. We see now more specifically how to correctly describe this kind of nonlocal holography, and how to exploit this interaction for plasmon imaging.

[6] See the last paragraph of Sec. 3.2.3 for a realistic explanation of the contrast and its grainy appearance.

[7] For a quantitative analysis, Rabi oscillations in the quantum ladder Hamiltonian should be taken into account. In that scenario, a higher field may give a lower EEG signal, see Fig. 2.12. In practical cases, with our apparatus' resolution, this effect is secondarily.

3.2.1 Holography principle

Holography allows capturing both the phase and the amplitude of a signal distribution by superimposing it with a known, fixed reference. This method was originally proposed by Dennis Gabor to improve the resolution of an electron microscope [308]. He first demonstrated the principle using light optics [308] [309], while holography with electrons was shown shortly after [310]. With the invention of intense coherent light sources (lasers), optical holography has become a popular technique for three-dimensional imaging of macroscopic objects, security applications [311] [312] and microscopic imaging [313].
Electron holography [314] [315] is an important technique in electron microscopy. Gabor's original idea envisaged an *in-line* scheme, basically exploiting the phase information contained in Fresnel micrographs.[8] A second method, termed *off-axis* electron holography [316] however prevaled, because guarantees a better recombination of signal and reference wave [315]. Off-axis schemes rely on an electron biprism to make the signal beam interfere with the reference plane wave. The subsequent hologram consists in an ensemble of interference fringes. Thin electrostatic wires are commonly used as biprisms [317] [318], and are often referred as Möllenstedt biprisms, from one of the inventors' name.
Off-axis electron holography has been successfully employed in materials science [319], and also to image electrostatic potentials [320] [321], included the most unequivocal proof of the Aharonov-Bohm effect [47]. It can be particularily useful in precisely imaging magnetic structures [322], such as superconductive vortices [323], skyrmions [324], and complex ferrimagnetic domains [325].
More generally, the holography principle can be extended to any kind of detection configuration involving a periodic signal undergoing interference, such as sound waves [326], X-rays [327], or femtosecond pulse waveforms (spectral holography) [328]. In recent years, various new experiments have been implemented to extend the concept of holography from a static imaging method to a dynamical probe, capable of recording the temporal evolution of both the amplitude and the phase of a signal. Time-resolved optical holography has been successfully realized in the femtosecond regime [329] [330], and was used in combination with photoemission for plasmon imaging with enhanced spatial resolution in tr-PEEM experiments [285] [294] [331], as seen in Fig. 3.11.
The introduction of temporal resolution in electron holography is more challenging, and so far the adopted schemes use temporal gating working in the microsecond timescale [332] [333]. Holography with ultrafast electron pulses should also be possible [60] [72], providing similar time resolution and allowing subpicosecond imaging of magnetic and electric fields to be performed. However, most applications of interest involve spatially-resolved phase dynamics of electromagnetic fields on the timescale of one to few fs. These include electronic excitations in condensed matter, non-radiative energy transfer in molecules, and excitonic currents and condensates, as well as optical fields in metamaterials and photonic crystals.

[8] Namely, defocused micrographs with Fresnel contours, analogue to Fresnel fringes with light.

What we demonstrate in the following –instead– is a time-domain holographic imaging technique implemented in UEM and based on the quantum coherent interaction of electron wavepackets with multiple optical fields. Rather than splitting and recombining a planar wave in space using a biprism, we make the electron wave interact with two different electromagnetic fields, reference and signal, placed in general at distant points along the longitudial coordinate z. That explains why it is primarily a time-domain and not a spatial holography. We illustrate this method by capturing attosecond/nanometer-resolved phase-sensitive movies of rapidly evolving local electromagnetic fields in plasmonic structures, as an example of nanoscale imaging of phase dynamics. We implement two configurations of the experiment. The first and simplest one, Sec. 3.2.2, relies on using electron pulses to map the optical interference between a polaritonic reference and a polaritonic signal, both excited with ultrashort light pulses, similarly to near-field optical or tr-PEEM instruments.
The second approach, Sec. 3.2.3, which is conceptually different and unique to UEM, is based on a Ramsey-type interference [229], and relies on the coherent modulation of the electron wave function by means of spatially separated reference and signal electromagnetic fields. Since the interaction with the sequence of optical fields is occurring along the electron propagation direction, the constraint imposed by high transverse electron coherence necessary for conventional electron holography is now removed. This limitation has so far prevented the practical realization of holography in time-resolved experiments using pulsed electrons, especially when using multi-electron pulses necessary for imaging applications.
Besides the implications in the investigation of ultrafast coherent processes at the nanometer length scale, we show that our approach could be used for accessing the quantum coherence of generic electronic states in a parallel fashion, which can be relevant for electron quantum optics applications.

3.2.2 Plasmon-plasmon (local) holography

A simple case of holographic UEM is based on local interference of two fields, which we choose to be two propagating SPPs. Next, we first review the interaction mechanism of the electron pulse with a single SPP, Fig. 3.12a, and then examine the holograms produced by interference between the two SPPs, Fig. 3.12b. In conventional PINEM, the electron pulse duration limits the spatial resolution in imaging a traveling SPP to $\Delta x \approx \Delta_e v_g$, where v_g is the plasmon group velocity. This is schematically shown in Fig. 3.12a. For the SPPs at the Ag-Si_3N_4 interface here studied, the resulting blurring in the real-space image is typically $\Delta x \approx 50$ μm, which is comparable with the plasmon decay length (~ 65 μm in our system). In Sec. 3.1.3 we saw that it is nevertheless possible to extract some temporal information by carefully and systematically fitting the temporal traces of the signal, but no propagating SPP wavefronts couldn be imaged, nor the phase velocity measured. This problem of blurring can be overcome via a holographic approach, which employs a second SPP wave, used as a reference, to create an interference pattern with the SPP of interest. Such interference forms only when both waves overlap in space and time, Fig. 3.12b. Let $\boldsymbol{k}_1$ and $\boldsymbol{k}_2$ be the wavevectors of the two SPPs. Both vectors lie

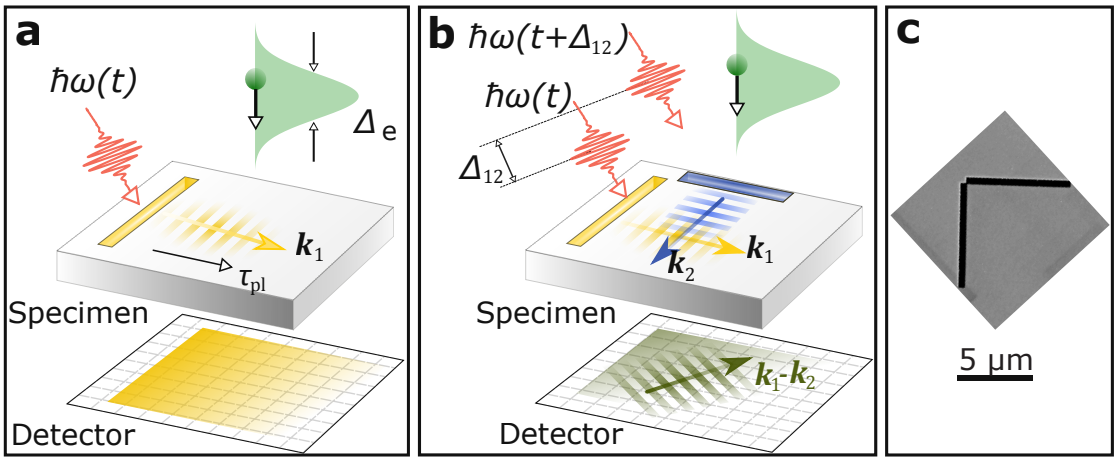

Figure 3.12 – Sketch of the controlled interference between two SPPs in a corner geometry. **a**: Excitation of an SPP from a NC. **b**: Excitation of two SPPs traveling in perpendicular directions. Being excited by different pulses, their delay Δ_{12} is tunable. **c**: SEM micrograph of the nanopatterned Ag-Si_3N_4 specimen.

in the $< xy >$ plane. The electric field of the overall pattern becomes

$$\mathscr{E}_z^{\text{tot}}(\boldsymbol{r},t) = \mathscr{E}_z^1 \cos(\boldsymbol{k}_1\cdot\boldsymbol{r}-\omega t) + \mathscr{E}_z^2 \cos(\boldsymbol{k}_2\cdot\boldsymbol{r}-\omega t+\varphi) = \\ = 2\mathscr{E}_z \cos\left(\frac{\boldsymbol{k}_1-\boldsymbol{k}_2}{2}\cdot\boldsymbol{r}-\frac{\varphi}{2}\right)\cos\left(\frac{\boldsymbol{k}_1+\boldsymbol{k}_2}{2}\cdot\boldsymbol{r}-\omega t+\frac{\varphi}{2}\right), \quad (3.4)$$

where we have considered $\mathscr{E}_z^1 = \mathscr{E}_z^2 \equiv \mathscr{E}_z$. The function $\mathscr{E}_z$ decays rapidly in z away of the Ag-Si_3N_4 interface, and has a slowly-varying envelope shape in the $< xy >$ plane, given by the optical excitation duration. Since the two waves are generated by phase-locked pulses, they will also be phase-locked. The phase shift between the two pulses enters via the parameter φ in Eq. 3.4.[9] Also, only the z-component of the electric field has been taken into account, because only the field component parallel to the electron momentum determines the inelastic electron scattering [137].

As the electron interacts with this field over many optical periods, the resulting interaction has to be averaged over the temporal coordinate, thus reducing the contribution of the rightmost cosine factor of Eq. 3.4 to a constant factor in the inelastic intensity, eliminating spatial oscillations with $\boldsymbol{k}_1+\boldsymbol{k}_2$ and leaving only those with $\boldsymbol{k}_1-\boldsymbol{k}_2$. The resulting energy-filtered image is thus a hologram with interference fringes of period $\Lambda = 2\pi/|\boldsymbol{k}_1-\boldsymbol{k}_2|$, as sketched in Fig. 3.12b. When the SPPs are launched by independent pulses, one can tune the relative delay φ between the reference and the field of interest with sub-cycle precision (330 as in our apparatus), therefore obtaining the real-space evolution of the phase of the electric field. The phase velocity of the wave can be directly extracted. Moreover, the finite duration of the reference pulse provides a temporal gate, effectively improving the temporal resolution of

[9] If the SPPs are generated by the same light pulse, $\varphi = 0$, unless a purely plasmonic phase shift has to be considered due to the geometry or nanofabrication.

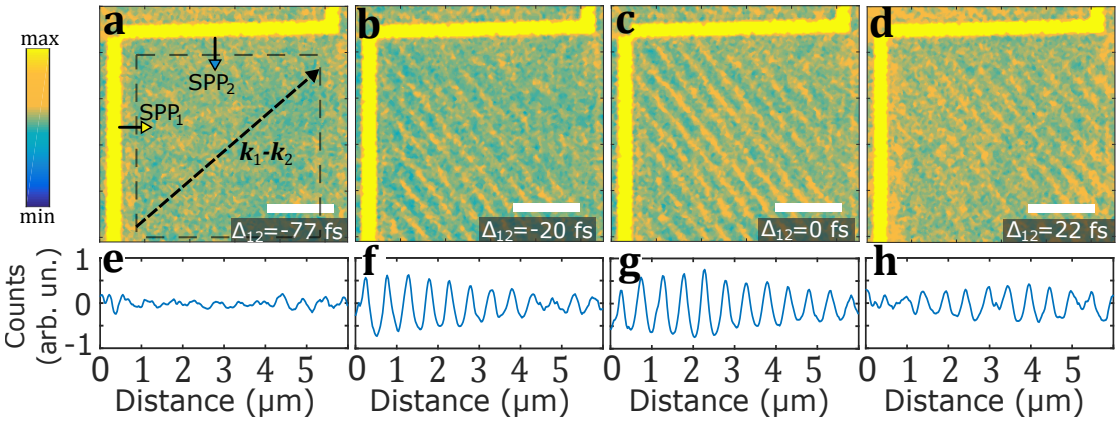

Figure 3.13 – Selected plasmon-plasmon holographic PINEM images at different delays. SPP_2 acts as reference, SPP_1 as signal. For increasing Δ_{12}, SPP_1 propagates from left to right, and the interference pattern moves from bottom-left to top-right. **a**-**d**: For $\Delta_{12} = -77$, -20, 0, and $+22$ fs, respectively. **e**-**h**: Corresponding profiles along the direction set by $\boldsymbol{k}_1 - \boldsymbol{k}_2$, averaged in the area delimited by the dashed square in panel a. Scale bars are 2 μm long.

PINEM in tracking group velocities down to the intensity autocorrelation of the laser pulse itself, in our case 80 fs, but which could attain ~ 1 fs with little further experimental effort, and eventually the as regime. Such resolution comes from the cross-correlation between the signal and the gated electron pulse, which has effectively the duration of the laser gate pulse, for us 55 fs, which creates the reference SPP. A similar concept has been presented in ref. [267] to control the temporal profile of the electron pulse using a sequence of two incoherent interactions with a visible and near-infrared (NIR) pulses, whereas here the adoption of two phase-locked light pulses provides a fundamentally higher signal-to-background ratio (~ 50%) and gives direct access to the phase dynamics.

To demonstrate the holographic PINEM concept we have implemented the experiment described in Fig. 3.12 using a nanostructure composed of two perpendicular slits, fabricated by Ga-ion milling of a 43 nm-thick Ag film deposited on a Si_3N_4 membrane, see Fig. 3.12c. The slits fully perforate the Ag layer, while penetrating only partially in the membrane underneath. Each slit radiates an SPP at the interface between the two materials when excited with light polarized normally to its long edge. The laser spotsize, ~ 25 μm FWHM is much larger than the slit distance and field of view. Nevertheless, the two SPPs were selectively excited by aligning the laser polarization ϕ_1 and ϕ_2 with the normal-to-edge direction of each slit; this was achieved by maximizing the PINEM response from a single pulse in the region of the sample where excitation only from one nanocavity was present. Being ϕ_1 rotated by 90° with respect to ϕ_2, the direct optical interference is negligible. The experiment is conducted at a critical angle condition, $\alpha = \alpha_C$, see Sec. 2.2.3, that minimizes the interaction of the electron with the interrupted light beam (inverse transition radiation).

In Fig. 3.13 we show the holograms formed by the two SPPs with relative pulse delays of

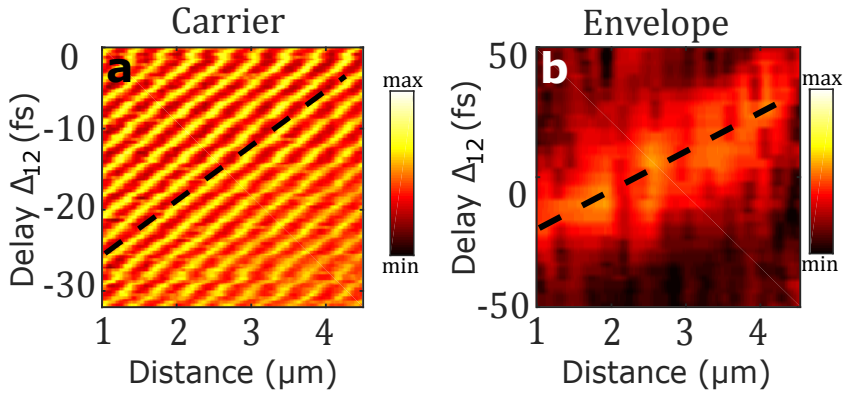

Figure 3.14 – **a**: Evolution of the plasmon-plasmon hologram's profiles as a function of Δ_{12}, as in Fig. 3.13e-h. The visible parallel lines are due to the propagation of the carrier function, and connected to the phase velocity v_ϕ of the SPP. **b**: Envelope of the holograms as a function of Δ_{12}. It is due to the propagation of the SPP pulse envelope, and connected to the group velocity v_g. These data were acquired in a separate delay scan, with larger time steps.

$\Delta_{12} = -77$, -20, 0, and 22 fs. These real-space images[10] of the plasmonic field are obtained by a variant of the PINEM methodology we developed recently, in which the elastic electrons are selected, instead of the inelastic, and a ZLP~ 8 eV is considered. For what is relevant here, we can consider it giving the 'negative' of the conventional PINEM images acquired with EEG only. We examine this method with more details in Sec. 4.3.1. By varying the delay between the two light pulses, the position of such interference patterns changes across the square area delimited by the two slits, moving from the left-bottom corner at negative time delays to the upper-right corner for positive delays, as can be seen in in the full movies in ref. [213]. This demonstrates the gating effect of the reference pulse, showing that the envelope of the interference pattern is defined by the optical and not the electron pulse duration. The intensity profiles at each time delay plotted along the direction set by $\boldsymbol{k}_1 - \boldsymbol{k}_2$ are shown in Fig. 3.14a and b.

Access to the phase dynamics allows us to measure the phase velocity v_ϕ, Fig. 3.14a, while the improved temporal resolution of this method enables the determination of the group velocity v_g, Fig. 3.14b.

In order to extract the correct v_ϕ and v_g, a geometric consideration should be done. These experiments were performed with the specimen tilted by an angle $\alpha = \alpha_C \approx 12°$ with respect to the z axis, while maintaining the normal to the surface within the plane defined by the light and electron beam directions. The presence of such tilt results first in a required recalibration of the measured distances by a projection factor $\sec(12°) = 1.022$. As a second, more important, effect, the tilt introduces delays in the plasmon emission from the NCs, as different parts of the NCs are exposed to the tilted light wavefront at different times. This results in an

[10] To make the contrast more visible, we subtracted a slowly varying background in the real-space images, approximated by a 2D parabolic function and originating predominantly in the beam shape and the non-holographic PINEM offset. The magnification of the images was calibrated with a 463 nm optical replica calibration sample. Furthermore, the presented images were median-filtered to remove off-scale pixels produced by cosmic rays. The same procedure is applied to the micrographs in Fig. 3.18b-d as well.

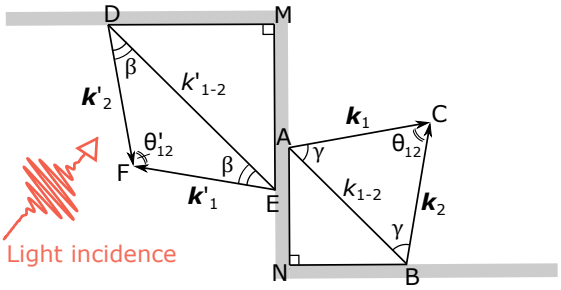

Figure 3.15 – Geometry of the stair-like emitters, allowing to measure the geometric correction factor for the hologram analysis and extraction of v_ϕ and v_g.

effective plasmon-polariton pulse front tilt. The periodicity of the hologram has an observed wavenumber $|\boldsymbol{k}_1 - \boldsymbol{k}_2| = 2k_{SPP}\sin(\theta_{12}/2)$, where θ_{12} is he angle between $\boldsymbol{k}_1$ and $\boldsymbol{k}_2$. Even if the two NCs are perpendicular, the complex tilt makes $\theta_{12} \neq 90°$.
In general, the tilt direction is not aligned with any of the emitters, and is not known accurately. We devised a stair-like emitters to retrieve in situ θ_{12}. In Fig. 3.15 we drew the stair-like source, with an arbitrary angle of incidence of the light in the rotated coordinate frame. The SPP wavefronts are tilted along the directions set by the vectors $\boldsymbol{k}_1$, $\boldsymbol{k}_2$, $\boldsymbol{k}'_1$, and $\boldsymbol{k}'_2$. Interference fringes will appear along the directions k_{1-2} and k'_{1-2} set by the vectors $\boldsymbol{k}_1 - \boldsymbol{k}_2$ and $\boldsymbol{k}_1 - \boldsymbol{k}'_2$, respectively. From the relations $2\gamma + \theta_{12} = 180°$, $2\beta + \theta'_{12} = 180°$, and $\theta_{12} + \theta'_{12} = 180°$, we find $\beta + \gamma = 90°$. Therefore the fringe wavenumbers are $|\boldsymbol{k}_1 - \boldsymbol{k}_2| = 2k_{SPP}\sin((180° - 2\gamma)/2) = 2k_{SPP}\cos\gamma$, and $\left|\boldsymbol{k}'_1 - \boldsymbol{k}'_2\right| = 2k_{SPP}\sin((180° - 2\beta)/2) = 2k_{SPP}\cos\beta$. It follows that $|\boldsymbol{k}_1 - \boldsymbol{k}_2|^2 + |\boldsymbol{k}_1 - \boldsymbol{k}_2|^2 = 4k_{SPP}^2$. Therefore, by measuring experimentally the fringe periodicity in both sides of this stair-like plasmonic emitter, the actual value of k_{SPP} can be accurately retrieved. Since in general $\beta \neq \gamma$, the fringe spacing is different on the two sides of the stair-like plasmonic emitter. This effect is similar to a Doppler shift, in which the two interfering wave have larger or smaller co-propagating momentum.
With this method we measured that in our experiment the slope of the fringes and of the envelope propagation in Fig. 3.14 are 0.71× lower than the corresponding plasmon velocity v_ϕ and v_g. We obtain the values $v_\phi = 2.69 \pm 0.05 \cdot 10^8$ m/s and $v_g = 1.95 \pm 0.07 \cdot 10^8$ m/s, which agree well with the estimated theoretical values of $v_\phi = 2.64 \cdot 10^8$ m/s and $v_g = 2.04 \cdot 10^8$ m/s, respectively. The theoretical values were calculated as in Fig. 3.6.[11]
Because our technique is essentially a spatially-resolved temporal cross-correlation method, the characterization of the wavepacket cross-correlation can be done with arbitrary precision, also better than the 330 as done here, resulting in a ~ 3 orders of magnitude advancement with respect to the standard PINEM methodology.

[11] The difference in v_g between the system here and in Sec. 3.1.3 is due to the Ag and Si_3N_4 layer thickness difference.

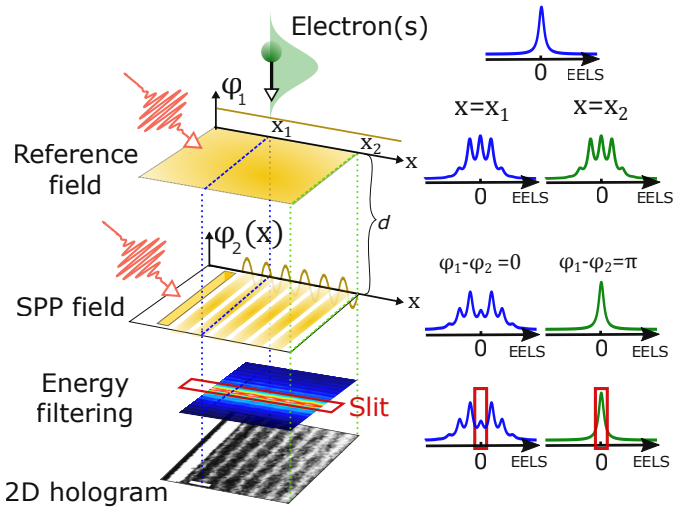

Figure 3.16 – Principle of spatially separated electron holography. On the left, the essential steps of this method, and on the right the corresponding calculated electron energy distributions.

3.2.3 Plasmon-far field (nonlocal) holography

The holographic approach presented above can be greatly generalized by utilizing the coherence between the different energy states of the quantum ladder in which the electronic wave function is split upon interacting with light, see Chap. 2 [141, 221, 222]. This method exploits the fact that the electrons carry information about the amplitude and phase of the optical field even after the interaction is finished. Thus, the result of any ensuing interaction of the electron will depend on the relative phase between the initial and subsequent optical fields [229]. This allows us to separate in space the interfering fields, enabling in turn the adoption of more practical reference fields.

In particular, we make use of a semi-infinite light field created by the reflection of the optical beam from an electron-transparent optical mirror, Fig. 3.16. The interrupted optical field interacts with the electrons via the inverse transition radiation effect, therefore creating a material-independent reference field, with nearly-constant spatial amplitude and phase, providing an optimum reference for holography. The interaction with this first optical field is captured in the spatially homogeneous coupling factor β_1, which is a complex number uniquely determined by the amplitude and phase of the optical field, as well as the electron trajectory [137]. Correspondingly, a coherent superposition of states on the quantum ladder takes place with the same probability everywhere, as visible in the electron spectra in the right part of Fig. 3.16, calculated with the analytical model of Sec. 2.1.1 with parameters $\Delta_{\mathrm{ph}} = 60$ fs, $\alpha = \alpha_{\mathrm{C}}$, $\vartheta = 35°$, and intensity of both reference and signal fields 0.13 GW/cm^2.

The interaction with the spatially varying signal field, occurring at a distance d further down the electron path, is captured by a space-dependent coupling factor $\beta_2(x, y)$. The total interaction is given by a simple sum of two complex numbers $\beta(x, y) = \beta_1 + \beta_2(x, y)$. The final energy distribution is defined by the modulus $\left|\beta(x, y)\right|$, which for slowly decaying plasmon fields is

predominantly defined by the spatially dependent phase difference $\Delta\varphi(x,y)$ between the two optical fields. The coherent interaction of the electron with reference and signal field hence results in a position-dependent electron energy distribution. By energy filtering, the hologram is obtained.

In Fig. 3.17a we show the experimentally measured variation of the electron energy distribution as a function of the electron beam from a directional plasmon emitter as in bottom of Fig. 3.16, formed as a result of the above-described spatially-separated interference, and acquired in SREELS mode. The distribution has the periodicity of the plasmon wavelength, both in the elastic and inelastic channels, which are in opposite phase, as shown in panel b. This fact can be appreciated in Fig. 3.17c, where we plot the energy profiles corresponding to the maximum (orange) and minimum (blue) of the elastic peak (that is, $\Delta\varphi = \pi$ and 0, respectively). The interaction strength β, Eq. 2.7, depends on the electric field amplitude linearly as

$$\beta(x,y) = \frac{q_e}{\hbar\omega}\left(\int_{-\infty}^{+\infty} \mathscr{E}_z^1(z) e^{-\frac{i\omega z}{v_0}} e^{-i\varphi_1} \mathrm{d}z + e^{-\frac{i\omega d}{v_0}} \int_{-\infty}^{+\infty} \mathscr{E}_z^2(x,y,z) e^{-\frac{i\omega z}{v_0}} e^{-i\varphi_2(x,y)} \mathrm{d}z\right). \quad (3.5)$$

Here, $(\mathscr{E}_z^1, \varphi_1)$ and $(\mathscr{E}_z^2, \varphi_2)$ are amplitudes and phases of reference and signal fields, respectively, and v_0 the velocity of the electron wavepacket. The linearity of this formula implies that the nonlocal interference contrast is mathematically equivalent to the previously discussed case of local interference. The only difference is a constant phase offset $\exp\{-i\omega d/v_0\}$ between the two fields, which can be compensated by properly choosing the mutual delay between them. For fields that significantly vary not only within the $< xy >$ plane but also along the z coordinate (3D nano-objects, non-planar plasmonic structures, etc.), the phase-factor $\exp\{-i\omega d/v_0\}$ produces an important contribution to the overall contrast. It reflects the change in the phase of the signal field due to retardation. In other words, it contains information on the z-distribution of the signal field, which can be directly retrieved because both the electron velocity and the light frequency are known quantities. This would allow for a complete three-dimensional phase tomography of the signal of interest to be performed, and could be used to reconstruct the complex electric field distribution around 3D particles or nanostructures.

The mathematical equivalence of local plasmon holography and spatially-separated quantum holography allows us to treat the recorded holograms with the same formalism of propagating and standing waves. In the spatially-separated case, the homogeneous reference field is non-collinear with respect to any propagating signal field, ensuring the formation of a standing wave pattern. Apart Fig. 3.16 and Fig. 2.24, we will see many nonlocal holograms in Chap. 4.

Intriguingly, an additional phase variation appears if the wavefront of the reference wave is tilted with respect to the mirrors surface, generating Doppler-like shifts [334] in the interference pattern. We present an observation of this effect in Fig. 3.18. We record holograms of an SPP radially propagating out of a ~ 800 nm-diameter nanohole carved in the Ag layer. The reference is the tilted wavefront of the light reflected from an Ag mirror and the plasmon signal travels as usual at the Ag-Si_3N_4 interface. The tilted wavefront can be described in Eq. 3.4 through the addition of the in-plane momentum component $\boldsymbol{k}_2 = \boldsymbol{k}_{\mathrm{ph}\parallel}$ coherently

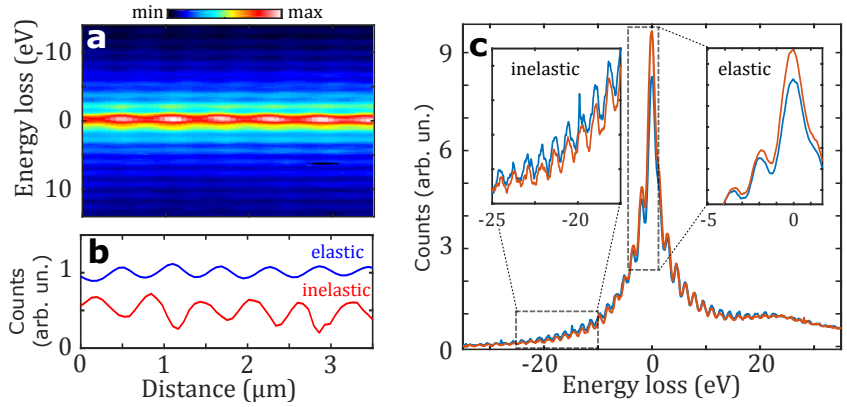

Figure 3.17 – Spectral modulations at the basis of spatially separated electron holography. **a**: Experimental SREELS map for a propagating plasmon out of a long nanoslit. **b**: The elastic and inelastic signal oscillate in antiphase as a function of the traveled distance. The elastic contribution was averaged between −1 and +1 eV, the inelastic between −27 and −12 eV. **c**: Electron spectra corresponding to maximum and minimum of such oscillations, averaged over four periods.

superimposing on the in-plane plasmon momentum $\boldsymbol{k}_1 = \boldsymbol{k}_{\mathrm{SPP}}$, whose direction is radial with respect to the center of the hole, see Fig. 3.18a. The magnitude and sign of the in-plane photon momentum component is $k_{\mathrm{ph}\parallel}(\vartheta) = (\omega/c)\sin\vartheta$. The resulting pattern exhibits a periodicity with wavenumber $|\boldsymbol{k}_1 - \boldsymbol{k}_2| = \left|\boldsymbol{k}_{\mathrm{SPP}} - \boldsymbol{k}_{\mathrm{ph}\parallel}(\vartheta)\right|$, which is direction-dependent and leads to the Doppler effect shown in Fig. 3.18b and d for a tilt $\vartheta = -20°$ and $+20°$, respectively. Line profiles around both sides of the hole clearly highlight the change in periodicity on opposite sides of the hole, Fig. 3.18e and g. This effect is naturally absent in the untilted hologram shown in Fig. 3.18c and in its line profile, Fig. 3.18f.
Given that in our case the $\boldsymbol{k}_{\mathrm{SPP}}$ are distributed over all the (in-plane) azimuthal angles ξ, the Doppler shift also evolves as a function of ξ. In particular, if we choose ξ to be null on the in-plane direction perpendicular to $\boldsymbol{k}_{\mathrm{ph}\parallel}$, the observed wavenumber $k_{\mathrm{obs}}(\vartheta,\xi)$ can be written as $k_{\mathrm{obs}}(\vartheta,\xi) = k_{\mathrm{SPP}}(1 + (k_{\mathrm{ph}\parallel}/k_{\mathrm{SPP}})\sin\xi)$, and the observed fringes are spaced by $\Lambda(\vartheta,\xi) = 2\pi/k_{\mathrm{obs}}(\vartheta,\xi)$. Therefore, from the Doppler holograms Fig. 3.18b-d we can directly find which is the direction of $\boldsymbol{k}_{\mathrm{ph}\parallel}$. For a flat specimen surface, it corresponds to the straight line across which the maximum Doppler shift is observed, which for holograms presented here roughly corresponds to the horizontal direction. Retrospectively, this information could have been useful for the local plasmon-plasmon holograms of Sec. 3.2.2.
The presence of Doppler effects in the local and especially nonlocal holography has to be kept in account when interpreting the holograms. Prior knowledge on the specimen structure (e.g. planar, wedged, etc.) and reference-field geometry may be required.

Finally, we can answer about the provenance of the curious contrast we dealt with in Sec. 3.1.3, see for instance Fig. 3.7. The fringes spaced by $\sim \lambda_{\mathrm{SPP}}$ have holographic origin (at $\alpha = \vartheta = 0°$), and the grainy nature of the wavefronts comes likely from the diffraction contrast from the

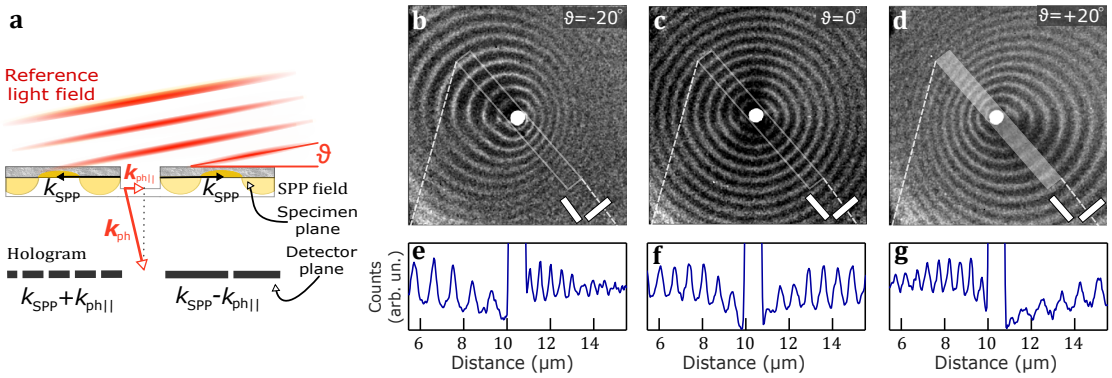

Figure 3.18 – Doppler patterns in spatially separated electron holography. **a**: Experiment's schema. A laser pulse creates both the reference field and the (plasmonic) signal field. In this 1D cartoon, the periodicity of the interference fringes is determined by the sign in the sum $k_{SPP} \pm k_{ph\parallel}$. **b**-**d**: Holograms for light incidence angle $\vartheta = -20°$, 0°, and +20°, respectively. The scale bars are 2 μm long. Scale bars in panels b and d account for the projection effect (factor $\sec(20°) = 1.065$ along the tilt direction), while the micrographs were not modified. **e**-**g**: Line profiles of the holographic fringes, obtained by averaging panels in the shaded region in panels a-d.

polycrystalline film. That contrast is present also in bright- dark- field imaging, and is not related to plasmonics. The micrographs reported in this section show neater SPP wavefronts, and are obtained with higher-quality Ag films, i.e. smaller nanocrystallites. However, zoomed-in image scrutiny highlights the diverse contrast brightness of the nanocrystallites also here. We also performed measurements on lower-quality films, with large, irregular grains of few-to-several hundreds of nm. In that case, while the ideal wavefront profile could still be followed, the grain contrast dominate the image. The comparison with bright-field microscopy confirms the proposed interpretation.

3.2.4 Conclusions and perspectives

Besides the direct implications in the visualization of phase-sensitive dynamics, our holographic approach can be useful for the characterization of the quantum state of a generic free-electron state, such as the one generated in the photoemission process from a solid-state material illuminated with UV light. This problem is of great interest not only for ultrafast microscopy, but also for free-electron lasers and attosecond physics [335]. It has been shown that in the photoemission process electrons carry information about the phase of the exciting optical field [336]. However, due to several uncontrolled factors, such as screening potentials, scattering events, or external field inhomogeneities, coherence is usually lost in part [337]. While in attosecond science reliable techniques have been developed to investigate this issue [338, 339], it is still a pending problem in UEM, which is particularly relevant when targeting sub-eV excitations [340] in condensed matter, where the relevant energy is smaller than or comparable with the electron energy spread, and thus beam coherence becomes an

important condition.
We stress that the quantum coherence of an electron state, while related, must not be confused with the coherence between the electrons usually discussed in the context of (biprism-based) electron holography. In the holographic sense, coherence is rather a measurement of the monochromaticity and phase stability of electron plane wave, whereas quantum coherence in the context of the present study describes our ability to determine whether an electron is in the pure state or rather entangled to the environment. In a quantum coherent state an electron can be in a superposition of states with vastly different energies, and as a consequence, not being very coherent in the holographic sense (i.e. not producing clear sinusoidal interference patterns when subjected to spatial interference experiments). The word coherence in the quantum sense indicates that the phase between different energy states is determined via time-evolution operator and is not random. In mathematical terms, quantum coherences of a state manifest in nonzero off-diagonal terms of its density matrix.
In our method, the interaction between the SPP and the electron makes a generic electronic quantum state ρ_{in} evolve unitarily into a space-dependent state $\rho_{\text{out}}(x)$. In this way, off-diagonal terms of ρ_{in} get projected onto the observable diagonal terms of $\rho_{\text{out}}(x)$. As our approach is able to simultaneously record spatial and spectral information (see Fig. 3.17a), we can readily determine how the energy distribution of the final electronic state varies with respect to x. This information can be used to identify and characterize the quantum coherences of the initial state.

Inspired by a recent work of Priebe *et al.* [228], in ref. [213], see Fig. 3.19, we report model calculations showing how our method could discriminate between a highly coherent (pure) and a fully incoherent (completely mixed) electron distribution, modeling the density matrix ρ_{in} of photoelectrons generated for example by UV illumination of a solid target. These states are then made to interact with a traveling plasmon polariton excited by a MIR optical field with a photon energy significantly smaller than the energy width of the photoemitted electrons. The MIR and UV pulses are considered mutually phase-locked (e.g. via harmonics generation process), so that the electron, if photo-emitted in a pure state, by carrying phase information imprinted from the UV light is also phase-locked to the MIR light.
First, we consider electrons emitted in a pure Gaussian state, Fig. 3.19a and b, for which the coherent interaction with the SPP field results in a generally asymmetric spectrogram, whose shape strongly depends on the phase difference between the SPP field and the UV photon used in the photoemission process. We stress that this phase dependence is a general property of any pure state spectrogram, while the asymmetry is not necessarily observed, and might be absent for some particular profiles of the wave functions. In contrast, when considering the spectrogram of a completely mixed Gaussian state, Fig. 3.19c and d, we find it to be symmetric and phase-independent. Thus, by observing the spatial dependence of the electron energy distribution, we can establish whether there is partial coherence in the photoemitted electrons.
This observation allows us to propose a further extension of UEM holographic imaging dis-

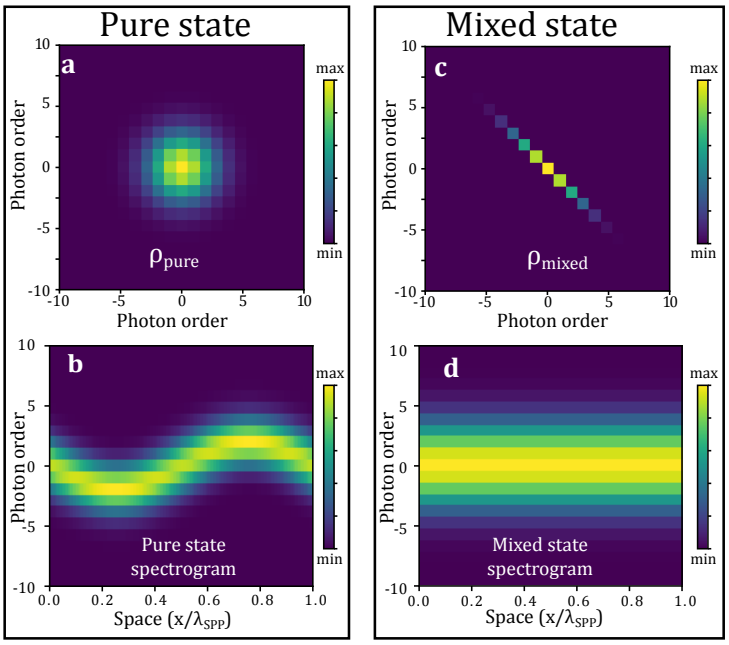

Figure 3.19 – Proposal for the determination of the coherence of photoemitted electrons. **a**: Density matrix for a fully coherent (pure) state created by photoemission. **b**: Spatially dependent spectrogram formed after interaction of the pure state with an SPP. **c**,**d**: Same as a and b, but for a completely mixed state. For the density matrix calculation methods, see ref. [213].

cussed above. Indeed, Fig. 3.19b suggests that the spectrogram formed by coherent photoelectrons could encode information about the spatial phase distribution of SPPs, even without making use of the reference optical field, providing the most practical realization of quantum-holographic UEM.

To conclude, we have demonstrated both local and spatially-separated holographic approaches based on ultrafast transmission electron microscopy. We have shown that these methods significantly improve the time resolution and, because they are phase sensitive, enable to determine the phase and group velocities of the propagating electromagnetic fields involved in the experiments.
Moreover, the nonlocal character of our method allows us to completely decouple the reference and probe fields, which is not possible when relying on near-field-optical or photoemission microscopy techniques. We highlight that our demonstration of spatially-separated quantum holography is made possible by exploiting the interaction with a semi-infinite light field, which provides a nearly-perfect material-independent reference. The extension of this method to any local collective field promoting periodic modulation of the electron wave function is straightforward, and offers a unique perspective to achieve nm and sub-femtosecond combined resolution in TEM. Possible objects of interest to be studied with this technique are atomic polarizabilities, excitons, phonons, and other collective and quasiparticle excitations in condensed matter systems. In addition, we propose a spatially-resolved detection method of coherences in electron quantum states with potential interest for electron quantum optics applications.

4 Shaping electron beams with near fields: ultrafast electron vortices

In Chap. 2 and Chap. 3 we saw examples of how to manipulate the free-electron wave function with near- and far-field electromagnetic waves. In this chapter, another relevant example is shown: the design and use of phase-shaped near fields to imprint variable phase distributions into the electron wave function. In particular, I will discuss the consversion of electron plane waves into vortex beams, with a defined orbital angular momentum (OAM). The material here presented is in significant part based on ref. [341] "*Ultrafast Generation and Control of an Electron Vortex Beam via Chiral Plasmonic Near Fields*", Nat. Mater. **18**, 573-579 (2019). Some paragraphs are reported verbatim. The last few paragraphs of the chapter contain materials from ref. [340], "*meV Resolution in Laser-Assisted Energy-Filtered Transmission Electron Microscopy*", ACS Photonics, **5**, 759-764 (2018).

4.1 Vortex beams

The quantum wave nature of both light and matter has enabled several tools to shape them into new wave structures defined by exotic non-trivial spatio-temporal properties [343]. Among these techniques, the impartment of a vortex onto their transverse phase profile is showing

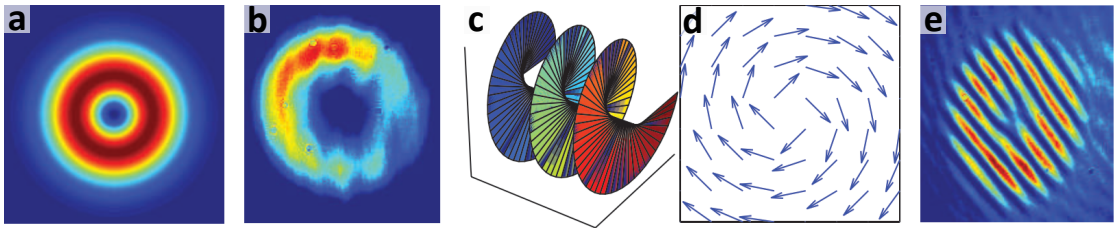

Figure 4.1 – Example of OAM light. **a**: Typical transverse intensity profile for a $m = 1$ beam, according to theory. **b**: Experimental profile for a vortex formed with a computer-generated hologram mask. **c**: Corresponding isophase surface, showing the corkscrew rotation. **d**: Sketch of the local momenta distribution of light near the phase singularity. **e**: Typical dislocation hologram. Figure adapted from Molina-Terriza *et al.*, ref. [342].

a significant impact in both applied and fundamental science. Vortices are stagnant points at which the phase is undefined, while along a contour around them it varies by an integer multiple m of 2π. The magnitude and sign of the quantization number m, also known as the topological charge, indicate the amount and the handedness, respectively, of the phase cycles surrounding the vortex [344, 345]. If the singularity is located along the wave's central axis z, it is simply accounted for by a phase factor $\exp\{im\phi\}$ in the wave function, where ϕ is the azimuthal angle. Provided that the modulus of the wave is circularly symmetric, then the presence of this term causes the wave to carry OAM, as it effectively becomes an eigenstate of the z component of the OAM operator $\hat{L}_z = -i\hbar\partial/\partial\phi$ with eigenvalue $m\hbar$.

The angular momentum of light has a possible spin part, the spin angular momentum (SAM), which is associated to the light polarization (right-handed or left-handed circular), and can have eigenvalues $\pm\hbar$ per photon [346, 347], and an orbital part, which depends on how light is structured in space, i.e. from its wavefront topology [348]. When the wavefront is twisted in space, a vortex singularity can be present, and light acquires an OAM $\pm m\hbar$, depending on how many twists $\pm m$ light does in one wavelength propagation. For this reason, the orbital component of the angular momentum can be arbitrarily high, while the spin component is limited to $\pm\hbar$ per photon. Spin and orbital angular momenta are well distinguished quantities within the paraxial approximation, while their separation might become non obvious in presence of tight foci [345].

In Fig. 4.1 we see an example of optical vortex beam with $m = 1$, from ref. [342]. Panels a and b show the theoretical and experimental intensity profiles of the beam in the plane perpendicular to the beam propagation direction. The intensity is vanishing at the center, and the beam has the shape of a torus.[1] Fig. 4.1c shows the isophase surface of the beam, modulo 2π. The wavefronts have a spiral pattern, resembling a winding staircase. The local momentum of the beam swirls around its singularity, Fig. 4.1d, analogously to how particles move in tornados, water whirlpools, rotating superfluids and to how spins orient in spin vortices: hence the name vortex for OAM-carrying light. When a $m = 1$ vortex beam is made to interfere with a plane wave ($m = 0$) in a slightly noncollinear geometry, the interference pattern reveals a 'screw'-type first-order dislocation [349, 350].[2] The number of interference fringes on one side is different from the number of fringes on the other, and the central dislocation is the topological defect bridging the two sides.

Vortex beams possess therefore a topological charge $Q = m$, which is encoded in the helical phase distribution[3] and visible in the dislocation hologram. Several methods have been devised to shape the phase distribution in light beam, convert topologically trivial into topologically nontrivial beams, and characterize their properties [345]. Among them, refractive phase plates, static diffractive gratings with dislocations, and diffractive holograms created by programmable spatial light modulators.

Optical vortices [348] have been generated at all visible and infrared wavelengths, down

[1] Alternatively referred as doughnut by sweet tooth physicists.

[2] Called 'fork', when paired with 'doughnut'.

[3] Sticking to the OAM gourmet counterparts, the $|m| = 0, 1, 2$ and 3 cases correspond to lasagne, trofie (or fusilli bucati), eliche, and fusilli pasta, respectively., See Fig. 4.2 for further details.

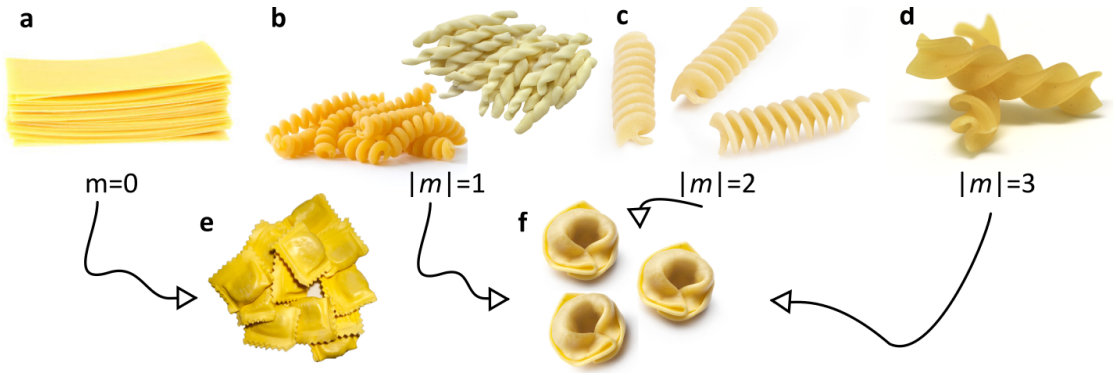

Figure 4.2 – Spiral pasta with variable topological charge m. *Phase distribution*: **a**: Lasagne sheets are topologically trivial, $m = 0$. **b**: Fusilli bucati (bottom) and trofie (top) are the same pasta in the topological sense ($|m| = 1$). **c**: Eliche have a double-helix structure, $|m| = 2$. **c**: The renowned fusilli have a triple-helix structure, $|m| = 3$.
Intensity distribution: **e**: For lasagne: ravioli. **f**: For topological pasta: tortellini. The central hole size should increase with the pasta vorticity.

to GHz waves, and recently also up to the extreme UV [351, 352], with synchrotron [353] and seeded-FEL radiation [354, 355], and to soft [356] and hard [357] X-rays. They have been extensively studied and employed within the context of classical and quantum communications [358–360], optical trapping [361, 362] quantum entanglement [363, 364], and nanostructured plasmonic devices [365]. Incidentally, their tight toroidal shape in the focus allowed for unprecedented superresolution fluorescence microscopy [31, 366]. This remarkable fact that the intensity distribution in the far field is determined and (~arbitrarily) controlled by the phase distribution of the beam has a broad spectrum of possible applications, which involves more in general Laguerre-Gaussian, high-order Bessel, and Mathieu beams. For example, it has been proposed that the tightly confined torus temperature profile imprinted by a vortex beam in a magnetic material could determine the nucleation of skyrmions and other magnetic topological defects [367, 368]. In that way, although not in a direct conversion process, the twist in the incident beam would determine a twist in the spin orientation.

Being vortices helical phase structures, their description does not apply solely to light beams, but readily extends to any matter wave whose phase can be controlled accurately enough. Any massive and massless quantum beam wave function can be in principle an eigenstate of the operator $\hat{L}_z$, hence carrying an OAM. This has been the case of beams of free electrons, for which an orbital momentum component has been measured [369, 370] on top of their intrinsic SAM ($\pm\hbar/2$).[4,5] Recently, vortices in electron waves have become increasingly present in modern science, especially in electron microscopy [372–375]. Combining the OAM of the vortex beam with the charge of the electrons results in an increased sensitivity to the magnetic

[4] Although electron sources in TEM are almost always unpolarized, see Sec. 1.1.2.

[5] While submitting this dissertation, an interesting report on neutron vortices has also been desposited in an online repository, ref. [371].

degrees of freedom. Notably, it allows to perform vortex-dependent magnetic dichroism experiments on the core ionization edges of magnetic atoms [370], down to atomic resolution for the visualization of antiferromagnetic lattices [376]. The contrast in this spectromicroscopy technique originates from the same selection rules of electron energy-loss magnetic chiral dichroism (EMCD) [377–380], which in turn gives the same information of the photon-based XMCD technique, but with much higher spatial resolution. The elastic scattering from local magnetic field curvatures can also give contrast for vortex beams, even for configurations in which an electron plane wave would result unaltered [381, 382]. Moreover, the use of vortex beams to enhance the spatial resolution in scanning EELS or EDX of thick specimens has been also proposed [383], together with low-loss dichroism in localized plasmon imaging [384, 385]. Altogether, it is interesting to note that chirality in matter can be probed by light via the spin degree of freedom, and by electrons via the orbital degree of freedom, but not vice versa [373]. As for their optical counterpart, electron beams that carry OAM can be produced by means of passive devices that directly modify their wave structure, such as spiral phase plates [369], along with amplitude [370] and phase holograms [386, 387]. With holographic masks, it has been proven that especially large OAM can be efficiently imparted to the electron wave functions ($200\hbar$ [388]). The electron's charge also allows obtaining a vortex by other methods, as with magnetic needles [389], programmable electrostatic displays [390], and tunable electrostatic phase devices [391]. In Fig. 4.3 we list some of the conceived methods to create OAM-carrying electron beams. Panel a portrays a spiral phase plate of order m. An electron with a sufficiently high transverse coherence acquires a phase ranging smoothly from 0 to $2\pi m$, due to the interaction with the atomic potential of the homogeneous material. The phase plate has fixed vorticity, and the vortex beam quality is typically limited by the smoothness and thickness precision of the fabricated plate. In Fig. 4.3b, a diffraction grating with a m_0-order edge dislocation is depicted. The diffracted orders carry a nonzero OAM. Despite the complexity in effectively collecting high diffraction orders, a dislocation of order m_0 creates $m = |m_0|$ vortices in the first diffraction orders, and $m = Nm_0$ in the N^{th} diffraction order,[6] hence mitigating the problem. In panel c, instead, a 'magnetic monopole' effective field configuration is created by a long, thin magnetic needle. By traversing the region around the monopole, an electron plane wave is transformed into an electron vortex of vorticity $m = \alpha_{\text{m}}$, where α_{m} is the magnetic flux strength, which should be finely tuned.

All the experimental implementations realized so far have been limited only to continuous wave vortex electron beams, restricting the range of possible applications mainly to the investigation of ground-state processes, whereas a huge amount of information resides in the exploration of the non-equilibrium dynamics. Static methods to impart a vortex phase distribution to the electron wave might of course be in principle used with pulsed electrons as well. The extremely high transverse beam coherence required for such methods to be effective, would terribly limit the throughput of the OAM-imprinting stage to a level that might be very challenging to measure experimentally. As a signature of fervid scientific discussions, it has

[6] $|N| = 0, 1, 3, 5\ldots$

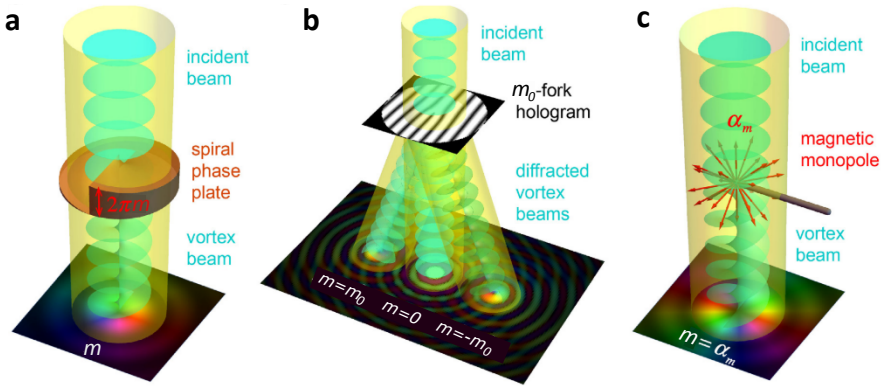

Figure 4.3 – Common methods to generate static electron vortex beams. **a**: A spiral phase plate. **b**: Diffraction grating with edge dislocations. **c**: Magnetic monopole field configuration. Image adapted from Bliokh *et al.*, ref. [373].

been recently proposed to transfer OAM from light beams to electron pulses via a Kapitza-Dirac interaction [392], or from plasmons via inelastic scattering [393]. Interestingly, nonzero photoelectrons' OAMs were discussed to be possible in the photoemission from materials with nontrivial Berry curvature of the spin wave function [394].

4.2 Photonic-based OAM transfer: ultrafast electron vortices

Here, we experimentally show that ultrafast vorticity can be imparted to charged particles by the interaction with strong local electromagnetic fields sustained by collective electronic modes. This is achieved by having ultrashort single-electron wavepackets interacting with an optically-excited femtosecond chiral plasmonic near field. This interaction induces an azimuthally varying phase shift on the electron's wave function, as mapped via ultrafast transmission electron microscopy. With respect to static approaches using passive phase masks, this method offers a higher degree of scalability to small length scales and a highly efficient dynamic phase control, inherited from the ability to manipulate the ultrafast plasmonic field. We demonstrate such level of phase manipulation using a sequence of two phase-locked light pulses to deftly control the properties of the vortex beam by delaying the pulses with attosecond precision. Our experimental results are described by means of a general theoretical framework that can be applied also to other charged particles, and thus potentially to other matter waves, such as proton beams. The ability to add OAM onto the latter could have fundamental implications on open questions in hadronic physics, where OAM-carrying protons could be used to address the origin of their spin (proton spin puzzle) [395].

4.2.1 Spin-to-orbital angular momentum conversion

Several recent studies have shown that a strong longitudinal phase modulation of the electron wave function can be achieved by the interaction with intense optical fields [141, 228, 253]. Given that OAM impartment relies on the modulation of an electron's transverse phase profile, a crucial aspect for the experimental realization is the ability to synthesize an optical field with a well-defined chirality that would extend over the transverse plane and be efficiently confined on the length scale defined by the electron coherence (on the order of $\lesssim 1$ μm for fs electron pulses). The usually adopted configurations are however not suitable for this task since the spin of the photon cannot be directly mapped into the OAM of the electron in a simple electron-photon interaction process, such as in inverse transition radiation. To fulfill these requirements the interaction needs to rely on the interruption of light propagation by a scattering object, or for example be mediated by a spatially-confined OAM-carrying optical field. This condition can be generated by the excitation of chiral SPPs [396–401], which relies on the SAM-to-OAM conversion in non-paraxial scattering and is a clear manifestation of the strong spin-orbit coupling of light when confined to subwavelength scales [396, 398]. When a circularly-polarized light beam encounters a properly designed nanoscale cavity, it is able to scatter into in-plane SPPs with a nonzero topological charge and helical phase distribution [396]. For a cylindrically-symmetric structure, the conservation of the total angular momentum quantum number restricts the plasmon OAM to be only $+\hbar$ or $-\hbar$ according to the helicity of the incident light plane-wave. Arbitrarily large values of plasmon OAM are instead possible by using incident light with high vorticity (e.g., Bessel beams), or clever nanostructuring [400].

We generate a chiral plasmonic field by illuminating a nanofabricated hole in an Ag-film deposited on a Si_3N_4 membrane (diameter ~ 0.8 μm) with circularly ($\sigma = \pm\hbar$ on average per photon) or elliptically ($0 < \sigma < \hbar$ on average per photon) polarized light carrying energy of $\hbar\omega = 1.57$ eV on average per photon, see Fig. 4.4a. The employed light field amplitudes were of approximately $8 - 10 \cdot 10^7$ V/m. Surface-plasmon polaritons (SPPs) are generated at the hole edge and radially propagate away within the Ag-Si_3N_4 interface with a phase distribution that can be directly mapped by means of the nonlocal holographic method described in Chap. 3, in which the electron wavepacket coherently interacts with both the semi-infinite and the polaritonic field. With such method, the position-dependent interference between the far-field reference and the plasmonic signal field gives rise to a spatially oscillating modulation of the electron wave function that can be imaged in real space, Fig. 4.4b. This interference mechanism allows us to directly access the phase distribution of the plasmon field itself. This is experimentally obtained by energy-filtered imaging, by selecting either the EEG signal only, or observing the depletion of the elastic signal. For both cases we refer as always as to inelastically-scattered maps, because the information comes from the absorption and emission of electromagnetic quanta. The holograms in this section are all acquired for normal light incidence, in order to avoid holographic Doppler effects (as in Fig. 3.18).
A typical EELS profile acquired in the region including and just surrounding the nanohole is

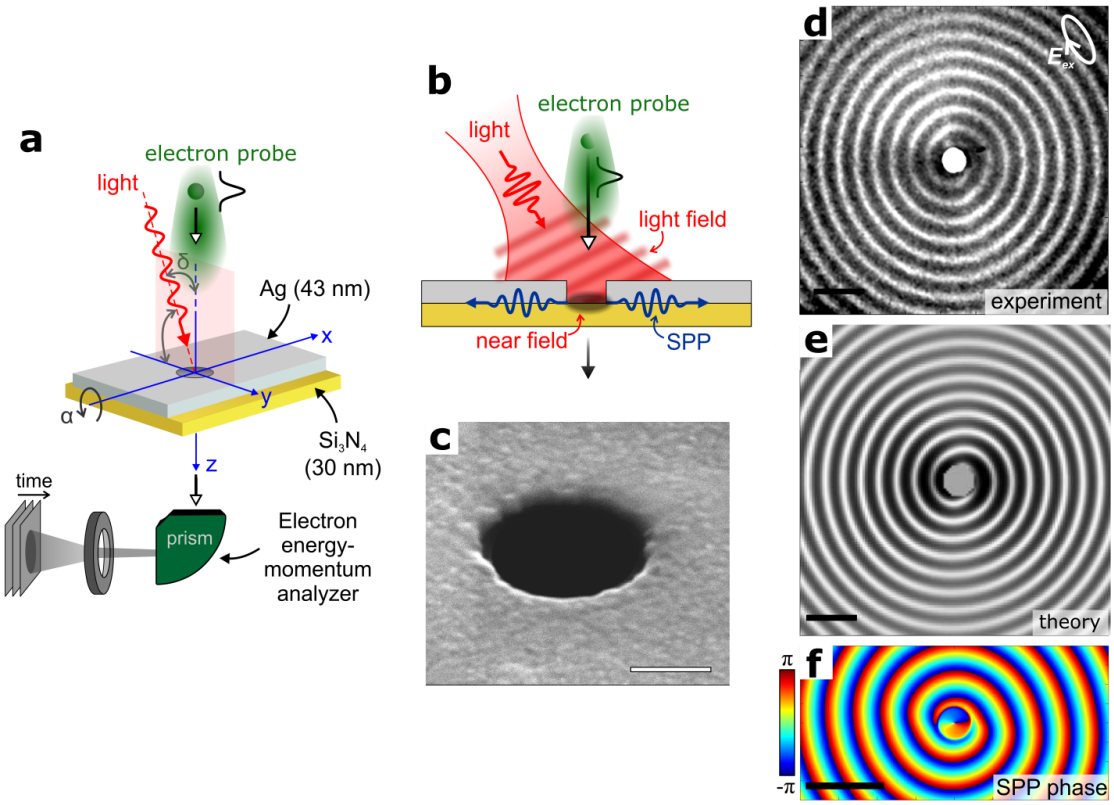

Figure 4.4 – Generation and detection of chiral SPPs. **a**: Experimental geometry and detection scheme. **b**: Holographic approach to image the propagating SPPs. **c**: SEM micrograph of the nanohole. **d**: Experimental holographic image, for $\alpha = \delta$ and elliptical light polarization. **e**: Corresponding calculated inelastic electron map with the same experimental parameter, using the semi-analytical theory developed in the text. **f**: Simulated phase map of $\mathscr{E}_z(x,y)$, from finite-difference-time-domain (FDTD) modeling. Scale bars are 2 μm in panels d-f, and 500 nm in panel c.

visible in Fig. 4.5. The spectrum is acquired with ≈ 1.1 eV ZLP, at $\alpha = \alpha_C$, to record only the contribution from the localized field. By the comparison with the EEL spectrum in absence of temporal coincidence between electrons and light, Fig. 4.5b, we also confirm that the near field excited by the electron probe itself is negligible, below our spectral sensitivity. From the background-to-ZLP ratio, we can estimate that the plasmonic field triggered by the swift electrons is at best < 1% of what excited by the highly-populated light pulses (> 10^{30} cm$^{-2}\cdot$s^{-1} instantaneous photon flux). The inelastically-scattered map measured for an elliptically polarized optical illumination when electron and light wavepackets are in temporal coincidence, is shown in Fig. 4.4d and displays the characteristic spiral phase pattern of a chiral SPP. This pattern is in agreement with the FDTD simulations shown in Fig. 4.4f, which take as input parameter the realistic experimental conditions (laser spotsize, elliptical polarization, etc.). There, the simulated phase profile of the electric field along the z-axis exhibits a spiral distribution that closely resembles the experimental image. Moreover, the simulations clearly show that the SPP field displays in the center of the hole a phase singularity of topological

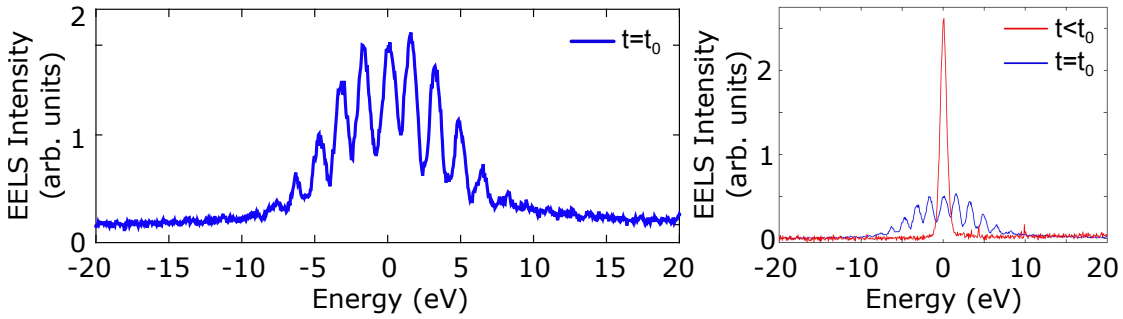

Figure 4.5 – **a**: Typical electron energy spectrum of the near field around the hole. $\alpha = \alpha_C$. **b**: The spectrum of panel a is plotted together with the spectrum in absence of temporal coincidence between light and electrons, $t < t_0$.

charge $m = 1$. This suggests that a 2π phase shift can be imprinted onto the electron's wave function by the interaction with such field, provided that the electron wave function coherently encloses the hole upon propagating through the device.
Further insights can be obtained through a semi-analytical theory. Upon propagation through the plasmon-supporting structure, the incident electron wave function $\psi_{\text{inc}}(R,\phi,z,t)$ gains inelastically scattered components:

$$\psi_\ell(R,\phi,z,t) = \psi_{\text{inc}}(R,\phi,z,t) J_\ell(2|\beta|) e^{i\ell \arg\{-\beta\} + i\ell\omega(z/v_0 - t)} \tag{4.1}$$

labelled by the integer ℓ, which corresponds to the number of plasmon-polaritons absorbed or emitted by a single electron, as seen in Chap. 2. Here, R and ϕ are the transverse cylindrical coordinates centered at the hole (radial distance and azimuthal angle, respectively), v_0 is the electron velocity, and J_ℓ is the ℓ^{th}-order Bessel function of the first kind. All of these scattered components are fully described in terms of the function $\beta(R,\phi)$, which captures the interaction of the electron with the light and SPP fields, and in this case can be written as:

$$\beta(R,\phi) \approx \theta(R - R_{\text{hole}}) \left\{ A + B\left[\cos\alpha_{\text{ph}} \cos\phi + \sin\alpha_{\text{ph}} e^{i\delta_{\text{ph}}} \sin\phi \frac{1}{\sqrt{k_{\text{SPP}} R}} \right] e^{i k_{\text{SPP}} R} \right\}. \tag{4.2}$$

The angles α_{ph} and δ_{ph} are the light beam polarization angles (azimuthal and polar, respectively), in the spherical coordinate system centered on the hole. k_{SPP} is the SPP wavevector, R_{hole} the hole radius, and the Heaviside function $\theta(R - R_{\text{hole}})$ is introduced because we aim at describing the interaction with the SPP in the film, not the localized near-field inside the hole, which we calculate via FDTD modeling. The light polarization, in general elliptical, reduces to linear when α_{ph} is a multiple of $\pi/2$, and in particular it lies in the plane defined by the electron and light linear momenta when $\alpha_{\text{ph}} = 0$. The coefficient A and B are independent on the position, are directly proportional to the incident field $\mathscr{E}_0$, and are obtained by integrating the field along the electron trajectory. The first term, A, represents the interaction of the electrons with the semi-infinite light field (reference), and depends on the light polarization angles as well, while the second term, B, accounts for the contribution of the SPP field radiated out of the circular NC. This last SPP contribution is divided by $\sqrt{R}$ to describe the propagation of the

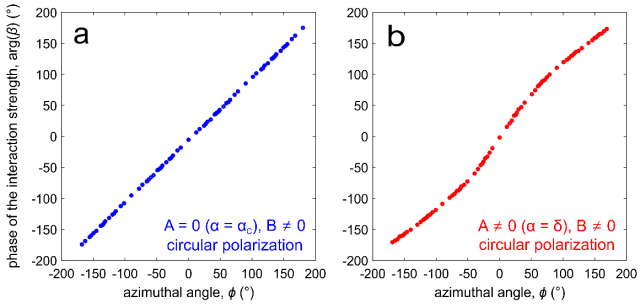

Figure 4.6 – Calculated phase of the interaction strength, $\arg\beta$, as a function of the azimuthal angle ϕ. **a**: For $A = 0$ ($\alpha = \alpha_C$, ideal mirror), $B \neq 0$. **b**: For $A \neq 0$ ($\alpha = \delta$, ideal mirror), $B \neq 0$.

'spherical' wave in two dimensions. To simplify Eq. 4.2, we can write $\beta \sim A + \tilde{B}\exp(ik_{SPP}R)$. Direct comparison between theory and experiment can be obtained for the real-space intensity distribution

$$I_{\text{inelastic}}(R,\phi) = \sum_{|\ell|=1}^{+\infty} \left|\psi_\ell\right|^2, \tag{4.3}$$

which nicely reproduces the experimental data. To quantitatively reproduce the experimental map, in Fig. 4.4e we took into account the large ZLP linewidth, and considered the depletion of that peak. A detailed discussion is presented in Sec. 4.3.1.

For any fixed $R > 0$, the inelastic electrons absorbing or emitting chiral plasmon-polaritons in the film pick a phase that varies of 2π as a function of the azimuthal angle ϕ. This can be appreciated also by plotting the phase of the interaction strength parameter β, $\arg\beta$ which enters in the free-electron wave function after the interaction, see Eq. 4.1. In Fig. 4.6 we show it for two cases. In panel a, $|\beta|$ is represented for a perfect mirror, circular polarization, and $\alpha = \alpha_C$, resulting in a vanishing contribution of the inverse transition radiation, $A = 0$. δ here is always $\sim 4.5°$. In panel b, the same quantity is represented for normal light incidence $\alpha = \delta$, hence $A \neq 0$, which corresponds to the case in which the holographic imaging is performed. We observe that $\arg\beta$ evolves nearly linearly with ϕ, that is $\arg\beta \propto \phi$. Since the electron wave function ψ_ℓ is proportional to $\exp\{i\ell\arg\{-\beta\}\} \propto \exp\{i\ell\phi\}$, then we can conclude that the plasmonic field at a given radius $R > 0$ acts as a phase plate of variable order $m\ell$, with $m = \pm 1$, and $\ell = 0, \pm 1, \pm 2 \ldots$. With reference to Fig. 4.4f, outside the hole the propagating plasmon shows obvious 2π phase rotations with the SPP wavelength in the radial direction. However, inside the hole the field is a homogeneous phase plate of order $|m| = 1$. This means that if an electron plane wave interacts with this plasmonic phase plate and one selects only the inelastic electrons in the ℓ^{th} photon order, one would get an electron OAM beam with vorticity of order ℓ.

This one-to-one correspondence between the complex optical field of the SPP and the transverse distribution of the electron wave function is further evidenced in Fig. 4.7 by comparing experiments and FDTD simulations for both circularly-polarized and linearly-polarized light

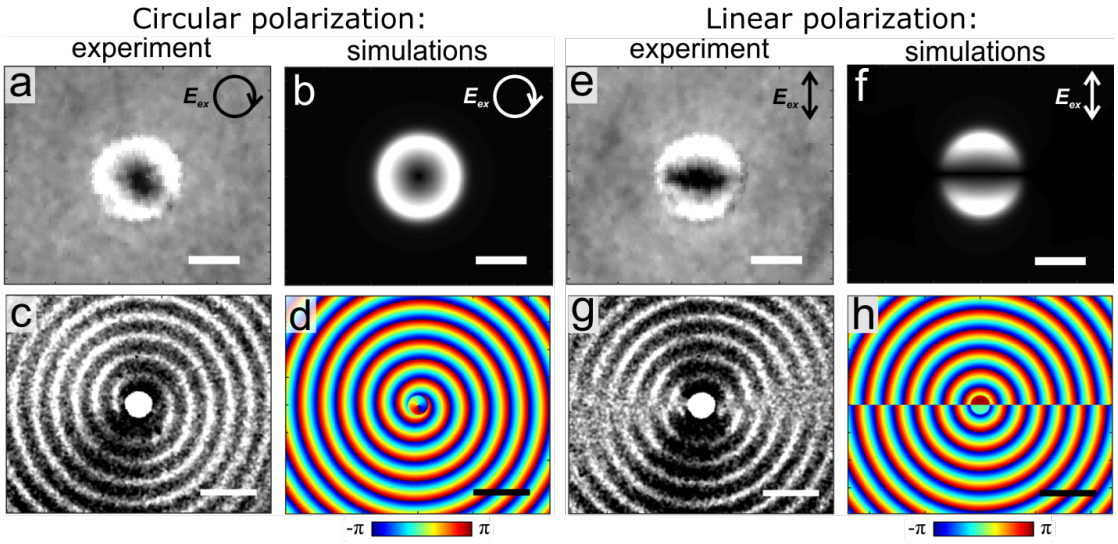

Figure 4.7 – Correspondence between the phase of the plasmonic field and the transverse distribution of the electron wave function. **a**,**e**: Experimental PINEM micrographs of the region around the hole, for circular (a) and linear (e) polarized light. **b**,**f**: Simulated spatial distribution of $|\beta|$ for the two polarization states. Scale bars in a, b, e, and f are 500 nm long. **c**,**g**: Experimental holographic micrographs of the region outside the hole, for circular (c) and linear (g) light polarization. **d**,**h**: Simulated spatial distribution of $\arg\beta$ in the $< xy >$ plane. Scale bars in c, d, g, and h are 2 μm long.

illumination. In Fig. 4.7a and e we show the experimentally-measured spatial distribution of the inelastically-scattered electrons inside the hole after subtraction of the corresponding energy-filtered map without laser excitation.[7] The resulting images, obtained for both polarization states, directly correlate with the simulated spatial distribution of the modulus of β reported in Fig. 4.7b and f. A zero-field region with cylindrical or mirror symmetry is visible inside the hole when circularly- or linearly-polarized light is used, respectively. For circular polarization, indeed, a chiral near field is generated inside the hole, and its intensity is radially symmetric and vanishes in the center of the hole, where the phase of the electric field is undefined. When the hole is excited by linear polarization, a dipolar field is created in the hole, and the intensity distribution features two lobes. The electric field in the two lobes oscillates in antiphase, meaning that a constant phase offset of π is present. The horizontal line perpendicular to the light polarization in the $< xy >$ plane is a nodal line, i.e. it has zero intensity.

The spatially oscillating pattern measured outside the hole for the two polarizations (Fig. 4.7c and g is a direct representation of the spatial distribution of the phase of β within the $< xy >$ plane, as visible in the FDTD simulations in Fig. 4.7d and h. Again, we observe that for circular polarization we have a spiral pattern, with a smooth rotation of the phase as a function of ϕ. For linear polarization both experimental and simulated maps give semicircular wavefronts dephased by π in the top and bottom part of the image. A nodal line bisects the maps along

[7] See also Sec. 4.3.1.

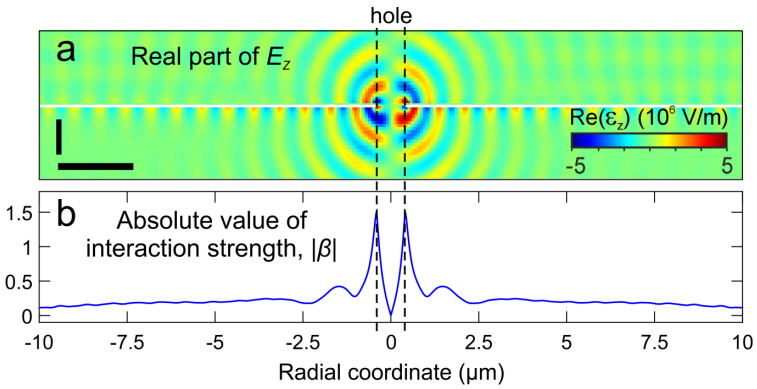

Figure 4.8 – **a**: FDTD simulation of $\mathrm{Re}\{\mathscr{E}_z(R,\phi_0,z)\}$, for circular polarization. Scale bars 2 μm horizontal, and 1 μm vertical. **b**: Profile $|\beta(R)|$, obtained by integrating panel a in Eq. 4.5.

the horizontal axis. A trained eye can see in Fig. 4.7g a tiny deviation from the pure dipolar picture, which is due to a remaining ellipticity of the light polarization, measured to be anyway $\lesssim 2\%$.

The simulated maps Fig. 4.7b and f are obtained by first solving with a commerical code, ref. [402], the Maxwell equations on a 3D mesh extending 45×45 μm^2 in the plane, and ±2 μm along the z axis. In Fig. 4.8a we report the real part of the electric field along z, as a function of the radial R and vertical z coordinate, $\mathrm{Re}\{\mathscr{E}_z(R,\phi_0,z)\}$, for circularly-polarized light excitation.[8] The electric field is maximum at the edge of the hole and decays away from it. Actually, the total field can be written in the following form, which highlights the dependence on ϕ solely through a phase factor, thus defining a vortex field:

$$\boldsymbol{\mathscr{E}}(R,\phi,z) = \left(\mathscr{E}_R(R,z)\hat{R} + \mathscr{E}_\phi(R,z)\hat{\phi} + \mathscr{E}_z(R,z)\hat{z}\right)e^{im\phi}, \tag{4.4}$$

with $m=\pm1$. The value of β can be directly estimated by utilizing its definition, Eq. 2.7:

$$\beta(R,\phi) = \frac{q_e}{\hbar\omega}\int_{-\infty}^{\infty}\mathscr{E}_z(R,\phi,z)e^{-i\omega z/v_0}, \tag{4.5}$$

and hence the $|\beta|$ maps Fig. 4.7b and f, and the $\arg\beta$ maps Fig. 4.7d and h. A profile of β plotted as a function of R is shown in Fig. 4.8b. The modulation of the electron wave function after the interaction is dominated by the coupling to the optical near field at the hole.

Because the population of the photon orders ℓ is strongly defined by the interaction strength β, the spatial distribution of the scattered electrons can be significantly modulated by the photon order ℓ. This can be seen in the space-energy maps shown in Fig. 4.9a and b for circular and linear polarizations, respectively. It is important to remind that these maps are integrated in one dimension, the horizontal in Fig. 4.7, over a distance of ≈ 1 μm, slightly larger than the hole, and therefore the spatial coordinate is integrated in R. Once recalled that the electrons away from the hole are blocked at ~ 90% in this specimen, if we name x and y the horizontal

[8] This result does not depend on the choice of ϕ_0.

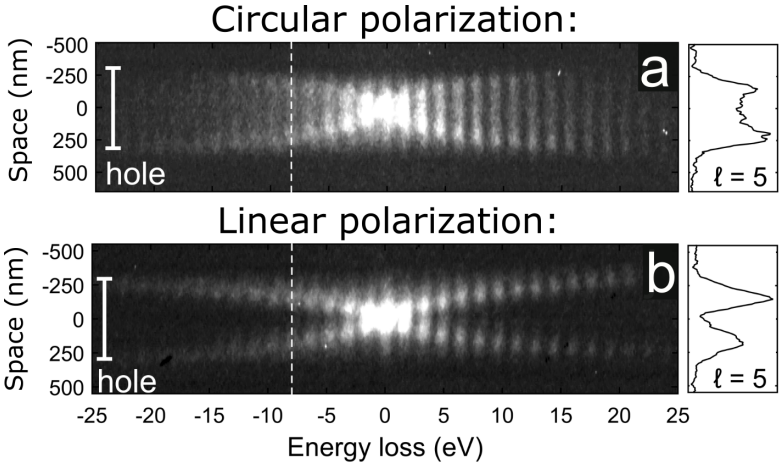

Figure 4.9 – Photon order distribution inside the hole. **a**,**b**: Bow-tie looking SREELS diagrams measured in the hole region for circular (a) and linear (b) polarization. On the sides, the spatial profile of the $+5^{\text{th}}$ photon order (dashed white line in the maps). The spatial dimension corresponds to the vertical direction y in Fig. 4.7, and the images are integrated in the other direction on a similar field of view.

and vertical axes in Fig. 4.7, the EELS in Fig. 4.9 is obtained as

$$\text{EELS}(y) = \int_{-X(y)}^{X(y)} \text{EELS}(x,y)\mathrm{d}x, \quad \text{where} \quad X(y) = \sqrt{R_{\text{hole}}^2 - y^2}. \tag{4.6}$$

This explains why the linear polarization case gives a neater picture.[9] We observe clearly that the low photon orders are confined around the center of the hole, while the high ℓs are backed against the hole edges. A thorough analysis can be found in Sec. 4.3.1, Fig. 4.21.

4.2.2 Transverse momentum maps of vortex beams

As noted before, the hole region for circular or partially-circular light polarization behaves as a vortex phase plate for electrons: for $0 < R < R_{\text{hole}}$ the phase of β does not depend on R, but just linearly on ϕ. This linear dependence translates into an overall phase factor $\exp\{\pm i\ell\phi\}$) in the wave function ψ_ℓ, which therefore carries an OAM of $\pm\ell\hbar$, as illustrated in the schematics of Fig. 4.10a. On a fundamental level, the transfer of the above phase profile relies on the impinging light field creating a chiral near field distribution with OAM of $\pm m\hbar$. In our case $|m|$ is equal to 1 due to the axial symmetry of the circular hole and to the $\pm\hbar$ units of the SAM carried by the circularly polarized Gaussian beam illuminating it. In a general case, the exchange of ℓ plasmons with the electron would thereafter result in a net transfer of $\ell m\hbar$ units of OAM. The use of non-axially-symmetric structures sustaining chiral SPPs with arbitrarily

[9] Yet, it does not present a truly 1D symmetry, since $|\beta|$ is distributed in a two half-moon shape, see Fig. 4.7e and f.

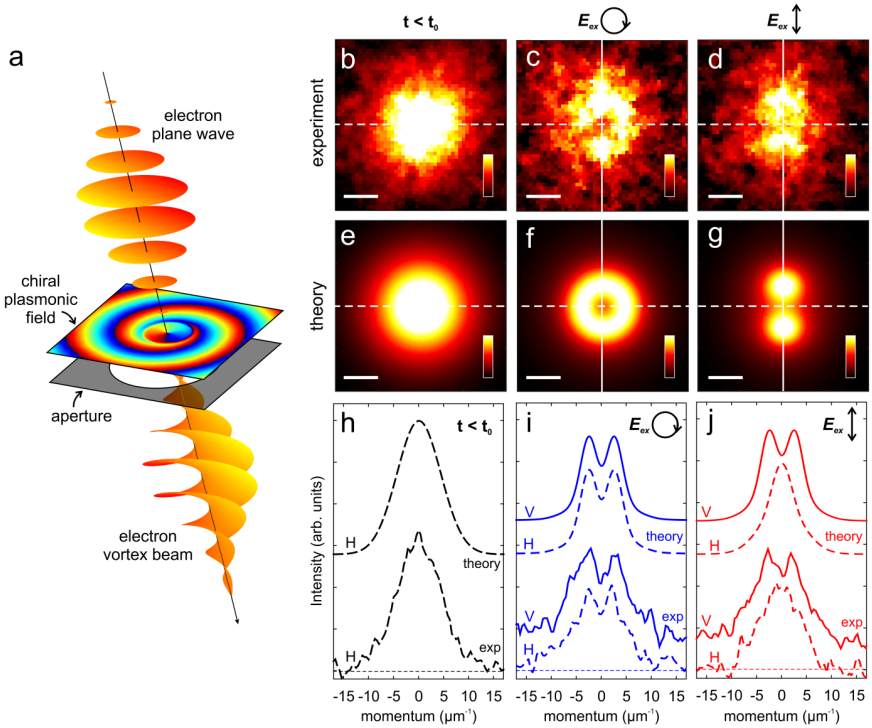

Figure 4.10 – Detection of the ultrafast electron vortex beam in momentum space. **a**: Conceptual sketch of the experiment. The transverse momentum distribution is visualized in HDD mode. **b**-**d**: Experimentally measured momentum patterns before the laser illumination (b), in presence of circularly-polarized light (c), and linearly-polarized light (d). **e**-**g**: Calculated distributions before the creation of the near field (e), and for circular (f) and linear (g) polarization. Scale bars are all 4 μm^{-1}. **h**-**j**: Vertical (V) and horizontal (H) profiles across the central part of the far-field images shown in panels b-d (experiments) and e-g (theory).

large values of m, such as spiral plasmonic lenses [396, 403, 404]), is considered a promising route to create high-OAM vortex electron beams. With our plasmonic phase plate, even if $|m| = 1$, the maximum exchanged OAM can still be high, since the highest occupied sideband order scales linearly with the electric field intensity. In practical cases, $|\ell|$ can be easily $10-20$. Because of the linearity of the interaction, our approach works at any value of the incident light intensity, and thus it is intrinsically robust with respect to the external parameters. Naturally, the efficiency of the process will be different according to the extent of the photoexcitation.

To further verify the OAM transfer, it is crucial to monitor the far-field intensity profile of the electron beam in the transversal-momentum space $< k_x k_y >$, and determine the changes produced by the of illumination of the nanohole. This is shown in Fig. 4.10c and i for a circularly polarized light beam in combination with a $\alpha = \alpha_C$ tilt to exclude the inverse transition radiation effect. Comparison between the reciprocal-space map measured under these conditions (Fig. 4.10c and i) and that acquired before optical illumination (Fig. 4.10b and e) reveals the characteristic destructive interference region at the electron beam center, which

attests the presence of a phase singularity in its transverse phase profile. We attribute the origin of this behavior to the chiral near field created at the hole, which dominates the coupling with the electron wavepacket and imprints on it a $2\pi\ell$ phase shift as inherited by the circularly-polarized optical illumination. To confirm that the reciprocal-space distribution of the electron beam is indeed determined by the phase profile of the optical field at the hole, we have performed additional experiments using a linearly-polarized light beam. This is shown in Fig. 4.10d and j, where a characteristic 2-lobed electron beam [405] is formed as a result of the uniform π phase shift generated across the hole, see Fig. 4.7e and f. Within this scenario, the momentum-resolved electron wave function $\psi_\ell(k_x,k_y)$ can be calculated as the Fourier transform of the real-space wave function $\psi_\ell(R,\phi)$:

$$\psi_\ell(k_x,k_y)=\int_{-\pi}^{\pi}\mathrm{d}\phi\int_0^{+\infty}R\mathrm{d}Re^{-i\boldsymbol{k}_\perp\cdot\boldsymbol{R}}\psi_\ell(R,\phi)\,, \tag{4.7}$$

where $\boldsymbol{k}_\perp=(k_x,k_y)$. Here, $\psi_\ell(R,\phi)$ is given by Eq. 4.1, where the incident wave function $\psi_{\mathrm{inc}}(R,\phi)$ has a lateral extension determined by the electron transverse coherence ($\sim 0.7-1$ μm), and the interaction strength β originated at the hole is extracted from FDTD simulations where the actual spatial distribution of the near field is considered, see Fig. 4.8b. The total Fourier-plane intensity is then obtained as:

$$I_F(k_x,k_y)=\sum_{\ell=-\infty}^{+\infty}\left|\psi_\ell(k_x,k_y)\right|^2, \tag{4.8}$$

that is, an incoherent sum of all the ℓ contributions. In the case $t<t_0$, a $\beta=0$ has been chosen to mimic the absence of optical illumination. The calculated maps, where a small momentum broadening is also included to take into account the experimental resolution, are shown in Fig. 4.10e-g and correctly reproduce the doughnut-shaped and the 2-lobed probability distribution observed in the experiment as induced by the chiral and dipolar transverse phase modulation, respectively.

Our experimental and theoretical results agree as well with standard electron vortex beam calculations. In that case, the effect of the chiral near field on the electron wave function is simulated by the interaction of a plane wave with a spatially-confined spiral phase plate of order ℓ, whose extension is determined by the hole diameter, see Fig. 4.11. The STEM CELL software tool [406] has been used for the simulations. The far-field amplitude of the momentum-resolved electron wave function $\psi_\ell(k_x,k_y)$ is the Fourier transform of the spiral phase plate, which is basically a top-hat function with a corkscrew phase factor $\exp\{\pm i\ell\phi\}$. The result is a hypergeometric Gaussian beam sampled in the far field. The total reciprocal-space intensity is obtained as $I(k_x,k_y)=\sum_{|\ell|=0}^{+\infty}w_\ell\left|\psi_\ell(k_x,k_y)\right|^2$, where the weights w_ℓ are extracted from the experimental spectrum Fig. 4.5a on the hole. We see, Fig. 4.11c and d that the assumption of the near field acting as a nanoscopic spiral phase plate of order ℓm, $|m|=1$ reproduces the experimental findings.

The experiments highlighted in Fig. 4.10 were performed in HDD mode on the retractable CCD detector before the GIF spectrometer. As a result, they were not filtered in energy. The figures shown are the sum of ~ 6 h acquisition at 1 MHz repetition rate, with 450 fs-long pulses,

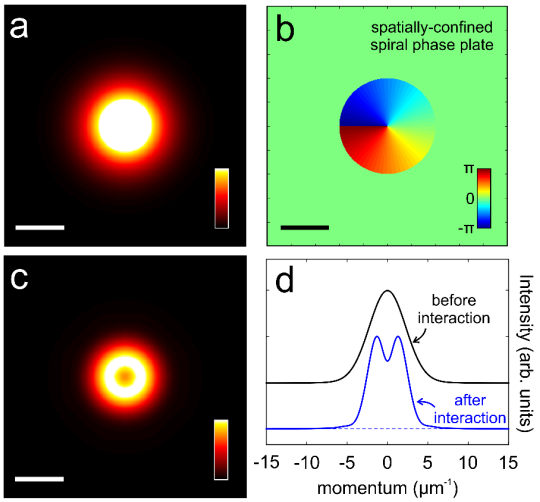

Figure 4.11 – Electron vortex beam calculations. **a**: Reciprocal-space intensity distribution of a plane wave. **b**: Spatially-confined phase singularity of order $\ell = 1$, with diameter $R_{\text{hole}} =$ 400 nm. **c**: Reciprocal-space intensity map for a beam passing through the phase singularity as in b. An incoherent sum over ℓ according to the spectrum Fig. 4.5a is done to obtain the final map. **d**: Line profiles across the central part of panels a and c. Scale bars are 4 μm^{-1} in a and c, and 400 nm in b.

and 3 mJ/cm^2 fluence. The single images are sequentially acquired before time-zero and in light-electron temporal coincidence for the two light polarizations. Long-term electron beam drifts in the TEM column are corrected by realigning the individual images before summing them together. A typical full-field HDD image is shown in Fig. 4.12. The alignment is carried out on the external ring, whose electrons are not in temporal coincidence with the near field (see Sec. 1.3.2), and therefore constitute an ideal reference –unaffected by photoinduced effects.

We observe that the far-field distribution has a visible dip in intensity, but such dip does not go to zero as in the ideal vortex case. This is caused to some extent by an experimental broadening (mainly due to the partial electron transverse coherence), but is chiefly due a remaining contribution of electrons not interacting with the plasmonic phase plate in the hole. We analyze here the various contributions to the experimental signal in the reciprocal-space plane.

In general, we can consider as OAM-carrying signal the detector counts coming from the electrons passing through the hole and populating a photon order $\ell \neq 0$, while electrons remaining with $\ell = 0$ are considered background, as well as all the electrons passing through the surrounding film and that reach the detector at $k \approx 0$. In order to minimize this last contribution, we placed a micrometer circular aperture just below the specimen plane (objective aperture). The aperture has a nominal ≈ 20 μm physical diameter, and we calibrated it to select a 15 ± 1 μm diameter from the specimen in HDD mode with 80 m camera length, therefore selecting an area $A_{\text{ap}} = 15^2\pi/4$ μm^2. This area is however still large compared to the hole area

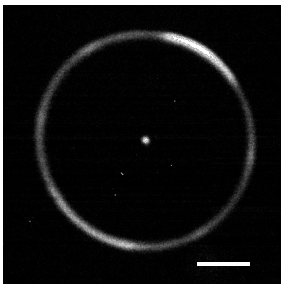

Figure 4.12 – Typical full-field HDD pattern. The images in Fig. 4.10 select only the central spot. The ring structure is (mostly) due to shank emission in the LaB_6 cathode. Scale bar $\approx 50\ \mu m^{-1}$.

$A_{hole} = 0.8^2\pi/4\ \mu m^2$. The thickness of the Ag layer for this specific experiment has also been increased to ~ 90 nm to assure a low transmissivity of the electrons, $T \approx 0.013$ in the HDD experimental conditions.[10] In fact, the real-space and reciprocal-space experiments reported here have been carried out with different Ag layer thicknesses, optimized to see through the film (real space) and through the hole (reciprocal space). The fraction of electrons that scatter inelastically in the hole is measured to be $\eta_0 \approx 0.9 \pm 0.05$, see Fig. 4.5a, and the probability for an electron crossing the thick region to absorb or emit an SPP is $\eta_1 \approx 0.58 \pm 0.1$.[11] By wrapping all together, we can estimate the 'dip'-to-background ratio to be

$$\frac{\eta_0 A_{hole}}{A_{hole} + T(1-\eta_1)(A_{ap} - A_{hole})}, \tag{4.9}$$

with all the parameters directly extracted from the experiments. In Eq. 4.9, the $(1-\eta_1)$ term in the denominator has been added to discount the background from the electrons scattered at higher angles by absorbing or emitting SPPs. Indeed, the electrons that change their energy of $\ell\hbar\omega_{SPP} = \ell\hbar\omega_{ph}$ by interacting with the propagating SPP, also acquire a transverse momentum $\ell\hbar k_{SPP}\cos\alpha_C$, in our geometry. One expects those electrons to dispose in an annular structure ($|\ell| = 1, 2\ldots$) at high angles. In our apparatus, at 80 m camera length, they distribute over such a large detector area that the density current they produce is overshadowed by the dark noise of the detector. For our purpose here, since $k_{SPP}\cos\alpha_C \approx k_{SPP} \approx 9\ \mu m^{-1}$, and the electron direct beam is $\approx 5\ \mu m^{-1}$ half width at half maximum (HWHM) wide (see Fig. 4.10h),[12] their contribution is negligible to the peak at $k \approx 0$, where we observe the intensity dip. By inserting the values of the experimental parameters in Eq. 4.9, one gets a dip that is $= 0.33 \pm 0.12$ of the total beam height, which is compatible with both our measurement and calculations in Fig. 4.10.

[10] Measured for our 90 nm-thick polycrystalline Ag film on 50 nm-thick amorphous Si_3N_4. While the bright-field transmissivity is 0.028, in HDD mode also most of the low-angle scattered electrons are filtered away. This contribution is particularly relevant for polycrystalline and amorphous materials, like our specimen.

[11] Measured as the mean value for $2 < R[\mu m] < 5$, which should represent a good estimate of the average between R_{hole} and 7.5 μm, the aperture radius.

[12] The momentum space was calibrated in the very same experimental conditions by using an optical replica specimen with 463 nm periodicity. The momenta are here always calculated as 2π/distance.

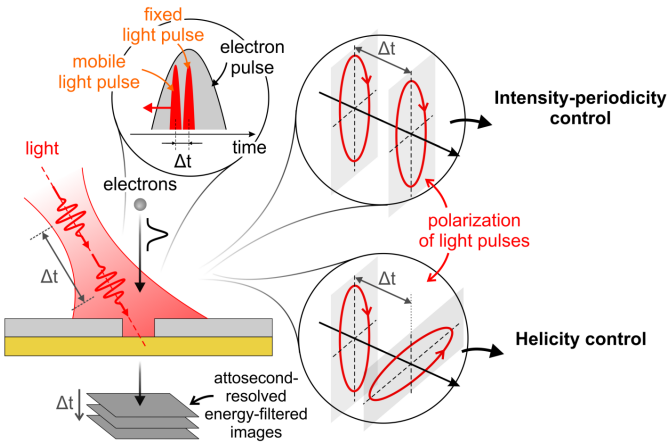

Figure 4.13 – Experiment schematics for the coherent control on intensity and wavelength (Fig. 4.14), and handedness (Fig. 4.16 and Fig. 4.17).

4.2.3 All-optical chirality flipping

An extremely interesting feature of our approach is the ability to dynamically control the vortex beam properties. This is possible thanks to the high degree of tunability of the optical field, which allows to coherently modulate the longitudinal and transverse phase profile of the electron wave function. This is achieved by manipulating the phase distribution of the plasmonic near field with attosecond precision using a sequence of two phase-locked 55 fs light pulses with a relative delay Δt between them varied in steps of 333 as.

We report here two experiments, illustrated schematically in Fig. 4.13. In the first we control the presence or absence of the plasmonic field, while in the second we control the sign of the topological charge associated with the vortex. Both effects result from the ability to finely tune the relative phase of the two optically-excited plasmons with the three-pulse scheme. In the first implemented configuration, we have used two elliptically-polarized light pulses with parallel major axes. The initial delay was set to $\Delta t^{\star} = 85$ fs, longer than their intensity autocorrelation, in order to minimize the optical interference between the two pulses, which remained below a $5 \cdot 10^{-2}$ level. When varying the delay time between the two optical pulses, the observed time-dependent evolution of the plasmonic pattern is a sequence of constructive and destructive interference between the optically-generated plasmons propagating at the Ag-Si_3N_4 interface, Fig. 4.14-c. The result is a coherent modulation of the intensity and of the spatial periodicity of the plasmonic fringes with a temporal period given by the optical cycle of 2.67 fs (see Fig. 4.14d and e and ref. [341] for the full movie). This effect, which cannot be related to a simple time-domain optical interference within the incident light field, see also Sec. 2.2.4, can be understood as the coherent interaction between two spatially- and temporally-localized plasmon wavepackets. In other words, plasmon-plasmon interference. We note that the periodicity of the observed SPP wavelength λ_{SPP} –which we measure by fitting

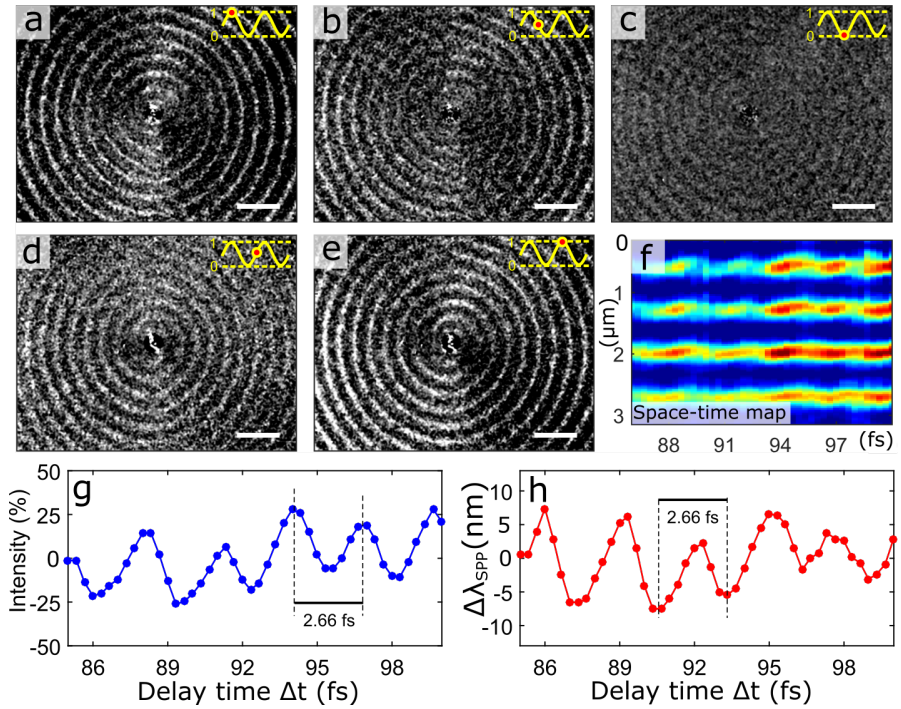

Figure 4.14 – Interferometric control over SPP intensity and wavelength, with two optically-separated pulses. **a**-**e**: Holographic SPP patterns for different delays with 333 as step. The two chiral SPPs constructively and destructively interfere in the film. The images have a background subtraction equal for all of them, in order to make easier to see their differences by eye. Scale bars 2 μm, $\alpha = \delta$. **f**: Space-time map, along the horizontal direction. **g**: Relative variation of the plasmonic intensity, from Fourier analysis. **h** Change in the measured wavelength $\Delta\lambda_{\mathrm{SPP}}$.

the corresponding peak of the spatial Fourier transform of the micrograph– varies within a bandwidth of ≈ 15 nm, i.e. approximately 2% of the central wavelength $\lambda^0_{\mathrm{SPP}} \approx 700$ nm. This corresponds as well to the bandwidth of the photoexciting light pulses (18 nm, i.e. ≈ 2% of bandwidth).

The analytical theory can describe well these three-pulse experiments, similarly to what done in Sec. 2.2.4, just by inserting the proper field distribution in time inside the formula for β. The oscillations are also reproduced (here not shown). This apparent breathing of the SPP mode can be understood intuitively on the basis of spectral interference. Even when identical wave packets are separated enough along the temporal coordinate to generate negligible time-domain interference, still they interfere in the frequency domain, the total spectrum being modulated by the (low) frequency $1/T$, where T is the temporal separation between the two pulses ($T = \Delta_2 - \Delta_1$ in our case). This phenomenon, which is at the basis of frequency combs [407], causes a spectral modulation, as illustrated in Fig. 4.15a. For two phase-locked Gaussian pulses, the two-pulse spectrum has been calculated via Fourier-transform analysis for the same delays as in the experiment. The spectrum for $\Delta_2 - \Delta_1 = 0$ has been added as a reference; the other delays are selected to represent a full optical cycle, sampled with $\pi/2$ phase

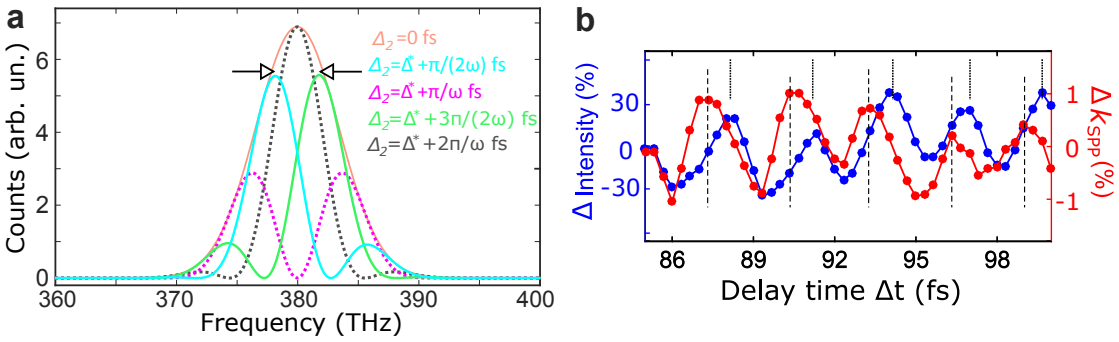

Figure 4.15 – Spectral interference as a possible physical mechanism for plasmon wavelength modulation. **a**: Calculated two-pulse spectra for an increasing pulse separation. One pulse is kept at $\Delta_1 = 0$, and the second delayed to $\Delta_2 = \Delta^\star \approx 90$ fs. From that value, it is further delayed in fractions of the optical carrier cycle. The orange curve is added as spectral reference, and corresponds to the single pulse scenario ($\Delta_2 = \Delta_1 = 0$), and the two black arrows mark the 1% of the central frequency. **b**: Intensity (blue, left axis) and wavenumber (red, right axis) variations as a function of the separation between the two optical pulses, from Fig. 4.14. Dashed lines are guides to the eye, identifying the maxima of the periodic modulations, which are orthogonal ($\pi/2$ phase shift).

steps. One can observe that the spectral intensity follows cosine-like oscillatory changes, while the spectral asymmetry has a sine-like behavior, i.e. it is phase offset by $\pi/2$. This argument suggests that the coherent modulations in intensity and fringe periodicity ought to be shifted by a $\pi/2$ phase. Fig. 4.15b confirms this suggestion, within the experimental resolution of the analysis.

In a second configuration, the elliptical polarization of the two light pulses is arranged such that their major axes are perpendicular to each other. The two pulses are here forced to interfere optically ($\Delta t \approx 0$): in this way, we effectively have a dynamic handle on the helicity of the phase singularity created at the center of the nanofabricated hole. Few frames are shown in Fig. 4.16a-c, while the full movie can be found in ref. [341]. The handedness of the spiral plasmonic phase distribution is observed to switch from clockwise to counter-clockwise within each optical cycle when varying Δt. The observed periodic modulation of the helicity of the plasmonic pattern is reported in Fig. 4.16f, and portrays the ability to control with high precision the sign of the topological charge of the electron vortex beam created by electron-plasmon interaction just by changing of an attosecond delay one of the two pulses. The analytical model can also well describe this phenomenon, as one can appreciate from Fig. 4.17, where the handedness of the spiral switches from counter-clockwise (panel b) to clockwise (panel f) within half of the optical cycle, ~ 1.33 fs. At a quarter optical cycle, Fig. 4.17d, the light has an overall linear polarization, and the plasmonic field arranges accordingly, with two lobes.

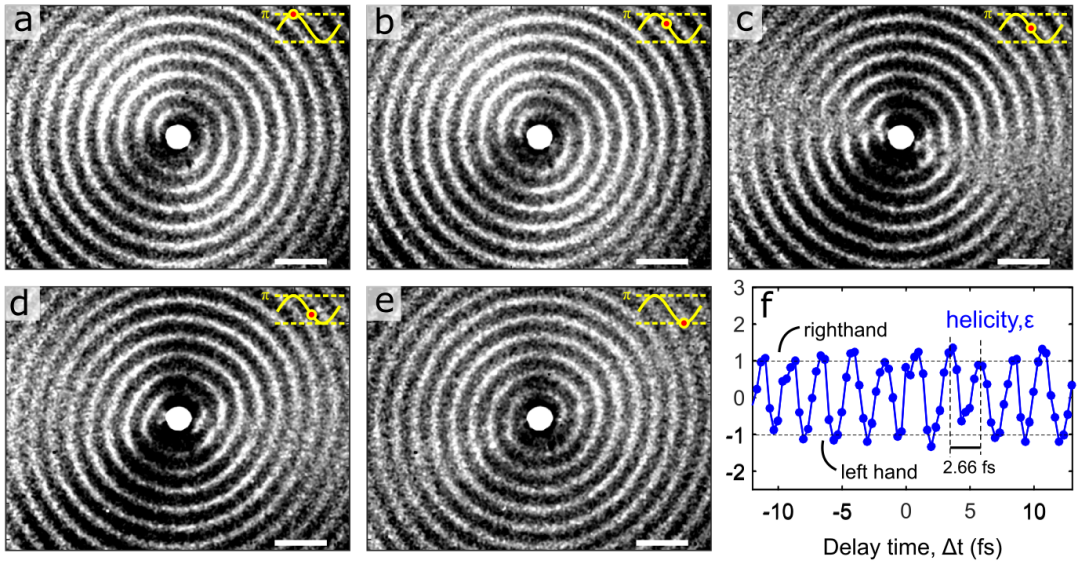

Figure 4.16 – All-optical control over the plasmon handedness: experimental. **a**-**e**: Holographic micrographs for different delays with 333 as step. Scale bars 2 μm, initial separation $\Delta t^{\star} = 12$ fs. **f**: Analysis of the helicity modulation as a function of the optical phase delay between the two elliptically-polarized light pulses.

4.2.4 Conclusions on charged particle vortices

With respect to commonly adopted methods using passive phase masks to produce electron vortex beams, our approach is intrinsically scalable to smaller length scales in the subwavelength regime. For example, for our excitation parameters, FDTD simulations suggest that a 200 nm diameter hole would have been preferable to the 800 nm hole employed here. By selecting proper materials and shorter excitation wavelengths, the optimal hole size can be made even smaller. This may be of paramount importance in situations where only a partial transverse coherence of the beam can be achieved (such as in the case of ultrashort electron pulses). This is even more crucial when our laser-based method for transferring OAM is extended to pulsed beams of heavier elementary and composite charged particles, as ions, where the constraint on the lateral coherence becomes stricter and limited to less than few tens of nanometers. In particular, OAM impartment in composite particles could be of interest for analyzing their internal structure [408].

In ref. [141] we propose that our photonic approach to transfer OAM to charged particles by means of inelastic interaction could be considered as a candidate method to create proton vortex beams. By shaping the proton wave function in a manner similar to that demonstrated here for electrons, the proton can acquire OAM-dependent density functions that will reflect its internal properties on the transverse spatial distribution. Recently, increasing efforts have been devoted to gaining an understanding of the proton spin in terms of its constituent particles [395], which is considered to remain one of the most important unanswered problems in hadronic physics. Concisely, the *proton spin puzzle*, or *crisis*, deals with the experimental

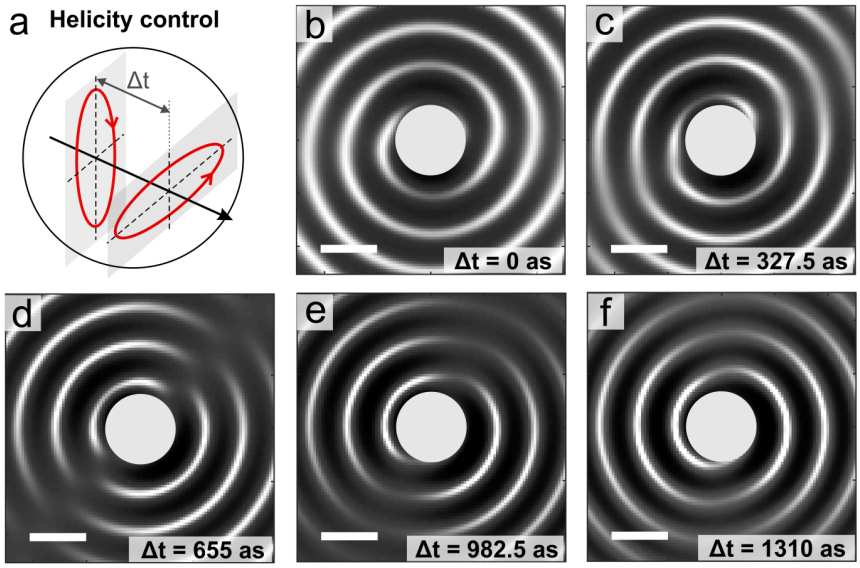

Figure 4.17 – Calculated all-optical control of the spiral handedness, hence topological charge of the free-electron wave function. **a**: Sketch of the experiment. **b**-**f**: Calculated inelastic maps for different values of Δt within half an optical cycle. The initial $\Delta t^{\star}$ is set to 0, scale bar 1 µm.

observation [409] that the spin of the proton ($\pm\hbar/2$) is only partially constituted by the sum of its three quark spins ($\pm\hbar/2$ each). The observation implied that a considerable orbital contribution should come from the partons (quarks and gluons) spinning inside the proton. Common experiments investigating the proton spin use energetic linearly-spin polarized muon beams hitting dense spin-polarized targets [410]. The perspective of adding OAM to the proton, in conjunction with relativistic spin-orbit effects in matter waves, could be of potential use to these studies [372, 411]. A possible study one could envisage involves measurements of the magnetic dipole moment for OAM-carrying protons. As detailed in ref. [341], the magnetic moment of a proton with OAM of order ℓ can deviate from the $\ell\mu_{\mathrm{N}}$ value typical of a point-like

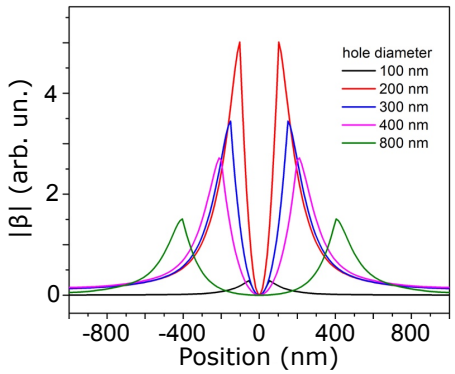

Figure 4.18 – Simulations of $|\beta|$ as a function of the hole diameter for illumination at 1.57 eV as in the experiments, with 40 nm Ag-layer thickness.

particle with nuclear magneton μ_N in presence of a strong overlap between the transverse component of the proton wave function and the spinning partons. Several schemes could be used to measure such a quantity, including a Stern-Gerlach-like approach [412] or devices that couple the OAM of a charged particle with its spin [413, 414]. The latter would be extremely valuable for probing the proton internal spin dynamics by means of OAM impartment, which could give insights into the role played by the OAM of its inner constituents in the determination of its total spin.

4.3 Further considerations on PINEM imaging

4.3.1 Comments about imaging near fields

In Chap. 3 and Chap. 4 I mentioned that the majority of the PINEM images were not acquired with the EEG counts only, but rather measuring the depletion of the ZLP. The motivation is plainly technical: it allows in many practical situations to collect a larger signal per unit of time, overcoming the CCD dark noise (see Sec. 1.5).
In fact, if a narrow ($\lesssim$ 1.1 eV) ZLP is employed, the average beam current has to be kept very low (~single- or few-electron(s) regime), and the EEG is even lower, especially if we consider that in order to discard the ZLP tails, the energy cutoff has to be placed at $\gtrsim$ 2 eV, de facto rejecting the $\ell = 1$ photon order, usually the most intense. This is the sole configuration that allows for the shortest electron pulses. However, in most cases having the shortest electron pulses is not required, either because only the 'static' field configuration[13] has to be imaged, or because the high temporal resolution is realized by the effective 'gating' in three-pulse experiments. EEG imaging –on the other side– can be performed also with a broader ZLP peak, for which electron chirp effects become more relevant, and pulses longer. In such a scenario, the EEG cutoff energy has to be increased, to reject the higher ZLP tails; nonetheless, its SNR outperforms that of the narrow-ZLP case. When the electron energy distribution is made larger than ~ 5 eV, the electron spectrum develops a structure with two horns. In that case, the temporal PINEM cross-correlation (i.e how the electron spectrum evolves as a function of the pump-probe delay), shows a ~linearly chirped depletion of the ~ 7 eV-broad ZLP; the light pulse is kept short (~ 55 fs), while the electron pulse envelope is ~ 600 fs. The depletion of the ZLP follows the electron chirp, and is symmetric only at t_0, where the photon pulse overlaps in time with the center of the electron pulse.
If we select in EFTEM a $\sim 4-5$ eV window at the center of a $\sim 6-8$ eV ZLP, at t_0, we can record images with two advantages:[14]

- A large, robust signal,

[13] Here 'static' is often < 1 ps, depending on the temporal duration of the pump excitation field.

[14] The term 'Anti-PINEM' has been coined by G. M. Vanacore and I. Madan after developing this EFTEM variant as a reaction to the frustration arosen by the poorness of EEG imaging for the low-contrast system they were studying. They expressed the desire to have the name 'Anti-PINEM' mentioned in this dissertation: here it is.

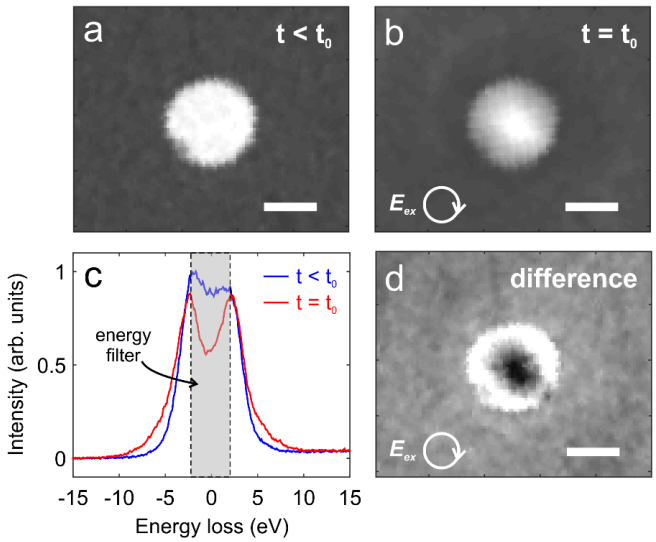

Figure 4.19 – Experimental procedure for ZLP-depletion PINEM imaging, utilized in Fig. 4.7a. **a**,**b**: EFTEM micrographs acquired before (a) and in coincidence (b) to the photon pulse. **c**: Electron spectra relative to a (clue curve) and b (red curve). The shaded area represents the energy window selected in EFTEM mode. **d**. The difference a – b gives the map of the near field intensity, Fig. 4.7a. $\alpha = \delta$, $\vartheta = 0°$; scale bars are 500 nm long.

- The simultaneous visualization of the structural contrast.

The robustness is meant here with respect to small beam shifts in the spectrometer and to the long-term photoemission efficiency drop for long-acquisition measurements. The increase of counts compared to a ~ 1.1 eV ZLP is here of a factor ~ 100 – 300. Besides that, one should add an extra factor 2 in the signal improvement, which accounts for the gain and loss sideband contribution. The visualization of the structural contrast is useful for a precise signal interpretation and for successfully running image re-alignment algorithms that could compensate drifts of the electron beam in the TEM column in long-acquisition measurements. One can visualize the background-free plasmonic field by simply subtracting the PINEM micrograph at t_0 to the micrograph at $t < t_0$, i.e. the bright field image of the specimen. For instance, we used this method for the visualization of the near field around the nanohole in Fig. 4.7a and e. We summarize it in Fig. 4.19, for the circular polarization case.

Several PINEM micrographs with different acquisition parameters are gathered in Fig. 4.20. The system imaged includes a VO_2 NW sticking in part on a Si_3N_4 membrane, and protruding with one end in vacuum. The Si edge of the TEM grid is visible on the left. A strong near field is photoexcited at the surface of the thick NW, as well as at the Si_3N_4 and Si edges. No propagating SPP is here present, since the excitation energy is above the plasmon frequency, see the radiative plasmon-polariton branch in Fig. 3.1. In Fig. 4.20a almost no contrast is visible because the EFTEM window is placed half on the ZLP and half outside, so that the PINEM contrast almost perfectly cancels out.[15] Fig. 4.20c corresponds to the background-free

[15] A feeble shadow tue to ZLP depletion can be seen around the NW, though.

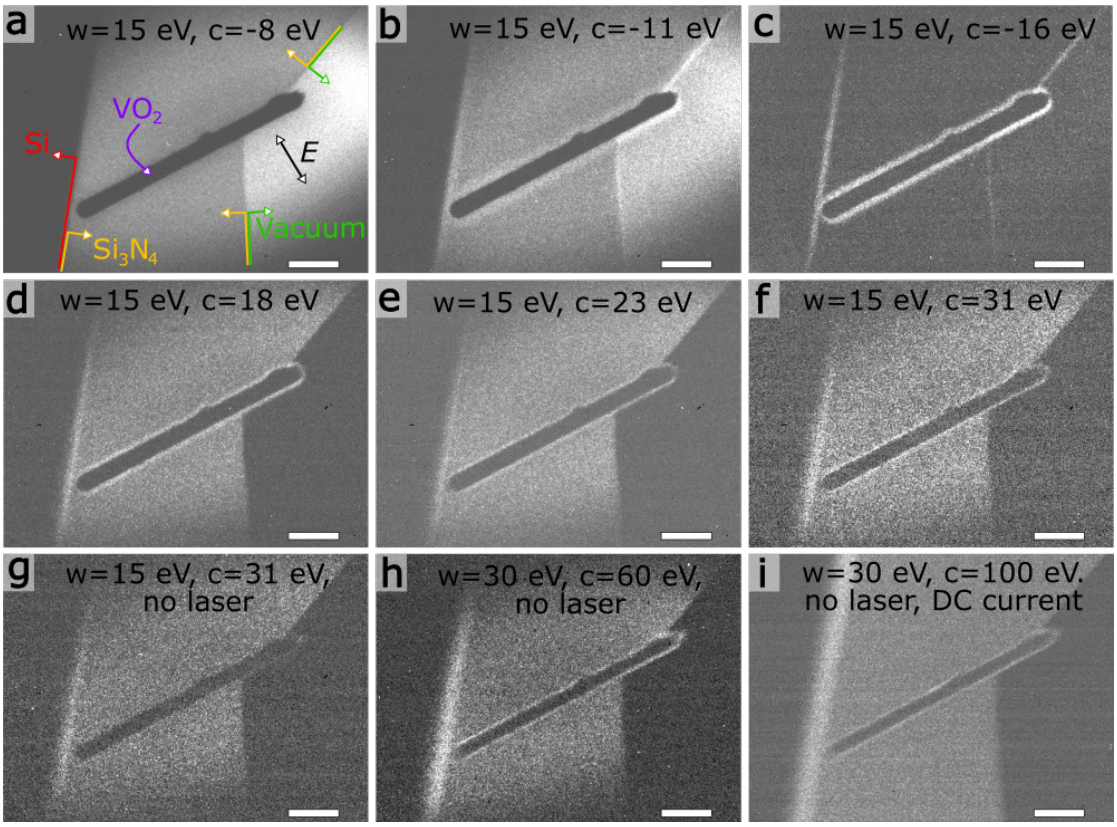

Figure 4.20 – PINEM imaging for different parameters. The system comprises a VO_2 NW at room temperature lying partially on a Si_3N_4 membrane, and partially jutting out in vacuum. The edge of the Si substrate is as well visible in the field of view. Light polarization is along the short NW axis, $\hbar\omega = 1.57$ eV, and fluence ≈ 0.8 mJ/cm^2. The ZLP is set to 8.5 eV FWHM, w indicates the EFTEM slit width, in eV, c the center position of such slit. **a**-**f**: Micrographs for the parameters shown in each panel. **g**: Same parameters as f, but without laser excitation. **h**: Same as g, for different w and c parameters. **i**: Micrograph acquired with the DC stream of thermionic electrons. Scale bars 2 µm. The elliptical shape of the electron beam in panels a-h was obtained by tuning the condenser stigmators.

PINEM, with EEG counts only, while panel b is an intermediate situation, where the contrast gives a $\approx 35\%$ larger decay length than panel c. Fig. 4.20d-f are acquired selecting the loss-side of the spectrum. The vacuum and Si_3N_4 regions are promptly distinguishable. By displacing the EFTEM window far away from the ZLP, a strongly localized contrast is obtained. In the loss side, the nearly-monochromatic laser-stimulated effect coexists with the broadband spontaneous plasmon emission effect. Indeed, Fig. 4.20f is a sum of both contributions, which can be disentangled by acquiring a micrograph in absence of light excitation, which is the same for photoelectron and thermionic sources (Fig. 4.20g-i).

The example of the nanohole as used for the electron vortex generation exemplifies also well some limits of PINEM imaging as it has been carried out so far. The choice of selecting the EEG or the depletion of the ZLP or any other large energy window is somehow arbitrary. Multilevel

Rabi oscillations, as visible for example in Fig. 2.4, make the spectrum greatly depending on the real space position, in a nontrivial way. Because of such oscillations, the occupation of the different photon orders is non-monotonic as a function of the field intensity; so, not only the obtained intensity profiles cannot be directly considered to quantitatively reproduce the field intensity profile, but –rigorously– not even the qualitative agreement is in general always assured. This remark is valid also for conventional (EEG only) PINEM, as illustrated in Fig. 2.12d for the ideal mirror case. In practical terms, what happens often is an effective 'saturation' of the inelastic signal, as for example in Fig. 2.12b, which causes a severe compression of the inelastic signal dynamic range. Above the 'saturation' threshold, the PINEM contrast is roughly the same whatever the field intensity. For this reason, the evaluation of the PINEM intensity profiles in real space should be performed with caution. For instance, the direct extraction of the spatial decay length of a plasmonic field around a nanostructure from PINEM EEG data would be prone to overestimate the true decay length. Similarly, the intensity profile of the spiral SPP wavefronts in Fig. 4.16 are not expected to be sinusoidal. This is especially visible when the contrast periodicity increases due to holographic Doppler (see Sec. 3.2.3, and specifically Fig. 3.18e-g, remembering that what is plotted there is the ZLP-depletion contrast). It should be said that oftentimes the interest resides in the presence or absence of certain features, in the symmetry of the fields [142, 341], in their evolution [143, 213], or in their periodicity [143, 340]. However, it has some value to investigate if a quantitative measure of the field in PINEM is possible beyond the weak-field limit.[16]

A route to overcome this issue is by systematically comparing experimental results and theoretical predictions. Once the best agreement is found, one can extract from the calculations the distribution of $\left|\beta(x,y)\right|$, hence the field intensity map. Still, this method may lead to some level of uncertainty for complex geometries, where the 3D simulation of the fields is demanding. Another possibility, adopted by A. Feist *et al.* [222], consists in having a small probe ($\lesssim 10-20$ nm) in STEM mode and record a spectrum at each point of the scan in $< xy >$. The correspondence between spectrum and $\left|\beta\right|$ is known, see Fig. 2.3c, and therefore the intensity map is retrieved.

When the specimen geometry allows it, the SREELS maps can give analogue information. In Fig. 4.9b we appreciate a sizable variation of sideband population as a function of the spatial coordinate, despite the effect is partly hindered by the average in Eq. 4.6. Although with a spatial resolution not allowing to observe Rabi oscillations, it reproduces in a single snapshot the envelope of the spectral evolution as a function of the near field, likewise in Fig. 2.8b we did for inverse transition radiation. Fig. 4.21a shows few selected loss spectra for different values of the spatial coordinate y, evidencing the high-ℓ population for $y \approx R_{\text{hole}}$.

The spatial intensity profiles inside the hole for linear polarization, extracted always from the space-energy bow-tie maps (see Fig. 4.9b), are plotted in Fig. 4.21b, highlighting also a large dependence on the selected photon orders. In Fig. 4.22 the analogue of Fig. 4.21b for

[16] Namely, when only $|\ell| \lesssim 2-3$ photon orders are populated, for coupling strengths lower than the first zero of $\mathscr{P}_0$. In this perturbative limit, PINEM competes with spontaneous emission, and gain/loss asymmetries may become visible [75]. It is a promising research line; since it does not require a high photon flux, it could make use of ns pump-probe pulses, with the probe pulses either pulsed or chopped in post selection, as proposed in Sec. 1.5.1.

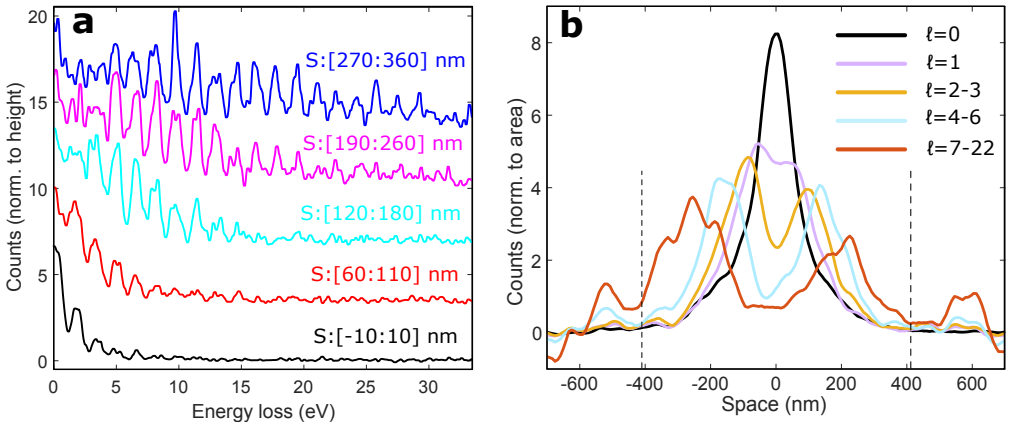

Figure 4.21 – Dependence of the spectral modulations inside the nanohole, from SREELS space-energy mapping for linear polarization (see Fig. 4.9b). **a**: Representative EEL profiles averaged over different ranges S along the spatial coordinate y orthogonal to the light in-plane polarization vector. They are all integrated in the other spatial direction, x. **b**: Representative energy-filtered spatial profiles across the hole for different energy windows. The spatial coordinate is y, and the spectral density is integrated along x. The dashed vertical lines mark approximately the hole region.

the large ZLP case (≈ 9.5 eV) is shown, together with the bow-tie space-energy map. Selected spatial profiles for variable energy windows are displayed, together with the ZLP-depletion signal (pink curve), which is obtained as the profile of a 6 eV-large window subtracted to the profile for the whole spectrum (black dashed curve). As we see, the ZLP-depletion PINEM profile is significantly smoothed out. Apart from the contribution discussed above, when the ZLP is larger than the photon energy, the measured counts in the selected energy window (say, ~ 4 eV) are a combination of the depleted $\ell = 0$ order in the center of the ZLP and the populated $|\ell| = 1$ and 2 orders of the tails. Albeit the depletion effect is stronger, it is tempered by the second phenomenon, and the resulting contrast is decreased. We experimentally optimized the energy window extension and ZLP width to maximize the signal, and found as good values $4-5$ eV for the window, and $7-8$ eV for the ZLP.

In Fig. 4.23 we simulated the ZLP-depletion images by taking the spectra given by the semi-analytical theory for the propagating SPP, and selecting only the counts of the energy windows, after having convoluted the spectra with the experimental ZLP. With reference to Eq. 4.2, fitting parameters $|B|^2 \approx 2.5$ and $\arg B \approx -107°$ were used to best match the intensity and phase of the chiral plasmon polariton. As expected, the three images, corresponding to energy windows of 1, 4, and 7.2 eV, show the same pattern, spatial periodicity, phase distribution, and chirality. The essential difference is just a change in the peak-to-valley contrast: largest for 1 eV, and decreasing for broader energy windows. The central panel, Fig. 4.23b, is what best corresponds to the experimental micrograph, Fig. 4.4d, and indeed comes from the same energy window selected in the experiments, ~ 4 eV. The theoretical map in Fig. 4.4e is taken with the same parameters, while the maps in Fig. 4.17 are simply obtained as depletion maps of the $\ell = 0$ order.

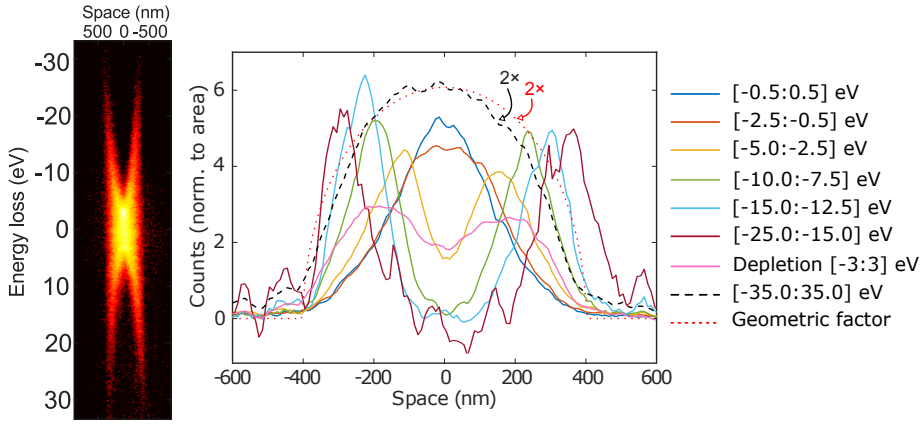

Figure 4.22 – **a**: Large-ZLP space-energy nanohole mapping for linear polarization. The ZLP is ≈ 9.5 eV FWHM. **b**: Selected energy-filtered spatial profiles across the hole for different energy windows. The spatial coordinate is y, and the spectral density is integrated along x. The dashed black curve is the sum of all counts, equivalent to the ZLP at $t < t_0$. The dotted red line is relative to the 'geometric factor' $\mathrm{Re}(R_{\mathrm{hole}}^2 - y^2)^{1/2}$.

To summarize, PINEM imaging is in general not an ideal technique to quantitatively extract the field distributions in space. A scanning probe in focused beam mode, comparison with simulations, and space-energy mapping in parallel beam mode are ways to overcome the problem. To select a $< \hbar\omega$ energy window in parallel beam mode and acquire different micrographs with the energy window centered around $\ell\hbar\omega$ has been proved impractical for infrared photons, but may be experimentally doable at visible frequencies. The method used in the majority of this thesis, based on the depletion of the ZLP presents some practical advantages, and produces qualitatively the 'negative' of the conventional EEG PINEM.

4.3.2 Mapping infrared resonances by infrared light with tunable wavelength

We employed the imaging method just described to capture the Fabry-Perot modes in Ag NWs at sub-eV energy. In Fig. 4.24 we report again on the imaging method, analogously to Fig. 4.19. Panel a well shows the advantage in using the depletion signal (blue-shaded area) instead of the EEG signal of, say, EEG> +5 eV. A precise map of the lobes of the Fabry-Perot mode of order $p = 16$ is visible in the difference image, Fig. 4.24d. For this experiment we employed NIR laser pulses with photon energy ranging from 0.8 to 1.1 eV, in large part smaller even than the narrow ~ 1 eV ZLP. It is therefore hard to extract any ultrafast spectral information at these energies in EELS mode; by following the plasmonic response of the system at different excitation wavelengths, the Fabry-Perot resonances can be however mapped, with the laser linewidth resolution, 20 meV in our experiment. This value is not only much smaller than the ZLP, but also of our GIF spectrometer resolution (50 meV).

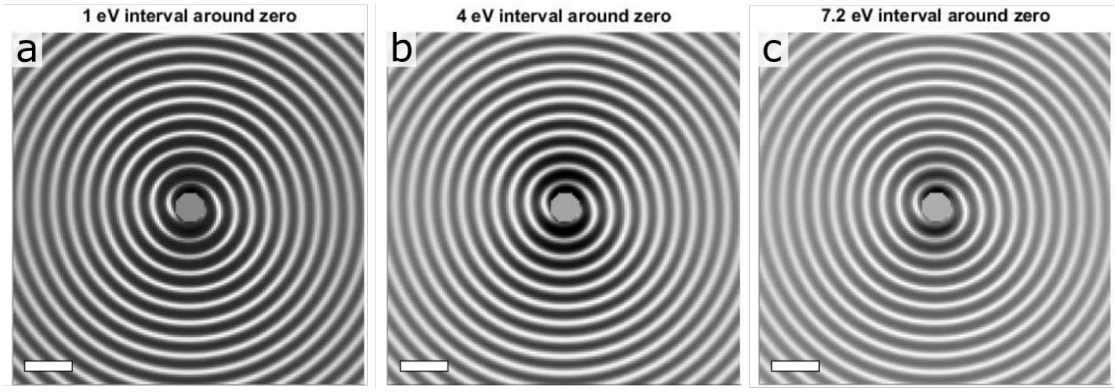

Figure 4.23 – Simulated PINEM micrographs as a function of the selected energy window in ZLP-depletion imaging. **a**-**c**: Selected energy window of 1 eV (a), 4 eV (b), and 7.2 eV (c), for the same ZLP width of 8 eV. Scale bars 2 μm.

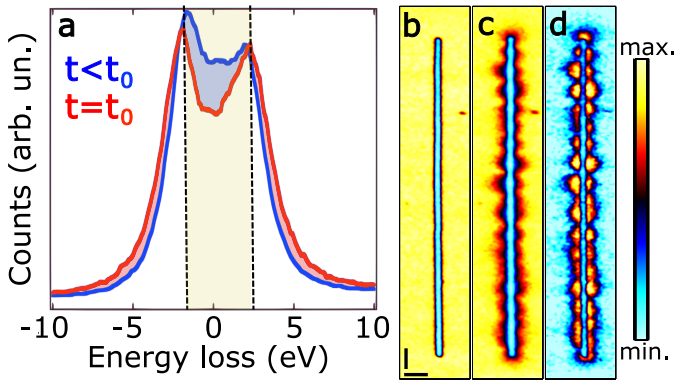

Figure 4.24 – Imaging method for the plasmonic Fabry-Perot modes in a NW. **a**: EEL spectrum before and at pump-probe coincidence. Shaded in blue/red the regions in which the spectral density decreases/increases at $t = t_0$. The semi-transparent orange-shaded central area was selected in EFTEM. **b**: EFTEM micrograph for $t < t_0$. **c**: Same, for $t = t_0$. **d**: Difference c – b. Scale bars 500 nm.

We dealt with Fabry-Perot resonances in Chap. 2 and Chap. 3, for SPPs propagating between two parallel sources. In Fig. 3.9 we also saw a Fabry-Perot resonance in a long nanocavity. For Babinet's principle, a nanowire, i.e. the complementary structure, is predicted to have the same properties, up to a π phase factor. So, a long NW can act as a resonator, and the SPP mode spiraling along its long axis can create a standing wave, if the optical length is a half integer of the SPP wavelength, that is

$$L_{\mathrm{SPP}} = p\frac{\lambda_{\mathrm{SPP}}}{2}, \tag{4.10}$$

for ideal end-cavity mirrors. We can also in first approximation consider L_{SPP} as the physical NW length L. Such resonances have been studied in TEM [209, 274, 415] and UEM [119, 142], with great details at 1.55 eV by L. Piazza, T. Lummen *et al.* in ref. [142]. The resonance wave-

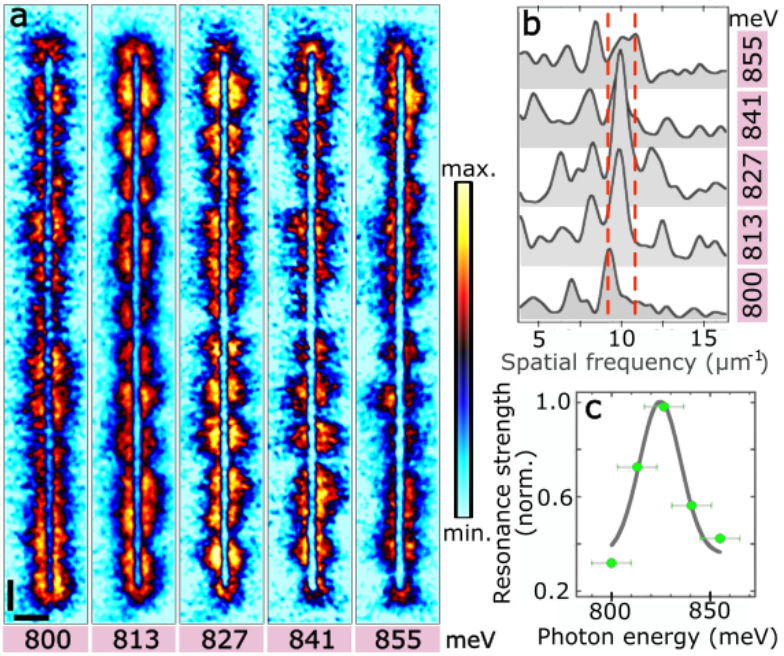

Figure 4.25 – Laser-assisted laser spectroscopy. **a**: PINEM micrographs for excitation energies around $\hbar\omega = 827$ meV, for the $p = 13$ resonance. Scale bars 500 nm. **b**: Corresponding (real part of the) Fourier transforms along the NW long axis. The spatial frequency adopts the 2π/distance convention. **c**: Integral of the Fourier intensity peaks in b in the region limited by the red dashed arrows, corresponding to $p = 13$.

length varies for different wire lengths. The approach in ref. [142] has been to find a wire with the optimal Fabry-Perot mode at 1.55 eV. In a slightly different approach, here we select a wire, any long wire, and tune the laser frequency to match one of its Fabry-Perot modes. In Fig. 4.25a we can appreciate how the strength of the mode increases when approaching the $p = 13$ resonance peak, and diminishes after. The 130 nm diameter and ~ 7.8 μm long wire has been placed on a Si_3N_4 TEM membrane. Since we desired to image only the standing wave pattern, the inverse transition radiation contribution has been minimized. The tunable NIR light comes from the signal of a two-stage OPA, as described in Sec. 1.3.1, and the incidence fluence (~ 5 mJ/cm^2) was equal for all photon energies.[17] The laser spotsize, $\sim 40-50$ μm FWHM diameter, is much larger than the field of view, and the polarization was set parallel to the wire, to efficiently excite the SPP mode along its long axis. Since the length of the NW is shorter than the SPP decay length, we can consider the field as composed by two counter-propagating SPPs, creating a standing wave pattern with periodicity $\lambda_{SPP}/2$.

The NW in Fig. 4.24 was chosen to be straight to facilitate the quantitative analysis of the lobes' distribution, but curved and bent NWs show as well good resonances [274], as confirmed for

[17] Attention had to be placed in having all the wavelengths focused to the same spotsize. This fact is in general untrue, since the minimum beam waist for a fixed focusing system scales linearly with the wavelength λ. For that reason, at each wavelength the laser spotsize was measured by means of a beam profiler in the focus, and –in case of noticeable changes– the incident power modified to reach the same fluence.

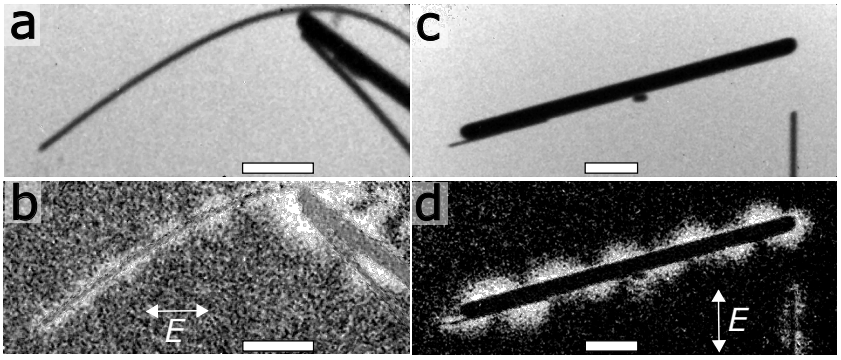

Figure 4.26 – More complex Fabry-Perot excitations in Ag NWs. **a**,**b**: Bright field (a) and PINEM (b) micrographs for a curved wire. **c**,**d**: Bright (c) and PINEM micrographs of an asymmetric mode in a 350 nm-thick calumet-shaped NW. The large bump (mouthpiece) does not affect the presence of the standing-wave mode, although it generates a localized dipolar near field. Scale bars 1 μm in all panels. The direction of the in-plane component of the electric field is indicated by a double arrow in each PINEM micrograph.

example by Fig. 4.26. There, we compare the bright field ($t < t_0$) and PINEM micrographs for a thin curved NW and a thick NW with a bump. In both cases, a clear Fabry-Perot resonance is visible. The optical excitation of curved wires may be more delicate than with electrons [274], since the two wire extrema should be oriented in the same direction for the mode to be excited efficiently by light. The tunability of the light polarization, conversely, gives an extra handle in the choice of the cavity mode; in Fig. 4.26d, for example we show an antisymmetric lobe distribution [142] photoexcited by an in-plane component of the electric field, oriented at $\approx 40^\circ$ with respect to the NW long axis.

The order of the resonance is simply obtained by counting the number of nodes along the wire, see Eq. 4.10. To quantitatively analyze the resonance, the PINEM signal distribution in Fig. 4.25a is taken, summed along the short NW axis, and Fourier transformed, Fig. 4.25b. In the wavevector space, a peak relative to the Fabry-Perot mode is present at the corresponding spatial frequency, as always calculated as 2π/distance. The area of such peak can be taken as a parameter to map the resonance. The result of how it varies with the excitation energy is displayed in Fig. 4.25c, together with a Gaussian fit with ~ 20 meV FWHM. If the excitation energy is tuned further away from the $p = 13$ resonance, other resonances can be excited. In Fig. 4.27 this is shown for $p = 13$, 14, 15, and 16, together with Gaussian fits of the Fabry-Perot resonance linewidth. Both even and odd modes are excited optically in the geometry of this experiment ($\alpha \neq \delta$), because of the skew angle of the long wire relative to the laser momentum [416]. Differently, for normal incidence ($\alpha = \delta$), only odd modes could be excited in a 1D resonator [142]. The 4 resonances we observe in our photon energy range have a linewidth which is just slightly larger than the $20-25$ meV excitation bandwidth, and therefore the natural resonance linewidth cannot be estimated very precisely. We extract a value $\lesssim 40$ meV, which is compatible with a resonance lifetime $\gtrsim 100$ fs, which is as well the laser pulse FWHM duration. From time-domain PINEM EELS data with narrow ZLP, with temporal resolution

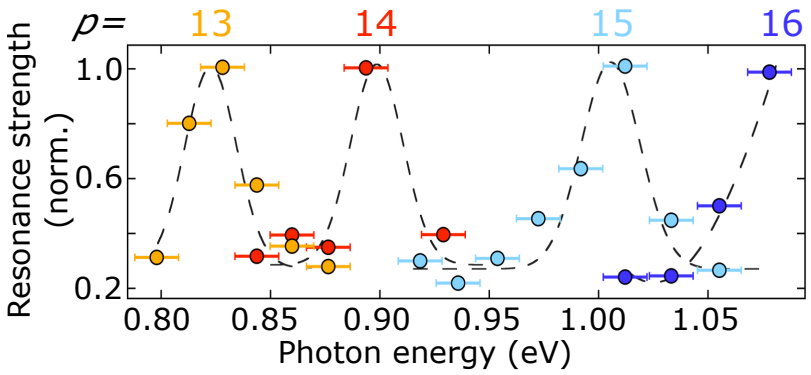

Figure 4.27 – Laser-assisted mapping of multiple resonances. The normalized plasmon resonance for modes with order p = 13–16 obtained upon scanning the laser energy between 0.8 eV (1550 nm) and 1.08 eV (1150 nm), with the same method as in Fig. 4.25. Error bars are estimates of the laser bandwidth, not uncertainties on the central photon energy, which is known more accurately.

250 fs, we also tentatively estimate a ~ 100 fs resonance lifetime.[18]
Regarding the spectral position of the resonances, from Eq. 4.10 we directly derive that all the Fabry-Perot resonances are evenly spaced along the energy axis, in first approximation,[19] and that $\Delta E = (\hbar c \pi)/L$. For the ≈ 7.8 µm NW used in Fig. 4.27 we find $\Delta E_{\mathrm{th}} \approx 80$ meV. The average energy spacing in Fig. 4.27 is $\Delta E_{\mathrm{exp}} = 90 \pm 10$ meV. Moreover, from the position and order of the resonance peaks we can directly extract the SPP energy-momentum dispersion. For all the 4 points along the dispersion curve we find a refractive index $n_{\mathrm{SPP}} = 1.18 \pm 0.05$.

Albeit we applied this method to map known plasmonic resonances in simple geometries, the concept of the experiment can be applied to numerous disparate low-energy collective modes in condensed matter physics that can be selectively excited by tunable light pulses [417]. For instance, it could be used to study graphene plasmons with long lifetime, and sharp linewidth [418, 419]. If energy-filtering is necessary to extract the signal, as in our case here, it would be hard to perform a measurement relative to an excitation that is at very low energy (say, $\lesssim$ 10 THz light), because in that case the spectra would not be discernible enough for the EFTEM to create a differential signal. However, an unprecedented spectroscopic precision may be achieved in mapping hundreds-meV modes with combined spatial resolution.
We therefore successfully decoupled the experimental energy resolution from the electron energy spread, allowing in principle to probe modes with few meV resolution, even with ~ 10 eV electron probes. Tremendous recent improvements in static STEM [34, 197, 420] brought the world best resolution to $\lesssim$ 5 meV [34]. Still, that value in pulsed instruments is

[18] The data fit reliably says that the lifetime is significantly shorter than 250 fs. Conservatively, this sets a $\gtrsim$ 20 meV constraint in the mode linewidth.

[19] This approximation here is partially justified because at energies < 1 eV the SPP dispersion is reasonably close to the light line, similarily to Fig. 3.6 at the Ag-vacuum interface, but for a NW geometry.

in general worsened by ~ 2 orders of magnitude, and often more[20]. Despite being applicable to a specific subset of physical systems, our method can for those systems compete with the best static TEM resolution. Since the resolution is inherited from light, a natural trade-off is present between energy and time resolution. An energy resolution down to 1 meV is possible for ~ 4 ps long pulses, and μeV resolution for longer pulses.[21] However, that constraint is truly fundamental for the laser pulse, but not for the technique itself, which can circumvent the apparent limit by using a third pulse.
In an ideal three-pulse experiment, a short light pulse is used as pump, a long, tunable light pulse with narrow bandwidth acts as spectroscopic gate, and the short electron pulse constitutes the probe. The pump pulse has to be set to minimize PINEM, so that it does not affect the measured response of the probe. Spectroscopic gate and probe are here imagined to be with their peaks in temporal coincidence. By changing the arrival time of the pump pulse, the evolution of the system can be mapped, by scanning in wavelength the gate pulse at each pump-probe delay, hence obtaining a reconstruction of the low-energy excitation mode. The dynamics photoinduced by the pump would manifest for example in a modification of the mode linewidth, as a shift, a broadening, or a hybridization. With such extension of the method reported here, one could benefit from a phenomenal sub-meV resolution still maintaining simultaneously the highest UEM resolution, in our case ~ 250 fs.[22]

4.3.3 Final statement: the TEM of the future

This idea to fully move the role of defining the energy resolution from the electron to the light excitation is analogue to the idea to transfer the temporal resolution from the electron pulse to the optical pulse in the three-pulse holography. Only partly sideways, the photonics-based method to imprint arbitrary phase profiles to the electron wave function has roots in the same context of ideas.
Intimately, the advent of ultrafast electron microscopy was motivated by the superior spatial resolution of electrons, and was developed despite photon-based techniques could easily outperform UEM in the temporal and spectroscopic domains. The works presented here give few tools that could contribute to the premises for a gedanken-TEM in which the spatial resolution is determined by the electrons, the temporal and energetic by light, and electron states are prepared and manipulated by intense optical pulses before and/or after the interaction with the specimen.

[20] The best values are ~ 0.24, ~ 0.7, and ~ 1.1 eV for GaAs, Schottky tungsten, and LaB_6 single-photon photoemission, respectively. See Chap. 1 for details.

[21] With our current fs laser system, we demonstrated a bandwidth as narrow as 4 meV at 790 nm, corresponding potentially to ~ 2.1 meV at 1500 nm. The experiments here reported were performed at ~ 37 meV bandwidth of the fundamental, i.e. about 20 meV at 1500 nm, value confirmed by measuring the spectrum of the SHG signal at 750 nm with a commercial spectrometer.

[22] The simplest proof-of-principle test one could perform is for example still on a high-quality (i.e. high Q-factor) nanowire resonator. The high-temperature jump ensuing from the pump excitation induces a modification in the metal permittivity function $\epsilon(\omega)$, which determines the SPP dispersion, hence shifting the resonance peak.

5 Skyrmions and laser pulses

In-situ and time-resolved electron microscopies on skyrmions constitute the focus of this chapter. After an introduction on magnetic imaging in a TEM, I will discuss about the first experimental realization of laser-induced manipulation of skyrmions, in a thin lamella of a chiral magnet, FeGe. Part of the results presented here are based on ref. [144] "*Laser-induced skyrmion writing and erasing in an ultrafast cryo-Lorentz transmission electron microscope*", Phys. Rev. Lett. **120** (11), 117201 (2018).

Spin ordering in solid state materials is one of the most studied branch in condensed matter physics, because of its fascinating physics and applications. The domain of spintronics [421] widely developed after the milestone discovery, about 30 years ago, of a giant magnetoresistance (GMR) effect [422,423] in multilayers of alternating ferromagnets and non-ferromagnets. GMR was swiftly incorporated into everyday technologies, such as hard disks and magnetoresistive random access memory (MRAM). Its success story serves as inspiration for scientists in fundamental and applied physics, even outside the magnetism community. Little more than 10 years ago, another noteworthy discovery path started off thanks to A. Bogdanov and co-workers, who predicted the existence of ground-state skyrmionic arrangements of spins in systems lacking space inversion symmetry [424]. The first experimental proof of magnetic skyrmions followed [425], and many others shortly after, initiating the domain of skyrmionics. Skyrmions are nanometric swirling spin textures characterized by a topological charge; they were quickly envisioned to be possible carriers of futuristic spintronics devices, in particular for digital memory storage.
Time has passed since then, the skyrmion research field steadily grew, and numerous advances were demonstrated; however, no palpable application has come out yet, as a result of the many physical and engineering problems related to stability, transport, miniaturization, and reproducibility of the skyrmion phenomenology. Albeit the arduousness to bridge fundamental research and market technology, the idea to exploit these topologically-protected spin twists in devices in not purely chimeric, although it will still have to pass through the frequently erratic process of scientific advancement. While in this dissertation I do not discuss

any practical skyrmionic device, the possibility to have optical manipulation of skyrmions is investigated. A simple optical write/erase scheme is presented for the first time. Laser pulses are used to dramatically accelerate the thermodynamic evolution of the system, determining the appearance and disappearance of magnetic phases. This exemplifies the major role played by the complex interplay between topological stability and thermodynamics in the nucleation and stability of skyrmions in matter [426].

5.1 Magnetic imaging with high-energy electrons

A detailed study of skyrmions at the nanoscale does require appropriate probes that can visualize the skyrmion particles individually in real space. Many powerful magnetic techniques [427], such as neutron scattering, vibrating sample magnetometry, GHz spectroscopy, and superconductiong quantum interference device (SQUID) provide with spatially-averaged magnetization information. Nanometric real-space imaging can be performed by means of magnetic force microscopy (MFM), spin-polarized scanning tunneling microscopy (STM), STXM, X-ray holography, scanning electron microscopy with polarization analysis (SEMPA) [428, 429], spin-polarized low-energy electron microscopy (SPLEEM) [430], magnetic microscopy using nitrogen vacancy (NV) centers in diamond, and to a lower extent by MOKE microscopy. Also, emerging techniques include scanning SQUID-on-tip magnetometry, and microfocus Brillouin light scattering (BLS). In this panorama, high-energy electrons stand out as a versatile probe with atomic resolution, magnetic sensitivity, and fast acquisition. Furthermore, they are used in table-top instruments, not requiring large and expensive infrastructures. Their versatility is manifested in the ability to perform magnetic imaging, magnetic diffraction, holography, and magnetic core-loss spectroscopy [145, 427, 431, 432].
The most used technique to probe magnetism with electrons is undoubtedly Lorentz transmission electron microscopy (LTEM) [433, 434] in Fresnel (defocused) configuration. The contrast mechanism is however rather general to all elastic techniques, and is a purely coherent scattering process: an electron wave propagating along $\hat{z}$ accumulates a phase

$$\phi(\boldsymbol{r}) = \frac{q_e}{\hbar}\Big[\frac{1}{v_0}\int_{-\infty}^{z} V(x,y,z')\mathrm{d}z' - \int_{-\infty}^{z} \boldsymbol{A}(x,y,z')\cdot\hat{\boldsymbol{z}}\mathrm{d}z'\Big] \tag{5.1}$$

in presence of a four-potential $(V/v_0, \boldsymbol{A})$. The expression in Eq. 5.1 represents the well known Aharonov-Bohm phase [46, 47], and it has very general validity. For instance, through the electrostatic term it describes the action of the elastic phase plate to create vortex electron beams [369, 370], and through the vector potential the 'magnetic monopole' method to twist the electron phase profile [389], as we saw in Sec. 4.1. The measurable quantities in an electron microscope are the phase differences as a function of (x, y). Since for magnetic imaging we are not interested in the electrostatic term $V(\boldsymbol{r})$, we can consider its corresponding phase term constant throughout the specimen, therefore not contributing to any phase difference along closed paths encompassing the whole specimen thickness. As usual, we place the detector at

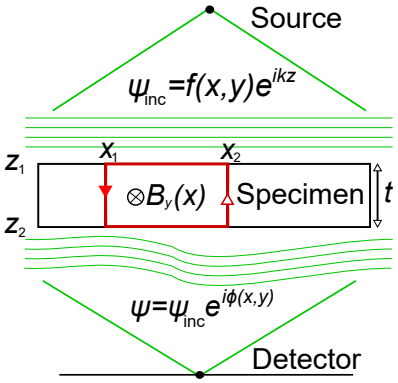

Figure 5.1 – Aharonov-Bohm phase shift in Lorentz microscopy: scheme of the specimen.

$z = +\infty$, finding a magnetic phase

$$\phi(x,y) = -\frac{q_e}{\hbar}\int_{-\infty}^{\infty} \boldsymbol{A}(x,y,z)\cdot\hat{z}\,\mathrm{d}z\,. \tag{5.2}$$

After having traversed the specimen, the electron wave function has the form

$$\psi(\boldsymbol{r}) = \psi_{\mathrm{inc}}(\boldsymbol{r})e^{i\phi(x,y)}\,. \tag{5.3}$$

To calculate the phase difference between two generic points (x_1,y_1) and (x_2,y_2), we can choose without loss of generality a coordinate system for which $y_1 = y_2 = 0$. The geometric Aharonov-Bohm phase shift ought to be

$$\Delta\phi_{1\to2} = \frac{q_e}{\hbar}\oint_{\mathrm{Path}} \boldsymbol{A}(x,y,z)\cdot\mathrm{d}\boldsymbol{\ell} = \frac{q_e}{\hbar}\iint_{\mathrm{Area}}\Big[\nabla\times\boldsymbol{A}(x,y,z)\Big]\cdot\mathrm{d}\boldsymbol{S} = \frac{q_e}{\hbar}\iint_{\mathrm{Area}}\boldsymbol{B}(x,y,z)\cdot\mathrm{d}\boldsymbol{S} = \frac{q_e}{\hbar}\Phi_B\,, \tag{5.4}$$

where Φ_B is the magnetic flux, and the sign of the phase difference depends on the running sense in the contour integral. As illustrated in Fig. 5.1, the area of the surface integral is considered to be in the $< xz >$ plane, and for any generic couple of points 1 and 2, the z axis always lies in the area. For this reason, what gives the phase shift $\Delta\phi_{1\to2}$ is the component of the magnetic field perpendicular to the electron propagation direction, i.e. in the specimen plane ($< xy >$). This peculiarity of Lorentz microscopy comes classically from its eponymous force $\boldsymbol{F} = -q_e\boldsymbol{v}_0\times\boldsymbol{B}$. The integral surface in Eq. 5.4 goes in principle from the electron source to the detector, passing through the points 1 and 2 of the specimen; in practice, the only region where there is a nonzero magnetic flux is at the specimen and eventually its close surroundings, to account for stray fields.

If we now consider the 'trivial' Aharonov-Bohm scenario, in which electrons probe locally a magnetization field (see Fig. 5.1) the phase shift can be calculated as

$$\Delta\phi_{1\to2} = \frac{q_e}{\hbar}\int_{z_1}^{z_2}\mathrm{d}z\int_{x_1}^{x_2} B_y(x)\mathrm{d}x = \frac{q_e t}{\hbar}\int_{x_1}^{x_2} B_y(x)\mathrm{d}x\,. \tag{5.5}$$

In the last step, we considered that the magnetic field is uniform along $\hat{z}$ within the specimen, which has a constant thickness t. Similarly, if $y_1 \neq y_2$, another phase $(-q_e t/\hbar)\int_{y_1}^{y_2} B_x(y)\mathrm{d}y$ should be added. It follows that a ferromagnetic domain behaves as a pure phase object to the electron wave, and that magnetic imaging is a phase contrast microscopy. Notably, magnetic phase shift through domain walls is typically much stronger than electrostatic shifts [145].

5.1.1 Lorentz-Fresnel microscopy

The position-dependent geometric phases accumulated by the specimen contain the magnetic information about the specimen. But how to extract this information? Detectors are sensitive only to the amplitude of signals, not to their phase, while here a phase-sensitive measurement is needed. The perhaps most direct way to extract such phase is by means of homodyne detection, for example holography, which is usually performed with an electrostatic biprism, as discussed in Sec. 3.2.1.
Nevertheless, the most common approach, LTEM, consists in mixing the phases coming from different (x, y) directly on the detector, by defocusing the image, without interference with an independent reference field. This fact determines a partial loss of information, which can however be regained by acquiring 3 micrographs and carrying out a transport-of-intensity equation (TIE) analysis. In the defocused image, the electron probability amplitudes from different (x, y) have a certain spatial overlap, and sum up coherently. Constructive and destructive interference regions determine a visible contrast, which is strong for positions around which a large in-plane magnetization change is present, i.e. around domain walls.
Despite we introduced the geometric phase formalism, a purely classical description allows frequently to describe the contrast and the technique satisfactorily. In a (semi)classical scenario, the high-energy electron is deflected by the magnetization in the specimen, as described by the Lorentz force:

$$\boldsymbol{F}_\mathrm{L} = -q_e \boldsymbol{v} \times \boldsymbol{B} = q_e v_0 \boldsymbol{B} \times \hat{z}. \tag{5.6}$$

While crossing the sample, they accumulate a deflection angle $\beta(x, y, z)$, which away from this interaction region is

$$\beta_\mathrm{L}(x, y) = \frac{q_e \lambda}{h} \int_{-\infty}^{\infty} B_\perp(x, y, z)\mathrm{d}z, \tag{5.7}$$

with $h = 2\pi\hbar$, λ the electron wavelength, and $B_\perp$ the in-plane component of the magnetic induction. Eq. 5.7 follows directly from Eq. 5.6, with the small-angle approximation $\tan\beta_\mathrm{L} \approx \beta_\mathrm{L}$, and utilizing de Brogile's $p = h/\lambda$, see Sec. 1.1.1. Once again, by considering a homogeneous magnetization B, we reduce to the deflection angle formula

$$\beta_\mathrm{L} = \frac{q_e \lambda B t}{h}. \tag{5.8}$$

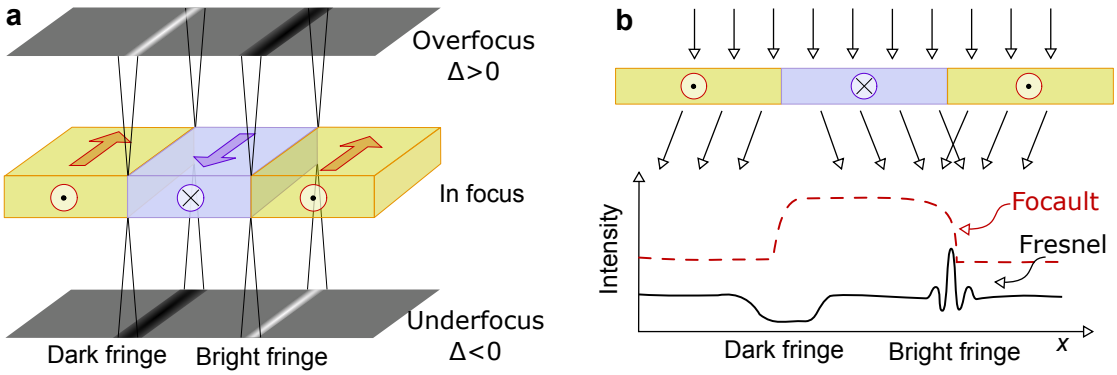

Figure 5.2 – Contrast origin in Lorentz-Fresnel electron microscopy. **a**: A schematic ray diagram for 180° domain walls. **b**: Same, with a qualitative sketch of the contrast (black curve). The red dashed curve is relative to Lorentz-Focault mode, see text. Deflection angles not in scale.

The same result can be derived readily from the quantum treatment, considering the Aharonov-Bohm phase Eq. 5.5 for uniform magnetization $B_y = B$:

$$\beta_L = \left| \frac{\Delta\phi_{1\to2}}{2\pi} \frac{\lambda}{\Delta_{1\to2}} \right| = \frac{q_e \lambda B t}{h}. \tag{5.9}$$

The length $\Delta_{1\to2}$ represents the distance between points 1 and 2 in the plane (in Eq. 5.5 $\Delta_{1\to2} = x_2 - x_1$). In this simple case, the quantum description hencereduces to the classical picture, and Eq. 5.9 shows their equivalence.

The deflection angle β_L is quite small: if we consider for instance a saturation magnetization $B = B_S = 0.5$ T, $t = 50$ nm, and 200 keV electrons, β_L is as small as $1.5 \cdot 10^{-5}$ rad, which is about 3 orders of magnitude smaller than Bragg angles for scattering from an atomic crystal.[1] The angular distribution of the inelastically scattered electron, instead, continuously spans through similar deflection angles, hence causing a potential loss of contrast, which prevents the use of thick specimens.

The contrast origin in Lorentz-Fresnel microscopy is illustrated schematically in Fig. 5.2a. As shown there, when a simple 180° domain wall is present, the electrons traversing the specimen in opposite domains are deflected in opposite directions. When the specimen is imaged in focus (for example by bright field imaging), no magnetic contrast is visible, because –in absence of aberrations– each (x, y) point at the specimen is mapped onto a (x', y') point at the detector, and no beam interference can take place. When the image is defocused by a distance Δ along $\hat{z}$, the beams coming from different regions of the specimen are mixed, and –for coherent electron waves– dark and bright interference fringes form. Dark and bright fringes correspond to locally diverging and converging beams. It follows that the contrast inverts when Δ changes sign. In a purely classical scenario, we may expect a substantial symmetry between dark and bright fringes. In reality (see Fig. 5.2b), bright (convergent) beams create a larger differential contrast, and can show in principle oscillations as well, as Fresnel fringes do.

[1] Being on such a different angular deflection scale, Bragg and Lorentz deflected electrons do not overlap in the back-focal plane. Actually, each Bragg spot is decorated by the Lorentz spots.

Intuitively, the contrast is enhanced at higher defoci, and for a given defocus, narrow domain walls generate a higher contrast, while delocalized spin rotations are harder to be imaged. For small defoci, the intensity can be described by the following expression:

$$I_\Delta(x,y) = 1 - \Delta \frac{q_e \mu_0 \lambda t}{h} \Big[\nabla \times \boldsymbol{M}(x,y) \Big] \cdot \hat{z}. \tag{5.10}$$

The derivation of this equation can be found in refs. [435, 436], and μ_0 here is the vacuum permeability. The meaning of Eq. 5.10 is simple and immediate, stating that the contrast is directly proportional to the defocus value and to the projection of the curl of the magnetization along $\hat{z}$, which confirms the observation that large in-plane spin curvatures give the highest contrast.

What described so far is sufficient for the correct interpretation of the data shown in the next sections, all based on Lorentz-Fresnel microscopy. However, it is worth mentioning that quantitative information from Fresnel micrographs can be retrieved via TIE analysis [437, 438]. The phase information is extracted by solving the partial differential equation

$$\nabla \cdot \big[I_0(x,y) \nabla \phi(x,y) \big] = -\frac{2\pi}{\lambda} \partial_z I(x,y), \tag{5.11}$$

which describes the variation in phase contrast as a function of defocus, and is also truly valid only in the small Δ limit. In practice, the derivative in the right side of Eq. 5.11 is evaluated numerically by acquiring images at 3 different defoci: Δ, 0, and $-\Delta$. A phase map is obtained from the TIEs, and if the contrast is magnetic,[2] a quantitative phase and amplitude characterization of the in-plane magnetization is obtained.[3]
Another operating mode in Lorentz microscopy is the Focault mode, which relies in blocking one or several Lorentz-scattered beams, altering in such a way the brightness level of different domains. In other words, it is the magnetic analogue to Bragg's dark field microscopy. In the back-focal plane of a TEM[4], the scattered beams are separated in space; with reference to Fig. 5.2, if in the back-focal plane the beams deflected to the left (from the pastel yellow region) are stopped, only the beam deflected to the right (lavender blue region) reaches the detector, brightening up that area (see the dashed red profile). Therefore, while Fresnel imaging allows to visualize domain walls, Focault mode images directly the domains. Moreover, coherent Foucault mode allows to directly access to the phase information, similarly to holography [439].

Importantly, the desire to probe magnetism in a TEM encounters a serious practical problem: the high magnification in a microscope is reached by immersing the specimen in the field of a strong lens, the objective lens, see Sec. 1.1.2. Since magnetic lenses are used, it means that a perpendicular magnetic field permeates the space surrounding the specimen, and it is

[2] For example by repeating the experiment with flipped specimen, and subtract away the electrostatic information, or by operating at different acceleration voltage.
[3] The only experimental parameters needed are t, λ, and Δ.
[4] See Sec. 1.1.2 for TEM diagrams and details.

typically 1 – 2 T in standard imaging conditions. This high field value causes the polarization of spins in the out-of-plane axis, preventing to image in-plane magnetic domains. Ideally, one would aspire to have an instrument that is able to perform high-magnification imaging in a magnetic-free environment, and eventually to use a magnetic field in situ as external parameter to enable the sampling of the magnetization pattern throughout the magnetic phase diagram and hysteresis loop. This condition is realized in modern microscopes by switching off the objective lens, and employing as imaging lens a specifically-designed Lorentz lens, situated below the specimen plane, and whose field lines do not cross the specimen area. This is the case for example of the Titan Themis FEG microscope (ThermoFisher Scientific, formerly FEI), which we used for instance to acquire Néel skyrmions data (not shown in the thesis). The UEM used in all other sections of this dissertation, has also an imaging lens below the specimen plane, called objective minilens. Its design is less specific for magnetic imaging, and its maximum magnification is 6000× ('low magnification mode'), although combining it with the magnification properties of the GIF spectrometer, a magnification higher than 60000× can be reached. Moreover, this lens configuration does not allow for a magnetic-free environment, the minimum remnant magnetic field at the specimen position being approximately 170 G.
The external magnetic field acts always along the $\hat{z}$ axis, and in our UEM it can have currently only one polarity.[5] An in-plane external magnetic field component can be generally applied to the sample by tilting the specimen, keeping in mind that this procedure diminishes the out-of plane field component and that it changes the projection on the $\hat{z}$ axis of the magnetization curl, hence possibly modifying the contrast.
Since many materials have intriguing magnetic phases below room temperature, it is common for Lorentz microscopists to work with low-temperature sample holders. The most used low-T holder concepts use either N_2 or He as refrigerant. In the work reported here, we made use of a liquid nitrogen sample holder (Gatan Inc, single tilt model 613)), which covers the range from ~ 78 to 328 K, in combination with a local heating circuit. The holder is designed to assure high stability, with minimum sample drift, and it operates with a small liquid N_2 reservoir with no need for transfer lines that couples it to external sources of mechanical vibrations. For some experiments, we also employed a liquid He holder (Gatan, ULTST single tilt), which reaches down to ≈ 4.5 K. The holder can work either in flowing mode, with the holder connected to the dewar by a transfer line, or isolated, for a maximum time ~ 40 min., after which its reservoir needs to be recharged again. We refer sometimes to the low-temperature magnetic microscopy as to cryo-LTEM, despite cryoEM is by other authors used only to refer to biological imaging in vitreous water [184].

Extensive static LTEM characterization of numerous specimens has been carried out during the preparation of the dissertation, comprising ferro- and ferri-magnetic domains and vortices in lamellae, nanostructures, and thin films, Bloch and Neél skyrmions in different systems

[5] In Titan Themis, for instance, it can switch sign –reason for which a full lens degaussing is possible. By the time of the discussion this thesis, we updated our UEM apparatus to allow for polarity reversal, but no experimental characterization is available yet.

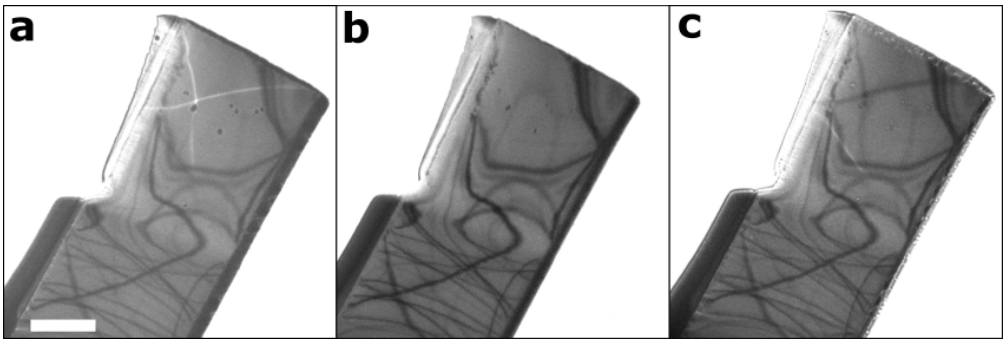

Figure 5.3 – Example of through-focus Fresnel-LTEM series. **a**: Overfocus **b**: In-foucs. **c**: Underfocus. The specimen is a ferrimagnetic lamella of Fe_3O_4, imaged at room temperature. The main magnetic feature is a vortex state (360° wall), and 4 domains with 90° domain walls between each other. The dark lines that do not turn bright upon defocus inversion are bent contours, and their origin is structural, not magnetic. Scale bar approximately 500 nm.

(FeGe, Cu_2OSeO_3, CoZnMn, and PtCo stacked multilayers), and superconducting vortices in MgB_2.
In Fig. 5.3 I report an example of magnetic domain wall configuration probed by Lorentz. The magnetic configuration is dominated by a vortex state, and it is imaged in overfocus, in-focus, and underfocus conditions.

5.1.2 Time-resolved Lorentz microscopy

Time-resolved Lorentz microscopies can be catalogued belonging to two categories: camera-rate and stroboscopic.[6] As discussed in Sec. 1.4 and Sec. 1.5, camera-rate LTEM is possible but limited to the ms temporal range [149–151]. The realization of Lorentz microscopy in stroboscopic mode has been proven for large domain walls in a strongly magnetized NiTi film [152], with nanosecond pulses, and extended to the picosecond timescale by Schliep *et al.* [153]. While redacting this thesis, sub-ps Lorentz imaging has been reported as well, addressing the ultrafast demagnetization of thin permalloy disks [440]. Since Lorentz contrast is a pure phase contrast, the transverse coherence of the electron beam can set the limit to the achievable spatial resolution.[7] Skyrmions and helical structures –in particular– present a significant experimental challenge, and their time-resolved LTEM investigation has been remained elusive so far.
Here we report on both sub-ps, ps, and ns LTEM imaging on different structures. A ns stroboscopic system has been designed and implemented with the specific goal to target skyrmion imaging (see Sec. 1.4 for the full motivation and details). Details on skyrmion imaging are left to Sec. 5.2 and Sec. 5.3.

[6] Single-shot magnetic imaging has never been reported so far –because of the high-coherence requirements.
[7] Although the resolution limits in LTEM come from different factors, like delocalization contrast. Highly defocused images cannot in general have very high magnifications, and even in the best state-of-the-art instruments, Lorentz lenses are not corrected for spherical aberrations. Recent exception is ref. [441], where atomic and 2 – 3 nm resolution were reached at nearly in focus and 10 μm defocus, respectively, in aberration-corrected LTEM.

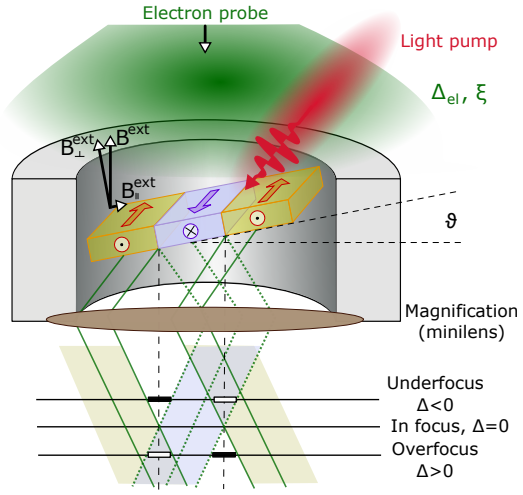

Figure 5.4 – Scheme for time-resolved LTEM. See text for the explanation of the symbols.

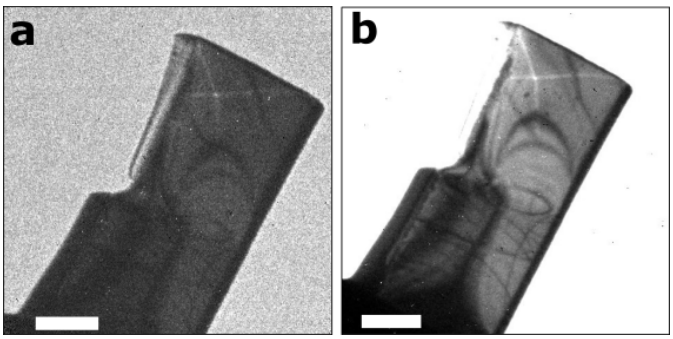

Figure 5.5 – Example of sub-ps and ps Fresnel-LTEM images. Both micrographs probe the same magnetic configuration as in Fig. 5.3. **a**: For photoelectrons at minimum Wehnelt voltage (see Sec. 1.1.2 and Sec. 1.3), assuring a $\lesssim 1$ ps pulsed beam. **b**: Same, for 'saturation' bias, with the pulses several ps long.

In Fig. 5.4 a diagram with the important parameters for tr-LTEM imaging is displayed. Together with the defocus value Δ, the magnification, and the specimen magnetization and texture, it is shown the external magnetic field, which decomposes into $B_{\perp}^{\mathrm{ext}}$ and $B_{\parallel}^{\mathrm{ext}}$ when the specimen is tilted by an angle $\vartheta = \arctan\left(B_{\parallel}^{\mathrm{ext}} / B_{\perp}^{\mathrm{ext}}\right)$. For the imaging to be possible, the electron beam should have a high transverse coherence ξ, which in field-of-view TEM corresponds to a high parallelness of the electron beam, typically achieved by using high spotsize parameters, small condenser apertures, and by spreading the electron beam on the specimen plane with the last condenser lens. The temporal duration of the electron pulses, Δ_e is included because it influences ξ in the space-charge regime.

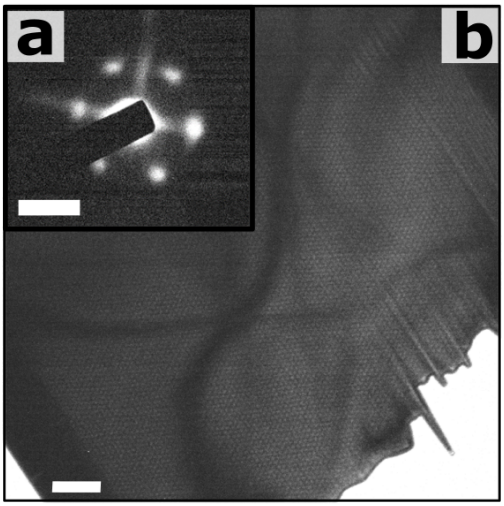

Figure 5.6 – Small-angle magnetic electron diffraction from a skyrmion lattice. **a**: Diffraction pattern, in HDD with 80 m camera length. Scale bar roughly 100 μm^{-1}. **b**: Corresponding real-space LTEM micrograph. Scale bar 500 nm. Both reciprocal and real space images are acquired with the thermionic source. The specimen is a FeGe lamella in its skyrmion phase.

5.1.3 Other imaging methods

In TEM and STEM, diverse magnetic imaging methods other than LTEM are possible. We already mentioned *electron holography*, which is extremely sensitive to Aharonov-Bohm phases, and has been used to image complex domains, superconducting vortices, Bloch skyrmions and other helical spin structures [47, 322–325, 442].
Similar phase information can be acquired by *differential phase contrast* (DPC) in STEM mode. Differential phase contrast (DPC) [443, 444] measures the deflection of a focused electron cone in a quadrant detector. The scan on the surface is performed in such a way to maintain the cone always at the center of the detector; only the in-plane magnetization deviates the electron trajectories. These deviations are considered, and the image is readily reconstructed. The DPC method can reach sub-nm resolution [445], and has been used for skyrmion imaging [446, 447] as well.
Other imaging methods include electron energy-loss magnetic chiral dichroism (EMCD) [378], and the use of *electron vortex* beams [376], as discussed in Sec. 4.1. Notably, EMCD recently allowed to perform atomically-resolved magnetic imaging [51].
Although it is not properly a real-space method, *small-angle electron diffraction* [448–453], which is performed in HDD mode, can be an insightful technique, and may present some advantages in stroboscopic experiments. The idea of the technique relies on the detection of the magnetic-deflected beams in reciprocal space. Since the deflection angles β_L are minute, small-angle magnetic electron diffraction requires high collimation of the incident beam and high spatial dispersion of the scattered beam at the detector, which from few meters to hundreds meters [452],[8] depending on the periodicity of the structure. Albeit being seldom used,

[8] In the microscope used in this thesis, the maximum 'standard' camera length is 80 m.

the power of this technique becomes explicit for magnetically periodic systems, especially in case of short-period modulations, such as in spin-density waves systems. Interestingly, skyrmions do arrange in periodic 2D lattices in chiral magnets, and therefore skyrmion small-angle electron diffraction has to be possible. In Fig. 5.6a we report such an HDD pattern taken from a FeGe lamella. We observe a 6-fold symmetry pattern, plus a streaking line which is caused by the diffraction from the geometrical edges of the small lamella. To the best of my knowledge, no previous small-angle electron diffraction pattern of a skyrmion crystal has been reported before. The corresponding LTEM image is displayed in Fig. 5.6b, showing a regular, single-domain lattice (with only minor orientational changes across the area, which are responsible for the angular width of the diffraction spots in Fig. 5.6). The Fourier transform of the real-space image (not shown) resembles the diffraction pattern. The diffraction pattern gives directly the symmetry of the spin texture, and the lattice constant. Furthermore, different crystal phases can be distinguished easily, namely single-crystal, polycrystalline, helical, mixed helical-skyrmion, and liquid. Moreover, the intensity of the diffraction spots returns a measure of the magnetization strength associated to the given periodicity. The information of the magnetic diffraction pattern is in this case equivalent to the Fourier transform of the real-space image, and it is therefore qualitatively similar to small-angle neutron scattering information. However, there are cases in which to work in reciprocal space can give significant benefits. Firstly, if the periodicity of the magnetic objects is smaller than the point resolution limit of LTEM (in general, $\sim 5-10$ nm). Secondly, in presence of strong fluctuations that make the system evolve faster than the real-space imaging acquisition rate. This second case may correspond for example to stroboscopic imaging of a skyrmion lattice annihilation. Experimentally, we observed that laser pulses can generate a plethora of "irreversible" effects in some skyrmion-hosting materials, meaning that the real-space configuration after the external stimulus has changed. A systematic study of the time scale of such processes cannot be studied by LTEM, since after million pulses of different spin configurations the contrast is completely washed out. Nevertheless, by means of small-angle electron scattering, it is in principle possible to follow the dynamics.[9]

5.2 Spin twists and their zoology

Magnetic skyrmions are spin curvatures in real space with nontrivial topology. They exist as ground states in many physical systems, ranging from ferro- or ferrimagnets lacking spatial inversion symmetry, to ferromagnetic surfaces, and antiferromagnetically-coupled layers.
More in general, skyrmions are stable particle-like field configurations in nonlinear continuous field models [424], and can exist in quite a few physical systems, from liquid crystals to cosmological scales. However, they exist in these scales as nonequilibrium phases, unlike in magnetic systems, where skyrmions can spontaneously appear as ground-state configurations. I will only present here a succinct overview on magnetic skyrmions: since they are such a

[9] Of course, the diffraction spot would show a ring, with or without features, depending on how isoprobable are all the real-space patterns that are created after each pulse. Even for a featureless ring, the annihilation/creation timescale is extracted from the ring intensity as a function of time.

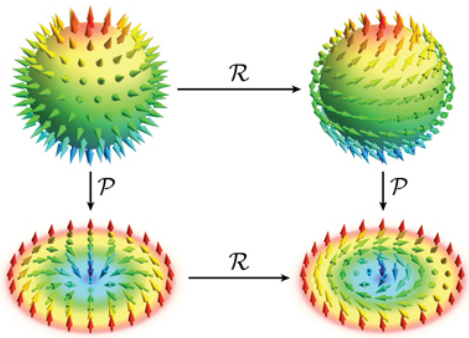

Figure 5.7 – Illustration of the skyrmion topology. The top 3D spheres are 3D vector representations of the spin configurations of Néel-like (left) and Bloch-like (right) skyrmions. The actual skyrmion configurations are the 2D projections at the bottom. Néel-type on the left, and Bloch-type on the right. R are rotation operators, P the stereographic projection, which maps the south pole into the center of the skyrmion, and the north pole into its periphery. P is a smooth and bijective function. Figure adopted from ref. [462].

popular research topic today, there are many excellent up-to-date reviews and books, as for example ref. [454], and [455–457]. Also, a very condensed introduction is repeated at the beginning of Sec. 5.3, focused more on the sub-field we were interested regarding the optical manipulation of these magnetic states..

History

It is hard to imagine if T. Skyrme could have thought that compact, swirling magnetic walls would have been named after him about 50 years since the publication of his nonlinear model to explain the stability of baryonic matter within a continuous field theory approach [458]. The idea to have skyrmionic states in magnetic crystals is usually credited to A. Bogdanov and co-workers, who already in 1989 predicted skyrmionic excitations in spin systems with broken inversion symmetry [459–461]. The spontaneous emergence of skyrmionic states focused initially on non-centrosymmetric materials with strong spin-orbit interaction, which leads to an antisymmetric term in the magnetic Hamiltonian that favors perpendicular spin configurations: the Dzyaloshinskii-Moriya interaction (DMI).

Spin twistology

The first classification usually done in skyrmionics consists in the separation between Néel and Bloch skyrmions. Bloch skyrmions are characterized by a 360° Bloch wall, with an in-plane rotating magnetization vector, while Néel skyrmions have an out-of-plane swirling magnetization wall. The two types are otherwise topologically equivalent, and in some cases in thick multilayered systems, hybrid Bloch-Néel walls can even coexist, separated only along

the 'columnar' axis [463, 464].
In Fig. 5.7 a textbook illustration [462] of the topological equivalence between Néel and Bloch skyrmions in reported. A 3D hedgehog sphere (top-left, winding number 1) is mapped into a 2D Néel skyrmion (bottom-left) via the stereographic projection P. Once the hedgehog sphere is 'combed' (i.e. a rotation R is applied to the the 3D vector field), a configuration with equal topology but different spin distribution is found (top-right). The stereographic projection of such configuration gives rise to a 2D Bloch skyrmion (bottom-right), which can also be obtained by a rotation of the 2D Néel skyrmion. With this illustration it is simple to observe that it is impossible to continuously tilt the spins in the 3D sphere to get them all parallel (ferromagnetic state = topological triviality).
Given a continuous magnetization distribution $\boldsymbol{M}(x,y) = M(x,y)\boldsymbol{n}(x,y)$, where $\boldsymbol{n}$ is a unitary vector, the topological charge of a skyrmion (called also winding number or skyrmion number) is defined as [455]:

$$Q = \frac{1}{4\pi}\iint \boldsymbol{n}\cdot\left(\frac{\partial \boldsymbol{n}}{\partial x}\times\frac{\partial \boldsymbol{n}}{\partial y}\right)\mathrm{d}x\mathrm{d}y. \tag{5.12}$$

This topological charge, which is always $|Q| = 1$ in this thesis, indicates how many times the spin vector wraps the 3D sphere as in Fig. 5.7.
Examples of LTEM images for Bloch and Néel skyrmions are reported in Fig. 5.8, for two different compounds. The LTEM signature of Bloch skyrmions (Fig. 5.8a) is the presence of bright or dark disks of contrast. The size of the disks depends on the defocus value (and transverse coherence of the electron beam). In a skyrmion lattice, however, the important parameter is the skyrmion lattice constant, which does not depend on the size of the bright or dark disks, but truly reproduces the real distance between skyrmions in the material. The Bloch skyrmion image is obtained with the specimen perpendicular to the electron illumination. In such a way, the LTEM contrast, Eq. 5.10, is maximized, since the curl of a Bloch skyrmion magnetization lies in the out-of-plane direction. For Néel skyrmions –instead– the curl of the magnetization lies in the specimen plane, and therefore no contrast is visible for perpendicular illumination. The micrograph in Fig. 5.8b (Néel skyrmions in a Pt-Co multilayer), is obtained with the specimen rotated by 30°, so that a nonzero projection of $\nabla\times\boldsymbol{M}(x,y,z)$ would be along $\hat{z}$. The resulting contrast is constituted by a pair of brigth and dark lobes, separated along the tilt axis direction. When the tilt is inverted, the contrast inverts from dark to bright and vice versa.

While I carried out measurements on both Bloch and Néel skyrmions, in the following I will focus on Bloch skyrmions only, and in particular in FeGe, which can be considered as a prototypical metallic chiral magnet, with nearly-room temperature Curie temperature. Another substantial difference one should mention is traced between proper bulk samples [425] and thin (though monocrystalline) samples [147]. Indeed, when the thickness of the specimen is smaller than the wavelength associated with the inverse of the wave vector in the conical state, skyrmions can be stabilized in a wider area of the phase diagram. This is the general case for

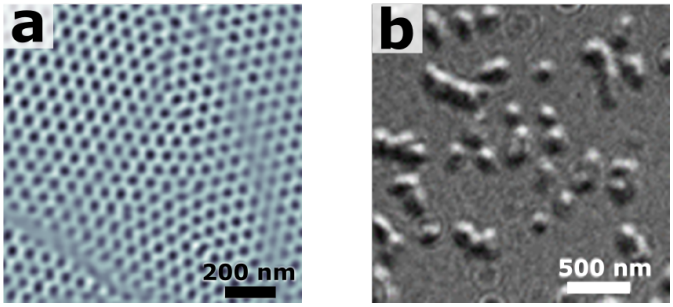

Figure 5.8 – Bloch and Néel skyrmion imaging in LTEM. **a**: Bloch skyrmion lattice (SkL) in FeGe, with specimen tilt 0°. Here $T = 200$ K, and $B \approx 500$ G. **b**: Néel domain walls and compact skyrmions in a Pt-Co multilayered structure. The specimen tilt is 30°, $T = 296$ K (RT), and $B = 0$ G after having created the skyrmions at $B \approx 1100$ G.

most of the TEM specimens, including FeGe [465].

5.3 Supercooled metastable Bloch skyrmions in FeGe: laser-driven creation

The creation, annihilation and motion of skyrmions in topological magnets[10] offer interesting perspectives for spintronics and data storage devices [455, 466]. While the former requires a simple and energy efficient way of manipulating the magnetic states, the latter aims at a fast and reliable way of writing/erasing and reading of individual skyrmions or skyrmion lattice segments in a confined volume. Furthermore, the study of the dynamics of the topological charge emergence introduces the concept of time into the physics of topological matter. Therefore, investigating the speed limit of skyrmion creation and annihilation is paramount for both fundamental and applied perspectives.

In general, the rate of skyrmions appearance as well as their persistence range in the host material's phase diagram depend on the balance between thermodynamic and topological stability [426]. Significant advances have been achieved in the control and manipulation of skyrmions in various hosting systems, ranging from insulating [467–471] to metallic [425, 465, 472–474], bulk and nanostructured helimagnets, to ultrathin heavy metals/ferromagnetic multilayered amorphous or polycrystalline films [475–478]. To date, two approaches compatible with current technology have been demonstrated: the application of an electric field, which leads to the skyrmion lattice rotation in insulating Cu_2OSeO_3 [467, 470], and spin-transfer torque induced skyrmion motion at ultralow current flow in metallic systems [472–474, 476, 479, 480].

As interesting alternatives, it has been shown that nanosecond magnetic field pulses can lead to the appearance and precession of skyrmions and skyrmion lattice segments [469, 477, 481], and it was demonstrated that collective modes of the skyrmion lattice were successfully in-

[10] We refer here generically to magnetic systems hosting topologically-protected spin structures.

duced by femtosecond (fs) laser pulses via the inverse Faraday effect, in simple words providing an effective magnetic field ultrashort pulse [469]. However, all of these observations were obtained via ensemble measurements and, to date, no spatially-resolved information on the dynamical response of skyrmions to time-varying stimuli and their intrinsic creation and annihilation speed is available. Such an information, besides addressing the fundamental question of how fast skyrmions can be created, is of pivotal importance for understanding the role of defects, edges and nanostructuring on the control of skyrmions. Furthermore, the creation or annihilation of skyrmions solely by optical pulses has remained elusive so far and would provide a unique handle in magneto-optical devices.

In a recent body of work, magnetic bubbles[11] were photogenerated in thin-films of ferrimagnetic rare earth-Fe-Co alloys [483–486]. Such magnetic textures are stabilized by uniaxial anisotropies and dipole-dipole interaction. The mechanism for their creation is based on the transient local heating above the Curie temperature [484, 487, 488] induced by a circularly polarized fs laser pulse [483–485]. Upon relaxation, the switched region defines the core of the magnetic bubble, and its size (≈ 0.3 μm or larger [485]) and shape are determined by the beam profile and intensity. Skyrmions in chiral magnets are fundamentally different from the magnetic bubbles. They are stabilized by the competition between the magnetic exchange and the DMI, and present a continuously whirling distribution of spins with a fixed chirality [455], determined solely by the crystal structure chirality. Such a spatial texture can be dramatically confined (down to few nm), and is intrinsically determined by the properties of the host material.

In the following, I report the generation and dynamical evolution of skyrmions in the prototypical itinerant chiral magnet FeGe, initiated by laser-induced heat pulses. Contrary to the previously reported mechanisms [367, 368, 485, 488],[12] our approach allows the creation of skyrmions without transiently reaching the paramagnetic state. Moreover, their size is independent on the laser beam diameter and fluence. These experiments provide an example of the optically driven edge-injection of topological charges.
To determine the time needed for skyrmions to be created or erased by laser pulses, we performed a combination of in-situ cryo-LTEM and nanosecond pump-probe cryo-LTEM (Fig. 5.10a). The in-situ cryo-LTEM are performed in Fresnel configuration at camera-rate temporal resolution (ms) using the continuous wave electron beam generated thermo-ionically, upon in-situ pulsed optical excitation of the specimen with tunable fs source (see Sec. 1.3).

[11] Magnetic bubbles [457, 482] are spin textures with a uniformly magnetized core separated from the oppositely magnetized surrounding by a domain wall. They are usually topologically trivial but can as well have non-trivial topological charges (chiral bubbles), as skyrmions. Unlike skyrmions, whose topological charge is defined by the sign of the DMI, the topological charge of magnetic bubbles is not uniquely given by the material properties, although the magnetization textures can be engineered by nano-fabrication, for example tuning the dipole-dipole interaction via changes of a thin film thickness.

[12] So far, experimental and theoretical efforts approached the problem by modeling a strongly localized heat excitation that locally favors spin flips, which during the cooling down rearrange in a skyrmion configuration.

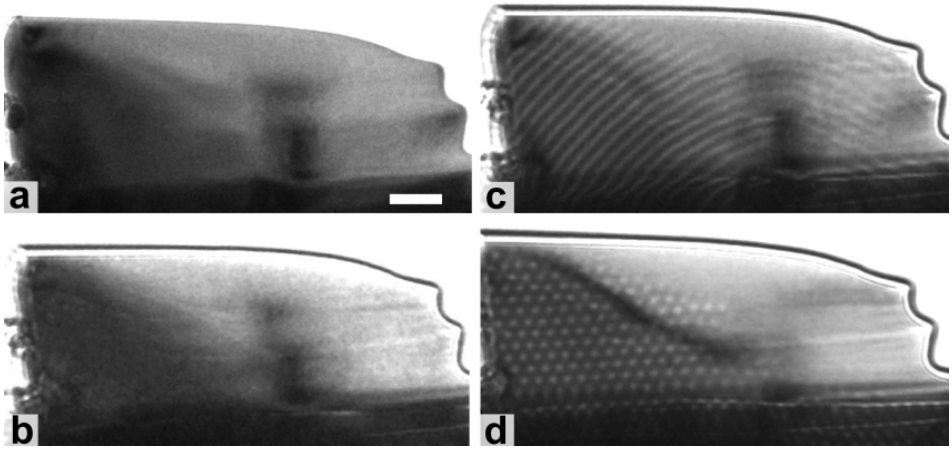

Figure 5.9 – Static LTEM characterization of the FeGe lamella. **a**: Bright field (BF) image (in focus): structural contrast. **b**: LTEM micrograph in the paramagnetic state, $T > T_C$: no magnetic contrast. **c**: LTEM micrograph for nearly-zero-field slow cooling to $T < T_C$. **d**: Same, for slow high-field-cooling at ~ 500 G, $T < T_C$. The sample becomes thicker in the bottom part, and is there connected to a Cu 'Omniprobe' TEM grid by a Pt contact. The scale bar in a is 250 nm and holds for all micrographs.

Nanosecond time-resolved stroboscopic experiments were carried out in pump-probe mode, as explained in details in Sec. 1.4, and sketched again here in Fig. 5.10a. The laser spot size was kept at least 30 times larger than the sample lateral dimension providing homogeneous illumination conditions.
The 60 nm thick FeGe sample was prepared by Ga ions FIB milling from a bulk FeGe crystal, employing a FEI 600 Nanolab dual beam system. The lamella thickness was estimated in situ from the percentage of inelastically scattered electrons, and the crystallinity of the specimen checked also in situ by selected-area electron diffraction (SAED). The sample was inserted in a liquid nitrogen cryogenic holder, and the external perpendicular magnetic field was controlled by variable objective lens excitation. The phase diagram of our nano-slab was determined by performing cryo-LTEM experiments at different temperatures and under different applied magnetic fields. A phase diagram sketch based on these experiments is depicted in Fig. 5.10b. The typical contrast for the different phases is displayed in Fig. 5.9, from a static characterization. Fig. 5.9a refers to a bright field (BF) image, outlining the shape and structural contrast. The central-left and bottom part of the specimen is a single crystal, while the top-right strip is polycrystalline, and does not show long-range ordered spin arrangements.[13] Fig. 5.9b represents the paramagnetic phase probed by cryo-LTEM, and displaying no contrast but the Fresnel fringes at the edges of the specimen. The imaging defocus length has been set here to ≈ 380 μm, and is roughly valid (±25%) for all the LTEM micrographs of the section. When cooled down below the Curie temperature, $T_C \approx 278$ K, in the minimum magnetic field

[13] In most of the conditions, actually, it does not show any visible magnetic contrast in LTEM. However, at low temperatures the system can be supercooled in such a way to show tiny (< 50 nm) spots of magnetic origin that appear very pinned and do not arrange in a lattice. The mechanism for the creation may be similar to ref. [489].

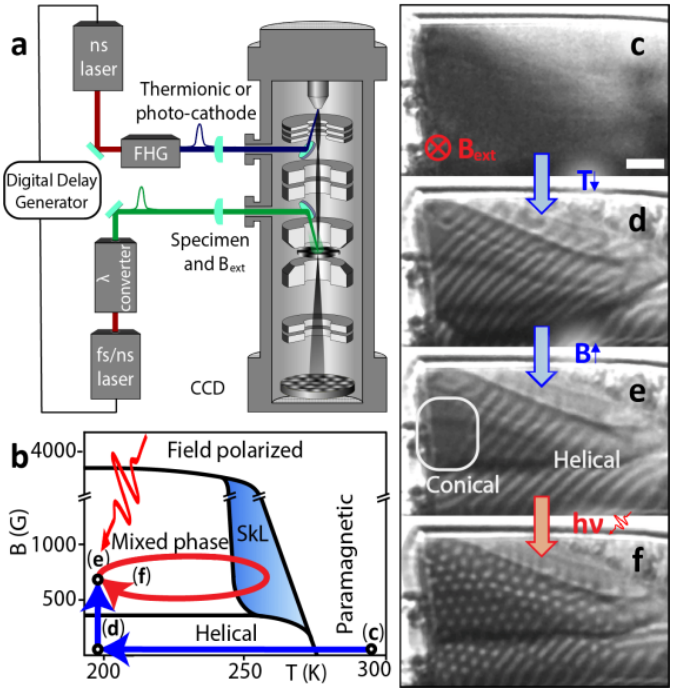

Figure 5.10 – Schematics of the skyrmion photocreation. **a**: A sketch of the experimental setup for in-situ and pump-probe cryo-Lorentz microscopy. **b**: Magnetic phase diagram of the FeGe nano-slab, as a function of temperature and perpendicular external magnetic field. Important paths in the phase diagram are drawn as arrows and discussed in the text. SkL indicates the skyrmion lattice. **c**-**f**:, Lorentz-Fresnel micrographs of the FeGe nano-slab, corresponding to the relative points in panel b. The skyrmion lattice in panel f is created by NIR fs laser pulses. Dark horizontal lines in the images are bent contours, and do not carry magnetic information. The scale bar is 250 nm.

achievable in our setup, 170 G, the material transforms to the helical phase, which is visible in LTEM as stripes [490], see Fig. 5.9c. This state is reached upon slow ($\sim K/s$) cooling.[14] Finally, Fig. 5.9d shows a well-ordered SkL obtained by field cooling the specimen at ~ 500 G.

The photocreation experiment has been designed following the c→d→e→f path in the phase diagram (Fig. 5.10b). Panels c and d are roughly equivalent to Fig. 5.9b and c.. When at low temperature (200 K) the perpendicular external field is increased to 400 G, the conical phase –whose contrast is indistinguishable from the field-polarized state in LTEM– is expected to be found based on previous experiments on wedged samples [491] and theoretical considerations [492]. In our sample, we observe either a coexistence of conical and helical phase (as in Fig. 5.10e), or the skyrmion phase, depending on the path followed in the phase diagram. The SkL is the thermodynamic ground state in the narrow region of phase space visible in Fig. 5.10b, above a characteristic field-dependent temperature $T_{\mathrm{SkL}\uparrow}$ irrespective of the initial magnetic texture, and, once formed, was observed to persist upon field cooling down to the

[14] We did not observe and do not expect a dependence on the cooling rate for helical state near T_C.

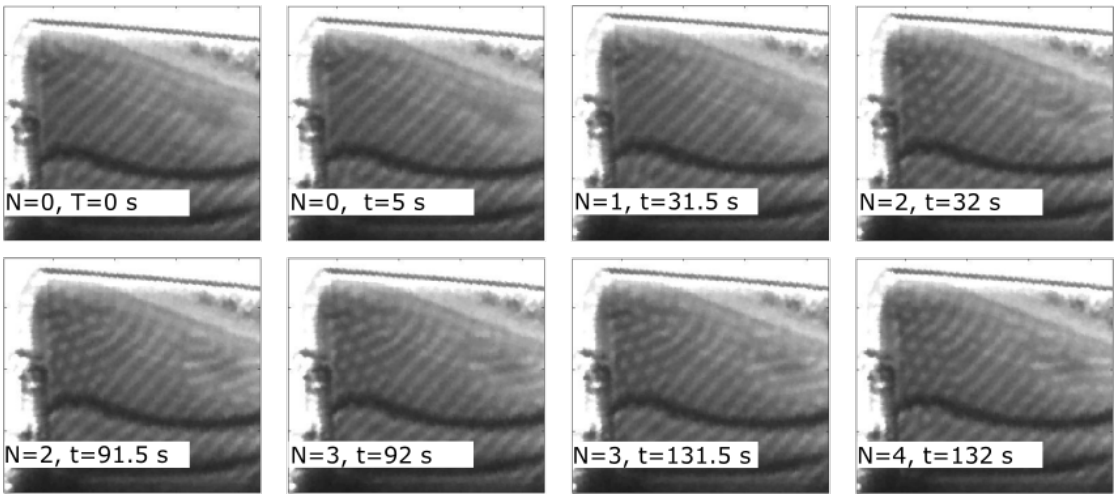

Figure 5.11 – Selected frames from the single shot photocreation. The full video can be seen in ref. [144]. N is the cumulative number of laser pulses shined, t the laboratory time. The frames are acquired sequentially. We see that the magnetization pattern is stable until a laser pulse is shined to the specimen. The transient evolution is not resolved by the slow camera-rate experiment, but after the creation, the pattern is again stable. Each frame is integrated for 0.5 s, with $T = 213$ K and $B = 700$ G.

lowest temperature that we could reach in our setup, 100 K. Skyrmions are therefore created as the ground state in the blue-colored area in Fig. 5.10b, comprised between $T_{\mathrm{SkL}\uparrow}$ and T_{C}, where both temperatures depend on the applied magnetic field. In other words, the magnetic state of the sample in the "Mixed phase" region of the phase diagram strongly depends on the field-dependent cooling and heating history, and on the previous magnetic field cycles at low temperature, highlighting the hysteretic nature of the magnetic phases in FeGe. The investigation of the complex history-dependent phases in chiral magnets is actually an active research field in itself [426, 489, 493–498].

To be clear, Fig. 5.10b is the *warming* phase diagram, and is tediously measured as follows: the sample is nearly-zero-field cooled to a set temperature T (~ 200 K), then the magnetic field increased to a value B_{ext}, and the specimen slowly heated, while keeping track of its magnetic phase. Once above the Curie point, the spin system resets its memory, and the experiment is repeated, with a new B_{ext}.[15]

The initial state for the photocreation experiments was hence prepared via the c→d→e path depicted in Fig. 5.10b, so that the sample was predominantly in the conical/helical phase (Fig. 5.10e), with no skyrmion present.

From this region of the phase diagram, upon the in-situ application of laser pulses, it is possible to write skyrmions in the material, see Fig. 5.10f. The fs single pulse experiments were conducted employing a mechanical shutter chopping a 20 Hz repetition rate beam. In

[15] This procedure has been carried out for fields $\lesssim 1800$ G, see for instance Fig. 5.14b; for higher fields the contrast becomes less clear (in absence of re-alignment), and the phase diagram interpolated up to where the specimen enters unmistakably into the field-polarized phase for $B_{\mathrm{ext}} \gtrsim 3600$ G.

ref. [144] the full camera-rate movies for the sequential laser-induced skyrmion creation are available; here we report a selected frame choice (Fig. 5.11 and Fig. 5.12), representing the evolution of the magnetization pattern. In Fig. 5.11 it is shown that the magnetization state is influenced solely by the pulse excitation, and does not evolve further, after a transient time, which for now we can only say it is shorter than ~ 100 ms.[16] In Fig. 5.12 the gradual filling of the lamella with skyrmions in displayed. We see that each laser pulse adds on average some new skyrmions to the lamella. The skyrmions are always created at the edges, and the contrast gradually migrates toward the inner specimen region. This effective phase boundary movement progresses mostly by breaking helices into merons and again to break the helical segment to create skyrmions. Skyrmions at the phase boundary display often irregular shapes, and their arrangement incorporates a high density of crystallographic defects, typically 5-7 dislocations. The creation at each pulse is stochastic, not deterministic, and it is interesting to note that the fluctuations in the magnetic contrast are likely to be present near the phase boundary, but not at the inner part of the SkL phase, where skyrmions tend to form a more regular lattice, and result mostly unaltered by the following laser pulses.

Skyrmions can then be fully erased by walking into the helical or field polarized phases and back, just by increasing or decreasing the external magnetic field, at constant temperature. Remarkably, large skyrmion lattice segments can be also erased by high fluence optical pulses, see Fig. 5.13 and discussion at the end of this section. We found that starting from 233 K, in a magnetic field of 400 G, a single 1.57 eV, 60 fs optical pulse of as little as 2 mJ/cm^2 is necessary to create a cluster of 10 to 14 skyrmions. Given the typical skyrmion diameter of 70 nm, and the knowledge of FeGe optical absorption, a rough estimate of the optical energy expense is $1 \cdot 10^{-14}$ J/skyrmion, offering interesting perspectives for energy efficient data storage [499, 500].
The optical energy expense to create a skyrmion was deduced from the absorbed optical fluence and the knowledge of the spot size of 80 μm and the average area occupied by a skyrmion (approximately 1400 nm^2).

To determine the mechanism for the light-induced skyrmion writing, we measured a fluence-dependence series and identified the energy per pulse necessary to create skyrmions starting from the different positions in the phase diagram, indicated by open circles in Fig. 5.14a. The experiments have been carried out with a 20 Hz pulse train, in order to suppress CW heating effects. We estimated the threshold value by observing the magnetic pattern and gradually increasing the laser illumination fluence.

The critical fluence is taken as the value to create well defined skyrmions, and its error bar (approximately 18%) is estimated by repeating the same experiment three times. The distribution of threshold values obtained for the different sample conditions is plotted as a color map in Fig. 5.14a. The threshold values are expressed in eV/Fe site, which is calculated from the

[16] The temporal resolution in this experiment is 500 ms, limited by the detector acquisition time, but it is better than ~ 100 ms for camera visualization, without data saving.

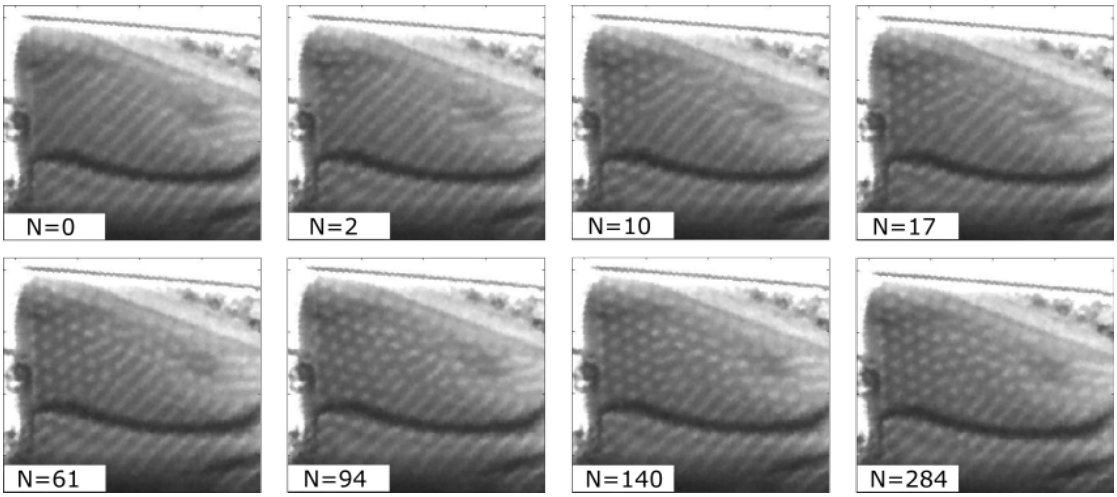

Figure 5.12 – Progressive filling of the specimen by single-pulse SkL photocreation. The images are selected frames from the full movie that can be found in ref. [144]. Each frame was acquired after the sample being illuminated by the number of pulses indicated in each panel. The frames were acquired sequentially, with the mechanical shutter for the laser synchronized with the acquisition camera. Each frame is integrated for 0.5 s, with $T = 213$ K and $B = 700$ G.

measured incident threshold laser fluence, knowing the penetration depth and reflectivity of FeGe from ref. [501], which are about 23 nm and 57%, respectively. In the graph of Fig. 5.14a, we also plot both the warming (red dots) and cooling (dashed red line) skyrmion stability regions of the material measured in absence of any photoexcitation. Above $T_{\mathrm{SkL}\uparrow}$ the skyrmion lattice forms thermally without external stimuli.
As visible, at lower temperatures a larger energy is required to create skyrmions, suggesting that the light-induced temperature rise in the material is responsible for their appearance. To test this hypothesis, we calculated the optical energy needed to cross $T_{\mathrm{SkL}\uparrow}$ as a function of the starting temperature for both the top and bottom surfaces of the sample. Two temperature evolution models were used. For the sub-10 ns dynamics, we used the two-temperature model (2TM) by Allen [502]. The thermal constants were taken from ref. [503] while the electron-phonon relaxation constant was estimated from ref. [502]. On the longer time scales, we have solved the one-dimensional heat diffusion equation on a length-scale of 40 times the sample size (real size of 500 nm was used). Having the laser spot much larger than the sample size, it was modeled by a homogeneous 20 ns long heat source. The Wiedemann-Franz law was used to estimate the heat conductivity from electrical transport data [504]. The quench rate was estimated from this solution at T_{C}, and it is of the order of K/µs.
The laser pulse energy needed to exceed $T_{\mathrm{SkL}\uparrow}$ for top and bottom surfaces are represented as solid red and blue lines in Fig. 5.14b, respectively. The measured absorbed laser energy threshold values as a function of the starting temperature for a magnetic field of $B = 750$ G and $B = 1040$ G are also displayed as red and green symbols, respectively. The experimental laser energy absorbed by the sample required to create skyrmions largely exceeds the theoretical value for the top surface and lies somewhat below the value for the bottom surface, suggest-

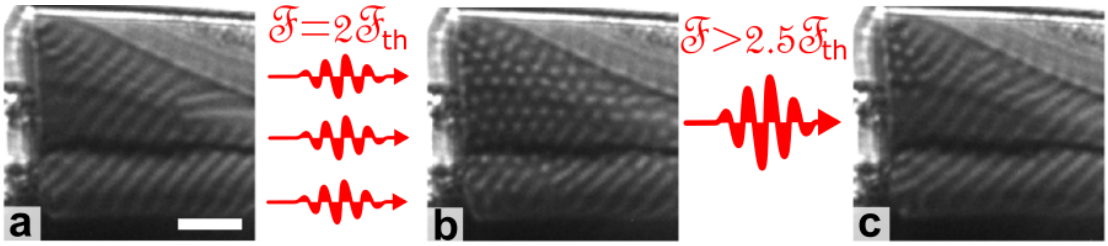

Figure 5.13 – SkL optical annihilation by higher-fluence pulses. **a**: Initial state, at 213 K and 950 G: the magnetization pattern is helical. **b**: Same, after photoexcitation with a train of pulses with $\mathcal{F} \approx \mathcal{F}_{th}$, where $\mathcal{F}_{th}$ is the threshold fluence: skyrmions have been created in the majority of the field of view, and the more pulses one applies, the larger the area covered by skyrmions. **c**: The configuration in b is excited by a single pulse with higher fluence, $\mathcal{F} \gtrsim 2.5\ \mathcal{F}_{th}$: most of the specimen regains the original helical magnetization, and only few skyrmions survive in the top-left corner, independently on the number of subsequent pulses applied to the system. Scale bar 250 nm.

ing that sufficiently thick portions of the slab surpass the critical temperature to induce the skyrmions formation. Importantly, the electronic and lattice temperatures follow a different dynamical evolution upon excitation by fast laser pulses. The light predominantly couples to the electronic subsystem resulting in a transient increase of the electronic temperature. The equilibration of the electronic and structural subsystems is mediated by the electron-phonon coupling and can be described by the mentioned 2TM [502]. Typically, the shorter the light pulses, the higher the electronic temperature, and the larger its difference to the lattice temperature at the early stage of the dynamics. Such a behavior is depicted in Fig. 5.15a, where the temporal evolution of the electronic and lattice temperature was obtained via the 2TM as a function of pulse duration.

To disentangle the role of these two subsystems, we performed a series of skyrmions photocreation threshold measurements as a function of the pulse duration, shown in Fig. 5.15b. It is evident that the threshold is independent of the laser pulse duration, suggesting that the photoinduced electronic temperature jump does not play a role in the formation of the skyrmions. To corroborate this idea, we show the photo-induced electronic and lattice temperature jump for different laser pulse durations above and below the threshold for photo-generating skyrmions, Fig. 5.15 and d. When only the electronic temperature far exceeds the critical value $T_{SkL\uparrow}$, no effect is observed on the magnetic pattern; conversely, if the lattice temperature is above $T_{SkL\uparrow}$, skyrmions are observed in the sample.
Moreover, the threshold for the photo-generation of skyrmions is also independent on the photon energy between 0.8 and 1.57 eV (see Fig. 5.16). This is expected for a thermally-induced phenomenon considering the rather featureless optical conductivity of FeGe in such an energy range [501].

The fact that a very large electronic temperature does not result in observable changes of

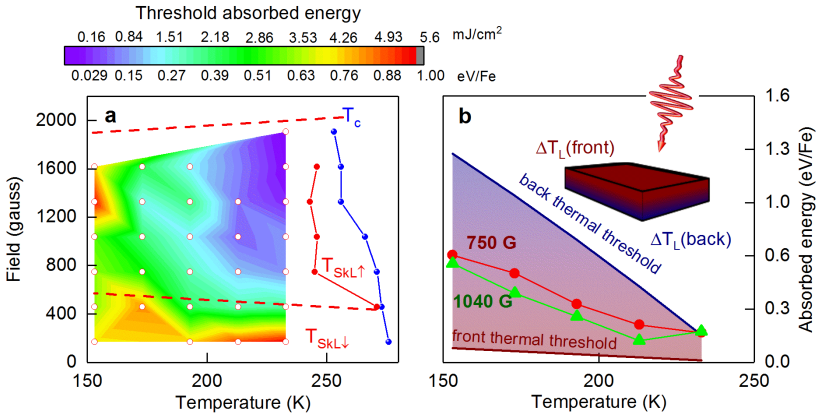

Figure 5.14 – Skyrmion photocreation phase diagram. **a**: The color map encodes the skyrmion photocreation energy threshold as a function of temperature and magnetic field. 60 fs long, linearly polarized 1.57 eV pulses were used. For comparison, the temperature at which skyrmions form upon field-warming ($T_{\mathrm{SkL}\uparrow}$) and the critical temperature for the skyrmion to paramagnetic transition (T_{C}) were measured experimentally and are shown as full symbols. The region of stability of the skyrmions after field cooling is enclosed between the straight red dashed lines $T_{\mathrm{SkL}\downarrow}$. **b**: Temperature dependence of the threshold at selected magnetic fields. For comparison, the fluence values required to warm-up the lattice to $T_{\mathrm{SkL}\uparrow}$ at the front (top) and back (bottom) surfaces of the sample are shown in red and blue respectively, for $T_{\mathrm{SkL}\uparrow} = 243$ K.

the system's magnetization, together with the insensitivity of the threshold to the driving pulses duration and wavelength, implies that the mechanism for creating skyrmions is a slow process. In the single-pulse writing experiments, the phase diagram during the excitation is the warming phase diagram, while shortly after the excitation (~ 100 ns) it switches into the cooling phase diagram, see Fig. 5.17 violet arrow, following an evolution similar to supercooling [494, 505]. The sudden quench of thermal fluctuations (~ K/µs) that takes place after the initial temperature jump freezes skyrmions in regions of the phase diagram where they were not present before the arrival of the laser pulse. This is consistent with previous reports showing that fast cooling rates, in the range of K/s, can homogeneously freeze-in skyrmions in different regions of the phase diagram [495]. Importantly, in our case the skyrmion creation occurs in the limited region of the sample either close to an edge or at the interface between magnetic phases, whilst the majority of the sample conserves its magnetic state (see Fig. 5.12). This is different from the slower equilibrium-cooling experiments when most of the sample converts into the skyrmion lattice, and showcases the role of the cooling rate in tipping the balance between topological protection and thermal fluctuations. In fact, the emergence of the skyrmions is expected to happen at the edges of the sample where such a balance is altered by the breaking of topological protection. This has been experimentally observed upon magnetic field variation [506] and rationalized theoretically for the pulsed suppression of the magnetization [507].

To test the reaction speed of the sample's magnetization to a sudden temperature jump, we

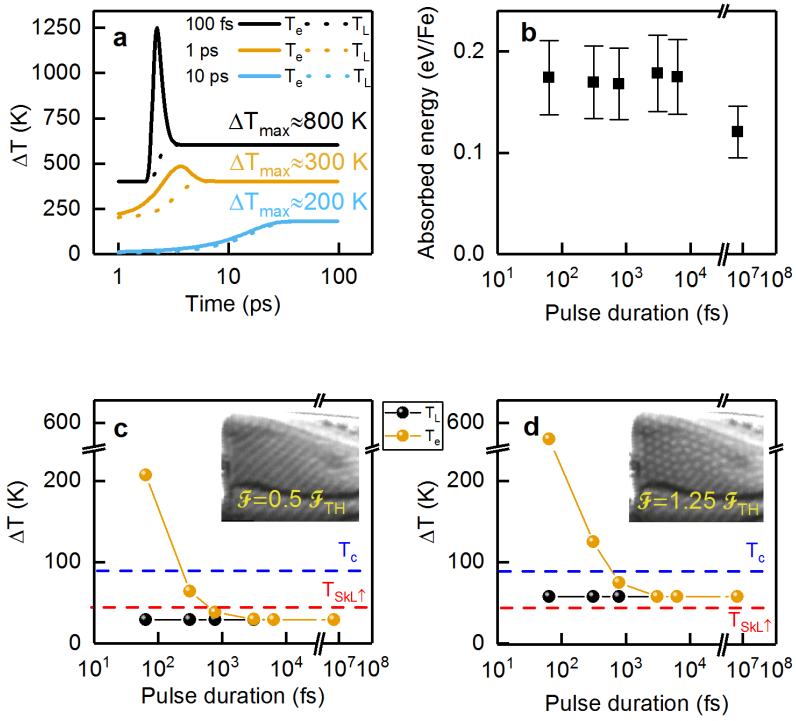

Figure 5.15 – Electron and lattice temperature evolution. **a**: Two-temperature model calculation of the electronic and lattice temperature evolution for three pulse durations, 100 fs, 1 ps, and 10 ps at the top surface of the sample (solid and dashed for electronic and lattice temperatures, respectively). **b**: Absorbed energy threshold for photocreation of skyrmions as a function of pulse duration. **c**,**d**: Peak variation of the depth-averaged electronic and lattice temperatures as a function of pulse duration at one half and just above the threshold fluence values. Red and blue dashed lines indicate the temperature variation required for thermal creation of skyrmions and critical temperature T_C upon field-warming. The insets show the cryo-LTEM images taken upon photoexcitation of the sample at 233 K and 400 G with 1.57 eV, 60 fs laser pulses.

performed a ns pump-probe experiment in proximity of the skyrmion to paramagnetic phase transition, Fig. 5.17 mustard yellow arrow. A 20 kHz train of 25 ns, 2.33 eV laser pulses with variable fluence was used to perturb the skyrmion lattice close to the critical temperature T_C. The evolution of the skyrmion lattice was monitored via a synchronized train of 30 ns-electron pulses, and the time delay was varied electronically, as sketched in Fig. 5.10a. We have chosen to study stroboscopically this transition because it is fully reversible when crossed at the slow rate of $<$ K/s , both heating and cooling, and does not involve any metastable state (see Fig. 5.18). The FeGe slab was kept at 257 K and 950 G.[17]

[17] We investigated here a different region of the same sample, with a large SkL area that could facilitate the analysis.

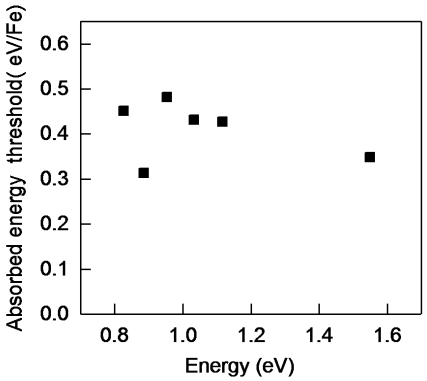

Figure 5.16 – SkL photocreation threshold dependence on the photon energy in the NIR range. The different photon energies were generated via OPA frequency conversion, see Sec. 1.3 and Sec. 4.3.2.

A portion of a typical Lorentz micrograph of the skyrmion lattice recorded with photoelectrons is depicted in Fig. 5.19a, together with its spatial Fourier Transform Fig. 5.19b. The temporal evolution of the skyrmion lattice constant, orientation angle, and magnetization strength for two fluences (approximately 1.5 and 5 mJ/cm^2) are plotted in Fig. 5.19c top and bottom panels, respectively. We found no significant modification to either the skyrmion lattice constant or its orientation angle. As the skyrmion lattice constant is given by the ratio between the DMI D and the exchange constant J ($d = 4\pi J/|D|$), and the two are independent physical quantities, it is reasonable to conclude that neither D nor J are affected by the laser pulses on the ns time scale. Contrary, the intensity of the magnetic contrast, estimated as the intensity of the magnetic Bragg peak obtained by Fourier transforming the real-space image, is found to decrease by 6 and 49 percent for 1.5 mJ/cm^2 and 5 mJ/cm^2 fluence, respectively. The time scale for the recovery of the magnetization depends on the fluence and reaches ~ 9 µs for the strongest photoexcitation tested (5 mJ/cm^2), confirming the idea that the magnetization dynamics is governed by the heat diffusion. These pump-probe data were fitted with a finite error-function rise-time exponential relaxation function. While the heat diffusion fit is more appropriate, it is not feasible to analytically solve the equation accounting for the actual shape of the sample and the heat sink. The exponential fit gives a reliable estimate of the initial remagnetization time scale.

We can now further understand the writing process. After the photon absorption, the energy is transferred to the lattice on the few-ps time scale. The consequent excitation of magnetic fluctuations favors the skyrmion creation at the sample edges and magnetic phase boundaries as long as $T > T_{\mathrm{SkL}\uparrow}$. After ~ 1 µs, the system supercools down into the region of the phase diagram ($T < T_{\mathrm{SkL}\uparrow}$) where magnetization does not further evolve. Since we only observe the formation of up to 14 skyrmions with each pulse and the optically written skyrmion lattice is highly disordered (compare Fig. 5.10f and Fig. 5.9d or Fig. 5.19a), we can claim that few µs are not sufficient for establishing long-range skyrmionic order, and skyrmions are formed as individual self-assembling entities.

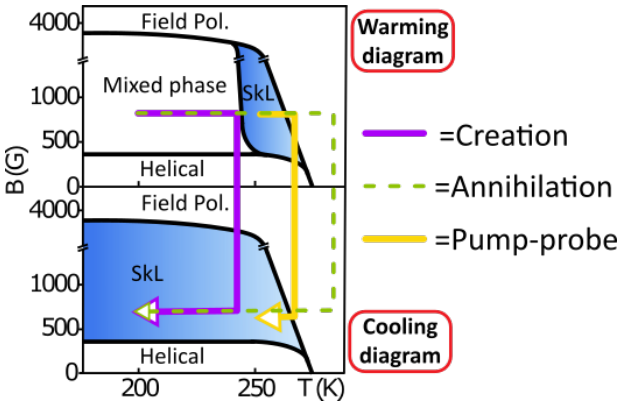

Figure 5.17 – Explanatory diagram of the experiments (arrows indicate temperature evolution). In the laser-induced skyrmion creation experiment the system can be considered in first approximation to switch from field-warming to field-cooling diagram. The skyrmion creation probability depends on the time t spent by the system such that $T_{\mathrm{SkL}\uparrow} < T(t) < T_{\mathrm{C}}$. For the laser-induced skyrmion erasing, $\max T(t) > T_{\mathrm{C}}$, which causes sample demagnetization before the field cooling brings the system at low temperature. For the pump-probe experiments of Fig. 5.19 the system's base temperature is between $T_{\mathrm{SkL}\uparrow}$ and T_{C}, and lasers induce a (partial) transient demagnetization.

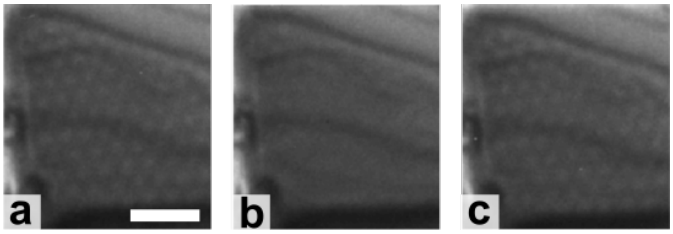

Figure 5.18 – Reversibility of the adiabatic paramagnetic transition at 950 G. **a**: Micrograph for $T \approx T_{\mathrm{C}} - 5$ K. **b**: Same, for $T \approx T_{\mathrm{C}} + 1$ K upon slow heating ($\lesssim 0.2$ K) from a. **c**: Same, for the initial temperature as in a, after slow cooling ($\lesssim 0.2$ K) from b. Scale bar 250 nm.

To corroborate this idea, see Fig. 5.17 dashed green arrow, we also performed an experiment where a single high-fluence pulse was applied to the sample in which the skyrmion lattice was already photoinduced (Fig. 5.13b). The system is first prepared as in the photocreation experiments via near-zero-field cooling and subsequent field excitation (Fig. 5.13a). When the excitation fluence is set to $\approx 2\mathscr{F}_{\mathrm{th}}$, the pulses induce skyrmion creation, and any extra pulse increases on average the number of skyrmions observed in the lamella (Fig. 5.13b), analogously to Fig. 5.12. From this configuration, if a single laser pulse with higher fluence ($> 2.5\mathscr{F}_{\mathrm{th}}$) is applied, the skyrmions in the specimen are largely erased. At this photoexcitation level, the sample transient temperature exceeds T_{C}, resulting in its complete demagnetization. As a consequence, the whole skyrmion lattice transiently disappears, and only few skyrmions reform during cooling close to the edge of the specimen, see Fig. 5.13c. Importantly, the

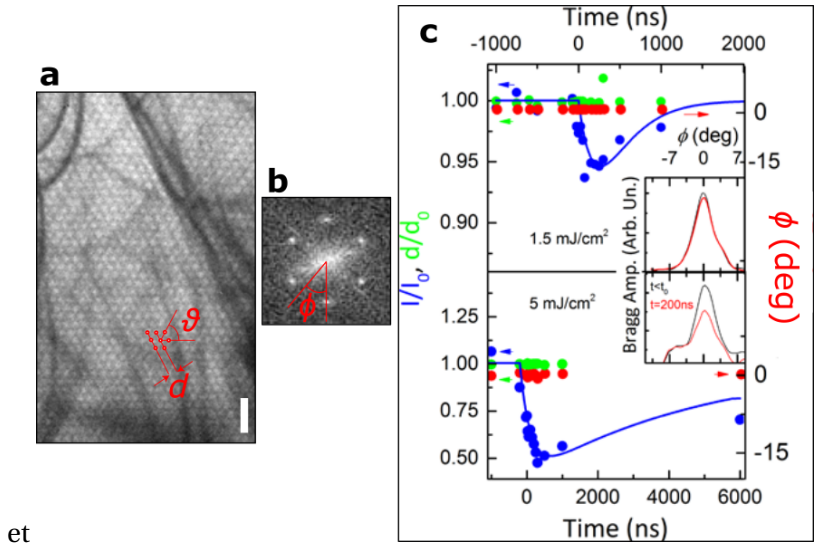

et

Figure 5.19 – Nanosecond pump-probe LTEM on skyrmions. **a**: Portion of the skyrmion lattice micrograph recorded with 25 ns photoelectron pulses. Scale bar is 250 nm. **b**: Spatial Fourier transform of the Lorentz micrograph, highlighting the SkL 6-fold symmetry. **c**: Pump-probe temporal dynamics of the skyrmion lattice parameters: skyrmion-skyrmion distance (d/d_0, with d_0 the distance at equilibrium, green symbols – left axis), orientation angle (red symbols – right axis) and magnetization strength (I/I_0, where I_0 is the magnetic Bragg peak intensity at equilibrium, blue symbols – left axis) at approximately 1.5 and 5 mJ/cm^2 fluence, top and bottom panel respectively. The solid blue curves are fits to the magnetization strength via a finite rise-time exponential relaxation function, yielding recovery time constants of 0.75 ± 0.3 µs at 1.5 mJ/cm^2, and 9.3 ± 4.4 µs at 5 mJ/cm^2. The insets show the magnetic Bragg peak profile before the arrival of the pump pulse (black) and after 200 ns (red). The curves were obtained averaging over all six Bragg peaks after having verified that all have the same dynamics, ruling out distortions of the skyrmion lattice.

skyrmion cluster size does not grow with the number of pulses and its position and shape differ after each individual laser pulse, confirming that each time the skyrmion formation starts from the (transient) paramagnetic state and not from a spin-ordered state.

In summary, we have shown that skyrmions can be written in a FeGe nano-slab via illumination with optical pulses of different colors and duration. Our space-time resolved observations highlighted that the light-induced formation of skyrmions takes place at the boundaries between magnetic domains and in proximity of the sample edges. The writing and erasing speed of the skyrmions was found to be governed by the cooling rate following the laser-induced temperature jump. In the present case, the speed limitation is a direct consequence of the heat diffusion rate (K/µs) in our nano-fabricated slab. A different behavior may be expected in non-metallic skyrmion hosts where the optical absorption can exhibit large energy gaps and light-induced excitations can have longer lifetimes. In such systems, also electronic effects may influence the fast dynamics of the skyrmions.

5.4 Perspectives on laser-induced and time-resolved magnetic microscopy

With the work done, we have showed ways to influence magnetism with light pulses. Based on our results, we suggest that increasing the cooling rate up to K/ps by connecting the sample to a heat-bath should result in the efficient skyrmion optical erasing by strong ps pulses. Indeed, in such a way the system will spend too little time in the regions of the phase diagram where skyrmions are thermodynamically favored to be created, and possibly no skyrmion would be created during such ultrafast cooling. The writing process would still be done by long ns pulses, whose pulse duration determines the thermalization time, hence disentangling it from the heat diffusion time constant, which may always differ from sample to sample. With such method, the control of the skyrmion cluster size could be attained by varying the duration of the writing pulse.
Furthermore, the modulation of the topological landscape via nanofabrication would also allow to tune the creation/annihilation speed of the skyrmions and especially their stability against external perturbations [481, 508]. In this way, a deterministic optical creation of skyrmions may be attained –which could be the basis for the study of an all-optical write/erase prototype device.
It should also be mentioned that we discussed in the previous section the creation and annihilation of skyrmions, because it represents the neater and most relevant manipulation effect we observed in our system. However, light pulses could induce in the skyrmion-host material a plethora of irreversible effects, as lattice rotations, fluctuations between helical and skyrmion state, displacement of skyrmion clusters in a field-polarized background, et cetera. These phenomena are observed having a highly stochastic nature, and their exploitation in a controlled experiment should thoroughly designed. The ns pump-probe experiment has been performed in a condition for which the skyrmion lattice is partially demagnetized, but not completely. Based on the temperature calculations we performed (see Fig. 5.14), it is compatible with a top surface above T_C and a bottom surface still nominally in the magnetically ordered state. At higher fluence, we could not follow the dynamics stroboscopically because the process is not reversible: at each pulse the skyrmion order is destroyed completely, and once the system cools down between one pulse and the following, it goes to a different magnetic state, which for instance it may be a SkL with skyrmions slightly rotated and translated with respect to before. In such a way, no real-space images can be acquired. Nevertheless, an approach based on small-angle electron diffraction may be adopted. There, a magnetically-ordered state which changes position every pulse would appear as a ring or points distributed on a ring-shaped area. As a consequence, the annihilation and creation timescales could be studied also in this regime. In particular, the two timescales can be different, for example the annihilation faster than the creation.
The laser-induced creation of skyrmions and skyrmionic textures will for sure continue with

different materials, also trying to exploit other mechanisms for the creation. For example, new experimental and theoretical studies were reported very recently, addressing the creation of large homochiral Néel bubbles and bubble lattices [509] with a laser-driven heat pulse, similarly to our work, and of isolated skyrmions in antiferromagnetic insulators [510], by inverse Faraday effect. It would be valuable to exploit the high electron temperature to complete the photoinduced creation of skyrmions on the ultrafast timescale (few ps), possibly induced by high fluctuations near T_C, analogously to the ultrafast creation of ferromagnetic vortices [505]. Still, our results pose some questions on the role of time scales in these processes and how fast they can be.
Furthermore, our observations on the stochasticity of the process are widely applicable and again can determine a serious limitation in the applications. While one may increase the writing reproducibility by inserting pinning sites and defects in general (which is particularly easy for interfacial skyrmions), it would come at the cost of reducing the skyrmion transport properties, which are desired for spintronics applications [466].
As hinted from Fig. 5.8b, we also carried out further experiments on a stacked Pt-Co multilayer with interfacial DMI. This system hosts Néel skyrmions [511,512] at room temperature, having a diameter $\sim$ 120 nm, and that can be imaged by LTEM in a tilted geometry [148,513,514], see Eq. 5.10 and Fig. 5.8b. Our preliminary laser-excitation experiments show that it is indeed possible to trigger the appearance of skyrmions and other labyrinth domains by using ultrafast laser pulses, although a high degree of pinning and stochasticity was present for our thin multilayer.

List of Figures

Acronyms

2TM two-temperature model.

AEM analytical electron microscopy.

ARPES angle-resolved photoemission spectroscopy.

BBO β-barium borate, β-BaB_2O_4.

BF bright field.

BLS Brillouin light scattering.

CARS coherent anti-Stokes Raman spectroscopy.

CBED convergent-beam electron diffraction.

CCD charge-coupled device.

CL cathodoluminescence.

CLA condensed lens aperture.

CMOS complementary metal-oxide semiconductor.

cryoEM electron cryomicroscopy.

CW continuous wave.

DC direct current.

DF dark field.

DFG difference frequency generation.

DLA dielectric laser accelaration.

DMI Dzyaloshinskii-Moriya interaction.

DOS density of states.

DP diffraction pattern.

DPC differential phase contrast.

DQE detector quantum efficiency.

DTEM dynamical transmission electron microscopy.

EDX energy-dispersive X-ray spectroscopy.

EEG electron energy gain.

EEGS electron energy gain spectroscopy.

EEL electron energy loss.

EELS electron energy loss spectroscopy.

EFTEM energy-filtered transmission electron microscopy.

EMCD electron energy-loss magnetic chiral dichroism.

EPFL École Polythechnique Fédérale de Lausanne.

FDTD finite-difference-time-domain.

FEG field-emission gun.

FEL free electron laser.

FIB focused ion beam.

FT Fourier transform.

FTIR Fourier-transform infrared spectroscopy.

FWHM full width at half maximum.

GIF Gatan imaging filter.

GMR giant magnetoresistance.

HDD high dispersion diffraction.

HPD hybrid pixel detector.

HRTEM high-resolution transmission electron microscopy.

HWHM half width at half maximum.

IR infrared.

LTEM Lorentz transmission electron microscopy.

LUMES Laboratory for Ultrafast Microscopy and Electron Scattering.

MAPS monolithic active pixel sensor.

MFM magnetic force microscopy.

MIR mid-infrared.

MOKE magneto-optical Kerr effect.

MRAM magnetoresistive random access memory.

MREELS momentum resolved electron energy loss spectroscopy.

NC nanocavity.

NIR near-infrared.

NP nanoparticle.

NV nitrogen vacancy.

NW nanowire.

OAM orbital angular momentum.

OPA optical parametric amplification.

PCB printed circuit board.

PINEM photon-induced near-field electron microscopy.

PSF point-spread function.

RF radio frequency.

RT room temperature.

SAM spin angular momentum.

SEM scanning electron microscopy.

SEMPA scanning electron microscopy with polarization analysis.

SkL skyrmion lattice.

SHG second harmonic generation.

SNOM scanning near-field optical microscopy.

SNR signal-to-noise ratio.

SPLEEM spin-polarized low-energy electron microscopy.

SQUID superconductiong quantum interference device.

SREELS spatially resolved electron energy loss spectroscopy.

STEM scanning transmission electron microscopy.

STM scanning tunneling microscopy.

STXM scanning transmission X-ray microscopy.

SUEM scanning ultrafast electron microscope.

TEM transmission electron microscopy.

THG third harmonic generation.

TIE transport-of-intensity equation.

tr-PEEM time-resolved photoemission electron microscopy.

UED ultrafast electron diffraction.

UEM ultrafast electron microscopy.

UHV ultra-high vacuum.

UTEM ultrafast transmission electron microscopy.

UV ultraviolet.

XMCD X-ray magnetic circular dichroism.

XRD X-ray diffraction.

YAG yittrium aluminum garnet, $Y_3Al_5O_{12}$.

ZLP zero-loss peak.

Bibliography

[1] Francesco Biamonti. *Vento largo*. Einaudi, Torino, 1991.

[2] R. L. Fork, B. I. Greene, and C. V. Shank. Generation of optical pulses shorter than 0.1 psec by colliding pulse mode locking. *Applied Physics Letters*, 38(9):671–672, 1981.

[3] D. J. Kuizenga. Mode locking of the cw dye laser. *Applied Physics Letters*, 19(8):260–263, 1971.

[4] Nobuhiko Sarukura, Yuzo Ishida, Hidetoshi Nakano, and Yoshihisa Yamamoto. cw passive mode locking of a Ti:sapphire laser. *Applied Physics Letters*, 56(9):814–815, 1990.

[5] D E Spence, P N Kean, and W Sibbett. 60-fsec pulse generation from a self-mode-locked Ti:sapphire laser. *Optics Letters*, 16(1):42–44, 1991.

[6] Donna Strickland and Gerard Mourou. Compression of amplified chirped optical pulses. *Optics Communications*, 55(6):447–449, 1985.

[7] Ahmed H Zewail. Femtochemistry : Atomic-Scale Dynamics of the Chemical Bond Using Ultrafast Lasers. *Angewandte Chemie International Edition*, 39:2586–2631, 2000.

[8] Claudio Giannetti, Massimo Capone, Daniele Fausti, Michele Fabrizio, Fulvio Parmigiani, and Dragan Mihailovic. Ultrafast optical spectroscopy of strongly correlated materials and high-temperature superconductors: a non-equilibrium approach. *Advances in Physics*, 65(2):58–238, 2016.

[9] Roberto Merlin. Generating Coherent THz Phonons with Light Pulses. *Solid State Communications*, 102(2):207–220, 1997.

[10] T. E. Stevens, J. Kuhl, and R. Merlin. Coherent phonon generation and the two stimulated Raman tensors. *Physical Review B*, 65:144304, 2002.

[11] Michael F. Becker, A. Bruce Buckman, Rodger M. Walser, Thierry Lépine, Patrick Georges, and Alain Brun. Femtosecond laser excitation dynamics of the semiconductor-metal phase transition in VO2. *Journal of Applied Physics*, 79(5):2404–2408, 1996.

[12] A. Cavalleri, Cs. Tóth, C. W. Siders, J. A. Squier, F. Ráksi, P. Forget, and J. C. Kieffer. Femtosecond structural dynamics in vo2 during an ultrafast solid-solid phase transition. *Physical Review Letters*, 87(23):237401, 2001.

[13] A. Cavalleri, Th Dekorsy, H. H.W. Chong, J. C. Kieffer, and R. W. Schoenlein. Evidence for a structurally-driven insulator-to-metal transition in VO2: A view from the ultrafast timescale. *Physical Review B*, 70:161102(R), 2004.

[14] Peter Baum, Ding-Shyue Yang, and Ahmed H Zewail. Four-dimensional Visualization of Transitional Structures in Phase Transformations by Electron Diffraction. *Science*, 318:788–792, 2007.

[15] D. Fausti, R. I. Tobey, N. Dean, S. Kaiser, A. Dienst, M. C. Hoffmann, S. Pyon, T. Takayama, H. Takagi, and A. Cavalleri. Light-induced superconductivity in a stripe-ordered cuprate. *Science*, 331:189–191, 2011.

[16] M. Mitrano, A. Cantaluppi, D. Nicoletti, S. Kaiser, A. Perucchi, S. Lupi, P. Di Pietro, D. Pontiroli, M. Riccò, S. R. Clark, D. Jaksch, and A. Cavalleri. Possible light-induced superconductivity in K3 C60 at high temperature. *Nature*, 530:461–464, 2016.

[17] L Stojchevska, I Vaskivskyi, T Mertelj, P Kusar, D Svetin, S Brazovskii, and D Mihailovic. Ultrafast switching to a stable hidden topologically protected quantum state in an electronic crystal. *Science*, 344:177–180, 2014.

[18] Shaul Mukamel. *Principles of nonlinear optical spectroscopy*. Oxford university press, New York, 1995.

[19] Matthias C. Hoffmann and József András Fülöp. Intense ultrashort terahertz pulses: Generation and applications. *Journal of Physics D: Applied Physics*, 44:083001, 2011.

[20] C Siders, A Cavalleri, K Sokolowski-Tinten, Cs. Tóth, T. Guo, M. Kammler, M. Horn von Hoegen, K.R. Wilson, D. von der Linde, and C.P.J. Barty. Direct Observation of Ultrafast Non-thermal Melting by Ultrafast X-ray Diffraction. *Science*, 286:1340–1342, 1999.

[21] G. Schütz, W. Wagner, W. Wilhelm, P. Kienle, R Zeller, R. Frahm, and G. Materlik. Absorption of Circularly Polarized X Rays in Iron. *Physical Review Letters*, 58(7):737–740, 1987.

[22] C. Jacobsen, S. Williams, E. Anderson, M.T. Browne, C.J. Buckley, D. Kern, J. Kirz, M. Rivers, and X. Zhang. Diffraction-limited imaging in a scanning transmission x-ray microscope. *Optics Communications*, 86:351–364, 1991.

[23] David B. Williams and Barry C. Carter. *Transmission Electron Microscopy*. Springer US, Boston MA, 2009.

[24] Max Knoll and Ernst Ruska. Das Elektronenmikroskop. *Zeitschrift für Physik*, 78(5-6):319–339, 1932.

[25] Ernst Ruska. The Development of the Electron Microscope and of Electron Microscopy (Nobel Lecture). *Angew. Chem. Int. Ed.*, 26(7):595–706, 1987.

[26] E. Abbe. Beiträge zur Theorie des Mikroskops und der mikroskopischen Wahrnehmung. *Archiv für mikroskopische Anatomie*, 9:413–420, 1873.

[27] M. Born and E. Wolf. *Principles of optics: electromagnetic theory of propagation, interference and diffraction of light*. Cambridge University Press, Cambridge, 7th edition, 1999.

[28] Louis de Broglie. Recherches sur la théorie des quanta. *Annales de Physique*, 3(10):22–128, 1925.

[29] Christoph Cremer and Thomas Cremer. Considerations on a laser-scanning-microscope with high resolution and depth of field. *Microscopica Acta*, 81(1):31–44, 1978.

[30] Christoph Cremer and Barry R. Masters. Resolution enhancement techniques in microscopy. *The European Physical Journal H*, 38:281–344, 2013.

[31] Stefan W. Hell and Jan Wichmann. Breaking the diffraction resolution limit by stimulated emission: stimulated-emission-depletion fluorescence microscopy. *Optics Letters*, 19(11):780, 1994.

[32] U. Dürig, D. W. Pohl, and F. Rohner. Near-field optical-scanning microscopy. *Journal of Applied Physics*, 59(10):3318–3327, 1986.

[33] Rolf Erni, Marta D. Rossell, Christian Kisielowski, and Ulrich Dahmen. Atomic-resolution imaging with a sub-50-pm electron probe. *Physical Review Letters*, 102(9):096101, 2009.

[34] O. L. Krivanek, N. Dellby, J. A. Hachtel, J. C. Idrobo, M. T. Hotz, B. Plotkin-Swing, N. J. Bacon, A. L. Bleloch, G. J. Corbin, M. V. Hoffman, C. E. Meyer, and T. C. Lovejoy. Progress in ultrahigh energy resolution EELS. *Ultramicroscopy*, 203:60–67, 2018.

[35] Joseph I. Goldstein, Dale E. Newbury, Joseph R. Michael, Nicholas W.M. Ritchie, John Henry J. Scott, and David C. Joy. *Scanning electron microscopy and X-ray microanalysis*. Springer, 2017.

[36] Ben G. Yacobi and David B. Holt. *Cothodoluminescence Microscopy of Inorganic Solids*. Springer Science & Business Media, 2013.

[37] Alexander Gubbens, Melanie Barfels, Colin Trevor, Ray Twesten, Paul Mooney, Paul Thomas, Nanda Menon, Bernd Kraus, Chengye Mao, and Brian McGinn. The GIF Quantum, a next generation post-column imaging energy filter. *Ultramicroscopy*, 110(8):962–970, 2010.

[38] M. Kuwahara, S. Kusunoki, X. G. Jin, T. Nakanishi, Y. Takeda, K. Saitoh, T. Ujihara, H. Asano, and N. Tanaka. 30-kV spin-polarized transmission electron microscope with GaAs-GaAsP strained superlattice photocathode. *Applied Physics Letters*, 101(3):033102, 2012.

[39] Xiuguang Jin, Burak Ozdol, Masahiro Yamamoto, Atsushi Mano, Naoto Yamamoto, and Yoshikazu Takeda. Effect of crystal quality on performance of spin-polarized photocathode. *Applied Physics Letters*, 105(20):203509, 2014.

[40] A. V. Crewe, D. N. Eggenberger, J. Wall, and L. M. Welter. Electron gun using a field emission source. *Review of Scientific Instruments*, 39(4):576–583, 1968.

[41] R. F. Egerton. Electron energy-loss spectroscopy in the TEM. *Reports on Progress in Physics*, 72(1), 2009.

[42] H.R. Hertz. Ueber einen Einfluss des ultravioletten Lichtes auf die electrische Entladung. *Annalen der Physic*, 267(8):983–1000, 1887.

[43] A Einstein. Generation and conversion of light with regard to a heuristic point of view. *Annalen der Physic*, 17(6):132–148, 1905.

[44] H. Boersch. Experimentelle Bestimmung der Energieverteilung in thermisch ausgelösten Elektronenstrahlen. *Zeitschrift für Physikr Physik*, 139(2):115–146, 1954.

[45] M. V. Berry. Quantal Phase Factors Accompanying Adiabatic Changes. *Proceedings of the Royal Society A*, 392:45–57, 1984.

[46] Y. Aharonov and D. Bohm. Significance of Electromagnetic Potentials in the Quantum Theory. *The Physical Review*, 115(3):485–491, 1959.

[47] Akira Tonomura, Nobuyuki Osakabe, Tsuyoshi Matsuda, Takeshi Kawasaki, Junji Endo, Shinichiro Yano, and Hiroji Yamada. Evidence for Aharonov-Bohm Effect with Magnetic Field Completely Shielded from Electron wave. *Phys. Rev. Lett.*, 56(8):792–795, 1986.

[48] L. Reimer, I. Fromm, P. Hirsch, U. Plate, and R. Rennekamp. Combination of EELS modes and electron spectroscopic imaging and diffraction in an energy-filtering electron microscope. *Ultramicroscopy*, 46:335–347, 1992.

[49] Koji Kimoto, Tomoko Sekiguchi, and Takashi Aoyama. Chemical shift mapping of Si L and K edges using spatially resolved EELS and energy-filtering TEM. *Microscopy*, 46(5):369–374, 1997.

[50] T. Walther. Electron energy-loss spectroscopic profiling of thin film structures: 0.39 nm line resolution and 0.04 eV precision measurement of near-edge structure shifts at interfaces. *Ultramicroscopy*, 96:401–411, 2003.

[51] Zechao Wang, Amir H. Tavabi, Lei Jin, Ján Rusz, Dmitry Tyutyunnikov, Hanbo Jiang, Yutaka Moritomo, Joachim Mayer, Rafal E. Dunin-Borkowski, Rong Yu, Jing Zhu, and Xiaoyan Zhong. Atomic scale imaging of magnetic circular dichroism by achromatic electron microscopy. *Nature Materials*, 17(3):221–225, 2018.

[52] Katsumi Ura, Hiromu Fujioka, and Teruo Hosokawa. Picosecond Pulse Stroboscopic Scanning Electron Microscope. *Journal of Electron Microscopy*, 27(4):247–252, 1978.

[53] O. Bostanjoglo, R. Elschner, Z. Mao, T. Nink, and M. Weingärtner. Nanosecond electron microscopes. *Ultramicroscopy*, 81(3-4):141–147, 2000.

[54] T. LaGrange, M. R. Armstrong, K. Boyden, C. G. Brown, G. H. Campbell, J. D. Colvin, W. J. DeHope, A. M. Frank, D. J. Gibson, F. V. Hartemann, J. S. Kim, W. E. King, B. J. Pyke, B. W. Reed, M. D. Shirk, R. M. Shuttlesworth, B. C. Stuart, B. R. Torralva, and N. D. Browning. Single-shot dynamic transmission electron microscopy. *Applied Physics Letters*, 89(4):044105, 2006.

[55] Ahmed H. Zewail. Four-Dimensional Electron Microscopy. *Science*, 328:187–193, 2010.

[56] Omar F. Mohammed, Ding Shyue Yang, Samir Kumar Pal, and Ahmed H. Zewail. 4D scanning ultrafast electron microscopy: Visualization of materials surface dynamics. *Journal of the American Chemical Society*, 133(20):7708–7711, 2011.

[57] Luca Piazza, Daniel J. Masiel, Thomas LaGrange, Brian W. Reed, Brett Barwick, and Fabrizio Carbone. Design and implementation of a fs-resolved transmission electron microscope based on thermionic gun technology. *Chemical Physics*, 423:79–84, 2013.

[58] Dayne A. Plemmons, Pranav K. Suri, and David J. Flannigan. Probing structural and electronic dynamics with ultrafast electron microscopy. *Chemistry of Materials*, 27(9):3178–3192, 2015.

[59] Gaolong Cao, Shuaishuai Sun, Zhongwen Li, Huanfang Tian, Huaixin Yang, and Jianqi Li. Clocking the anisotropic lattice dynamics of multi-walled carbon nanotubes by four-dimensional ultrafast transmission electron microscopy. *Scientific Reports*, 5:1–7, 2015.

[60] Armin Feist, Nora Bach, Nara Rubiano da Silva, Thomas Danz, Marcel Möller, Katharina E. Priebe, Till Domröse, J. Gregor Gatzmann, Stefan Rost, Jakob Schauss, Stefanie Strauch, Reiner Bormann, Murat Sivis, Sascha Schäfer, and Claus Ropers. Ultrafast transmission electron microscopy using a laser-driven field emitter: Femtosecond resolution with a high coherence electron beam. *Ultramicroscopy*, 176:63–73, 2017.

[61] Jingya Sun, Vasily A. Melnikov, Jafar I. Khan, and Omar F. Mohammed. Real-Space Imaging of Carrier Dynamics of Materials Surfaces by Second-Generation Four-Dimensional Scanning Ultrafast Electron Microscopy. *Journal of Physical Chemistry Letters*, 6(19):3884–3890, 2015.

[62] R. K. Li and P. Musumeci. Single-Shot MeV Transmission Electron Microscopy with Picosecond Temporal Resolution. *Physical Review Applied*, 2:024003, 2014.

[63] K. Bücker, M. Picher, O. Crégut, T. LaGrange, B. W. Reed, S. T. Park, D. J. Masiel, and F. Banhart. Electron beam dynamics in an ultrafast transmission electron microscope with Wehnelt electrode. *Ultramicroscopy*, 171:8–18, 2016.

[64] Kimberlee C Collins, David W Chandler, A Alec Talin, and Joseph R Michael. Development of Scanning Ultrafast Electron Microscope Capability. Technical Report October, Sandia National Laboratories, 2016.

[65] Shaozheng Ji, Luca Piazza, Gaolong Cao, Sang Tae Park, Bryan W. Reed, Daniel J. Masiel, and Jonas Weissenrieder. Influence of cathode geometry on electron dynamics in an ultrafast electron microscope. *Structural Dynamics*, 4:054303, 2017.

[66] Young Min Lee, Young Jae Kim, Ye Jin Kim, and Oh Hoon Kwon. Ultrafast electron microscopy integrated with a direct electron detection camera. *Structural Dynamics*, 4:044023, 2017.

[67] Jinfeng Yang, Yoichi Yoshida, and Hidehiro Yasuda. Ultrafast electron microscopy with relativistic femtosecond electron pulses. *Microscopy*, 67(5):291–295, 2018.

[68] J. Williams, F. Zhou, T. Sun, Z. Tao, K. Chang, K. Makino, M. Berz, P. M. Duxbury, and C. Y. Ruan. Active control of bright electron beams with RF optics for femtosecond microscopy. *Structural Dynamics*, 4:044035, 2017.

[69] W. Verhoeven, J. F.M. van Rens, E. R. Kieft, P. H.A. Mutsaers, and O. J. Luiten. High quality ultrafast transmission electron microscopy using resonant microwave cavities. *Ultramicroscopy*, 188:85–89, 2018.

[70] Makoto Kuwahara, Yoshito Nambo, Kota Aoki, Kensuke Sameshima, Xiuguang Jin, Toru Ujihara, Hidefumi Asano, Koh Saitoh, Yoshikazu Takeda, and Nobuo Tanaka. The Boersch effect in a picosecond pulsed electron beam emitted from a semiconductor photocathode. *Applied Physics Letters*, 109:013108, 2016.

[71] Chao Lu, Tao Jiang, Shengguang Liu, Rui Wang, Lingrong Zhao, Pengfei Zhu, Yaqi Liu, Jun Xu, Dapeng Yu, Weishi Wan, Yimei Zhu, Dao Xiang, and Jie Zhang. Imaging nanoscale spatial modulation of a relativistic electron beam with a MeV ultrafast electron microscope. *Applied Physics Letters*, 112:113102, 2018.

[72] F. Houdellier, G. M. Caruso, S. Weber, M. Kociak, and A. Arbouet. Development of a high brightness ultrafast Transmission Electron Microscope based on a laser-driven cold field emission source. *Ultramicroscopy*, 186:128–138, 2018.

[73] Maurizio Zani, Vittorio Sala, Gabriele Irde, Silvia Maria Pietralunga, Cristian Manzoni, Giulio Cerullo, Guglielmo Lanzani, and Alberto Tagliaferri. Charge dynamics in aluminum oxide thin film studied by ultrafast scanning electron microscopy. *Ultramicroscopy*, 187:93–97, 2018.

[74] Xuewen Fu, Shawn D. Pollard, Bin Chen, Byung Kuk Yoo, Hyunsoo Yang, and Yimei Zhu. Optical manipulation of magnetic vortices visualized in situ by Lorentz electron microscopy. *Science Advances*, 4:eaat3077, 2018.

[75] P. Das, J.D. Blazit, M. Tencé, L.F. Zagonel, Y. Auad, Y.H. Lee, X.Y. Ling, A. Losquin, C. Colliex, O. Stéphan, F.J. García de Abajo, and M. Kociak. Stimulated electron energy loss and gain in an electron microscope without a pulsed electron gun. *Ultramicroscopy*, 203:44–51, 2019.

[76] Kangpeng Wang, Rafael Dahan, Michael Shentcis, Yaron Kauffmann, and Ido Kaminer. Transmission Nearfield Optical Microscopy (TNOM) of Photonic Crystal Bloch Modes. In *Conference on Lasers and Electro-Optics*, page JTh5B.9. OSA Technical Digest, 2019.

[77] T van Oudheusden. *Electron source for subrelativistic single-shot femtosecond diffraction*. PhD thesis, Eindhoven University of Technology, 2010.

[78] J. F.M. van Rens, W. Verhoeven, J. G.H. Franssen, A. C. Lassise, X. F.D. Stragier, E. R. Kieft, P. H.A. Mutsaers, and O. J. Luiten. Theory and particle tracking simulations of a resonant radiofrequency deflection cavity in TM110 mode for ultrafast electron microscopy. *Ultramicroscopy*, 184:77–89, 2018.

[79] I. G.C. Weppelman, R. J. Moerland, J. P. Hoogenboom, and P. Kruit. Concept and design of a beam blanker with integrated photoconductive switch for ultrafast electron microscopy. *Ultramicroscopy*, 184:8–17, 2018.

[80] I. G. C. Weppelman, R. J. Moerland, L. Zhang, E. Kieft, P. Kruit, and J. P. Hoogenboom. Pulse length, energy spread, and temporal evolution of electron pulses generated with an ultrafast beam blanker. *Structural Dynamics*, 6:024102, 2019.

[81] A. Lassise, P. H.A. Mutsaers, and O. J. Luiten. Compact, low power radio frequency cavity for femtosecond electron microscopy. *Review of Scientific Instruments*, 83(4), 2012.

[82] Jiaqi Qiu, Gwanghui Ha, Chunguang Jing, Sergey V. Baryshev, Bryan W. Reed, June W. Lau, and Yimei Zhu. GHz laser-free time-resolved transmission electron microscopy: A stroboscopic high-duty-cycle method. *Ultramicroscopy*, 161:130–136, 2016.

[83] G S Plows and W C Nixon. Stroboscopic scanning electron microscopy. *Journal of Physics E: Scientific Instruments*, 1:595–600, 1968.

[84] T. Hosokawa, H. Fujioka, and K. Ura. Gigahertz stroboscopy with the scanning electron microscope. *Review of Scientific Instruments*, 49(9):1293–1299, 1978.

[85] G V Spivak and A E Luk'yanov. Observation of p–n junctions under pulsed conditions by means of an electron mirror microscope. *Bulletin of the Academy of Sciences USSR (Physics Series)*, 30:809–812, 1966.

[86] O Bostanjoglo and T Nink. Liquid motion in laser pulsed Al, Co and Au films. *Applied Surface Science*, 109-110:101–105, 1997.

[87] Thomas LaGrange, Bryan W. Reed, and Daniel J. Masiel. Movie-mode dynamic electron microscopy. *MRS Bulletin*, 40(1):23–28, 2015.

[88] M. K. Santala, B. W. Reed, S. Raoux, T. Topuria, T. Lagrange, and G. H. Campbell. Irreversible reactions studied with nanosecond transmission electron microscopy movies: Laser crystallization of phase change materials. *Applied Physics Letters*, 102:174105, 2013.

[89] Thomas P Wangler. *RF Linear accelerators*. John Wiley & Sons, 2008.

[90] T. Van Oudheusden, P. L.E.M. Pasmans, S. B. Van Der Geer, M. J. De Loos, M. J. Van Der Wiel, and O. J. Luiten. Compression of subrelativistic space-charge-dominated electron bunches for single-shot femtosecond electron diffraction. *Physical Review Letters*, 105:264801, 2010.

[91] Germán Sciaini and R. J.Dwayne Miller. Femtosecond electron diffraction: Heralding the era of atomically resolved dynamics. *Reports on Progress in Physics*, 74:096101, 2011.

[92] Giulia Fulvia Mancini, Barbara Mansart, Saverio Pagano, Bas Van Der Geer, Marieke De Loos, and Fabrizio Carbone. Design and implementation of a flexible beamline for fs electron diffraction experiments. *Nuclear Instruments and Methods in Physics Research, Section A: Accelerators, Spectrometers, Detectors and Associated Equipment*, 691:113–122, 2012.

[93] O. J. Luiten, S. B. Van Der Geer, M. J. De Loos, F. B. Kiewiet, and M. J. Van Der Wiel. How to realize uniform three-dimensional ellipsoidal electron bunches. *Physical Review Letters*, 93:094802, 2004.

[94] P. Musumeci, J. T. Moody, R. J. England, J. B. Rosenzweig, and T. Tran. Experimental generation and characterization of uniformly filled ellipsoidal electron-beam distributions. *Physical Review Letters*, 100:244801, 2008.

[95] Jared Maxson, David Cesar, Giacomo Calmasini, Alexander Ody, Pietro Musumeci, and David Alesini. Direct Measurement of Sub-10 fs Relativistic Electron Beams with Ultralow Emittance. *Physical Review Letters*, 118:154802, 2017.

[96] D. Cesar, J. Maxson, P. Musumeci, Y. Sun, J. Harrison, P. Frigola, F. H. O'Shea, H. To, D. Alesini, and R. K. Li. Demonstration of Single-Shot Picosecond Time-Resolved MeV Electron Imaging Using a Compact Permanent Magnet Quadrupole Based Lens. *Physical Review Letters*, 117:024801, 2016.

[97] Thomas LaGrange, Geoffrey H. Campbell, B. W. Reed, Mitra Taheri, J. Bradley Pesavento, Judy S. Kim, and Nigel D. Browning. Nanosecond time-resolved investigations using the in situ of dynamic transmission electron microscope (DTEM). *Ultramicroscopy*, 108(11):1441–1449, 2008.

[98] O.-H. Kwon, B. Barwick, H. S. Park, J. S. Baskin, and A. H. Zewail. 4D visualization of embryonic, structural crystallization by single-pulse microscopy. *Proceedings of the National Academy of Sciences*, 105(25):8519–8524, 2008.

[99] L. Nikolova, T. Lagrange, B. W. Reed, M. J. Stern, N. D. Browning, G. H. Campbell, J. C. Kieffer, B. J. Siwick, and F. Rosei. Nanocrystallization of amorphous germanium films observed with nanosecond temporal resolution. *Applied Physics Letters*, 97:203102, 2010.

[100] J. Spencer Baskin, Brett Barwick, Oh-Hoon Kwon, Ahmed H. Zewail, and Hyun Soon Park. Direct Observation of Martensitic Phase-Transformation Dynamics in Iron by 4D Single-Pulse Electron Microscopy. *Nano Letters*, 9(11):3954–3962, 2009.

[101] Sang Tae Park, David J. Flannigan, and Ahmed H. Zewail. Irreversible chemical reactions visualized in space and time with 4D electron microscopy. *Journal of the American Chemical Society*, 133(6):1730–1733, 2011.

[102] Bin Chen, Xuewen Fu, Mykhaylo Lysevych, Hark Hoe Tan, and Chennupati Jagadish. Four-dimensional Probing of Phase Reaction Dynamics in Au/GaAs Nanowires. *Nano Letters*, 19(2):791–786, 2019.

[103] Matthieu Picher, Kerstin Bücker, Thomas LaGrange, and Florian Banhart. Imaging and electron energy-loss spectroscopy using single nanosecond electron pulses. *Ultramicroscopy*, 188:41–47, 2018.

[104] Ulrich J. Lorenz and Ahmed H. Zewail. Observing liquid flow in nanotubes by 4D electron microscopy. *Science*, 344(6191):1496–1500, 2014.

[105] Daniel R. Cremons, Dayne A. Plemmons, and David J. Flannigan. Femtosecond electron imaging of defect-modulated phonon dynamics. *Nature Communications*, 7:11230, 2016.

[106] Armin Feist, Nara Rubiano da Silva, Wenxi Liang, Claus Ropers, and Sascha Schäfer. Nanoscale diffractive probing of strain dynamics in ultrafast transmission electron microscopy. *Structural Dynamics*, 5:014302, 2018.

[107] J. Spencer Baskin, Hyun Soon Park, and Ahmed H. Zewail. Nanomusical systems visualized and controlled in 4D electron microscopy. *Nano Letters*, 11(5):2183–2191, 2011.

[108] Oh Hoon Kwon, Brett Barwick, Hyun Soon Park, J. Spencer Baskin, and Ahmed H. Zewail. Nanoscale mechanical drumming visualized by 4D electron microscopy. *Nano Letters*, 8(11):3557–3562, 2008.

[109] Daniel R. Cremons, Daniel X. Du, and David J. Flannigan. Picosecond phase-velocity dispersion of hypersonic phonons imaged with ultrafast electron microscopy. *Physical Review Materials*, 1:073801, 2017.

[110] K J Gaffney and H.N. Chapman. Imaging Atomic Structure and Dynamics with Ultrafast X-ray Scattering. *Science*, 316:1444–1448, 2007.

[111] L. Piazza, C. Ma, H. X. Yang, A. Mann, Y. Zhu, J. Q. Li, and F. Carbone. Ultrafast structural and electronic dynamics of the metallic phase in a layered manganite. *Structural Dynamics*, 1:014501, 2014.

[112] Shuaishuai Sun, Linlin Wei, Zhongwen Li, Gaolong Cao, Y. Liu, W. J. Lu, Y. P. Sun, Huanfang Tian, Huaixin Yang, and Jianqi Li. Direct observation of an optically induced charge density wave transition in 1T-TaSe2. *Physical Review B*, 92:224303, 2015.

[113] Aycan Yurtsever and A. H. Zewail. 4D Nanoscale Diffraction. *Science*, 326:708–712, 2009.

[114] A. Yurtsever and A. H. Zewail. Kikuchi ultrafast nanodiffraction in four-dimensional electron microscopy. *Proceedings of the National Academy of Sciences*, 108(8):3152–3156, 2011.

[115] Aycan Yurtsever, Sascha Schaefer, and Ahmed H. Zewail. Ultrafast kikuchi diffraction: Nanoscale stress-strain dynamics of wave-guiding structures. *Nano Letters*, 12(7):3772–3777, 2012.

[116] W. Liang, G. M. Vanacore, and A. H. Zewail. Observing (non)linear lattice dynamics in graphite by ultrafast Kikuchi diffraction. *Proceedings of the National Academy of Sciences*, 111(15):5491–5496, 2014.

[117] F. Carbone, O.-H. Kwoon, and A. H. Zewail. Dynamics of Chemical Bonding Mapped by Energy-Resolved 4D Electron Microscopy. *Science*, 325:181–184, 2009.

[118] Renske M. van der Veen, Thomas J. Penfold, and Ahmed H. Zewail. Ultrafast core-loss spectroscopy in four-dimensional electron microscopy. *Structural Dynamics*, 2:024302, 2015.

[119] Brett Barwick, David J. Flannigan, and Ahmed H. Zewail. Photon-induced near-field electron microscopy. *Nature*, 462:902–906, 2009.

[120] Vladimir A Lobastov, Ramesh Srinivasan, and Ahmed H Zewail. Four-dimensional ultrafast electron microscopy. *Proceedings of the National Academy of Sciences of the United States of America*, 102(20):7069–73, 2005.

[121] Brett Barwick, Hyun Soon Park, Oh-Hoon Kwon, J. Spencer Baskin, and Ahmed H. Zewail. 4D Imaging of Transient Structures and Morphologies in Ultrafast Electron Microscopy. *Science*, 322:1227–1231, 2008.

[122] B. W. Reed, T. Lagrange, R. M. Shuttlesworth, D. J. Gibson, G. H. Campbell, and N. D. Browning. Solving the accelerator-condenser coupling problem in a nanosecond dynamic transmission electron microscope. *Review of Scientific Instruments*, 81:053706, 2010.

[123] IDES Inc. https://www.ides-inc.com/.

[124] Robert W. Boyd. *Nonlinear Optics*. Academic Press, San Diego, third edition, 2003.

[125] Giulio Cerullo and Sandro De Silvestri. Ultrafast optical parametric amplifiers. *Review of Scientific Instruments*, 74(1):1–18, 2003.

[126] C. Kittel. *Introduction to Solid State Physics*. Wiley, New York, 1976.

[127] Hongliang Liu, Xin Zhang, Shuyu Ning, Yixin Xiao, and Jiuxing Zhang. The electronic structure and work functions of single crystal LaB6 typical crystal surfaces. *Vacuum*, 143:245–250, 2017.

[128] D.-S. Yang, O. F. Mohammed, and A. H. Zewail. Scanning ultrafast electron microscopy. *Proceedings of the National Academy of Sciences*, 107(34):14993–14998, 2010.

[129] Peter Hommelhoff, Yvan Sortais, Anoush Aghajani-Talesh, and Mark A. Kasevich. Field Emission Tip as a Nanometer Source of Free Electron Femtosecond Pulses. *Physical Review L*, 96:077401, 2006.

[130] C. Ropers, D. R. Solli, C. P. Schulz, C. Lienau, and T. Elsaesser. Localized multiphoton emission of femtosecond electron pulses from metal nanotips. *Physical Review Letters*, 98:043907, 2007.

[131] Gabriele Ferrini, Francesco Banfi, Claudio Giannetti, and Fulvio Parmigiani. Non-linear electron photoemission from metals with ultrashort pulses. *Nuclear Instruments and Methods in Physics Research, Section A: Accelerators, Spectrometers, Detectors and Associated Equipment*, 601:123–131, 2009.

[132] R. Bormann, M. Gulde, A. Weismann, S. V. Yalunin, and C. Ropers. Tip-enhanced strong-field photoemission. *Physical Review Letters*, 105:147601, 2010.

[133] Michael Krüger, Markus Schenk, and Peter Hommelhoff. Attosecond control of electrons emitted from a nanoscale metal tip. *Nature*, 475:78–81, 2011.

[134] Simon Vogelgesang, Sascha Schäfer, Claus Ropers, Murat Sivis, and Gero Storeck. Nanotip-based photoelectron microgun for ultrafast LEED. *Structural Dynamics*, 4:044024, 2017.

[135] S. Vogelgesang, G. Storeck, J. G. Horstmann, T. Diekmann, M. Sivis, S. Schramm, K. Rossnagel, S. Schäfer, and C. Ropers. Phase ordering of charge density waves traced by ultrafast low-energy electron diffraction. *Nature Physics*, 14(2):184–190, 2018.

[136] Erik Kieft, Karl B. Schliep, Pranav K. Suri, and David J. Flannigan. Effects of thermionic-gun parameters on operating modes in ultrafast electron microscopy. *Structural Dynamics*, 2:051101, 2015.

[137] Sang Tae Park, Milo Lin, and Ahmed H. Zewail. Photon-induced near-field electron microscopy (PINEM): Theoretical and experimental. *New Journal of Physics*, 12:123028, 2010.

[138] Dayne A. Plemmons, Sang Tae Park, Ahmed H. Zewail, and David J. Flannigan. Characterization of fast photoelectron packets in weak and strong laser fields in ultrafast electron microscopy. *Ultramicroscopy*, 146:97–102, 2014.

[139] Peter Baum. On the physics of ultrashort single-electron pulses for time-resolved microscopy and diffraction. *Chemical Physics*, 423:55–61, 2013.

[140] M. Aidelsburger, F. O. Kirchner, F. Krausz, and P. Baum. Single-electron pulses for ultrafast diffraction. *Proceedings of the National Academy of Sciences*, 107(46):19714–19719, 2010.

[141] G. M. Vanacore, I. Madan, G. Berruto, K. Wang, E. Pomarico, R. J. Lamb, D. McGrouther, I. Kaminer, B. Barwick, F. Javier García De Abajo, and F. Carbone. Attosecond coherent control of free-electron wave functions using semi-infinite light fields. *Nature Communications*, 9:2694, 2018.

[142] L. Piazza, T. T.A. Lummen, E. Quiñonez, Y. Murooka, B. W. Reed, B. Barwick, and F. Carbone. Simultaneous observation of the quantization and the interference pattern of a plasmonic near-field. *Nature Communications*, 6:6407, 2015.

[143] Tom T.A. Lummen, Raymond J. Lamb, Gabriele Berruto, Thomas Lagrange, Luca Dal Negro, F. Javier García De Abajo, Damien McGrouther, Brett Barwick, and Fabrizio Carbone. Imaging and controlling plasmonic interference fields at buried interfaces. *Nature Communications*, 7:13156, 2016.

[144] G. Berruto, I. Madan, Y. Murooka, G. M. Vanacore, E. Pomarico, J. Rajeswari, R. Lamb, P. Huang, A. J. Kruchkov, Y. Togawa, T. LaGrange, D. McGrouther, H. M. Rønnow, and F. Carbone. Laser-Induced Skyrmion Writing and Erasing in an Ultrafast Cryo-Lorentz Transmission Electron Microscope. *Physical Review Letters*, 120:117201, 2018.

[145] J. N. Chapman. The investigation of magnetic domain structures in thin foils by electron microscopy. *Journal of Physics D: Applied Physics*, 17(4):623–647, 1984.

[146] X. Z. Yu, Y. Onose, N. Kanazawa, J. H. Park, J. H. Han, Y. Matsui, N. Nagaosa, and Y. Tokura. Real-space observation of a two-dimensional skyrmion crystal. *Nature*, 465:901–904, 2010.

[147] S. Seki, X. Z. Yu, S. Ishiwata, and Y. Tokura. Observation of skyrmions in a multiferroic material. *Science*, 336:198–201, 2012.

[148] Shawn D. Pollard, Joseph A. Garlow, Jiawei Yu, Zhen Wang, Yimei Zhu, and Hyunsoo Yang. Observation of stable Néel skyrmions in cobalt/palladium multilayers with Lorentz transmission electron microscopy. *Nature Communications*, 8:14761, 2017.

[149] J. Rajeswari, H. Ping, G. F. Mancini, Y. Murooka, T. Latychevskaia, D. McGrouther, M. Cantoni, E. Baldini, J. S. White, A. Magrez, T. Giamarchi, H. M. Rønnow, and F. Carbone. Filming the formation and fluctuation of Skyrmion domains by cryo-Lorentz Transmission Electron Microscopy. *Proceedings of the National Academy of Sciences*, 112(46):14212–14217, 2015.

[150] Ping Huang, Marco Cantoni, Alex Kruchkov, Jayaraman Rajeswari, Arnaud Magrez, Fabrizio Carbone, and Henrik M. Rønnow. In Situ Electric Field Skyrmion Creation in Magnetoelectric Cu2OSeO3. *Nano Letters*, 18(8):5167–5171, 2018.

[151] Raymond James Lamb. *Exploring methods for imaging dynamics in transmission electron microscopy*. PhD thesis, University of Glasgow, 2017.

[152] Hyun Soon Park, J. Spencer Baskin, and Ahmed H. Zewail. 4D Lorentz electron microscopy imaging: Magnetic domain wall nucleation, reversal, and wave velocity. *Nano Letters*, 10(9):3796–3803, 2010.

[153] Karl B. Schliep, P. Quarterman, Jian Ping Wang, and David J. Flannigan. Picosecond Fresnel transmission electron microscopy. *Applied Physics Letters*, 110(2):222404, 2017.

[154] Pieter Kruit and Guus H. Jansen. Space charge and statistical Coulomb effects. In Jon Orloff, editor, *Handbook of Charged Particle Optics*, pages 275–318. CRC Press, Boca Raton, FL, 1997.

[155] Ivan V. Bazarov, Bruce M. Dunham, and Charles K. Sinclair. Maximum achievable beam brightness from photoinjectors. *Physical Review Letters*, 102:104801, 2009.

[156] Judy S. Kim, Thomas LaGrange, Bryan W. Reed, Mitra L. Taheri, Michael R. Armstrong, Wayne E. King, Nigel D. Browning, and Geoffrey H. Campbell. Imaging of Transient Structures Using Nanosecond in Situ TEM. *Science*, 321:1472–1475, 2008.

[157] Kimball Physics. TEM cathode Ta ES-042 on JEOL K filament.

[158] Applied Physics Technologies. TEM cathode LaB6 90/16-90 on JEOL base.

[159] David R. Lide, editor. *CRC Handbook of Chemistry and Physics, Internet Version 2005*. CRC Press, Boca Raton, FL, 2005.

[160] R.H. Fowler. The analysis of photoelectric sensitivity curves for clean metals at various temperatures. *Physical Review*, 38:45–56, 1931.

[161] David H. Dowell and John F. Schmerge. Quantum efficiency and thermal emittance of metal photocathodes. *Physical Review Special Topics - Accelerators and Beams*, 12:074201, 2009.

[162] T. Srinivasan-Rao, J. Fischer, and T. Tsang. Photoemission studies on metals using picosecond ultraviolet laser pulses. *Journal of Applied Physics*, 69(5):3291–3296, 1991.

[163] Weaverm J.H., D.W. Lynch, and C. G. Olson. Optical properties of V, Ta, and Mo from 0.1 to 35 eV. *Physical Review B*, 10(2):501–516, 1974.

[164] Michael R. Armstrong, Ken Boyden, Nigel D. Browning, Geoffrey H. Campbell, Jeffrey D. Colvin, William J. DeHope, Alan M. Frank, David J. Gibson, Fred Hartemann, Judy S.

Kim, Wayne E. King, Thomas B. LaGrange, Ben J. Pyke, Bryan W. Reed, Richard M. Shuttlesworth, Brent C. Stuart, and Ben R. Torralva. Practical considerations for high spatial and temporal resolution dynamic transmission electron microscopy. *Ultramicroscopy*, 107(4-5):356–367, 2007.

[165] Todd Anderson, Ivan V. Tomov, and P. M. Rentzepis. Laser-driven metal photocathodes for picosecond electron and x-ray pulse generation. *Journal of Applied Physics*, 71(10):5161–5167, 1992.

[166] R. Turchetta, J. D. Berst, B. Casadei, G. Claus, C. Colledani, W. Dulinski, Y. Hu, D. Husson, J. P. Le Normand, J. L. Riester, G. Deptuch, U. Goerlach, S. Higueret, and M. Winter. Monolithic Active Pixel Sensor for charged particle tracking and imaging using standard VLSI CMOS technology. *Nuclear Instruments and Methods in Physics Research, Section A: Accelerators, Spectrometers, Detectors and Associated Equipment*, 458(3):677–689, 2001.

[167] G. Deptuch, A. Besson, P. Rehak, M. Szelezniak, J. Wall, M. Winter, and Y. Zhu. Direct electron imaging in electron microscopy with monolithic active pixel sensors. *Ultramicroscopy*, 107(8):674–684, 2007.

[168] Marco Battaglia, Devis Contarato, Peter Denes, Dionisio Doering, Piero Giubilato, Tae Sung Kim, Serena Mattiazzo, Velimir Radmilovic, and Sarah Zalusky. A rad-hard CMOS active pixel sensor for electron microscopy. *Nuclear Instruments and Methods in Physics Research, Section A: Accelerators, Spectrometers, Detectors and Associated Equipment*, 598(2):642–649, 2009.

[169] Shery L Y Chang, Christian Dwyer, Juri Barthel, Chris B. Boothroyd, and Rafal E. Dunin-Borkowski. Performance of a direct detection camera for off-axis electron holography. *Ultramicroscopy*, 161:90–97, 2016.

[170] Quantum Detectors. https://quantumdetectors.com/n/products/merlinem/.

[171] A. R. Faruqi and Sriram Subramaniam. CCD detectors in high-resolution biological electron microscopy. *Quarterly Reviews of Biophysics*, 33(1):1–27, 2000.

[172] R. N. Clough, G. Moldovan, and A. I. Kirkland. Direct detectors for electron microscopy. *Journal of Physics: Conference Series*, 522(1), 2014.

[173] A. R. Faruqi, R. Henderson, and L. Tlustos. Noiseless direct detection of electrons in Medipix2 for electron microscopy. *Nuclear Instruments and Methods in Physics Research, Section A: Accelerators, Spectrometers, Detectors and Associated Equipment*, 546(1-2):160–163, 2005.

[174] G. McMullan, S. Chen, R. Henderson, and A. R. Faruqi. Detective quantum efficiency of electron area detectors in electron microscopy. *Ultramicroscopy*, 109(9):1126–1143, 2009.

[175] El Sayed Eid, Tony Y. Chan, Eric R. Fossum, Richard H. Tsai, Robert Spagnuolo, John Deily, Wheaton B. Byers, and Joseph C. Peden. Design and characterization of ionizing radiation-tolerant CMOS APS image sensors up to 30 Mrd (Si) total dose. *IEEE Transactions on Nuclear Science*, 48(6):1796–1806, 2001.

[176] A. R. Faruqi and G. McMullan. Electronic detectors for electron microscopy. *Current opinion in structural biology*, 17:549–555, 2007.

[177] M Campbell, H M Heijne, G Meddeler, E Pernigotti, and W Snoeys. A Readout Chip for a 64 x 64 Pixel Matrix with 15-bit Single Photon Counting. *IEEE Transactions on Nuclear Science*, 45(3):751–753, 1998.

[178] Medipix Collaboration. https://medipix.web.cern.ch/.

[179] R. Ballabriga, J. Alozy, G. Blaj, M. Campbell, M. Fiederle, E. Frojdh, E. H M Heijne, X. Llopart, M. Pichotka, S. Procz, L. Tlustos, and W. Wong. The medipix3RX: A high resolution, zero dead-time pixel detector readout chip allowing spectroscopic imaging. *Journal of Instrumentation*, 8(2), 2013.

[180] S. Procz, K. A. Wartig, A. Fauler, A. Zwerger, J. Luebke, R. Ballabriga, G. Blaj, M. Campbell, M. Mix, and M. Fiederle. Medipix3 CT for material sciences. *Journal of Instrumentation*, 8(1):1–10, 2013.

[181] Matus Krajnak, Damien McGrouther, Dzmitry Maneuski, Val O'Shea, and Stephen McVitie. Pixelated detectors and improved efficiency for magnetic imaging in STEM differential phase contrast. *Ultramicroscopy*, 165:42–50, 2016.

[182] A. P.H. Butler, N. G. Anderson, R. Tipples, N. Cook, R. Watts, J. Meyer, A. J. Bell, T. R. Melzer, and P. H. Butler. Bio-medical X-ray imaging with spectroscopic pixel detectors. *Nuclear Instruments and Methods in Physics Research, Section A: Accelerators, Spectrometers, Detectors and Associated Equipment*, 591:141–146, 2008.

[183] Richard Plackett, I. Horswell, E. N. Gimenez, J. Marchal, David Omar, and N. Tartoni. Merlin: a fast versatile readout system for Medipix3. *Journal of Instrumentation*, 8(C01038), jan 2013.

[184] J. Dubochet, M. Adrian, J.-J. Chang, J.-C. Homo, J. Lepault, A. W. McDowall, and P. Schultz. Cryo-electron microscopy of vitrified specimens. *Quarterly Reviews of Biophysics*, 21(2):129–228, 1988.

[185] Jacqueline L.S. Milne and Sriram Subramaniam. Cryo-electron tomography of bacteria: Progress, challenges and future prospects. *Nature Reviews Microbiology*, 7(9):666–675, 2009.

[186] C. R. Booth, P. E. Mooney, B. C. Lee, M. Lent, and A. J. Gubbens. K2: A Super-Resolution Electron Counting Direct Detection Camera for Cryo-EM. *Microscopy and Microanalysis*, 18(S2):78–79, 2012.

[187] Benjamin E. Bammers, Ryan H. Rochat, Joanita Jakana, Dong-Hua Chen, and Wah Chiu. Direct electron detection yields cryo-EM reconstructions at resolutions beyond 3/4 Nyquist frequency. *Journal of Structural Biology*, 177(3):589–601, 2012.

[188] Xueming Li, Paul Mooney, Shawn Zheng, Christopher R. Booth, Michael B. Braunfeld, Sander Gubbens, David A. Agard, and Yifan Cheng. Electron counting and beam-induced motion correction enable near-atomic-resolution single-particle cryo-EM. *Nature Methods*, 10(6):584–590, 2013.

[189] J. A. Mir, R. Clough, R. MacInnes, C. Gough, R. Plackett, I. Shipsey, H. Sawada, I. MacLaren, R. Ballabriga, D. Maneuski, V. O'Shea, D. McGrouther, and A. I. Kirkland. Characterisation of the Medipix3 detector for 60 and 80 keV electrons. *Ultramicroscopy*, 182:44–53, 2017.

[190] Ye-Jin Kim and Oh-Hoon Kwon. Use of a Direct Electron-Detection Camera in Ultrafast Electron Microscopy for Low Dose Rate Time-Resolved Imaging. *Microscopy and Microanalysis*, 24(S1):1962–1963, 2018.

[191] Gatan Inc. http://www.gatan.com/k3-camera.

[192] Hari Shroff, Catherine G Galbraith, James a Galbraith, Helen White, Jennifer M. Gillette, Scott Olenych, Michael W Davidson, and Eric Betzig. Dual-color superresolution imaging of genetically expressed probes within individual adhesion complexes. *Proceedings of the National Academy of Sciences of the United States of America*, 104(51):20308–20313, 2007.

[193] Claude E. Shannon. Communication In The Presence Of Noise. *Proceedings of the Institute of Radio Engeneers*, 37(1):10–21, 1949.

[194] M. Maiorino, G. Mettivier, E. Manach, C. Frojdh, L. Tlustos, M.C. Montesi, P. Russo, C. Ponchut, M. Chmeissani, O. Gal, X. Llopart, J. Ludwig, and A. Zwerger. First experimental tests with a CdTe photon counting pixel detector hybridized with a Medipix2 readout chip. *IEEE Transactions on Nuclear Science*, 51(5):2379–2385, 2004.

[195] C. Fröjdh, H. Graafsma, H. E. Nilsson, and C. Ponchut. Characterization of a pixellated CdTe detector with single-photon processing readout. *Nuclear Instruments and Methods in Physics Research, Section A: Accelerators, Spectrometers, Detectors and Associated Equipment*, 563:128–132, 2006.

[196] J. Geiger. Excitation of surface phonons (Frölich modes) by keV electrons in small magnesium oxide particles. *Journal of the Physical Society of Japan*, 36(615), 1974.

[197] Maureen J. Lagos, Andreas Trügler, Ulrich Hohenester, and Philip E. Batson. Mapping vibrational surface and bulk modes in a single nanocube. *Nature*, 543:529–532, 2017.

[198] Jaysen Nelayah, Mathieu Kociak, Odile Stéphan, F. Javier García De Abajo, Marcel Tencé, Luc Henrard, Dario Taverna, Isabel Pastoriza-Santos, Luis M. Liz-Marzán, and Christian

Colliex. Mapping surface plasmons on a single metallic nanoparticle. *Nature Physics*, 3:348–353, 2007.

[199] Christian Colliex, Mathieu Kociak, and Odile Stéphan. Electron Energy Loss Spectroscopy imaging of surface plasmons at the nanometer scale. *Ultramicroscopy*, 162:A1–A24, 2016.

[200] F J García de Abajo and M Kociak. Electron energy-gain spectroscopy. *New Journal of Physics*, 10:073035, 2008.

[201] H. Boersch, J. Geiger, and W. Stickel. Interaction of 25-keV Electrons with Lattice Vibrations in LiF. Experimental Evidence for Surface Modes of Lattice Vibration. *Physical Review Letters*, 17(7):379–381, 1966.

[202] Maureen J. Lagos and Philip E. Batson. Thermometry with Subnanometer Resolution in the Electron Microscope Using the Principle of Detailed Balancing. *Nano Letters*, 18:4556–4563, 2018.

[203] Juan Carlos Idrobo, Andrew R. Lupini, Tianli Feng, Raymond R. Unocic, Franklin S. Walden, Daniel S. Gardiner, Tracy C. Lovejoy, Niklas Dellby, Sokrates T. Pantelides, and Ondrej L. Krivanek. Temperature Measurement by a Nanoscale Electron Probe Using Energy Gain and Loss Spectroscopy. *Physical Review Letters*, 120(9):095901, 2018.

[204] Arthur Losquin and Tom T.A. Lummen. Electron microscopy methods for space-, energy-, and time-resolved plasmonics. *Frontiers of Physics*, 12(1):127301, 2017.

[205] Archie Howie. Electrons and photons: exploiting the connection. *Institute of Physics Conference Series*, 161:311–314, 1999.

[206] A. Howie. Stimulated excitation electron microscopy and spectroscopy. *Ultramicroscopy*, 151:116–121, 2015.

[207] P.M. Woodward. A method of calculating the field over a plane aperture required to produce a given polar diagram. *Journal of the Institution of Electrical Engineers*, 93:1554–1558, 1947.

[208] J. D. Lawson. Lasers and accelerators. *IEEE Transaction on Nuclear Science*, NS-26(3):4217–4219, 1979.

[209] F. J. García de Abajo. Optical excitations in electron microscopy. *Reviews of Modern Physics*, 82(1):209–275, 2010.

[210] Aycan Yurtsever and Ahmed H. Zewail. Direct visualization of near-fields in nanoplasmonics and nanophotonics. *Nano Letters*, 12(6):3334–3338, 2012.

[211] Sang Tae Park, Aycan Yurtsever, John Spencer Baskin, and Ahmed H. Zewail. Graphene-layered steps and their fields visualized by 4D electron microscopy. *Proceedings of the National Academy of Sciences*, 110(23):9277–9282, 2013.

[212] D. J. Flannigan, B. Barwick, and A. H. Zewail. Biological imaging with 4D ultrafast electron microscopy. *Proceedings of the National Academy of Sciences*, 107(22):9933–9937, 2010.

[213] Ivan Madan, Giovanni M. Vanacore, Enrico Pomarico, Gabriele Berruto, Raymond J. Lamb, Damien Mcgrouther, Tom T.A. Lummen, Tatiana Latychevskaia, F. Javier García de Abajo, and Fabrizio Carbone. Holographic imaging of electromagnetic fields via electron-light quantum interference. *Science Advances*, 5:eaav8358, 2019.

[214] C. J. Joachain, N. J Kylstra, and R. M. Potvliege. *Atoms in intense laser fields*. Cambridge University Press, New York, 2012.

[215] Yuya Morimoto, Reika Kanya, and Kaoru Yamanouchi. Laser-assisted electron diffraction for femtosecond molecular imaging. *Journal of Chemical Physics*, 140(6), 2014.

[216] Yuya Morimoto, Reika Kanya, and Kaoru Yamanouchi. Light-Dressing Effect in Laser-Assisted Elastic Electron Scattering by Xe. *Physical Review Letters*, 115:123201, 2015.

[217] Aycanvan Yurtsever, Renske M. van der Veen, and Ahmed H. Zewail. Subparticle Ultrafast Spectrum Imaging in 4D Electron Microscopy. *Science*, 335:59–64, 2012.

[218] Haihua Liu, John Spencer Baskin, and Ahmed H. Zewail. Infrared PINEM developed by diffraction in 4D UEM. *Proceedings of the National Academy of Sciences*, 113(8):2041–2046, 2016.

[219] F. Javier Garcia de Abajo, Ana Asenjo-Garcia, and Mathieu Kociak. Multiphoton absorption and emission by interaction of swift electrons with evanescent light fields. *Nano Letters*, 10(5):1859–1863, 2010.

[220] T. Plettner, R. L. Byer, E. Colby, B. Cowan, C. M S Sears, J. E. Spencer, and R. H. Siemann. Visible-laser acceleration of relativistic electrons in a semi-infinite vacuum. *Physical Review Letters*, 95:134801, 2005.

[221] F. O. Kirchner, A. Gliserin, F. Krausz, and P. Baum. Laser streaking of free electrons at 25 keV. *Nature Photonics*, 8:52–57, 2014.

[222] Armin Feist, Katharina E. Echternkamp, Jakob Schauss, Sergey V. Yalunin, Sascha Schäfer, and Claus Ropers. Quantum coherent optical phase modulation in an ultrafast transmission electron microscope. *Nature*, 521:200–203, 2015.

[223] A. Asenjo-Garcia and F. J. García De Abajo. Plasmon electron energy-gain spectroscopy. *New Journal of Physics*, 15:103021, 2013.

[224] Sang Tae Park and Ahmed H Zewail. Relativistic E ff ects in Photon-Induced Near Field Electron Microscopy. *The Journal of Chemical Physics A*, 116:11128–11133, 2012.

[225] Mathieu Kociak. Quantum control of free electrons. *Nature*, 521:166–167, 2015.

[226] D. J. Griffiths. *Introduction to Quantum Mechanics*. Pearson Prentice Hall, Upper Saddle River (NJ), 2005.

[227] I I Rabi, S Millman, P Kusch, and J R Zacharias. The Molecular Beam Resonance Method for Measuring Nuclear Magnetic Moments. *Physical Review*, 55:526–535, 1939.

[228] Katharina E. Priebe, Christopher Rathje, Sergey V. Yalunin, Thorsten Hohage, Armin Feist, Sascha Schäfer, and Claus Ropers. Attosecond electron pulse trains and quantum state reconstruction in ultrafast transmission electron microscopy. *Nature Photonics*, 11(12):793–797, 2017.

[229] Katharina E. Echternkamp, Armin Feist, Sascha Schäfer, and Claus Ropers. Ramsey-type phase control of free-electron beams. *Nature Physics*, 12(11):1000–1004, 2016.

[230] C. Pellegrini, A. Marinelli, and S. Reiche. The physics of x-ray free-electron lasers. *Reviews of Modern Physics*, 88(1):015006, 2016.

[231] Karl Bane, Gil Travish, Ziran Wu, David H. Dowell, Robert J. Noble, Ken Soong, Levi Schachter, Chia-Ming Chang, Robert L. Byer, Benjamin Cowan, Amit Mizrahi, Sami Tantawi, Christopher McGuinness, Chunguang Jing, Behnam Montazeri, R. Joel England, Gregory R. Werner, Jay Dawson, Rodney B. Yoder, Peter Hommelhoff, James Rosenzweig, Brian Naranjo, Stephen J. Wolf, Cho-Kuen Ng, Christopher Sears, Yen-Chieh Huang, Wei Gai, Robert B. Palmer, Edgar Peralta, and James E. Spencer. Dielectric laser accelerators. *Reviews of Modern Physics*, 86(4):1337–1389, 2014.

[232] E. A. Peralta, K. Soong, R. J. England, E. R. Colby, Z. Wu, B. Montazeri, C. McGuinness, J. McNeur, K. J. Leedle, D. Walz, E. B. Sozer, B. Cowan, B. Schwartz, G. Travish, and R. L. Byer. Demonstration of electron acceleration in a laser-driven dielectric microstructure. *Nature*, 503:91–94, 2013.

[233] John Breuer and Peter Hommelhoff. Laser-based acceleration of nonrelativistic electrons at a dielectric structure. *Physical Review Letters*, 111:134803, 2013.

[234] PL Kapitza and PAM Dirac. Reflection of electrons from standing light waves. *Proceedings of the Cambridge Philosophical Society*, 29:297–300, 1933.

[235] Daniel L Freimund, Kayvan Aflatooni, and Herman Batelaan. Observation of the Kapitza-Dirac effect. *Nature*, 413:142–143, 2001.

[236] H. Batelaan. Colloquium: Illuminating the Kapitza-Dirac effect with electron matter optics. *Reviews of Modern Physics*, 79(3):929–941, 2007.

[237] A Gover and Y Pan. Dimension-dependent stimulated radiative interaction of a single electron quantum wavepacket. *Physics Letters A*, 382(23):1550–1555, 2018.

[238] V. L. Ginzburg and M. Frank. Radiation from a uniformly moving electron passing from one medium to another. *Zhurnal Eksperimentalnoy i Teoriticheskoy phisiki*, 16:15–22, 1946.

[239] S. J. Smith and E. M. Purcell. Visible light from localized surface charges moving across a grating. *Physical Review*, 92:1069, 1953.

[240] Arthur H. Compton. A Quantum Theory of the Scattering of X-rays by Light Elements. *Physical Review*, 21(5):483–502, 1923.

[241] Pavel A. Cherenkov. Visible emission of clean liquids by action of γ radiation. *Doklady Akademii Nauk SSSR*, 2:451, 1934.

[242] E. D. Courant, C. Pellegrini, and W. Zakowicz. High-energy inverse free-electron-laser accelerator. *Physical Review A*, 127:849–874, 1985.

[243] K Mizuno, J. Pae, T. Nozokido, and K. Furuya. Experimental evidence of the inverse Smith–Purcell effect. *Nature*, 328:45–47, 1987.

[244] D. Andrick and L. Langhans. Measurement of free-free transitions in e–Ar scattering. *Journal of Physics B: Atomic and Molecular Physics*, 9(15), 1976.

[245] A. Weingartshofer, J. K. Holmes, G. Caudle, E. M. Clarke, and H. Krüger. Direct observation of multiphoton processes in laser-induced free-free transitions. *Physical Review Letters*, 39(5):269–270, 1977.

[246] R. H. Pantell and M. A. Piestrup. Free-electron momentum modulation by means of limited interaction length with light. *Applied Physics Letters*, 32(11):781–783, 1978.

[247] J. A. Edighoffer and R. H. Pantell. Energy exchange between free electrons and light in vacuum. *Journal of Applied Physics*, 50(10):6120–6122, 1979.

[248] P. Agostini, F. Fabre, G. Mainfray, and G. Petite. Free-Free Transitions Following Six-Photon Ionization of Xenon Atoms. *Physical Review Letters*, 42(17):1127–1130, 1979.

[249] P. B. Johnson and R. W. Christy. Optical onstants of the Noble Metals. *Physical Review B*, 6(12):4370–4379, 1972.

[250] Edward D. Palik, editor. *Handbook of Optical Constants of Solids*. Academic Press, San Diego, 1985.

[251] C. Kealhofer, W. Schneider, D. Ehberger, A. Ryabov, F. Krausz, and P. Baum. All-optical control and metrology of electron pulses. *Science*, 352(6284):429–433, 2016.

[252] A Ryabov and P Baum. Electron microscopy of electromagnetic waveforms. *Science*, 353(6297):374–377, 2016.

[253] Yuya Morimoto and Peter Baum. Diffraction and microscopy with attosecond electron pulse trains. *Nature Physics*, 14:252–256, 2018.

[254] Sang Tae Park, Oh Hoon Kwon, and Ahmed H. Zewail. Chirped imaging pulses in four-dimensional electron microscopy: Femtosecond pulsed hole burning. *New Journal of Physics*, 14:053046, 2012.

[255] Mohammed T. Hassan, Haihua Liu, John Spencer Baskin, and Ahmed H. Zewail. Photon gating in four-dimensional ultrafast electron microscopy. *Proceedings of the National Academy of Sciences*, 112(42):12944–12949, 2015.

[256] Jiao Lin, J P Balthasar Mueller, Qian Wang, Guanghui Yuan, Nicholas Antoniou, Xiao-Cong Yuan, and Federico Capasso. Polarization-controlled tunable directional coupling of surface plasmon polaritons. *Science*, 340:331–334, 2013.

[257] C. Hernández-García, J. A. Pérez-Hernández, T. Popmintchev, M. M. Murnane, H. C. Kapteyn, A. Jaron-Becker, A. Becker, and L. Plaja. Zeptosecond High Harmonic keV X-Ray Waveforms Driven by Midinfrared Laser Pulses. *Physical Review Letters*, 111(3):033002, 2013.

[258] J. B. Kortright and R. S. DiGennaro. Multilayer mirrors as power filters in insertion device beamlines. *Review of Scientific Instruments*, 60(7):1995–1998, 1989.

[259] Deutsches Elektronen-Synchrotron DESY. The European X-Ray Laser Project XFEL, 2018.

[260] M. Ossiander, F. Siegrist, V. Shirvanyan, R. Pazourek, A. Sommer, T. Latka, A. Guggenmos, S. Nagele, J. Feist, J. Burgdörfer, R. Kienberger, and M. Schultze. Attosecond correlation dynamics. *Nature Physics*, 13:280–285, 2017.

[261] R. Du Rietz, D. J. Hinde, M. Dasgupta, R. G. Thomas, L. R. Gasques, M. Evers, N. Lobanov, and A. Wakhle. Predominant time scales in fission processes in reactions of S, Ti and Ni with W: zeptosecond versus attosecond. *Physical Review Letters*, 106(5):052701, 2011.

[262] Benedikt Rudek, Sang Kil Son, Lutz Foucar, Sascha W. Epp, Benjamin Erk, Robert Hartmann, Marcus Adolph, Robert Andritschke, Andrew Aquila, Nora Berrah, Christoph Bostedt, John Bozek, Nicola Coppola, Frank Filsinger, Hubert Gorke, Tais Gorkhover, Heinz Graafsma, Lars Gumprecht, Andreas Hartmann, Günter Hauser, Sven Herrmann, Helmut Hirsemann, Peter Holl, André Hömke, Loic Journel, Christian Kaiser, Nils Kimmel, Faton Krasniqi, Kai Uwe Kühnel, Michael Matysek, Marc Messerschmidt, Danilo Miesner, Thomas Möller, Robert Moshammer, Kiyonobu Nagaya, Björn Nilsson, Guillaume Potdevin, Daniel Pietschner, Christian Reich, Daniela Rupp, Gerhard Schaller, Ilme Schlichting, Carlo Schmidt, Florian Schopper, Sebastian Schorb, Claus Dieter Schröter, Joachim Schulz, Marc Simon, Heike Soltau, Lothar Strüder, Kiyoshi Ueda, Georg Weidenspointner, Robin Santra, Joachim Ullrich, Artem Rudenko, and Daniel Rolles. Ultra-efficient ionization of heavy atoms by intense X-ray free-electron laser pulses. *Nature Photonics*, 6:858–865, 2012.

[263] Peter Baum and Ahmed H. Zewail. Attosecond Free Electron Pulses for Diffraction and Microscopy. *Proceedings of the National Academy of Sciences of the United States of America*, 104(47):18409–18414, 2009.

[264] S. A. Hilbert, C. Uiterwaal, B. Barwick, H. Batelaan, and A. H. Zewail. Temporal lenses for attosecond and femtosecond electron pulses. *Proceedings of the National Academy of Sciences*, 106(26):10558–10563, 2009.

[265] M. Kozák, T. Eckstein, N. Schönenberger, and P. Hommelhoff. Inelastic ponderomotive scattering of electrons at a high-intensity optical travelling wave in vacuum. *Nature Physics*, 14:121–126, 2017.

[266] M. Kozák, J. McNeur, K. J. Leedle, H. Deng, N. Schönenberger, A. Ruehl, I. Hartl, J. S. Harris, R. L. Byer, and P. Hommelhoff. Optical gating and streaking of free electrons with sub-optical cycle precision. *Nature Communications*, 8:1–7, 2017.

[267] M. Th. Hassan, J. S. Baskin, B. Liao, and A. H. Zewail. High-temporal-resolution electron microscopy for imaging ultrafast electron dynamics. *Nature Photonics*, 11(7):425–430, 2017.

[268] Ferenc Krausz and Misha Ivanov. Attosecond physics. *Reviews of Modern Physics*, 81(1):163–234, 2009.

[269] Peter Baum and Ahmed H. Zewail. 4D attosecond imaging with free electrons: Diffraction methods and potential applications. *Chemical Physics*, 366(1-3):2–8, 2009.

[270] Stefan Alexander Maier. *Plasmonics: Fundamentals and Applications*. Springer, 1st edition, 2007.

[271] Ekmel Ozbam. Plasmonics : Merging Photonics and. *Science*, 311:189–194, 2006.

[272] William L Barnes, Alain Dereux, and Thomas W. Ebbesen. Subwavelength Optics. *Field Guide to Digital Micro-Optics*, 424:824–830, 2015.

[273] Matthew E. Stewart, Christopher R. Anderton, Lucas B. Thompson, Joana Maria, Stephen K. Gray, John A. Rogers, and Ralph G. Nuzzo. Nanostructured Plasmonic Sensors. *Chemical Reviews*, 108:494–521, 2008.

[274] David Rossouw and Gianluigi A. Botton. Plasmonic response of bent silver nanowires for nanophotonic subwavelength waveguiding. *Physical Review Letters*, 110:066801, 2013.

[275] Frank H.L. Koppens, Darrick E. Chang, and F. Javier García De Abajo. Graphene plasmonics: A platform for strong light-matter interactions. *Nano Letters*, 11:3370–3377, 2011.

[276] Marinko Jablan, Marin Soljačić, and Hrvoje Buljan. Plasmons in graphene: Fundamental properties and potential applications. *Proceedings of the IEEE*, 101(7):1689–1704, 2013.

[277] F. Javier García de Abajo. Graphene Plasmonics: Challenges and Opportunities. *ACS Photonics*, 1:135–152, 2014.

[278] Liang Jie Wong, Ido Kaminer, Ognjen Ilic, John D. Joannopoulos, and Marin Soljačić. Towards graphene plasmon-based free-electron infrared to X-ray sources. *Nature Photonics*, 10(1):46–52, 2016.

[279] Xuejun Liu, Yong Wang, and Eric O. Potma. A dual-color plasmonic focus for surface-selective four-wave mixing. *Applied Physics Letters*, 101:081116, 2012.

[280] Christoph Böhm, Joachim Bangert, Wolfgang Mertin, and Erich Kubalek. Optical microscopy. *Journal of Physics D*, 27:2237–2240, 1994.

[281] H. Gersen, T. J. Karle, R. J P Engelen, W. Bogaerts, J. P. Korterik, N. F. Van Hulst, T. F. Krauss, and L. Kuipers. Real-space observation of ultraslow light in photonic crystal waveguides. *Physical Review Letters*, 94:073903, 2005.

[282] Martin Wagner, Alexander S. McLeod, Scott J. Maddox, Zhe Fei, Mengkun Liu, Richard D. Averitt, Michael M. Fogler, Seth R. Bank, Fritz Keilmann, and D. N. Basov. Ultrafast dynamics of surface plasmons in InAs by time-resolved infrared nanospectroscopy. *Nano Letters*, 14:4529–4534, 2014.

[283] Yoshio Nishiyama, Kohei Imura, and Hiromi Okamoto. Observation of Plasmon Wave Packet Motions via Femtosecond Time-Resolved Near-Field Imaging Techniques. *Nano Letters*, 15:7657–7665, 2015.

[284] H. Petek and S. Ogawa. Femtosecond time-resolved two-photon photoemission studies of electron dynamics in metals. *Progress in Surface Science*, 56(4):239–310, 1997.

[285] Atsushi Kubo, Ken Onda, Hrvoje Petek, Zhijun Sun, Yun S. Jung, and Hong Koo Kim. Imaging of surface plasmon dynamics in nanostructured silver films. *Nano Letters*, 5(6):1123–1127, 2005.

[286] Atsushi Kubo, Niko Pontius, and Hrvoje Petek. Femtosecond microscopy of surface plasmon polariton wave packet evolution at the silver/vacuum interface. *Nano Letters*, 7(2):470–475, 2007.

[287] M. Aeschlimann, M. Bauer, D. Bayer, T. Brixner, S. Cunovic, F. Dimler, A. Fischer, W. Pfeiffer, M. Rohmer, C. Schneider, F. Steeb, C. Struber, and D. V. Voronine. Spatiotemporal control of nanooptical excitations. *Proceedings of the National Academy of Sciences*, 107(12):5329–5333, 2010.

[288] Lingxiao Zhang, Atsushi Kubo, Leiming Wang, Hrvoje Petek, and Tamar Seideman. Imaging of surface plasmon polariton fields excited at a nanometer-scale slit. *Physical Review B*, 84:245442, 2011.

[289] Christoph Lemke, Christian Schneider, Till Leißner, Daniela Bayer, Jörn W. Radke, Alexander Fischer, Pascal Melchior, Andrey B. Evlyukhin, Boris N. Chichkov, Carsten Reinhardt, Michael Bauer, and Martin Aeschlimann. Spatiotemporal characterization of SPP pulse propagation in two-dimensional plasmonic focusing devices. *Nano Letters*, 13:1053–1058, 2013.

[290] Christoph Lemke, Till Leißner, Andrey Evlyukhin, Jörn W. Radke, Alwin Klick, Jacek Fiutowski, Jakob Kjelstrup-Hansen, Horst Günter Rubahn, Boris N. Chichkov, Carsten Reinhardt, and Michael Bauer. The interplay between localized and propagating plasmonic excitations tracked in space and time. *Nano Letters*, 14:2431–2435, 2014.

[291] Yu Gong, Alan G. Joly, Dehong Hu, Patrick Z. El-Khoury, and Wayne P. Hess. Ultrafast imaging of surface plasmons propagating on a gold surface. *Nano Letters*, 15:3472–3478, 2015.

[292] Erik Mårsell, Arthur Losquin, Robin Svärd, Miguel Miranda, Chen Guo, Anne Harth, Eleonora Lorek, Johan Mauritsson, Cord L. Arnold, Hongxing Xu, Anne L'Huillier, and Anders Mikkelsen. Nanoscale Imaging of Local Few-Femtosecond Near-Field Dynamics within a Single Plasmonic Nanoantenna. *Nano Letters*, 15:6601–6608, 2015.

[293] Sergey I. Bozhevolnyi, Igor I. Smolyaniov, and Anatoly V. Zayats. Near-field microscopy of surface-plasmon polaritons: Localization and internal interface imaging. *Physical Review B*, 51(24):17916–17924, 1995.

[294] Christoph Lemke, Till Leißner, Stephan Jauernik, Alwin Klick, Jacek Fiutowski, Jakob Kjelstrup-Hansen, Horst-Günter Rubahn, and Michael Bauer. Mapping surface plasmon polariton propagation via counter-propagating light pulses. *Optics Express*, 20(12):12877–12884, 2012.

[295] Till Leißner, Christoph Lemke, Jacek Fiutowski, Jörn Willers Radke, Alwin Klick, Luciana Tavares, Jakob Kjelstrup-Hansen, Horst Günter Rubahn, and Michael Bauer. Morphological tuning of the plasmon dispersion relation in dielectric-loaded nanofiber waveguides. *Physical Review Letters*, 111:046802, 2013.

[296] Christoph Lemke, Till Leißner, Alwin Klick, Jacek Fiutowski, Jörn Willers Radke, Martin Thomaschewski, Jakob Kjelstrup-Hansen, Horst Günter Rubahn, and Michael Bauer. The complex dispersion relation of surface plasmon polaritons at gold/para-hexaphenylene interfaces. *Applied Physics B: Lasers and Optics*, 116:585–591, 2014.

[297] M. Bauer, C. Wiemann, J. Lange, D. Bayer, M. Rohmer, and M. Aeschlimann. Phase propagation of localized surface plasmons probed by time-resolved photoemission electron microscopy. *Applied Physics A*, 88:473–480, 2007.

[298] Mathieu Kociak, Odile Stéphan, Michael G. Walls, Marcel Tencé, and Christian Colliex. *Spatially Resolved EELS: The Spectrum-Imaging Technique and Its Applications*. Springer, 2011.

[299] Michel Bosman, Vicki J. Keast, Masashi Watanabe, Abbas I. Maaroof, and Michael B. Cortie. Mapping surface plasmons at the nanometre scale with an electron beam. *Nanotechnology*, 18:165505, 2007.

[300] Bernhard Schaffer, Ulrich Hohenester, Andreas Trügler, and Ferdinand Hofer. High-resolution surface plasmon imaging of gold nanoparticles by energy-filtered transmission electron microscopy. *Physical Review B*, 79:041401 (R), 2009.

[301] F. J. García De Abajo, A. Rivacoba, N. Zabala, and N. Yamamoto. Boundary effects in Cherenkov radiation. *Physical Review B*, 69:155420, 2004.

[302] Brett Barwick and Ahmed H. Zewail. Photonics and Plasmonics in 4D Ultrafast Electron Microscopy. *ACS Photonics*, 2(10):1391–1402, 2015.

[303] Takuo Tanemura, Krishna C. Balram, Dany Sebastien Ly-Gagnon, Pierre Wahl, Justin S. White, Mark L. Brongersma, and David A.B. Miller. Multiple-wavelength focusing of surface plasmons with a nonperiodic nanoslit coupler. *Nano Letters*, 11:2693–2698, 2011.

[304] M. Bai, C. Guerrero, S. Ioanid, E. Paz, M. Sanz, and N. García. Measuring the speed of a surface plasmon. *Physical Review B*, 69:1154166, 2004.

[305] Vasily V. Temnov, Ulrike Woggon, José Dintinger, Eloise Devaux, and Thomas W. Ebbesen. Measuring group velocity of surface plasmons by surface plasmon interferometry. *Optics Letters*, 32(10):1235–1237, 2007.

[306] David Rossouw and Gianluigi A. Botton. Resonant optical excitations in complementary plasmonic nanostructures. *Optics Express*, 20(7):6968–6973, 2012.

[307] F. J. García De Abajo, B. Barwick, and F. Carbone. Electron diffraction by plasmon waves. *Physical Review B*, 94:041404(R), 2016.

[308] Dennis Gabor. A new microcopic principle. *Nature*, (4098):777–778, 1948.

[309] Dennis Gabor. Microscopy by reconstructed wave-fronts. *Proceeding of the Royal Society of London*, 197:454–487, 1949.

[310] M. E. Haine and T. Mulvey. The Formation of the Diffraction Image with Electrons in the Gabor Diffraction Microscope. *Journal of the Optical Society of America*, 42(10):763–773, 1952.

[311] Bahram Javidi and Takanori Nomura. Securing information by use of digital holography. *Optics Letters*, 25(1):28–30, 2007.

[312] Bahram Javidi, Artur Carnicer, Masahiro Yamaguchi, Takanori Nomura, Elisabet Pérez-Cabré, María S. Millán, Naveen K. Nishchal, Roberto Torroba, John Fredy Barrera, Wenqi He, Xiang Peng, Adrian Stern, Yair Rivenson, A. Alfalou, C. Brosseau, Changliang Guo, John T. Sheridan, Guohai Situ, Makoto Naruse, Tsutomu Matsumoto, Ignasi Juvells, Enrique Tajahuerce, Jesús Lancis, Wen Chen, Xudong Chen, Pepijn W.H. Pinkse, Allard P. Mosk, and Adam Markman. Roadmap on optical security. *Journal of Optics*, 18:083001, 2016.

[313] W. Xu, M. H. Jericho, I. A. Meinertzhagen, and H. J. Kreuzer. Digital in-line holography for biological applications. *Proceedings of the National Academy of Sciences*, 98(20):11301–11305, 2002.

[314] Akira Tonomura. Applications of electron holography. *Reviews of Modern Physics*, 59(3):639–669, 1987.

[315] Hannes Lichte and Michael Lehmann. Electron holography - Basics and applications. *Reports on Progress in Physics*, 71:016102, 2008.

[316] G. Möllenstedt and H. Wahl. Elektronenholographie und Rekonstruktion mit Laserlicht. *Die Naturwissenschaften*, 55(7):340–341, 1968.

[317] G. Möllenstedt and H. Düker. Fresnelscher Interferenzversuch mit einem Biprisma für Elektronenwellen. *Die Naturwissenschaften*, 42(2):41, 1955.

[318] G. Möllenstedt and H. Düker. Beobachtungen und Messungen an Biprisma-Interferenzen mit Elektronenwellen. *Zeitschrift für Physik*, 145(3):377–397, 1956.

[319] Paul A. Midgley and Rafal E. Dunin-Borkowski. Electron tomography and holography in materials science. *Nature Materials*, 8:271–280, 2009.

[320] W. D. Rau, P. Schwander, F. H. Baumann, W. Höppner, and A. Ourmazd. Two-dimensional mapping of the electrostatic potential in transistors by electron holography. *Physical Review Letters*, 82(12):2614–2617, 1999.

[321] C. Gatel, A. Lubk, G. Pozzi, E. Snoeck, and M. Hÿtch. Counting elementary charges on nanoparticles by electron holography. *Physical Review Letters*, 111:025501, 2013.

[322] Rafal E. Dunin-Borkowski, Martha R. McCartney, Ulysses Lins, Marcos Farina, Peter R. Buseck, and Richard B. Frankel. Magnetic microstructure of bacterial magnetite by electron holography. *Science*, 282:1868–1870, 1998.

[323] J E Bonevich, K Harada, T Matsuda, H Kasai, T Yoshida, G Pozzi, and A Tonomura. Electron Holography Observation of Vortex Lattices in a Superconductor '. *Physical Review Letters*, 70(19):2952–2955, 1993.

[324] András Kovács, Zi-An Li, Kiyou Shibata, and Rafal E. Dunin-Borkowski. Lorentz microscopy and off-axis electron holography of magnetic skyrmions in FeGe. *Resolution and Discovery*, 1(1):2–8, 2016.

[325] Takeshi Kasama, Nathan S. Church, Joshua M. Feinberg, Rafal E. Dunin-Borkowski, and Richard J. Harrison. Direct observation of ferrimagnetic/ferroelastic domain interactions in magnetite below the Verwey transition. *Earth and Planetary Science Letters*, 297:10–17, 2010.

[326] J. D. Maynard, E. G. Williams, and Y. Lee. Nearfield acoustic holography: I. Theory of generalized holography and the development of NAH. *The Journal of the Acoustical Society of America*, 78(4):1395–1413, 1985.

[327] S Eisebitt, J Lüning, W F Schlotter, M Lörgen, O Hellwig, W Eberhardt, and J Stöhr. Lensless imaging of magnetic nanostructures by X-ray spectro-holography. *Nature*, 432:885–888, 2004.

[328] A. M. Weiner, D. E. Leaird, D. H. Reitze, and E. G. Paek. Spectral holography of shaped femtosecond pulses. *Optics Letters*, 17(3):224–226, 1992.

[329] Tadas Balciunas, Andrius Melninkaitis, Gintaras Tamosauskas, and Valdas Sirutkaitis. Time-resolved off-axis digital holography for characterization of ultrafast phenomena in water. *Optics Letters*, 33(1):58–60, 2008.

[330] A Rebane and Jack Feinberg. Time-resolved holography. *Nature*, 351:378–380, 1991.

[331] Maciej Dabrowski, Yanan Dai, Adam Argondizzo, Qiang Zou, Xuefeng Cui, and Hrvoje Petek. Multiphoton Photoemission Microscopy of High-Order Plasmonic Resonances at the Ag/Vacuum and Ag/Si Interfaces of Epitaxial Silver Nanowires. *ACS Photonics*, 3(9):1704–1713, 2016.

[332] T. Niermann, M. Lehmann, and T. Wagner. Gated interference for time-resolved electron holography. *Ultramicroscopy*, 182:54–61, 2017.

[333] Vadim Migunov, Christian Dwyer, Chris B. Boothroyd, Giulio Pozzi, and Rafal E. Dunin-Borkowski. Prospects for quantitative and time-resolved double and continuous exposure off-axis electron holography. *Ultramicroscopy*, 178:48–61, 2017.

[334] L. Yin, V. K. Vlasko-Vlasov, A. Rydh, J. Pearson, U. Welp, S. H. Chang, S. K. Gray, G. C. Schatz, D. B. Brown, and C. W. Kimball. Surface plasmons at single nanoholes in Au films. *Applied Physics Letters*, 85(3):467–469, 2004.

[335] V. S. Yakovlev, J. Gagnon, N. Karpowicz, and F. Krausz. Attosecond streaking enables the measurement of quantum phase. *Physical Review Letters*, 105:073001, 2010.

[336] M. Wollenhaupt, A. Assion, D. Liese, C. Sarpe-Tudoran, T. Baumert, S. Zamith, M. A. Bouchene, B. Girard, A. Flettner, U. Weichmann, and G. Gerber. Interferences of ultrashort free electron wave packets. *Physical Review Letters*, 89:173001, 2002.

[337] W. A. Okell, T. Witting, D. Fabris, C. A. Arrell, J. Hengster, S. Ibrahimkutty, A. Seiler, M. Barthelmess, S. Stankov, D. Y. Lei, Y. Sonnefraud, M. Rahmani, T. Uphues, S. A. Maier, J. P. Marangos, and J. W. G. Tisch. Temporal broadening of attosecond photoelectron wavepackets from solid surfaces. *Optica*, 2(4):383–387, 2015.

[338] Y. Mairesse and F. Quéré. Frequency-resolved optical gating for complete reconstruction of attosecond bursts. *Physical Review A*, 71:011401(R), 2005.

[339] C. Bourassin-Bouchet and M. E. Couprie. Partially coherent ultrafast spectrography. *Nature Communications*, 6:6465, 2015.

[340] Enrico Pomarico, Ivan Madan, Gabriele Berruto, Giovanni Maria Vanacore, Kangpeng Wang, Ido Kaminer, F. Javier García De Abajo, and Fabrizio Carbone. meV Resolution in Laser-Assisted Energy-Filtered Transmission Electron Microscopy. *ACS Photonics*, 5:759–764, 2018.

[341] G. M. Vanacore, G. Berruto, I. Madan, E. Pomarico, P. Biagioni, R. J. Lamb, D. McGrouther, O. Reinhardt, I. Kaminer, B. Barwick, H. Larocque, V. Grillo, E. Karimi, F. J. García de Abajo, and F. Carbone. Ultrafast Generation and Control of an Electron Vortex Beam via Chiral Plasmonic Near Fields. *Nature Materials*, 18:573–579, 2019.

[342] Gabriel Molina-Terriza, Juan P. Torres, and Lluis Torner. Twisted photons. *Nature Physics*, 3:305–310, 2007.

[343] Halina Rubinsztein-Dunlop, Andrew Forbes, Michel V. Berry, M. R. Dennis, David L. Andrews, Masud Mansuripur, Cornelia Denz, Christina Alpmann, Peter Banzer, Thomas Bauer, Ebrahim Karimi, Lorenzo Marrucci, Miles Padgett, Monika Ritsch-Marte, Natalia M. Litchinitser, Nocholas P. Bigelow, C. Rosales-Guzmán, A. Belmonte, J. P. Torres, Tyler W. Neely, Mark Baker, Reuven Gordon, Alexander B Stilgoe, Jacquiline Romero, Andrew G. White, Robert Fickler, Alan E. Willner, Guodong Xie, Benjamin McMorran, and Andrew M. Weiner. Roadmap on structured light. *Journal of Optics*, 19:013001, 2017.

[344] M. S. Soskin, V. N. Gorshkov, M. V. Vasnetsov, J. T. Malos, and N. R. Heckenberg. Topological charge and angular momentum of light beams carrying optical vortices. *Physical Review A*, 56(5):4064–4075, 1997.

[345] Alison M. Yao and Miles J. Padgett. Orbital angular momentum: origins, behavior and applications. *Advances in Optics and Photonics*, 3:161–204, 2011.

[346] J. H. Poynting. The Wave Motion of a Revolving Shaft, and a Suggestion as to the Angular Momentum in a Beam of Circularly Polarised Light. *Proceeding of the Royal Society of London*, 82:560–567, 1909.

[347] Richard A. Beth. Mechanical detection and measurement of the angular momentum of light. *Physical Review*, 5:115–125, 1936.

[348] L. Allen, M. W. Beijersbergen, R. J.C. Spreeuw, and J. P. Woerdman. Orbital angular momentum of light and the transformation of Laguerre-Gaussian laser modes. *Physical Review A*, 45(11):8185–8189, 1992.

[349] J.F. Nye and M.V. Berry. Dislocations in wave trains. *Proc. R. Soc. London A*, 336:165–190, 1974.

[350] V. Yu. Bazhenov, M. V. Vasnetsov, and M. S. Soskin. Laser beams with screw dislocations in their wavefronts. *Pis'ma Zhurnal Eksperimentalnoy i Teoriticheskoy phisiki*, 52(8):1037–1039, 1990.

[351] R. Géneaux, A. Camper, T. Auguste, O. Gobert, J. Caillat, R. Taïeb, and T. Ruchon. Synthesis and characterization of attosecond light vortices in the extreme ultraviolet. *Nature Communications*, 7:12583, 2016.

[352] D. Gauthier, P. Rebernik Ribic, G. Adhikary, A. Camper, C. Chappuis, R. Cucini, L. F. Dimauro, G. Dovillaire, F. Frassetto, R. Géneaux, P. Miotti, L. Poletto, B. Ressel, C. Spezzani, M. Stupar, T. Ruchon, and G. De Ninno. Tunable orbital angular momentum in high-harmonic generation. *Nature Communications*, 8:14971, 2017.

[353] J. Bahrdt, K. Holldack, P. Kuske, R. Müller, M. Scheer, and P. Schmid. First observation of photons carrying orbital angular momentum in undulator radiation. *Physical Review Letters*, 111:034801, 2013.

[354] Erik Hemsing, Andrey Knyazik, Michael Dunning, Dao Xiang, Agostino Marinelli, Carsten Hast, and James B. Rosenzweig. Coherent optical vortices from relativistic electron beams. *Nature Physics*, 9:549–553, 2013.

[355] Primož Rebernik Ribič, Benedikt Rösner, David Gauthier, Enrico Allaria, Florian Döring, Laura Foglia, Luca Giannessi, Nicola Mahne, Michele Manfredda, Claudio Masciovecchio, Riccardo Mincigrucci, Najmeh Mirian, Emiliano Principi, Eléonore Roussel, Alberto Simoncig, Simone Spampinati, Christian David, and Giovanni G. De. Extreme-ultraviolet vortices from a free-electron laser. *Physical Review X*, 7:031036, 2017.

[356] J. C.T. Lee, S. J. Alexander, S. D. Kevan, S. Roy, and B. J. McMorran. Laguerre–Gauss and Hermite–Gauss soft X-ray states generated using diffractive optics. *Nature Photonics*, 13(3):205–209, 2019.

[357] Andrew G Peele, Philip J Mcmahon, David Paterson, Chanh Q Tran, Adrian P Mancuso, Keith A Nugent, Jason P Hayes, Erol Harvey, Barry Lai, and Ian Mcnulty. Observation of an x-ray vortex. *Optics Letters*, 27(20):1752–1754, 2002.

[358] Graham Gibson, Johannes Courtial, Miles J. Padgett, Mikhail Vasnetsov, Valeriy Pas'ko, Stephen M. Barnett, and Sonja Franke-Arnold. Free-space information transfer using light beams carrying orbital angular momentum. *Optics Express*, 12(22):5448–5456, 2004.

[359] Nenad Bozinovic, Yang Yue, Yongxiong Ren, Moshe Tur, Poul Kristensen, Hao Huang, Alan E Willner, and Siddharth Ramachandran. Multiplexing in Fibers. *Science*, 340:1545–1548, 2013.

[360] Alicia Sit, Frédéric Bouchard, Robert Fickler, Jérémie Gagnon-Bischoff, Hugo Larocque, Khabat Heshami, Dominique Elser, Christian Peuntinger, Kevin Günthner, Bettina

Heim, Christoph Marquardt, Gerd Leuchs, Robert W. Boyd, and Ebrahim Karimi. High-Dimensional Intra-City Quantum Cryptography with Structured Photons. *Optica*, 4(9):1006–1010, 2016.

[361] David G Grier. A revolution in optical manipulation. *Nature*, 424:810–6, 2003.

[362] Miles Padgett and Richard Bowman. Tweezers with a twist. *Nature Photonics*, 5(6):343–348, 2011.

[363] Alois Mair, Alipasha Vaziri, Gregor Weihs, and Anton Zeilinger. Entanglement of the orbital angular momentum states of photons. *Nature*, 412:313–316, 2001.

[364] Jonathan Leach, Barry Jack, Jacqui Romero, Anand K Jha, Alison M Yao, Sonja Franke-arnold, David G Ireland, Robert W Boyd, Stephen M Barnett, and Miles J Padgett. Quantum Correlations in Optical Angle–Orbital Angular Momentum Variables. *Science*, 329:662–665, 2010.

[365] Pierfrancesco Zilio, Elettra Mari, Giuseppe Parisi, Fabrizio Tamburini, and Filippo Romanato. Angular momentum properties of electromagnetic field transmitted through holey plasmonic vortex lenses. *Optics Letters*, 37(15):3234, 2012.

[366] Francisco Balzarotti, Yvan Eilers, Klaus C Gwosch, Arvid H Gynnå, Volker Westphal, Fernando D Stefani, Johan Elf, and Stefan W Hell. Nanometer resolution imaging and tracking of fluorescent molecules with minimal photon fluxes. *Science*, 355:606–612, 2017.

[367] Hiroyuki Fujita and Masahiro Sato. Ultrafast generation of skyrmionic defects with vortex beams: Printing laser profiles on magnets. *Physical Review B*, 95(5):1–12, 2017.

[368] Hiroyuki Fujita and Masahiro Sato. Encoding orbital angular momentum of light in magnets. *Physical Review B*, 96(6):1–6, 2017.

[369] Masaya Uchida and Akira Tonomura. Generation of electron beams carrying orbital angular momentum. *Nature*, 464:737–739, 2010.

[370] J. Verbeeck, H. Tian, and P. Schattschneider. Production and application of electron vortex beams. *Nature*, 467:301–304, 2010.

[371] D. Sarenac, C. Kapahi, W. C. Chen, Charles W. Clark, D. G. Cory, M. G. Huber, I. Taminiau, K. Zhernenkov, and D. A. Pushin. Generation and detection of spin-orbit coupled neutron beams. *ArXiv:1904.09520v1*, 2019.

[372] Konstantin Yu Bliokh, Yury P. Bliokh, Sergey Savel'Ev, and Franco Nori. Semiclassical dynamics of electron wave packet states with phase vortices. *Physical Review Letters*, 99:190404, 2007.

[373] K. Y. Bliokh, I. P. Ivanov, G. Guzzinati, L. Clark, R. Van Boxem, A. Béché, R. Juchtmans, M. A. Alonso, P. Schattschneider, F. Nori, and J. Verbeeck. Theory and applications of free-electron vortex states. *Physics Reports*, 690:1–70, 2017.

[374] S. M. Lloyd, M. Babiker, G. Thirunavukkarasu, and J. Yuan. Electron vortices: Beams with orbital angular momentum. *Reviews of Modern Physics*, 89(3):035004, 2017.

[375] Hugo Larocque, Ido Kaminer, Vincenzo Grillo, Gerd Leuchs, Miles J. Padgett, Robert W. Boyd, Mordechai Segev, and Ebrahim Karimi. 'Twisted' electrons. *Contemporary Physics*, 59(2):126–144, 2018.

[376] Juan Carlos Idrobo, Ján Rusz, Jakob Spiegelberg, Michael A. McGuire, Christopher T. Symons, Ranga Raju Vatsavai, Claudia Cantoni, and Andrew R. Lupini. Detecting magnetic ordering with atomic size electron probes. *Advanced Structural and Chemical Imaging*, 2:5, 2016.

[377] C Hébert and P Schattschneider. A proposal for dichroic experiments in the electron microscope. *Ultramicroscopy*, 96:463–468, 2003.

[378] P. Schattschneider, S. Rubino, C. Hébert, J. Rusz, J. Kuneš, P. Novák, E. Carlino, M. Fabrizioli, G. Panaccione, and G. Rossi. Detection of magnetic circular dichroism using a transmission electron microscope. *Nature*, 441(7092):486–488, 2006.

[379] Peter Schattschneider, Michael Stöger-Pollach, Stefano Rubino, Matthias Sperl, Christian Hurm, Josef Zweck, and Ján Rusz. Detection of magnetic circular dichroism on the two-nanometer scale. *Physical Review B*, 78:104413, 2008.

[380] Ján Rusz, Shunsuke Muto, Jakob Spiegelberg, Roman Adam, Kazuyoshi Tatsumi, Daniel E. Bürgler, Peter M. Oppeneer, and Claus M. Schneider. Magnetic measurements with atomic-plane resolution. *Nature Communications*, 7:12672, 2016.

[381] Alexander Edström, Axel Lubk, and Ján Rusz. Elastic Scattering of Electron Vortex Beams in Magnetic Matter. *Physical Review Letters*, 116:127203, 2016.

[382] Vincenzo Grillo, Tyler R. Harvey, Federico Venturi, Jordan S. Pierce, Roberto Balboni, Frédéric Bouchard, Gian Carlo Gazzadi, Stefano Frabboni, Amir H. Tavabi, Zi An Li, Rafal E. Dunin-Borkowski, Robert W. Boyd, Benjamin J. McMorran, and Ebrahim Karimi. Observation of nanoscale magnetic fields using twisted electron beams. *Nature Communications*, 8:869, 2017.

[383] Axel Lubk, Laura Clark, Giulio Guzzinati, and Jo Verbeeck. Topological analysis of paraxially scattered electron vortex beams. *Physical Review A*, 87:033834, 2013.

[384] A. Asenjo-Garcia and F. J. García De Abajo. Dichroism in the interaction between vortex electron beams, plasmons, and molecules. *Physical Review Letters*, 113:066102, 2014.

[385] Tyler R. Harvey, Jordan S. Pierce, Jordan J. Chess, and Benjamin J. McMorran. Demonstration of electron helical dichroism as a local probe of chirality. *arXiv:1507.01810 [cond-mat.mtrl-sci]*, 2015.

[386] B. J. McMorran, A. Agrawal, I. M. Anderson, a. a. Herzing, H. J. Lezec, J. J. McClelland, and J. Unguris. Supporting materials for: Electron Vortex Beams with High Quanta of Orbital Angular Momentum. *Science*, 331:192–195, 2011.

[387] E. Mafakheri, A. H. Tavabi, P. H. Lu, R. Balboni, F. Venturi, C. Menozzi, G. C. Gazzadi, S. Frabboni, A. Sit, R. E. Dunin-Borkowski, E. Karimi, and V. Grillo. Realization of electron vortices with large orbital angular momentum using miniature holograms fabricated by electron beam lithography. *Applied Physics Letters*, 110:093113, 2017.

[388] Vincenzo Grillo, Gian Carlo Gazzadi, Erfan Mafakheri, Stefano Frabboni, Ebrahim Karimi, and Robert W. Boyd. Holographic generation of highly twisted electron beams. *Physical Review Letters*, 114:034801, 2015.

[389] Armand Béché, Ruben Van Boxem, Gustaaf Van Tendeloo, and Jo Verbeeck. Magnetic monopole field exposed by electrons. *Nature Physics*, 10:26–29, 2013.

[390] Jo Verbeeck, Armand Béché, Knut Müller-Caspary, Giulio Guzzinati, Minh Anh Luong, and Martien Den Hertog. Demonstration of a 2 × 2 programmable phase plate for electrons. *Ultramicroscopy*, 190:58–65, 2018.

[391] Giulio Pozzi, Peng Han Lu, Amir H. Tavabi, Martial Duchamp, and Rafal E. Dunin-Borkowski. Generation of electron vortex beams using line charges via the electrostatic Aharonov-Bohm effect. *Ultramicroscopy*, 181:1339–1351, 2017.

[392] Jonathan Handali, Pratistha Shakya, and Brett Barwick. Creating electron vortex beams with light. *Optics Express*, 23(4):5236–5243, 2015.

[393] Wei Cai, Ori Reinhardt, Ido Kaminer, and F. Javier García De Abajo. Efficient orbital angular momentum transfer between plasmons and free electrons. *Physical Review B*, 98:045424, 2018.

[394] Ryuji Takahashi and Naoto Nagaosa. Berry curvature and orbital angular momentum of electrons in angle-resolved photoemission spectroscopy. *Physical Review B*, 91:245133, 2015.

[395] Christine A. Aidala, Steven D. Bass, Delia Hasch, and Gerhard K. Mallot. The spin structure of the nucleon. *Reviews of Modern Physics*, 85:655–691, 2013.

[396] Y. Gorodetski, A. Niv, V. Kleiner, and E. Hasman. Observation of the spin-based plasmonic effect in nanoscale structures. *Physical Review Letters*, 101:043903, 2008.

[397] Yuri Gorodetski, Sergey Nechayev, Vladimir Kleiner, and Erez Hasman. Plasmonic Aharonov-Bohm effect: Optical spin as the magnetic flux parameter. *Physical Review B*, 82:125433, 2010.

[398] K. Y. Bliokh, F. J. Rodríguez-Fortuño, F. Nori, and A. V. Zayats. Spin-orbit interactions of light. *Nature Photonics*, 9(12):796–808, 2015.

[399] Letizia Capitanio, Rosine Lallement, Jean Luc Vergely, Meriem Elyajouri, and Ana Monreal-Ibero. Three-dimensional mapping of the local interstellar medium with composite data. *Astronomy & Astrophysics*, 606:A65, 2017.

[400] G. Spektor, D. Kilbane, A. K. Mahro, B. Frank, S. Ristok, L. Gal, P. Kahl, D. Podbiel, S. Mathias, H. Giessen, F.-J. Meyer zu Heringdorf, M. Orenstein, and M. Aeschlimann. Revealing the subfemtosecond dynamics of orbital angular momentum in nanoplasmonic vortices. *Science*, 355:1187–1191, 2017.

[401] Wei-Yi Tsai, Quan Sun, Guangwei Hu, Pin Chieh Wu, Ren Jie Lin, Cheng-Wei Qiu, Kosei Ueno, Hiroaki Misawa, and Din Ping Tsai. Twisted Surface Plasmons with Spin-Controlled Gold Surfaces. *Advanced Optical Materials*, 7:1801060, 2019.

[402] Lumerical Inc. FDTD Solutions, 2017.

[403] Tomoki Ohno and Shintaro Miyanishi. Study of surface plasmon chirality induced by Archimedes' spiral grooves. *Optics Express*, 14(13):6285, 2006.

[404] Seong-Woo Cho, Junghyun Park, Seung-Yeol Lee, Hwi Kim, and Byoungho Lee. Coupling of spin and angular momentum of light in plasmonic vortex. *Optics Express*, 20(9):10083–10094, 2012.

[405] Giulio Guzzinati, Armand Béché, Hugo Lourenço-Martins, Jérôme Martin, Mathieu Kociak, and Jo Verbeeck. Probing the symmetry of the potential of localized surface plasmon resonances with phase-shaped electron beams. *Nature Communications*, 8:14999, 2017.

[406] Vincenzo Grillo and Enzo Rotunno. STEM_CELL: A software tool for electron microscopy: Part I-simulations. *Ultramicroscopy*, 125:97–111, 2013.

[407] Th. Udem, R. Holzwarth, and T. W. Hänsch. Optical frequency metrology. *Nature*, 416:233–237, 2002.

[408] Hugo Larocque, Ido Kaminer, Vincenzo Grillo, Robert W Boyd, and Ebrahim Karimi. A matter of quantum. *Nature Physics*, 14, 2018.

[409] "EMC collaboration". A measurement of the spin asymmetry and determination of the structure function g1 in deep inelastic muon-proton scattering. *Physics Letters B*, 206(2):364–370, 1988.

[410] "COMPASS Collaboration". The COMPASS experiment at CERN. *Nuclear Instruments and Methods in Physics Research A*, 577:455–518, 2007.

[411] Konstantin Y. Bliokh, Mark R. Dennis, and Franco Nori. Relativistic electron vortex beams: Angular momentum and spin-orbit interaction. *Physical Review Letters*, 107:174802, 2011.

[412] Tyler R. Harvey, Vincenzo Grillo, and Benjamin J. McMorran. Stern-Gerlach-like approach to electron orbital angular momentum measurement. *Physical Review A*, 95:021801 (R), 2017.

[413] Ebrahim Karimi, Lorenzo Marrucci, Vincenzo Grillo, and Enrico Santamato. Spin-to-orbital angular momentum conversion and spin-polarization filtering in electron beams. *Physical Review Letters*, 108:044801, 2012.

[414] Vincenzo Grillo, Amir H. Tavabi, Federico Venturi, Hugo Larocque, Roberto Balboni, Gian Carlo Gazzadi, Stefano Frabboni, Peng Han Lu, Erfan Mafakheri, Frédéric Bouchard, Rafal E. Dunin-Borkowski, Robert W. Boyd, Martin P.J. Lavery, Miles J. Padgett, and Ebrahim Karimi. Measuring the orbital angular momentum spectrum of an electron beam. *Nature Communications*, 8:15536, 2017.

[415] D. Rossouw, M. Couillard, J. Vickery, E. Kumacheva, and G. A. Botton. Multipolar plasmonic resonances in silver nanowire antennas imaged with a subnanometer electron probe. *Nano Letters*, 11:1499–1504, 2011.

[416] Jens Dorfmüller, Ralf Vogelgesang, R Thomas Weitz, Carsten Rockstuhl, Christoph Etrich, Thomas Pertsch, Falk Lederer, and Klaus Kern. Fabry-Perot Resonances in One-Dimensional Plasmonic Nanostructures. *Nano Letters*, 9(6):2372–2377, 2009.

[417] Enrico Pomarico, Ye-Jin Kim, F. Javier García de Abajo, Oh-Hoon Kwon, Fabrizio Carbone, and Renske M. van der Veen. Ultrafast electron energy-loss spectroscopy in transmission electron microscopy. *MRS Bulletin*, 43:497–503, 2018.

[418] A. N. Grigorenko, M. Polini, and K. S. Novoselov. Graphene plasmonics. *Nature Photonics*, 6:749–758, 2012.

[419] D. N. Basov, M. M. Fogler, and F. J. García De Abajo. Polaritons in van der Waals materials. *Science*, 354(6309):1992, 2016.

[420] Ondrej L. Krivanek, Tracy C. Lovejoy, Niklas Dellby, Toshihiro Aoki, R. W. Carpenter, Peter Rez, Emmanuel Soignard, Jiangtao Zhu, Philip E. Batson, Maureen J. Lagos, Ray F. Egerton, and Peter A. Crozier. Vibrational spectroscopy in the electron microscope. *Nature*, 514(7521):209–212, 2014.

[421] Igor Zutic, Jaroslav Fabian, and S. Das Sarma. Spintronics: Fundamentals and applications. *Reviews of Modern Physics*, 76(2):323–410, 2004.

[422] M N Baibich, J M Broto, A Fert, F. Nguyen Van Dau, F Petroff, P Eitenne, G Creuzet, A Friederich, and J Chazelas. Giant magnetoresistance of (001)Fe/(001)Cr magnetic superlattices. *Physical Review Letters*, 61(21):2472–2475, 1988.

[423] G. Binasch, P. Grünberg, F. Saurenbach, and W. Zinn. Enhanced magnetoresistance in layered structures with antiferromagnetic interlayer exchange. *Physical Review B*, 39(7):4828–4830, 1989.

[424] U. K. Rößler, A. N. Bogdanov, and C. Pfleiderer. Spontaneous skyrmion ground states in magnetic metals. *Nature*, 442(7104):797–801, 2006.

[425] S. Mühlbauer, B. Binz, F. Jonietz, C. Pfleiderer, A. Rosch, A. Neubauer, R. Georgii, and P. Böni. Skyrmion lattice in a chiral magnet. *Science*, 323:915–919, 2009.

[426] Hiroshi Oike, Akiko Kikkawa, Naoya Kanazawa, Yasujiro Taguchi, Masashi Kawasaki, Yoshinori Tokura, and Fumitaka Kagawa. Interplay between topological and thermodynamic stability in a metastable magnetic skyrmion lattice. *Nature Physics*, 12:62–66, 2016.

[427] H Hopster and H P Oepen, editors. *Magnetic Microscopy and Nanostructures*. Springer, 2005.

[428] M. R. Scheinfein, J. Unguris, M. H. Kelley, D. T. Pierce, and R. J. Celotta. Scanning electron microscopy with polarization analysis (SEMPA). *Review of Scientific Instruments*, 61(10):2501–2527, 1990.

[429] Teruo Kohashi. Spin-polarized scanning electron microscopy. *Microscopy*, 62(1):177–191, 2013.

[430] N. Rougemaille and A. K. Schmid. Magnetic imaging with spin-polarized low-energy electron microscopy. *The European Physical Journal Applied Physics*, 50:20101, 2010.

[431] C. Phatak, A. K. Petford-Long, and M. De Graef. Recent advances in Lorentz microscopy. *Current Opinion in Solid State and Materials Science*, 20:107–114, 2016.

[432] Duc-The Ngo and Luise Theil Kuhn. In situ transmission electron microscopy for magnetic nanostructures. *Advances in Natural Sciences: Nanoscience and Nanotechnology*, 7:045001, 2016.

[433] M. E. Hale, H. W. Fuller, and H. Rubinstein. Magnetic domain observations by electron microscopy. *Journal of Applied Physics*, 30(5):789–791, 1959.

[434] H. Boersch and H. Raith. Elektronenmikroskopische Abbildung Weißscher Bezirke in dünnen ferromagnetischen Schichten. *Die Naturwissenschaften*, 46(20):574, 1959.

[435] M. Beleggia, M. A. Schofield, V. V. Volkov, and Y. Zhu. On the transport of intensity technique for phase retrieval. *Ultramicroscopy*, 102(1):37–49, 2004.

[436] S. McVitie and M. Cushley. Quantitative Fresnel Lorentz microscopy and the transport of intensity equation. *Ultramicroscopy*, 106(4-5):423–431, 2006.

[437] D. Paganin and K. A. Nugent. Noninterferometric phase imaging with partially coherent light. *Physical Review Letters*, 80(12):2586–2589, 1998.

[438] Kazuo Ishizuka and Brendan Allman. Phase measurement of atomic resolution image using transport of intensity equation. *Journal of Electron Microscopy*, 54(3):191–197, 2005.

[439] J.N. Chapman, A. B. Johnston, L. J. Heyderman, W. A.P. Nicholson, and B. Bormans. Coherent Magnetic Imaging by TEM. *IEEE Transactions on Magnetics*, 30(6):4479–4484, 1994.

[440] Nara Rubiano Da Silva, Marcel Möller, Armin Feist, Henning Ulrichs, Claus Ropers, and Sascha Schäfer. Nanoscale Mapping of Ultrafast Magnetization Dynamics with Femtosecond Lorentz Microscopy. *Physical Review X*, 8(3):31052, 2018.

[441] Takuro Nagai, Koji Kimoto, Koji Inoke, and Masaki Takeguchi. Real-space observation of nanoscale magnetic phase separation in dysprosium by aberration-corrected Lorentz microscopy. *Physical Review B*, 96:100405(R), 2017.

[442] Hyun Soon Park, Xiuzhen Yu, Shinji Aizawa, Toshiaki Tanigaki, Tetsuya Akashi, Yoshio Takahashi, Tsuyoshi Matsuda, Naoya Kanazawa, Yoshinori Onose, Daisuke Shindo, Akira Tonomura, and Yoshinori Tokura. Observation of the magnetic flux and three-dimensional structure of skyrmion lattices by electron holography. *Nature Nanotechnology*, 9(5):337–342, 2014.

[443] N. H. Dekkers and H. de Lang. Differential Phase Contrast in a STEM. *Optik*, 41(4):452–456, 1974.

[444] J. N. Chapman, P. E. Batson, E. M. Waddell, and R. P. Ferrier. The direct determination of magnetic domain wall profiles by differential phase contrast electron microscopy. *Ultramicroscopy*, 3:203–214, 1978.

[445] S. Majert and H. Kohl. High-resolution STEM imaging with a quadrant detector-Conditions for differential phase contrast microscopy in the weak phase object approximation. *Ultramicroscopy*, 148:81–86, 2015.

[446] Takao Matsumoto, Yuji Kohno, Yeong-gi So, Hidetaka Sawada, Yuichi Ikuhara, and Naoya Shibata. Direct observation of Σ7 domain boundary core structure in magnetic skyrmion lattice. *Science Advances*, 2:e1501280, 2016.

[447] D McGrouther, R J Lamb, M Krajnak, S McFadzean, S McVitie, R L Stamps, A O Leonov, A N Bogdanov, and Y Togawa. Internal structure of hexagonal skyrmion lattices in cubic helimagnets. *New Journal of Physics*, 18(9):095004, 2016.

[448] M. J. Goringe and J. P. Jakubovics. Electron diffraction from periodic magnetic fields. *The Philosophical Magazine: A Journal of Theoretical Experimental and Applied Physics*, 15:393–403, 1967.

[449] R. H. Wade. Electric Diffraction from a Magnetic Phase Grating. *Phys. Status Solidi*, 19:847, 1967.

[450] T. Koyama, Y. Togawa, K. Takenaka, and S. Mori. Ferromagnetic microstructures in the ferromagnetic metallic phase of La0.825Sr0.175MnO3. *Journal of Applied Physics*, 111(7):109–112, 2012.

[451] Y. Togawa, T. Koyama, K. Takayanagi, S. Mori, Y. Kousaka, J. Akimitsu, S. Nishihara, K. Inoue, A. S. Ovchinnikov, and J. Kishine. Chiral magnetic soliton lattice on a chiral helimagnet. *Physical Review Letters*, 108(10):21–25, 2012.

[452] Tsukasa Koyama, Shin Ichiro Yano, Yoshihiko Togawa, Yusuke Kousaka, Shigeo Mori, Katsuya Inoue, Jun Ichiro Kishine, and Jun Akimitsu. Unconventional magnetic domain structure in the ferromagnetic phase of MnP single crystals. *Journal of the Physical Society of Japan*, 81:043701, 2012.

[453] Y. Togawa, T. Koyama, Y. Nishimori, Y. Matsumoto, S. McVitie, D. McGrouther, R. L. Stamps, Y. Kousaka, J. Akimitsu, S. Nishihara, K. Inoue, I. G. Bostrem, Vl E. Sinitsyn, A. S. Ovchinnikov, and J. Kishine. Magnetic soliton confinement and discretization effects arising from macroscopic coherence in a chiral spin soliton lattice. *Physical Review B*, 92(22):220412(R), 2015.

[454] S. Seki and M Mochuzuki. *Skyrmions in magnetic materials*. Springer, London, 2016.

[455] Naoto Nagaosa and Yoshinori Tokura. Topological properties and dynamics of magnetic skyrmions. *Nature Nanotechnology*, 8(12):899–911, 2013.

[456] Giovanni Finocchio, Felix Büttner, Riccardo Tomasello, Mario Carpentieri, and Mathias Kläui. Magnetic skyrmions: From fundamental to applications. *Journal of Physics D: Applied Physics*, 49:423001, 2016.

[457] Albert Fert, Nicolas Reyren, and Vincent Cros. Magnetic skyrmions: Advances in physics and potential applications. *Nature Reviews Materials*, 2:17031, 2017.

[458] T. H. R. Skyrme. A unified theory of mesons and baryons. *Nuclear Physics*, 31:556–569, 1962.

[459] A. Bogdanov and D. A. Yablonskii. Thermodynamically stable "vortices" states in magnetically ordered crystals. The mixed state of magnets. *Zhurnal Eksperimentalnoy i Teoriticheskoy phisiki*, 95(1):178–182, 1989.

[460] A. Bogdanov and A. Hubert. Thermodynamically stable magnetic vortex states in magnetic crystals. *Journal of Magnetism and Magnetic Materials*, 138(3):255–269, 1994.

[461] A. N. Bogdanov and U. K. Rößler. Chiral Symmetry Breaking in Magnetic Thin Films and Multilayers. *Physical Review Letters*, 87(3):037203, 2001.

[462] C. Schütte. *Skyrmions and Monopoles in Chiral Magnets & Correlated Heterostructures*. PhD thesis, University of Cologne, 2014.

[463] William Legrand, Jean Yves Chauleau, Davide Maccariello, Nicolas Reyren, Sophie Collin, Karim Bouzehouane, Nicolas Jaouen, Vincent Cros, and Albert Fert. Hybrid chiral domain walls and skyrmions in magnetic multilayers. *Science Advances*, 4:eaat0415, 2018.

[464] Shilei Zhang, Gerrit van der Laan, Jan Müller, Lukas Heinen, Markus Garst, Andreas Bauer, Helmuth Berger, Christian Pfleiderer, and Thorsten Hesjedal. Reciprocal space tomography of 3D skyrmion lattice order in a chiral magnet. *Proceedings of the National Academy of Sciences*, 115(25):6386–6391, 2018.

[465] X. Z. Yu, N. Kanazawa, Y. Onose, K. Kimoto, W. Z. Zhang, S. Ishiwata, Y. Matsui, and Y. Tokura. Near room-temperature formation of a skyrmion crystal in thin-films of the helimagnet FeGe. *Nature Materials*, 10(2):106–109, 2011.

[466] Albert Fert, Vincent Cros, and João Sampaio. Skyrmions on the track. *Nature Nanotechnology*, 8(3):152–156, 2013.

[467] J. S. White, K. Prša, P. Huang, A. A. Omrani, I. Živković, M. Bartkowiak, H. Berger, A. Magrez, J. L. Gavilano, G. Nagy, J. Zang, and H. M. Rønnow. Electric-field-induced skyrmion distortion and giant lattice rotation in the magnetoelectric insulator Cu2OSeO3. *Physical Review Letters*, 113:107203, 2014.

[468] M. Mochizuki, X. Z. Yu, S. Seki, N. Kanazawa, W. Koshibae, J. Zang, M. Mostovoy, Y. Tokura, and N. Nagaosa. Thermally driven ratchet motion of a skyrmion microcrystal and topological magnon Hall effect. *Nature Materials*, 13:241–246, 2014.

[469] N. Ogawa, S. Seki, and Y. Tokura. Ultrafast optical excitation of magnetic skyrmions. *Scientific Reports*, 5:9552, 2015.

[470] J. S. White, I. Levatić, A. A. Omrani, N. Egetenmeyer, K. Prša, I. Živković, J. L. Gavilano, J. Kohlbrecher, M. Bartkowiak, H. Berger, and H. M. Rønnow. Electric field control of the skyrmion lattice in Cu 2OSeO3. *Journal of Physics Condensed Matter*, 24:432201, 2012.

[471] Y. Onose, Y. Okamura, S. Seki, S. Ishiwata, and Y. Tokura. Observation of magnetic excitations of skyrmion crystal in a helimagnetic insulator Cu2OSeO3. *Physical Review Letters*, 109:037603, 2012.

[472] T. Schulz, R. Ritz, A. Bauer, M. Halder, M. Wagner, C. Franz, C. Pfleiderer, K. Everschor, M. Garst, and A. Rosch. Emergent electrodynamics of skyrmions in a chiral magnet. *Nature Physics*, 8(4):301–304, 2012.

[473] X. Z. Yu, N. Kanazawa, W. Z. Zhang, T. Nagai, T. Hara, K. Kimoto, Y. Matsui, Y. Onose, and Y. Tokura. Skyrmion flow near room temperature in an ultralow current density. *Nature Communications*, 3:988, 2012.

[474] F. Jonietz, S. Mulbauer, C. Pfleiderer, A. Neubauer, W. Munzer, A. Bauer, T. Adams, R. Georgii, P. Boni, R. A. Duine, K. Everschor, M. Garst, and A. Rosch. Spin Transfer Torques in MnSi. *Science*, 330:1648–1652, 2010.

[475] Pin Jui Hsu, André Kubetzka, Aurore Finco, Niklas Romming, Kirsten Von Bergmann, and Roland Wiesendanger. Electric-field-driven switching of individual magnetic skyrmions. *Nature Nanotechnology*, 12(2):123–126, 2017.

[476] Marine Schott, Anne Bernand-Mantel, Laurent Ranno, Stefania Pizzini, Jan Vogel, Hélène Béa, Claire Baraduc, Stéphane Auffret, Gilles Gaudin, and Dominique Givord. The Skyrmion Switch: Turning Magnetic Skyrmion Bubbles on and off with an Electric Field. *Nano Letters*, 17:3006–3012, 2017.

[477] Seonghoon Woo, Kai Litzius, Benjamin Krüger, Mi Young Im, Lucas Caretta, Kornel Richter, Maxwell Mann, Andrea Krone, Robert M. Reeve, Markus Weigand, Parnika Agrawal, Ivan Lemesh, Mohamad Assaad Mawass, Peter Fischer, Mathias Kläui, and Geoffrey S.D. Beach. Observation of room-temperature magnetic skyrmions and their current-driven dynamics in ultrathin metallic ferromagnets. *Nature Materials*, 15(5):501–506, 2016.

[478] Niklas Romming, Christian Hanneken, Matthias Menzel, Jessica E. Bickel, Boris Wolter, Kirsten von Bergmann, André Kubetzka, and Roland Wiesendanger. Writing and Deleting Single Magnetic Skyrmions. *Science*, 341:636–639, 2013.

[479] Kai Litzius, Ivan Lemesh, Benjamin Krüger, Pedram Bassirian, Lucas Caretta, Kornel Richter, Felix Büttner, Koji Sato, Oleg A. Tretiakov, Johannes Förster, Robert M. Reeve, Markus Weigand, Iuliia Bykova, Hermann Stoll, Gisela Schütz, Geoffrey S.D. Beach, and Mathias Klaüi. Skyrmion Hall effect revealed by direct time-resolved X-ray microscopy. *Nature Physics*, 13:170–175, 2017.

[480] Xiuzhen Yu, Daisuke Morikawa, Yusuke Tokunaga, Masashi Kubota, Takashi Kurumaji, Hiroshi Oike, Masao Nakamura, Fumitaka Kagawa, Yasujiro Taguchi, Taka Hisa Arima, Masashi Kawasaki, and Yoshinori Tokura. Current-Induced Nucleation and Annihilation of Magnetic Skyrmions at Room Temperature in a Chiral Magnet. *Advanced Materials*, 29:1606178, 2017.

[481] Felix Büttner, C. Moutafis, M. Schneider, B. Krüger, C. M. Günther, J. Geilhufe, C. V.Korff Schmising, J. Mohanty, B. Pfau, S. Schaffert, A. Bisig, M. Foerster, T. Schulz, C. A.F. Vaz, J. H. Franken, H. J.M. Swagten, M. Kläui, and S. Eisebitt. Dynamics and inertia of skyrmionic spin structures. *Nature Physics*, 11(3):225–228, 2015.

[482] N. S. Kiselev, A. N. Bogdanov, R. Schäfer, and U. K. Rössler. Comment on "giant skyrmions stabilized by dipole-dipole interactions in thin ferromagnetic films". *Physical Review Letters*, 107:179701, 2011.

[483] C. D. Stanciu, F. Hansteen, A. V. Kimel, A. Kirilyuk, A. Tsukamoto, A. Itoh, and Th Rasing. All-optical magnetic recording with circularly polarized light. *Physical Review Letters*, 99:047601, 2007.

[484] T. Ogasawara, N. Iwata, Y. Murakami, H. Okamoto, and Y. Tokura. Submicron-scale spatial feature of ultrafast photoinduced magnetization reversal in TbFeCo thin film. *Applied Physics Letters*, 94:162507, 2009.

[485] M. Finazzi, M. Savoini, A. R. Khorsand, A. Tsukamoto, A. Itoh, L. Duò, A. Kirilyuk, Th Rasing, and M. Ezawa. Laser-induced magnetic nanostructures with tunable topological properties. *Physical Review Letters*, 110:177205, 2013.

[486] Andrei Kirilyuk, Alexey V. Kimel, and Theo Rasing. Ultrafast optical manipulation of magnetic order. *Reviews of Modern Physics*, 82(3):2731–2784, 2010.

[487] A. R. Khorsand, M. Savoini, A. Kirilyuk, A. V. Kimel, A. Tsukamoto, A. Itoh, and Th Rasing. Role of magnetic circular dichroism in all-optical magnetic recording. *Physical Review Letters*, 108:127205, 2012.

[488] Wataru Koshibae and Naoto Nagaosa. Creation of skyrmions and antiskyrmions by local heating. *Nature Communications*, 5:5148, 2014.

[489] Xiuzhen Yu, Daisuke Morikawa, Tomoyuki Yokouchi, Kiyou Shibata, Naoya Kanazawa, Fumitaka Kagawa, Taka hisa Arima, and Yoshinori Tokura. Aggregation and collapse dynamics of skyrmions in a non-equilibrium state. *Nature Physics*, 14(8):832–836, 2018.

[490] Masaya Uchida, Yoshinori Onose, Yoshio Matsui, and Yoshinori Tokura. Real-space observation of helical spin order. *Science*, 311(5759):359–361, 2006.

[491] A. O. Leonov, Y. Togawa, T. L. Monchesky, A. N. Bogdanov, J. Kishine, Y. Kousaka, M. Miyagawa, T. Koyama, J. Akimitsu, Ts Koyama, K. Harada, S. Mori, D. McGrouther, R. Lamb, M. Krajnak, S. McVitie, R. L. Stamps, and K. Inoue. Chiral Surface Twists and Skyrmion Stability in Nanolayers of Cubic Helimagnets. *Physical Review Letters*, 117:087202, 2016.

[492] M. N. Wilson, A. B. Butenko, A. N. Bogdanov, and T. L. Monchesky. Chiral skyrmions in cubic helimagnet films: The role of uniaxial anisotropy. *Physical Review B - Condensed Matter and Materials Physics*, 89:094411, 2014.

[493] A. Bauer, M. Garst, and C. Pfleiderer. History dependence of the magnetic properties of single-crystal Fe1-xCoxSi. *Physical Review B*, 93:235144, 2016.

[494] K. Karube, J. S. White, N. Reynolds, J. L. Gavilano, H. Oike, A. Kikkawa, F. Kagawa, Y. Tokunaga, H. M. Rønnow, Y. Tokura, and Y. Taguchi. Robust metastable skyrmions and their triangular-square lattice structural transition in a high-temperature chiral magnet. *Nature Materials*, 15(12):1237–1242, 2016.

[495] Johannes Wild, Thomas N G Meier, Simon Pöllath, Matthias Kronseder, Andreas Bauer, Alfonso Chacon, Marco Halder, Marco Schowalter, Andreas Rosenauer, Josef Zweck, Jan Müller, Achim Rosch, Christian Pfleiderer, and Christian H Back. Entropy-limited topological protection of skyrmions. *Science Advances*, 3:e1701704, 2017.

[496] Taro Nakajima, Yasuhiro Inamura, Takayoshi Ito, Kazuki Ohishi, Hiroshi Oike, Fumitaka Kagawa, Akiko Kikkawa, Yasujiro Taguchi, Kazuhisa Kakurai, Yoshinori Tokura, and Taka Hisa Arima. Phase-transition kinetics of magnetic skyrmions investigated by stroboscopic small-angle neutron scattering. *Physical Review B*, 98:014424, 2018.

[497] A. Chacon, L. Heinen, M. Halder, A. Bauer, W. Simeth, S. Mühlbauer, H. Berger, M. Garst, A. Rosch, and C. Pfleiderer. Observation of two independent skyrmion phases in a chiral magnetic material. *Nature Physics*, 14(9):936–941, 2018.

[498] Andreas Bauer, Alfonso Chacon, Marco Halder, and Christian Pfleiderer. Skyrmion Lattices Far from Equilibrium. In Axel Zang, Jiadong; Cros, Vincent; Hoffmann, editor, *Topology in Magnetism*. Springer, springer edition, 2018.

[499] Achim Rosch. Skyrmions: Moving with the current. *Nature Nanotechnology*, 8(3):160–161, 2013.

[500] Achim Rosch. Spintronics: Electric control of skyrmions. *Nature Nanotechnology*, 12(2):103–104, 2017.

[501] V. Guritanu, D. van der Marel, J. Teyssier, T. Jarlborg, H. Wilhelm, M. Schmidt, and F. Steglich. Optical evidence for heavy charge carriers in FeGe. *Physical Review B*, 75:155114, 2007.

[502] Philip B. Allen. Theory of thermal relaxation of electrons in metals. *Physical Review Letters*, 59(13):1460–1463, 1987.

[503] H. Wilhelm, A. O. Leonov, U. K. Rößler, P. Burger, F. Hardy, C. Meingast, M. E. Gruner, W. Schnelle, M. Schmidt, and M. Baenitz. Scaling study and thermodynamic properties of the cubic helimagnet FeGe. *Physical Review B*, 94:144424, 2016.

[504] N. A. Porter, J. C. Gartside, and C. H. Marrows. Scattering mechanisms in textured FeGe thin films: Magnetoresistance and the anomalous Hall effect. *Physical Review B*, 90:024403, 2014.

[505] Tim Eggebrecht, Marcel Möller, J. Gregor Gatzmann, Nara Rubiano Da Silva, Armin Feist, Ulrike Martens, Henning Ulrichs, Markus Münzenberg, Claus Ropers, and Sascha Schäfer. Light-Induced Metastable Magnetic Texture Uncovered by in situ Lorentz Microscopy. *Physical Review Letters*, 118:097203, 2017.

[506] Haifeng Du, Renchao Che, Lingyao Kong, Xuebing Zhao, Chiming Jin, Chao Wang, Jiyong Yang, Wei Ning, Runwei Li, Changqing Jin, Xianhui Chen, Jiadong Zang, Yuheng Zhang, and Mingliang Tian. Edge-mediated skyrmion chain and its collective dynamics in a confined geometry. *Nature Communications*, 6:8504, 2015.

[507] Jan Müller, Achim Rosch, and Markus Garst. Edge instabilities and skyrmion creation in magnetic layers. *New Journal of Physics*, 18:065006, 2016.

[508] Xuebing Zhao, Chiming Jin, Chao Wang, Haifeng Du, Jiadong Zang, Mingliang Tian, Renchao Che, and Yuheng Zhang. Direct imaging of magnetic field-driven transitions of skyrmion cluster states in FeGe nanodisks. *Proceedings of the National Academy of Sciences*, 113(18):4918–4923, 2016.

[509] Soong Geun Je, Pierre Vallobra, Titiksha Srivastava, Juan Carlos Rojas-Sánchez, Thai Ha Pham, Michel Hehn, Gregory Malinowski, Claire Baraduc, Stéphane Auffret, Gilles Gaudin, Stéphane Mangin, Hélène Béa, and Olivier Boulle. Creation of Magnetic Skyrmion Bubble Lattices by Ultrafast Laser in Ultrathin Films. *Nano Letters*, 18:7362–7371, 2018.

[510] Rohollah Khoshlahni, Alireza Qaiumzadeh, Anders Bergman, and Arne Brataas. Ultrafast generation and dynamics of isolated skyrmions in antiferromagnetic insulators. *Physical Review B*, 99:054423, 2019.

[511] C. Moreau-Luchaire, C. Moutafis, N. Reyren, J. Sampaio, C. A.F. Vaz, N. Van Horne, K. Bouzehouane, K. Garcia, C. Deranlot, P. Warnicke, P. Wohlhüter, J. M. George, M. Weigand, J. Raabe, V. Cros, and A. Fert. Additive interfacial chiral interaction in multilayers for stabilization of small individual skyrmions at room temperature. *Nature Nanotechnology*, 11(5):444–448, 2016.

[512] Soong Geun Je, Duck Ho Kim, Sang Cheol Yoo, Byoung Chul Min, Kyung Jin Lee, and Sug Bong Choe. Asymmetric magnetic domain-wall motion by the Dzyaloshinskii-Moriya interaction. *Physical Review B*, 88(21):214401, 2013.

[513] Min He, Gang Li, Zhaozhao Zhu, Ying Zhang, Licong Peng, Rui Li, Jianqi Li, Hongxiang Wei, Tongyun Zhao, X Zhang, Shouguo Wang, Shi-zeng Lin, Lin Gu, Guoqiang Yu, J W Cai, and Bao-gen Shen. Evolution of topological skyrmions across the spin reorientation transition in Pt/Co/Ta multilayers. *Physical Review B*, 97:174419, 2018.

[514] Senfu Zhang, Junwei Zhang, Yan Wen, Eugene M Chudnovsky, and Xixiang Zhang. Thermally assisted skyrmions creation in Pt/Co/Ta multilayer films. *arXiv:1807.05335*, 2018.

Gabriele Berruto – CURRICULUM VITÆ

Address: Av. de Longemalle 7, 1020 Renens VD, CH
Nationality: Italian
Birth: May 11th 1990, Sanremo, IT
Phone: +41 787547125
E-mail: gabriele.berruto@epfl.ch
gabriele.berruto@gmail.com
Skype: gabriele.ghil.berruto

Education

April 2015 – June 2019	**Ph.D., physics** École Polytechnique Fédérale de Lausanne, CH Topics: ultrafast electron microscopy and spectroscopy, plasmonics, nonequilibrium physics, diffraction, magnetism, skyrmions, in-situ phase transformations. Title: *Fast and ultrafast electron microscopies for skyrmions and plasmonics.* Group: Laboratory for ultrafast microscopy and electron scattering. Thesis supervisor: Fabrizio Carbone.
Dec. 2014 – April 2015	**Internship** École Polytechnique Fédérale de Lausanne, CH Topics: ultrafast laser physics.
Sept. 2012 – Oct. 2014	**M.Sc., physics** Università degli Studi di Trieste, IT Topics: condensed matter physics, experimental physics, nonlinear optics, time-domain spectroscopy. Title: *Pump-probe experiments with ultrashort mid-infrared light pulses.* Thesis supervisor: Daniele Fausti. Thesis co-supervisors: Fulvio Parmigiani, Francesco Randi. Final mark: 110/110 cum laude
Sept. 2013 – Febr. 2014	**Exchage student** Universidad Complutense de Madrid, ES Topics: nanophysics, advanced materials.
Sept. 2009 – Sept. 2012	**B.Sc., physics** Università degli Studi di Trieste, IT Final mark: 110/110 cum laude
Sept. 2004 – July 2009	**High school** Liceo Scientifico 'Aprosio', Ventimiglia, IT Final mark: 100/100

Research projects (selected)

December 2014 – April 2019	**Ultrafast electron microscopies** EPFL Laboratory management, installation, characterization, and optimization of different systems, including ultrafast mode-locked and Q-switched lasers, nonlinear optics and pump-probe setups, direct detection cameras, transmission electron microscopes for imaging, diffraction, and spectroscopy.
September 2015 – April 2019	**Photon-induced near-field electron microscopy** EPFL Experimental study of the inelastic interaction between free electrons and electromagnetic fields, either localized or near a surface. Electron energy gain and loss spectroscopy, and energy-filtered transmission electron microscopy of those fields. Development of new techniques to image propagating plasmons in a TEM.
March 2018 – August 2018	**Ultrafast reflection high-energy electron diffraction** EPFL Study of the photoinduced Verwey transition in an ultrafast electron crystallography setup.
April 2015 – March 2018	**Optical manipulation of spin textures** EPFL Imaging of magnetic skyrmions in Lorentz microscopy. Bloch and Néel type. Use of laser pulses to promote the skyrmion creation, annihilation, and change in the magnetization texture.
February 2014 – October 2014	**Ultrafast laser physics - mid-IR source** Università di Trieste Development, implementation and characterization of an ultrafast mid-IR CEP-stable source, based on two twin OPAs sharing the same white-light seed, and a DFG stage. $5 < \lambda[\mu\text{m}] < 18$, i.e. $70 < h\nu[\text{meV}] < 250$.

Publications and conferences

Peer-reviewed publications

G. Berruto*, I. Madan*, Y. Murooka, G.M. Vanacore, E. Pomarico, J. Rajeswari, R.J. Lamb, P. Huang, A.J. Kruchkov, Y. Togawa, T. LaGrange, D. McGrouther, H.M. Rønnow, and F. Carbone. Laser-induced skyrmion writing and erasing in an ultrafast cryo-lorentz transmission electron microscope, in *Physical Review Letters*, vol. 120, n. 11, p. 117201, 2018.

G.M. Vanacore*, G. Berruto*, I. Madan, E. Pomarico, P. Biagioni, R.J. Lamb, D. McGrouther, O. Reinhardt, I. Kaminer, B. Barwick, H. Larocque, V. Grillo, E. Karimi, F.J. García de Abajo, and F. Carbone. Generation and control of an ultrafast electron vortex beam via chiral plasmonic near-fields, in *Nature Materials* vol. 18, p. 573-579, 2019.

G.M. Vanacore*, I. Madan*, G. Berruto, K. Wang, E. Pomarico, R.J. Lamb, D. McGrouther, I. Kaminer, B. Barwick, F.J. García de Abajo, and F. Carbone. Attosecond coherent control of free-electron wave functions using semi-infinite light fields, in *Nature Communications*, vol. 9, p. 2694, 2018.

I. Madan*, G.M. Vanacore*, E. Pomarico, G. Berruto, R.J. Lamb, D. McGrouther, T.T.A. Lummen, T. Latychevskaia, F.J. García de Abajo, and F. Carbone. Holographic imaging of electromagnetic fields via electron-light quantum interference, in *Science Advances*, vol. 5, n. 5, eaav8358, 2019.

E. Pomarico, I. Madan, G. Berruto, G.M. Vanacore, K. Wang, I. Kaminer, F.J. García de Abajo, and F. Carbone. meV resolution in laser-assisted energy-filtered transmission electron microscopy, in *ACS Photonics*, vol. 5, n. 3, p. 759-764, 2018.

T.T.A. Lummen, R.J. Lamb, G. Berruto, T. LaGrange, L. Dal Negro, F.J. García De Abajo, D. McGrouther, B. Barwick, and F. Carbone. Imaging and controlling plasmonic interference fields at buried interfaces, in *Nature Communications*, vol. 7, p. 13156, 2016.

T. Latychevskaia*, S.-K. Son*, Y. Yang, D. Chancellor, M. Brown, S. Ozdemir, I. Madan, G. Berruto, F. Carbone, A. Mishchenko, and K.S. Novoselov. Stacking transition in rhombohedral graphite, in *Frontiers in Physics*, vol. 14, n. 1, p. 13608, 2019.

*: Equally contributing authors.

Articles in preparation

G. Berruto, G.M. Vanacore, T.T.A. Lummen, [...] and F. Carbone. Exotic electron-plasmon effects in high-fluence PINEM, *in preparation*, 2019.†

G. Berruto, I. Madan, S. Saha, [...] F. Carbone, and L. Heydermann. On magnetic field and optical pulse excitations of interfacial skyrmions in a stacked Pt/Co multilayer, *in preparation*, 2019.†

F. Pennacchio, G.M. Vanacore, G. Berruto, [...] and F. Carbone. The Verwey transition in magnetite studied by ultrafast electron crystallography, *in preparation*, 2019.†

G. Berruto, I. Madan, G.M. Vanacore, [...] and F. Carbone. Imaging radiated light wavefronts in an electron microscope, *in preparation*, 2019.†

†: Tentative title and partial author list.

Seminars (selection)

Contributed talk at the APS March meeting, Boston, US, March 2019.

Contributed talk at the DPG spring meeting, Berlin, DE, March 2018.

Contributed talk at the Joint SPS-ÖPG Annual Meeting, Geneva, CH, August 2017.

Invited lecture (on behalf of F. Carbone/I. Madan) at the 'New trends in chiral magnetism' Summer School, Lausanne, CH, August 2018.

Invited talk at the Superstripes conference, Ischia, IT, July 2019.

Invited talk at the yearly symposium of the interdisciplinary center of electron microscopy (CIME), Lausanne, CH, February 2018.

Invited talk at the accelerator group, Department of Physics, University of California Los Angeles (UCLA), Los Angeles, US, March 2019.

Invited talk at the 'POB' seminar of the EPFL Photonics Chapter, Lausanne, CH, March 2018.

Posters (selection)

'New Trends in Chiral Magnetism' Summer School, Lausanne, CH, August 2018.

'Molecular Ultrafast Science and Technology' (MUST) Annual Meeting, Grindelwald, CH, January 2018.

'Femtochemistry' (FEMTO13) Conference, Cancun, MX, August 2017.

'Electron Microscopy with High Temporal Resolution' (EMHTR) workshop, Strasbourg, FR, May 2017.

'Skyrmion Magnetism' (SKYMAG) Conference, Paris, FR, May 2017.

Other conferences attended (selection)

'Electronic States and Phases Induced by Electric or Optical Impacts' (IMPACT2016) Summer School, Cargèse, FR, August 2016.

'Imaging with Femtosecond Electron and X-ray pulses' (IFEXS) workshop, Trieste, IT, February 2016.

'Molecular Ultrafast Science and Technology' (MUST) Annual Meeting, Engelberg, CH, January 2015 and 2016.

Teaching

Teaching assistant for courses

- Physique du solide I (Solid State Physics I), 3rd year B.Sc. physics, EPFL.
  Lecturers: Fabrizio Carbone, Marina Pivetta.
  Years: 2015/2016, 2016/2018, 2017/2018.
  Language: French.
  Topics: Free electrons, Drude, Sommerfeld, Bloch, crystal structure.

- Physique du solide I (Solid State Physics I), 3rd year B.Sc. physics, EPFL.
  Lecturers: Henrik Rønnow.
  Years: 2018/2019.
  Language: French.
  Topics: Free electrons, Drude, Sommerfeld, Bloch, crystal structure.

- Solid State Physics II, 3rd year B.Sc. physics, EPFL.
  Lecturers: Oleg Yazyev.
  Years: 2016, 2017, 2018.
  Language: English.
  Topics: Tight-binding, transport, magnetism, phonons, superconductivity.

Organization tasks

Safety delegate ('CoSec') of the LUMES group in EPFL, 2015–2019.

Risk assesment and management, hazard reduction, and promotion of safety culture and procedures within the group, working in collaboration with the Safety Department.

FSB Running Team co-organizer, 2016–2018.

Promotion, management, and training organizer of the running team of the Faculty of Basic Sciences, EPFL, with up to ~70 *runners.*

Awards and distinctions

- 2018 'Outstanding teaching assistant' prize by the Doctoral School in Physics, EPFL.
- 2012–2014 'Luciano Fonda' scholarship , founded by Sincrotrone Trieste (Trieste's synchrotron and free electron laser).

  2 years full M.Sc. scholarship for excellent students in condensed matter and synchrotron-related areas, Trieste.
- 2013/2014 student mobility 'Erasmus' 6-months scholarship, Madrid.
- 2011/2012 'G. Brautti' prize, awarded in September 2013.

  Intended to award one excellent B.Sc. physics student from the university of Bari, Lecce, or Trieste.
- 2009–2012 'Luciano Fonda' scholarship, founded by Collegio per le Scienze 'L. Fonda'.

  3 years full B.Sc. scholarship for excellent students in physics, Trieste.

Languages

Italian: native speaker. **English**: full professional proficiency.
French: advanced level. **Spanish**: advanced level.

Other interests

Sport: track and field, middle-distance and long-distance running.
Outdoor activities: hiking, mountaineering, some ski.
Music: studied clarinet, mostly classical. 5^{th} year exam at the Conservatory of Genova 'N. Paganini', IT, 2008. [Diploma 7 years total.]

**Ce document a été imprimé au Centre d'impression EPFL,
imprimerie climatiquement neutre, certifiée myClimate.**